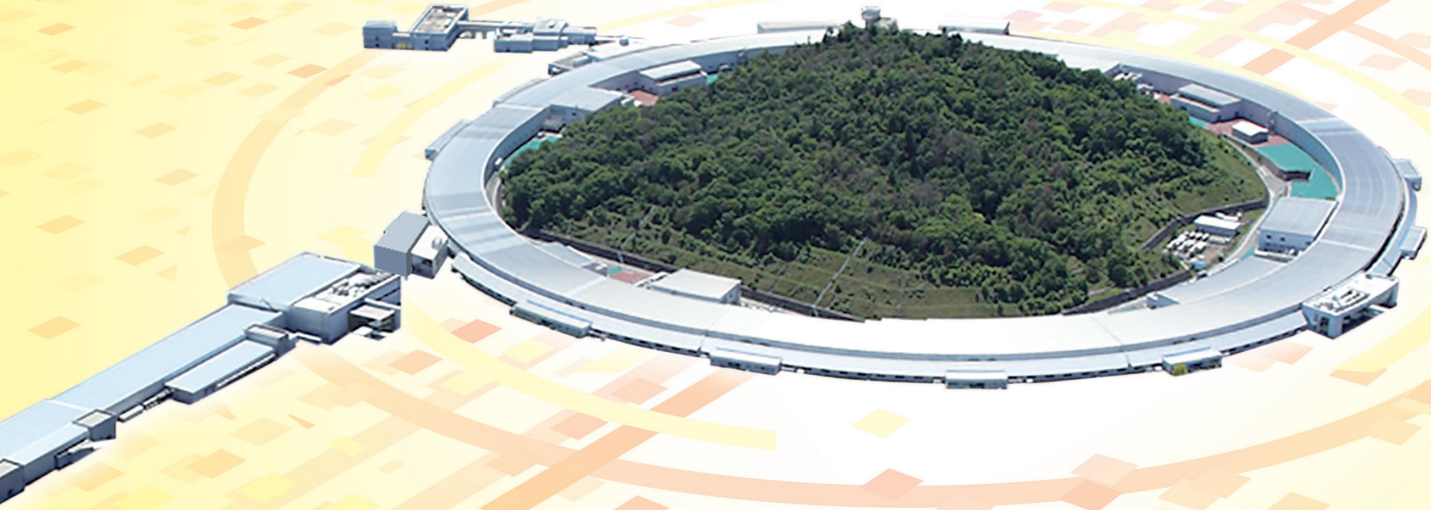

Research Frontiers 2023

SPring-8
SACLA

ISSN 2433-5126
SPring-8 Document D2024-010

SPring-8/SACLA Research Frontiers 2023

CONTENTS

Physical Science

Chemical Science

Earth & Planetary Science

Industrial Applications

Accelerators & Beamlines Frontiers 110

Facility Status 114

Note: The principal publication(s) concerning each article is indicated with all author's names in italics in the list of references.

PREFACE

We are pleased to announce the publication of SPring-8/SACLA Research Frontiers 2023. JASRI's mission is to support users and ensure transparent and fair selection of experimental proposals as a user promotion organization of SPring-8 and SACLA registered with the Ministry of Education, Culture, Sports, Science and Technology of Japan (MEXT). Another mission of JASRI is to manage SPring-8 and SACLA, which are owned by RIKEN. In other words, JASRI works closely with RIKEN to operate and maintain SPring-8 and SACLA, located on the same campus, whose synergy produces groundbreaking results.

SPring-8 welcomed over 15,000 users in 2023, who came to conduct more than 2,000 experiments. Currently, SPring-8 users publish upwards of 1,000 research papers annually. Meanwhile, SACLA users have published over 50 research papers.

In 2023, several SPring-8 and SACLA users were awarded prestigious prizes for their achievements in science and technology. For example, Professor Kazuto Yamauchi (Osaka University) was awarded the Medal with Purple Ribbon in the fall of 2023 for his contributions to the development and commercialization of high-precision X-ray mirrors for SPring-8 and SACLA. Professor Ryosuke Kodama (Osaka University) was also awarded the Medal with Purple Ribbon in the fall of 2023 for his research in plasma science. Dr. Saori Imada-Kawaguchi (JASRI) was awarded the Morita Prize by the Japanese Association of University Women for her contribution to the development of synchrotron radiation X-ray measurements of liquid samples at high temperatures and pressures and its application to the study of extraterrestrial nuclei and meteorites.

This volume contains two comprehensive reviews. The first review, written by Professor Kazuto Yamauchi (Osaka University) presents his group's research and development pertaining to focusing mirrors for synchrotron X-rays. The ultimate focusing of XFEL beams at SACLA BL3 down to 7 nm was achieved and successfully applied for the observation of Ly_{α} and Ly_{β} emission from Cr films. In another review, Dr. Alfred Q. R. Baron (RIKEN SPring-8 Center/JASRI), describes his group's recent endeavor regarding high-pressure science, liquids, thin films, and composite materials using meV-resolved inelastic X-ray scattering.

In the main part of this volume, active users of SPring-8 describe the essence of their results in fields including Life Science, Physical Science, Chemical Science, Earth & Planetary Science, and Industrial Applications. In addition, the principal activity reports on SPring-8/SACLA facilities are included in the part and Accelerators & Beamlines Frontiers and Facility Status.

I am very grateful to the many authors and experts who contributed their papers this volume. Special thanks are due to Dr. Toyohiko Kinoshita, Ms. Marcia Obuti-Daté and the members of the editorial board for their continuous efforts.

Yoshiyuki Amemiya
President
Japan Synchrotron Radiation Research Institute (JASRI)

Editor's Note

This is the 2023 issue of SPring-8/SACLA Research Frontiers, which presents the outstanding scientific outcomes of SPring-8 and SACLA in 2022 and 2023. The best scientific achievements were selected annually from more than 1,000 papers published using SPring-8 or SACLA. Protein crystallography remains a highly active field, and research on a variety of functional materials aimed to achieving sustainable development goals (SDGs) is ongoing.

This issue contains two reviews. One is written by Prof. Kazuto Yamauchi (Osaka University), who is the leader in the development of the "OSAKA mirror." He introduced a method focus X-rays effectively using precisely fabricated optics. Consequently, ~7 nm focusing was realized. In the review, machining and polishing processes and figure-correction methods are introduced. The other review is written by Dr. Alfred Baron (RIKEN/SPring-8). He reviewed the activities and instrumentations of meV-resolution inelastic scattering experiments. The atomic dynamics of various materials are currently being investigated using the high-performance inelastic scattering X-ray monochromators at BL35XU and BL43LXU. In the review, examples of high-pressure science, liquids, thin films, and complex materials are introduced in addition to future plans.

SPring-8/SACLA Research Frontiers is composed primarily of two sections. The first presents the scientific results (Scientific Frontiers) and the second provides additional information regarding hard and soft infrastructures that support scientific research. Although some important parameters, such as the operation, time are provided in the second section, other information and more complete statistical data on the operation of SPring-8 and SACLA are available on the website, thus enabling access to more updated information (**http://www.spring8.or.jp/en/about_us/spring8data/**). Additionally, the full text of SPring-8/SACLA Research Frontiers is available on the SPring-8 website (**http://www.spring8.or.jp/en**). For the list of publications by SPring-8 users and staff, please visit the publication database at **http://www.spring8.or.jp/en/science/publication_database/**.

On behalf of all the editors, I would like to thank those who have helped us by recommending excellent research results suitable for publication in this issue, as well as the users, and staff of SPring-8, who have contributed their reports.

Toyohiko Kinoshita
Japan Synchrotron Radiation Research Institute (JASRI)

Editorial Board

Scientific Frontiers

Review Article

Ultimate condensation of synchrotron radiation X-rays and its application to exploring cutting-edge X-ray science

1. Introduction

Since their discovery by Röntgen in 1895, X-rays have played an indispensable role in a wide range of fields, including basic science, medicine, and engineering. In the fields of life science and material science, in particular, their high permeability to thick materials and their interactions with crystals and atoms have been effectively utilized, providing analytical methods that cannot be reproduced by other means. In recent years, high-brilliance X-ray sources such as SPring-8 have been widely utilized, and most recently, the X-ray free-electron laser has provided spatially coherent ultrashort pulsed X-rays, ushering in a new era of X-ray application technologies. These high brilliance X-ray sources have a significant advantage in increasing the photon density when focused on them because of their small source size and divergence. Consequently, the race to reduce the focus size has intensified worldwide since the late 1990s, and various optical elements, such as zone plates, lenses, and mirrors, have achieved focusing of 100 nm or less. Mirrors have advantages over other elements owing to their high focusing efficiency, large working distance, and low chromatic aberrations. However, the fabrication of mirrors is significantly more difficult than other elements. Since 2000, we have been involved in developing a precision X-ray mirror from the standpoint of optical fabrication and metrology and have achieved the world's first sub-30-nm focusing and sub-10-nm focusing by compensation optics [1,2]. This paper discusses the accuracy required on the mirror surface to condense coherent X-rays down to the theoretical limit owing to diffraction and the fabrication and metrology methods to achieve condensation to the limit. Thereafter, it presents the realization of single-nanometer focusing of the Japanese X-ray free electron laser (XFEL), the SPring-8 angstrom compact free electron laser (SACLA), and its application to observe X-ray nonlinear optical phenomena to demonstrate the significance of X-ray condensation.

2. Required shape accuracy of the focusing mirror

To focus coherent X-rays under diffraction limitations, all X-rays entering the aperture of the focusing element must be in a constructive interference state at the focal point. The mirror surface must have extremely high accuracy: according to Rayleigh's criterion, the wavefront error of the X-rays must be less than $\lambda/4$ in peak-to-valley (PV), where λ is the X-ray wavelength. This yields the following equation (1) for grazing incidence mirror optics:

$$d < \lambda / 8\sin\theta , \quad (1)$$

where θ is the grazing incidence angle, and d is the shape error of the mirror surface. When the X-ray energy was 10 keV, and the grazing incidence angle was 5 mrad, the acceptable shape error d was 3 nm PV. Because the mirror is several hundred millimeters long, it is extremely difficult to achieve the required accuracy. Shape errors with relatively long periods were related to the formation of unwanted side lobes in the focusing profile. When the distance between the side lobe and the main peak is N times wider than the main peak width, the shape error with a period of 1/N of the mirror length is the origin. Another problem is the speckle noise on the reflected beam, which corresponds to X-rays passing relatively far from the focal point and generates severe intensity fluctuation when the focused X-rays

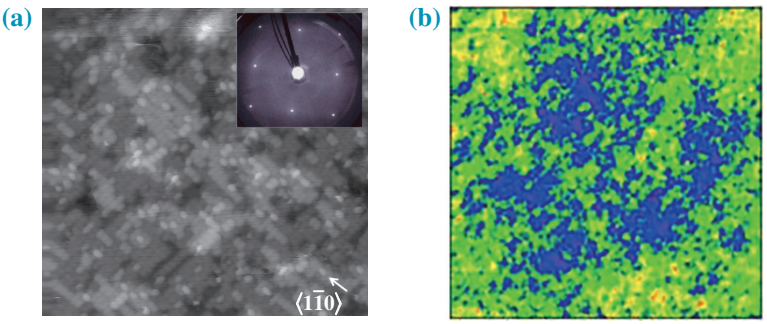

Fig. 1. STM images of EEM processed Si (001) with view areas of (**a**) 20 nm × 20 nm and (**b**) 100 nm × 100 nm. In (a), each dot corresponds to each atom, the position of which is crystallographically reasonable. The inserted figure in (a) is a LEED spot obtained simultaneously with an electron beam energy of 65 eV. In (b), each atomic layer is color-coded, and 95% of the entire area is seen to be composed of three atomic layers.

are observed in the far field. This problem has been attributed to short-period shape errors ranging from 0.1 to several millimeters. These errors must be less than 1 nm PV to reduce the speckle noise sufficiently. Furthermore, short-period roughness is related to scattering into wider angular regions; atomic smoothness is required in the X-ray regime.

3. Fabrication technologies

We developed elastic emission machining (EEM) [3] as a fabrication method and relative angle-determinable stitching interferometry (RADSI) [4] as a shape measurement method, both of which are being comprehensively developed to realize a deterministic fabrication system for precision X-ray mirrors. EEM employs fine powder particles that react to workpiece materials. The particles were applied to the surface of the workpiece using ultrapure water. When they come in contact with the workpiece surface, chemical reactions between the interfacial atoms are induced, and when the flow of ultrapure water removes them, atom-by-atom removal proceeds. Figure 1 shows scanning tunneling microscopy (STM) images of an EEM-processed Si (001) surface with view areas of 20 nm × 20 nm and 100 nm × 100 nm. After the EEM processing, the surface was rinsed with ultrapure water, introduced into an ultrahigh-vacuum chamber, and observed by STM without heating. In the 20 nm × 20 nm image, each dot corresponds to each atom, and the position is crystallographically reasonable, meaning that no damage is introduced onto the surface, which is also understood from the low-energy electron diffraction (LEED) image. The image of 100 nm × 100 nm is color-coded per atomic layer, and 95% of the observed area is seen to be within the three atomic layers (±1 atomic layer) indicated by blue, green, and yellow. The extremely smooth surface, thus obtained, effectively increases the X-ray reflectivity. An EEM head using a nozzle flow can process a mirror surface with a small footprint of a 50 μm diameter circle and scan over the entire mirror surface to deterministically remove shape errors. An accuracy of more than 1 nm PV was achieved, sufficient to realize diffraction-limited focusing and suppress speckle noise. The shorter period roughness is automatically reduced to the atomic level through the machining principle of EEM.

The mirror shape was tested using a stitching Fizeau interferometer called RADSI. In conventional stitching interferometry, the most significant factor that degrades measurement accuracy is the relative angle error between neighboring sub-apertures. The angle is typically estimated to minimize the degree of discrepancy in the common area using the measured shapes of neighboring sub-apertures, although the measured data contain some degree of ambiguity owing to systematic and/or random errors. In contrast, the relative angle was determined *in situ* during the RADSI measurements. The shapes of the sub-apertures on the curved and flat mirrors were measured simultaneously, as shown in Fig. 2. Then, both mirrors were inclined together at the same angle, and both the neighboring sub-apertures and the shape of the flat mirror were measured again. The difference between the two measurements of the flat mirror gives the relative angles between the neighboring sub-apertures, from which the relative angle can be calculated with an accuracy of nearly 10^{-8} rad. When this operation is repeated, the relative angles between all the neighboring sub-apertures can be obtained. The inclination of the flat mirror can be changed independently and adjusted accordingly, such that the density of the interference fringes on the flat mirror is appropriate. Shorter period shapes were measured using a microscopic interferometer and pasted onto the shapes measured by RADSI. With these procedures, shape errors from short periods of less than 10 μm to long periods up to the entire mirror length can be mapped with a precision better than 1 nm PV. The measurement coordinates were related to those of the EEM machine, which was applied to deterministic fabrication. A typical shape-error correction process is shown in Fig. 3. It can be seen that the shape error of several tens of nanometers was improved to 2 nm PV after three cycles of correction processes.

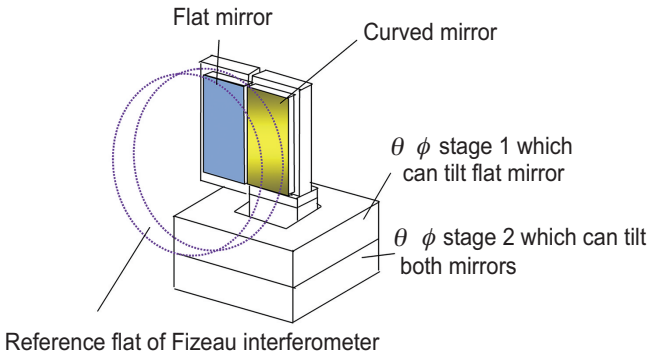

Fig. 2. Schematic drawing of RADSI. Flat and curved mirrors are simultaneously measured, inclined together by the tilting stage 2, and measured together again. In this procedure, the shapes of neighboring two sub-apertures on the test mirror and the angle difference between the two sub-apertures are obtained. The angle difference relates to the posture difference of the flat mirror before and after the inclination. The flat mirror can be inclined alone by tilting stage 1, which is set on stage 2 to reset the posture of the flat mirror to have an appropriate density of interference fringes.

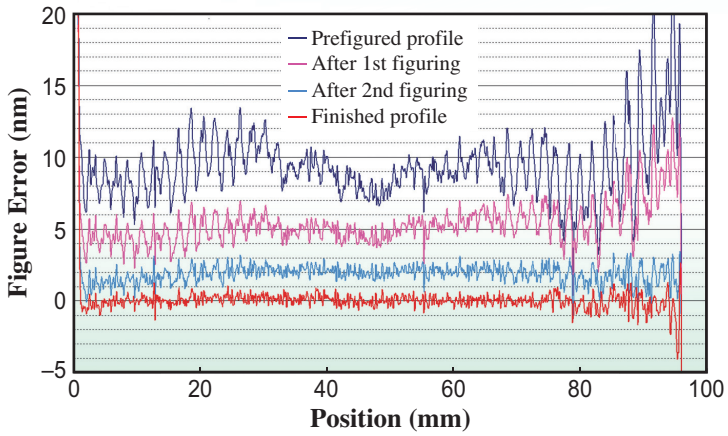

Fig. 3. Typical figure correction property through the deterministic figuring process composed of EEM and RADSI.

4. Ultimate focusing of XFEL

Here, we present the latest status of XFEL. To date, Kirkpatrick–Baez (KB) mirrors have been used to focus synchrotron radiation X-rays. However, this optical system is prone to coma aberration and very sensitive to errors in the grazing incidence angle. This tendency is particularly pronounced when focusing on a size of 10 nm or less, where an accuracy of 0.1 μrad is required in the grazing incidence angle. This characteristic of KB mirrors makes the optical system unstable, and unfortunately, the practical application of a focused beam down to less than 10 nm is not yet possible. To solve this problem, we propose using Wolter type I or type III optics, which can drastically reduce the coma aberration, and attempts are being made to use type III optics to focus the XFEL of SACLA. The SACLA has a very compact configuration owing to its C-band accelerator and in-vacuum undulator, which are original Japanese technologies. The optical hutch is compact, and focusing optics must be installed inside it. Wolter type III can achieve a sufficiently large demagnification factor even in optics at a short distance from the light source because a convex mirror placed upstream allows the principal plane of the optics to be closer to the focal point. The optical configuration is shown in Fig. 4. The working distance was longer than 40 mm despite the ultimate condensation down to a single nanometer size. The wavefront of the focused beam was evaluated to be better than $\lambda/4$ by grating interferometry and ptychography. The focusing profiles were calculated using the measured wavefronts, as shown in Fig. 5. The focus size was approximately 7 nm in horizontal and vertical directions, with an estimated peak intensity of 10^{22} W/cm^2.

5. Nonlinear optical phenomena in a hard X-ray regime

When X-rays hit an atom, a vacancy is formed in the inner shell. The upper electron falls into the vacancy, and the energy difference is observed as the energy of the fluorescent X-ray or Auger electron. These phenomena are widely used in condensed matter science. As this process is completed within a time of about femtoseconds, the phenomena can be understood by assuming that an inner-shell vacancy does not exist. In other words, these phenomena occurred in perfect proportion to the intensity of the pump X-rays. However, in the case of intense XFEL irradiation, the excitation by another photon can be observed before the inner-shell vacancy disappears, and the nature of the excitation is not proportional to the pump X-ray intensity. In the early 2010s, we achieved sub-50-nm focusing of the XFEL at SACLA using a conventional KB configuration. The focused beam was successfully used to observe nonlinear optical phenomena in the X-ray regime, such as two-photon absorption in Ge [5], saturable absorption in Fe [6], and inner-shell lasing in Cu [7].

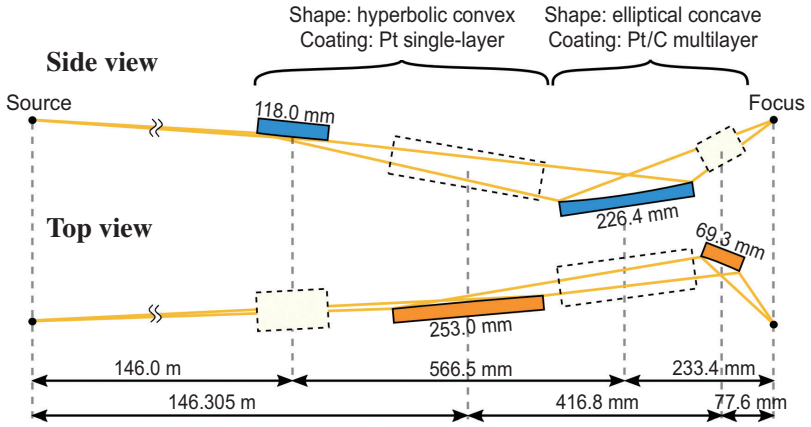

Fig. 4. Optical configuration of Wolter type III mirrors installed at SACLA. In the side and top views, blue and orange mirrors condense the X-ray beam in the vertical and horizontal directions, respectively.

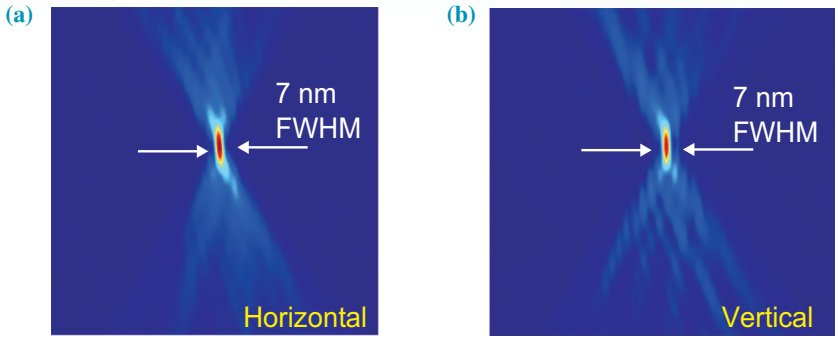

Fig. 5. Beam profiles in **(a)** horizontal and **(b)** vertical directions estimated by the measured wavefront.

Most recently, using Wolter type III optics, fluorescence X-ray spectra from Cr films were observed using an ultimately focused beam with a spot size and peak intensity of 7×7 nm^2 and 1×10^{22} W/cm^2 or higher, respectively. Figure 6 shows the emitted fluorescence spectra. The horizontal axis shows the energy of the fluorescence X-rays, and the vertical axis represents the position of the Cr film along the optical axis. The most intense, minimally focused beam irradiated the Cr film at 0, and a defocused beam was used when the Cr film moved away from the best focus. The bright peak of fluorescence X-ray at the energy of 5415 eV corresponds to the Kα line, and many hyper satellites are observed; A and B, respectively, correspond to Ly$_\alpha$ and Ly$_\beta$, which are X-ray fluorescence from the Cr^{+23} state with only one electron. Interestingly, the intensity decreased when the Cr film was at the best focus, indicating the formation of perfectly bare Cr^{+24}. This was the world's first observation under X-ray pumping [8]. This demonstration shows that Wolter optics enable stable operation even with highly focused beams of less than 10 nm.

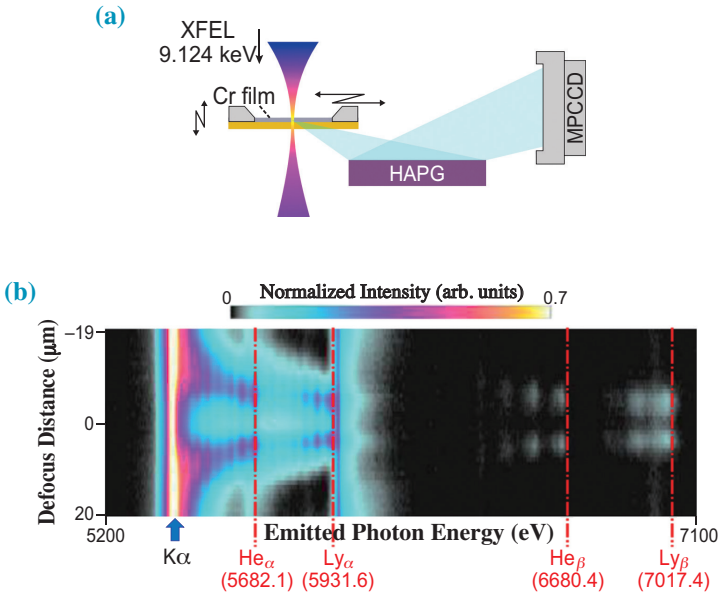

Fig. 6. **(a)** Experimental setup and **(b)** fluorescence spectra emitted from a Cr film hit by focused XFEL down to 7 nm. Kα peak is at 5415 eV.

6. Conclusion

This paper reviews our research and development of focusing mirrors for synchrotron X-rays. The latest results were introduced, namely, the ultimate focusing of XFEL at SACLA BL3 down to 7 nm and an observation of Ly$_\alpha$ and Ly$_\beta$ emission from a Cr film. The developed single-nanometer X-ray beam will be introduced into BL21XU and used for routine semiconductor evaluation.

Kazuto Yamauchi

Osaka University-RIKEN Center for Science and Technology,
Osaka University

Email:
yamauchi.kazuto.ourcst@osaka-u.ac.jp

References

[1] H. Mimura *et al.*: Appl. Phys. Lett. **90** (2007) 051903.
[2] H. Mimura *et al.*: Nat. Phys. **6** (2010) 122.
[3] K. Arima *et al.*: Surf. Sci. Lett. **600** (2006) L185.
[4] H. Mimura *et al.*: Rev. Sci. Instrum. **76** (2005) 045102.
[5] K. Tamasaku *et al.*: Nat. Photonics **8** (2014) 313.
[6] H. Yoneda *et al.*: Nat. Commun. **5** (2014) 5080.
[7] H. Yoneda *et al.*: Nature **524** (2015) 446.
[8] J. Yamada *et al.*: Nat. Photonics - in press (2024).

Review Article

meV-resolved inelastic X-ray scattering

Introduction

Inelastic X-ray scattering with meV-resolution (IXS) allows investigation of atomic dynamics in condensed matter systems, including phonons in crystalline materials, and various excitations in glasses, liquids, and low-dimensional materials. The meV and (nm to) Å scales probed by IXS are exactly the scales relevant to understanding the equilibrium dynamics of most condensed matter systems. Thus, there is a general need to probe excitations on these scales as a basic spectroscopy, including for investigation of *superconductivity, thermal transport, thermoelectricity, ferroelectricity, multi-ferroicity, metal-insulator transitions, viscosity, fragility, relaxations and dispersion in disordered materials, behavior near critical points, localized modes in clathrates or cage compounds, elasticity, etc*. Further, atomic dynamics have a role in many phase transitions, both as related to the previous list of properties, and as generally relevant to structural changes and, e.g., the appearance of precursors to charge density waves. There is increasing interest in the interaction of phonons with other systems, including electron-phonon coupling (e.g., Kohn anomalies, Peierls instabilities, and generalizations there-of), magnon-phonon coupling, and interaction with other quasi-particles. Other recent topics of interest include the topology of phonon dispersion bands (e.g., Dirac points) and phonons carrying angular momentum. All of these drive an interest in – even a necessity of – probing equilibrium atomic dynamics at meV scales.

IXS offers two notable advantages relative to the main alternative technique, inelastic neutron scattering (INS). In particular, the high flux and brilliance of modern X-ray sources means IXS can probe small (~10 micron scale) samples, allowing measurements of sample volumes some 7, or more, orders of magnitude smaller than those needed for INS. This is important for investigating new materials, where the few cubic mm size single-crystals needed for INS are often not available, for measuring samples in extreme, e.g., high pressure, conditions, or for measuring thin films. It also offers generally "easy access" in that the first step for a potential IXS user is "find a good quality ~0.1–1 mm size sample crystal" as opposed to "grow (or assemble) a few cubic mm of perfect crystal" as needed for INS. A more subtle opportunity with IXS is improved investigation of disordered materials: kinematic limits in neutron scattering, where the energy of the neutron probe is comparable to that of the phonon, do not affect IXS, allowing substantially improved data quality with IXS for disordered materials. A more detailed review of IXS, including a thorough comparison to INS with a focus on crystalline systems can be found in [1,2] while a recent overview of work on disordered materials in Japan can be found in [3]. It is worth emphasizing that the spectrometers at SPring-8 BL35XU [4] and SPring-8 BL43LXU [5] (see Fig. 1), after many years of effort [6-9], now lead the field, providing better resolution, higher flux, more analyzers, and generally better stability/reliability than is available at other facilities [1,2]. Figure 2 gives an overview of possible operating conditions.

Fig. 1. SPring-8 meV-IXS Spectrometers. Top: BL35XU in ~2000 while the lower panels are recent photos of the spectrometer arms at BL35XU (middle) and BL43LXU (bottom).

Eulerian Cradle Single Crystals Thin films	2.5 – 800 K (closed cycle systems)
No Eulerian Cradle Polycrystal Powders Liquids, Glasses	<1900 K (furnace) <3000 K (laser heated DAC) <7 T (cryomagnet) <1500 K <300 bar (gas pressure for liquids)

Resolution FWHM (meV)	X-ray Energy (keV)	Reflection Si (nnn)
2.8	17.79	(9 9 9)
1.2	21.75	(11 11 11)
1.1	23.72	(12 12 12)
0.7	25.70	(13 13 13)
0.35	29.66	(15 15 15)

Fig. 2. Table of the IXS operating conditions. Resolutions vary from 2.8 to 0.35 meV, depending on details. The resolution in the table is the value after optimization at BL43LXU while BL35XU now operates only at the (9 9 9) and (11 11 11) with slightly worse resolution than listed. Focused beam sizes at the sample are ~80 microns at BL35XU, and ~50 microns at BL43LXU, however these can be reduced to 20 and 5 microns, respectively, by KB mirrors that are customed designed for IXS. Additional information may be found at https://beamline.harima.riken.jp/en/bl_info/bl43lxu_info_en.html https://beamline.harima.riken.jp/bl43lxu/ and http://www.spring8.or.jp/wkg/BL35XU/instrument/lang-en/INS-0000001392/instrument_summary_view

High Pressure Science

One area of longstanding work at SPring-8 has been the use of IXS to measure elastic properties, especially the speed of sound, of materials under high pressure and, sometimes, at high temperature, in diamond anvil cells (DACs). This information is critical to interpret seismological measurements of the earth: the only directly measured information about the earth's interior is the local sound velocity and the density, as determined by seismology and is, e.g., encoded in the Preliminary Reference Earth Model (PREM) [10]. Thus, in order to investigate the material composition, temperature, and structure of the earth's interior, one must compare the model velocity and density values, e.g., PREM, with lab measurements of reference systems: surprising as it may be, IXS provides one of the better ways of measuring sound velocities of samples under extreme pressure. Therefore, in 2007 RIKEN's Materials Dynamics Laboratory began a program to make these measurements possible, focusing internal manpower on the subject and initiating collaboration with external groups. The program has now broadened, and has been able to achieve ever higher pressures and temperatures, with, most recently the attainment of pressures comparable with the earth's inner core [11].

One notes that while measurements of acoustic modes are conceptually simple (measure the dispersion and determine the slope in the long-wavelength, Q→0, limit), practically they are extremely challenging as one must isolate the signal from a few microns of sample encased in several mm of diamond. They have required the development of specialized instrumentation, beyond the already challenging task of preparing samples in DACs at pressures up to 300 GPa. Recent critical improvements have included the development of a multilayer reverse KB setup to achieve a 5 micron spot size [9] (now the smallest beam available for meV-IXS world-wide) and a Soller screen to improve the signal to noise [9]. The multilayer KB was a relatively early multilayer focusing element at SPring-8 and pushed the limits of the multilayer deposition control. The "reverse" designation refers to the fact the setup focuses more strongly in the vertical than in the horizontal, as is needed to overcome the impact of upstream optics and achieve a round beam on the sample.

The operation of the Soller screen is shown in Fig. 3. If one wanted to collect only a single scattering angle, a slit would be sufficient to remove most the background from the diamonds. More generally, one would like a series of parallel foils, a Soller slit, to permit collection of a larger solid angle. However, Soller slit fabrication is extremely difficult when the needed spacing between channels is ~0.05 mm. Instead, the Soller screen employs two screens with laser cut holes and some dead space between adjacent channels. This, unfortunately, reduces the number of analyzer columns at BL43LXU from

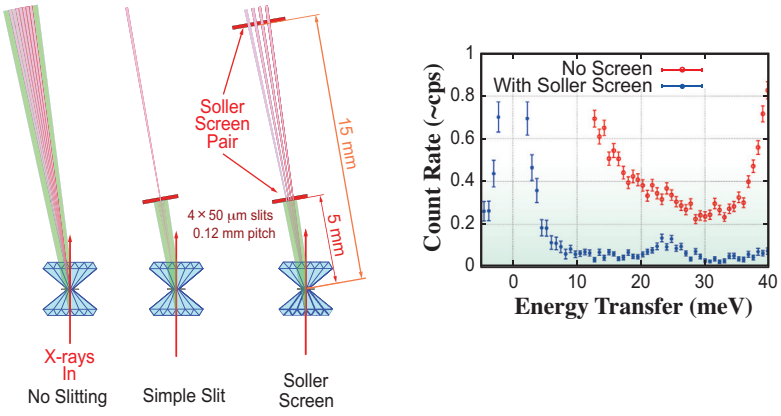

Fig. 3. Soller screen. Left Panel: Conceptual setup for the Soller screen compared to no slitting, or a simple single slit. The Soller screen reduces the background (green) from the diamonds, while still allowing the scattering from the sample to reach the analyzers. Right Panel: Improved data quality with the Soller screen – the peak at 24 meV is the desired signal and is essentially buried in the background from the diamonds without the screen.

7 to 4, but reduces the background from the diamonds and allows one to observe the signal (see Fig. 3). When measuring a single spectrum requires 1 to 2 days, as is often needed at pressures > 150 GPa, the factor of 4 improvement relative to simple slit is critical, reducing the time for a measurement at one pressure to 2 or 3 days from, e.g., 1–2 weeks.

The high pressure setup has been used to investigate many materials, include solid iron at up to 3000 K and 160 GPa [12], solid iron at room temperature to 300 GPa [11] and various iron compounds, usually in the range of 20 to 150 GPa [13-18]. Also, as described on p. 102 (Submission by Ikuta *et al.*) of this issue, some measurements have recently allowed the creation of a new primary pressure scale to pressures in excess of 220 GPa, the first such scale available to multi-megabar pressures[19]. We have also begun investigating glasses under pressure [20-22].

Another extremely difficult class of DAC experiments has been investigations of liquids at high pressure and temperature. This is important as the outer core of the earth is liquid. Work has included both pure iron and iron-compounds [23-27]. In these experiments one has the added difficulty of maintaining the sample stably over the several-hour time scale of the measurements, as liquids easily migrate in the cell. Measurements were possible by essentially creating a sapphire cell *inside* the DAC to confine the liquid [23]. Even so, these are very challenging experiments and pressures have, so far, been limited to < 100 GPa.

The work described above used polycrystalline samples, but there has also been a lot of effort to make measurements on single crystal samples, as this allows determination of the complete elasticity tensor. An efficient way to do this using the 2D analyzer arrays at SPring-8 was published in 2008 [28] and the method has since been extended to multiple materials [29-34]. Notably, however, crystal quality can sometimes degrade significantly at higher pressures, so that the maximum pressure successfully used in single crystal work is about 50 GPa. None the less, the method gives relatively precise values for most elastic constants.

Liquids

As noted above, IXS is a particularly good technique to investigate disordered materials as IXS allows access to atomic dynamics at mesoscale correlation lengths (say 1–10 nm^{-1}) that cannot be matched by neutron scattering. We do not review that work here, as a recent publication [3] discussed such work at SPring-8. However, we mention one example where IXS allowed the resolution of a long-standing controversy about the mesoscale dynamics of water. In particular, high-quality data with sub-meV energy resolution and excellent momentum transfer resolution was obtained at BL43LXU. Careful data treatment then showed that, despite two separate groups suggesting that there was an anomalous extra mode in water, in fact, the lineshape could be well explained by including a bipolar interaction between the quasi-elastic scattering of the water and the acoustic mode [35] (see Fig. 4). This contribution, reminiscent of a Fano profile seen in Raman scattering, was fully expected from theory, but had been neglected in earlier analyses.

Thin Films

Thin film measurements are interesting because there are a variety of materials that are essentially only available in thin-film form – including "bulk" materials that are stabilized by the substrate, or materials where one is creating some sort of periodic or semi-periodic layered structure as may be especially interesting for thermal engineering. However, the obvious problem is that the samples are thin, with an exceptionally thick film being ~1 micron thick, and more typical thicknesses being ~100 nm or less. Then, for IXS, one typically employs a grazing incidence geometry, where the beam is incident nearly parallel to the surface as this helps to increase the path in the sample and hence the signal. While this limits the range of momentum transfers that can be measured, it does allow measurements to take place. However, such work requires both rather careful calculations that properly take account of the tilting of the incident X-ray beam by upstream focusing elements (e.g., [36]), and additional stages and specialized setups to deal with proper alignment at grazing incidence. This work has largely been done at BL35XU. The first published thin film work

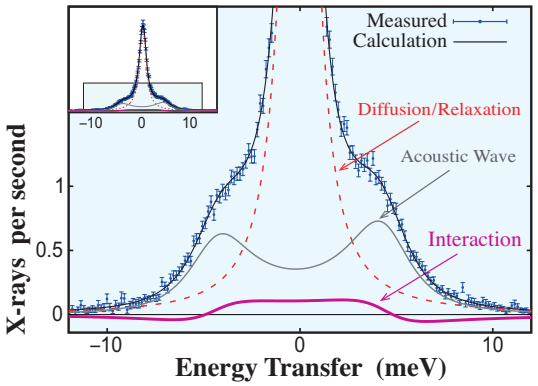

Fig. 4. Interaction contribution in water. Spectrum at Q = 2.5 nm^{-1} with ~0.9 meV resolution expanded to show the various contributions. The inset shows the full spectrum. Fits without the interaction added a weak mode at low energy that is not needed when the correct, interacting, lineshape is used. After [35].

was done to investigate the phonon structure InGaAs/GaAsP quantum well structures [37] with later work investigating "bulk" ScN [38] and a HfN/HfSc superlattice [39]; work is continuing.

Complex Materials: IXS/Structural Complementarity

As noted above there are many types of complex materials (ferroelectrics, superconductors, CDW materials, clathrates/cage compounds, frustrated materials, etc.) where IXS is a useful probe of material properties – as is often made easier because the sample size for IXS can be small. These measurements are too large a topic to review here, and instead we refer the reader to [1,2] and references therein. However, there is an increasing tendency to simultaneously investigate the detailed structural characteristics as seen in diffuse scattering and the phonon behavior in parallel studies. While, broadly speaking, this is unsurprising, as IXS essentially probes the excited states of structure, it is worth mentioning specifically as we see this as a growing trend. In particular, work recently investigated the detailed orbital shapes and anomalous phonon dynamics FeV_2O_4 [40] and other work in showed the impact of lone pair electrons in dynamics of InTe [41] (See also the article on p. 64 by Zhang and Iversen). In the specific context of SPring-8, we believe the combination of single crystal diffraction measurements at BL02B1 with IXS measurements at BL35XU or BL43LXU will be increasingly powerful.

Future Plans for IXS at SPring-8

Future plans for IXS are expected to proceed in several directions, aside from a constant improvement in sample environments. Most immediately, the area detectors that have been shown to be extremely useful at BL43LXU [42,43] will be installed also at BL35XU, permitting easier attainment of higher resolution. This will be matched, funding permitting, by modification temperature control system that should both improve the stability from the ~1 mK rms observed at BL35XU to the <0.2 mK observed at BL43LXU, and improve the resolution [7]. Meanwhile, especially at BL35XU, we will continue to optimize the setup for investigating thin films. We also expect to integrate single crystal diffraction measurements, and especially thermal diffuse scattering (TDS) measurements, more fully with the IXS setups. Finally, the very recent success [44] in achieving 0.35 meV resolution at BL43LXU will allow IXS studies of disordered materials at very low momentum transfers, $0.5 < Q < 1.0$ nm^{-1}, a regime that is important for the understanding the crossover from long-wavelength continuum dynamics to the microscale, but has never been directly probed previously by any method.

Alfred Q. R. Baron[a,b]

[a] RIKEN SPring-8 Center
[b] Japan Synchrotron Radiation Research Institute (JASRI)

Email: baron@spring8.or.jp

References

[1] A.Q.R. Baron: High-Resolution Inelastic X-ray Scattering I&II in Synchrotron Light Sources and Free-Electron Lasers, Springer (2016) pp. 1643.
[2] A.Q.R. Baron: Cond-Mat 1504.01098 (2020).
[3] A.Q.R. Baron: Hamon, Japanese Soc. Neutron Sci. **34** (2024) 3. (in Japanese)
[4] A.Q.R. Baron *et al.*: J. Phys. Chem. Solids **61** (2000) 461.
[5] A.Q.R. Baron: SPring-8 Information **15** (2010) 14.
[6] A.Q.R. Baron *et al.*: Nucl. Instrum. Meth. Phys. Res. A **467–8** (2001) 627.
[7] D. Ishikawa *et al.*: J. Synchrotron Rad. **22** (2015) 3.
[8] D. Ishikawa and A.Q.R. Baron: J. Synchrotron Rad. **28** (2021) 804.
[9] A.Q.R. Baron *et al.*: AIP Conf. Proc. **2054** (2019) 20002 and Cond-Mat 1807.03620 (2018).
[10] A. M. Dziewonski and D. L. Anderson: Phys. Earth Planet. Inter. **25** (1981) 297.
[11] D. Ikuta *et al.*: Nat. Commun. **13** (2022) 7211.
[12] T. Sakamaki *et al.*: Sci. Adv. **2** (2016) e1500802.
[13] T. Sakairi *et al.*: Am. Mineral. **103** (2018) 6072.
[14] R. Tanaka *et al.*: Prog. Earth Planet. Sci. **7** (2020) 23.
[15] S. Takahashi *et al.*: Comptes Rendus Geosci. **351** (2019) 190.
[16] Y. Shibazaki *et al.*: Earth Planet. Sci. Lett. **313–314** (2012) 79.
[17] S. Kamada *et al.*: Am. Mineral. **99** (2014) 98.
[18] W. L. Mao *et al.*: J. Geophys. Res. Solid Earth **113** (2008) B09213.
[19] D. Ikuta *et al.*: Sci. Adv. **9** (2023) eadh8706.
[20] A. Cunsolo *et al.*: Sci. Rep. **5** (2015) 14996.
[21] I. Mashino *et al.*: work in progress.
[22] T. Sakamaki *et al.*: work in progress.
[23] Y. Nakajima *et al.*: Nat. Commun. **6** (2015) 8942.
[24] T. Komabayashi *et al.*: Am. Mineral. **100** (2015) 2602.
[25] S. I. Kawaguchi *et al.*: J. Geophys. Res. Solid Earth **122** (2017) 3624.
[26] K. Umemoto *et al.*: Geophys. Res. Lett. **41** (2014) 6712.
[27] Y. Kuwayama *et al.*: Phys. Rev. Lett. **124** (2020) 165701.
[28] H. Fukui *et al.*: J. Synchrotron Rad. **15** (2008) 618.
[29] A. Yoneda *et al.*: Nat. Commun. **5** (2014) 5080.
[30] H. Fukui *et al.*: J. Phys. Cond. Mat. **29** (2017) 245401.
[31] A. Yoneda *et al.*: Jpn. J. Appl. Phys. **56** (2017) 095801.
[32] S. Kamada *et al.*: Comptes Rendus Geosci. **351** (2019) 236.
[33] H. Fukui *et al.*: High Pressure Res. **40** (2020) 465.
[34] H. Fukui *et al.*: J. Appl. Phys. **132** (2022) 55902.
[35] D. Ishikawa and A.Q.R. Baron: J. Phys. Soc. Jpn. **90** (2021) 83602.
[36] W. Zhao and A.Q.R. Baron: unpublished (2020).
[37] H. Xia *et al.*: Appl. Phys. Lett. **110** (2017) 043102.
[38] H. Uchiyama *et al.*: Phys. Rev. Lett. **120** (2018) 235901.
[39] S. Chakraborty *et al.*: Appl. Phys. Lett. **117** (2020) 111901.
[40] T. Manjo *et al.*: Mater. Adv. **3** (2022) 3192.
[41] J. Zhang *et al.*: Angew. Chem. Int. Ed. (2023) e202218458.
[42] A.Q.R. Baron and D. Ishikawa: Nucl. Instrum. Meth. Phys. Res. A **1049** (2023) 168101.
[43] A.Q.R. Baron *et al.*: work in progress.
[44] D. Ishikawa *et al.*: work in progress.

Structural evidence for intermediates during O_2 formation in Photosystem II

The splitting of water into electrons, protons and molecular oxygen driven by sunlight is the first step in the solar-to-chemical energy conversion in natural photosynthesis. This reaction is catalyzed by a tetra-manganese cluster (Mn_4CaO_5 cluster; called oxygen evolving complex or OEC) located in a negatively charged pocket of the enzyme Photosystem II (PS II, Fig. 1), coordinated by several water molecules and amino acids such as Aspartate, Glutamate and Histidine. The enzyme, located in the thylakoid membrane, is connected to the lumen via several water channels that are likely responsible for water and proton transfer in PS II. Understanding the enzymatic process in PS II is important for developing efficient artificial photosynthetic devices, preferably from earth-abundant elements like Mn and Ca.

In order to catalyze the reaction, the OEC progressively accumulates four oxidizing equivalents from the charge separation that happens at the reaction center upon absorption of each photon. A redox active tyrosine residue, Y_Z, connects the reaction center with the OEC. With the generation of each oxidizing equivalent, the enzyme forms an intermediate (called S-states, S_i, i = 0 to 4) in the Kok cycle formalism, (Fig. 1(c)) with structural and electronic changes previously tracked by our group using XFELs for the meta-stable S-states as well as during the $S_2 \rightarrow S_3$ transition [1,2]. Structural studies of various S-state intermediates of PS II have also been reported by others [3]. However, the structural details of the final $S_3 \rightarrow [S_4] \rightarrow S_0$ steps are unclear. This transition, which is the slowest (taking several milliseconds to complete) and perhaps the most difficult transition during the catalytic reaction, is where the O–O bond is formed along with the release of two protons, insertion of a water molecule and the resetting of the enzyme to the most reduced S_0 state. By performing time-resolved X-ray crystallography at SACLA **BL2** and at the MFX beamline at LCLS, our group has now determined the structure of PS II at various timepoints along the $S_3 \rightarrow S_0$ transition [4]. We used our drop-on-tape (DOT) sample delivery setup to perform all the experiments that allows for precise and efficient illumination of the PS II samples, with the required delay times between the S-state transitions necessary for opening of the acceptor quinone sites. Further details of the experimental and analysis methods can be found in the following Ref. 4. In total, seven timepoint structures as well as the structures of the meta-stable S_3 and the most reduced S_0 states were determined. For clarity, the timepoints discussed are the time-delays between the 3rd visible laser flash and the XFEL X-ray probe.

We tracked the electron density changes of the oxygen O5, the newly inserted oxygen O_X (also called O6, inserted in the $S_2 \rightarrow S_3$ transition) and the terminal waters (W1–W4) by constructing omit maps of the individual oxygen atoms (Fig. 2(a)). The electron density of the O_X atom becomes asymmetric between 250–500 μs with a reduction in intensity after 500 μs, dropping to the noise level between 1200–2000 μs. For O5, the density remained approximately constant in all the timepoints except for a decrease in the 1200 μs dataset. At 730 μs, the omit densities of O5, W2 and W3 become anisotropic and suggest a high mobility of these ligands. We also tracked the Mn1–Mn4 distance and the Y_Z-H190 distance over the timepoints. The Y_Z re-reduction (based on Y_Z-H190 environment changes) occurs after 500 μs and is mostly complete

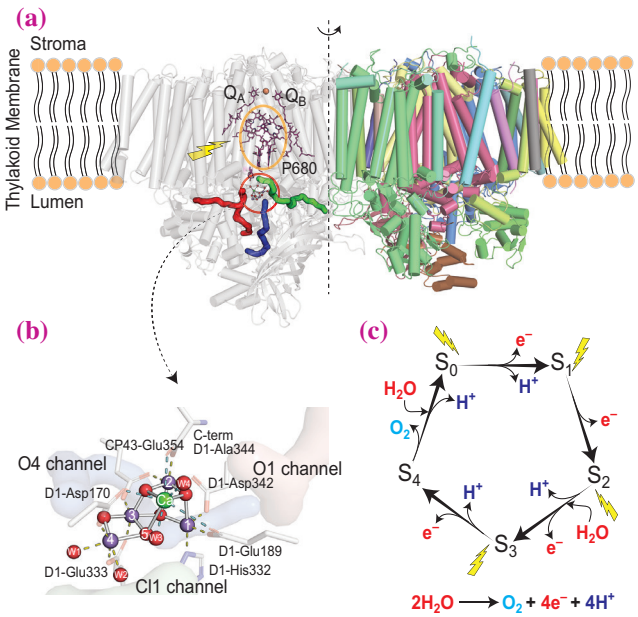

Fig. 1. Overview of Photosystem II (PS II) and the water oxidation reaction **(a)** The enzyme PS II is embedded in the thylakoid membrane of cyanobacteria, algae, and higher plants. The highlighted regions include the reaction center (orange circle) where charge separation occurs and the oxygen evolving complex (OEC; red circle) where the water oxidation reaction takes place. **(b)** Detailed view of the OEC in the dark-stable S_1 state and the surrounding amino acids and water channels. **(c)** The Kok cycle for the water oxidation reaction. Starting from the S_0 state, absorption of a photon at the reaction center leads to extraction of an electron from the OEC and oxidation of the Mn-cluster to the next S-state. Water oxidation occurs after the formation of the transient S_4 state.

by 1200 μs. The Mn1–Mn4 distance, which is an indicator for the presence of O_X contracted after 1200 μs, suggesting a delay between Y_Z re-reduction and O_X disappearance. This indicates the possibility of a reduced intermediate (such as a peroxide-like species) prior to O_2 formation and release. Among the O–O bond formation candidates (Fig. 2(b)), O5–O_X appears to best fit the current data based on their proximity and lower occupancy of O5 at 1200 μs. However, bond formation involving O5–W2 or O5–W3 cannot be excluded at this time.

We also observed several changes in the protein environment, including regions 10–15 Å away from the OEC like the proton gate region (Glu65–Glu312–Arg334) that are possible structural signatures of a proton release. For example, a clear rotation of Glu65 by about 60° is seen (Fig. 2) at two different time-points, similar to the change seen in the $S_2 \rightarrow S_3$ transition, that can be attributed to the release of two protons during this transition. The events leading to the resetting of the enzyme also appears to be quite slow as seen in the reappearance of W20, a water molecule that is part of a key hydrogen bond network near the OEC, in the 4000 μs timepoint, which is later than the disappearance of O_X.

Overall, the results show the well-orchestrated time-resolved changes between the Mn-cluster and the water and protein environment which is necessary to catalyze the water splitting reaction under ambient conditions. These findings bring us closer to understanding one of the most consequential chemical reactions in nature and using the knowledge for designing sustainable energy technologies from earth-abundant materials.

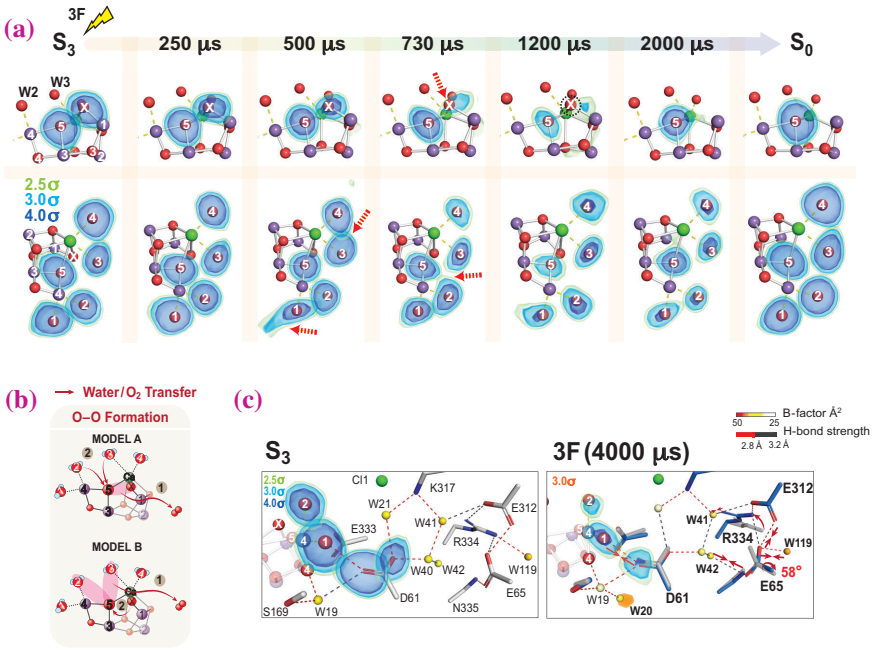

Fig. 2. Changes in the OEC and the broader enzyme environment in the $S_3 \rightarrow S_0$ transition **(a)** Electron density changes of O5, O_X and terminal waters (W1–W4) over the course of the transition. **(b)** The two possible O–O bond formation models based on the results of the study. **(c)** Changes in the proton gate region of the Cl1 channel. A rotation of the Glu65 is seen which is indicative of proton transfer to the bulk. W20, a key water molecule near the OEC, also appears to return very late in the transition suggesting a slow resetting of the enzyme.

A. Bhowmick*, J. Kern, V. K. Yachandra and J. Yano

Molecular Biophysics and Integrated Bioimaging Division, Lawrence Berkeley National Laboratory, USA

*Email: abhowmick@lbl.gov

References

[1] J. Kern *et al.*: Nature **563** (2018) 421.
[2] M. Ibrahim *et al.*: Proc. Natl. Acad. Sci. USA **117** (2020) 12624.
[3] M. Suga *et al.*: Science **366** (2019) 334.
[4] *A. Bhowmick, R. Hussein, I. Bogacz, P. S. Simon, M. Ibrahim, R. Chatterjee, M. D. Doyle, M. H. Cheah, T. Fransson, P. Chernev, I.-S. Kim, H. Makita, M. Dasgupta, C. J. Kaminsky, M. Zhang, J. Gätcke, S. Haupt, I. I. Nangca, S. M. Keable, A. O. Aydin, K. Tono, S. Owada, L. B. Gee, F. D. Fuller, A. Batyuk, R. Alonso-Mori, J. M. Holton, D. W. Paley, N. W. Moriarty, F. Mamedov, P. D. Adams, A. S. Brewster, H. Dobbek, N. K. Sauter, U. Bergmann, A. Zouni, J. Messinger, J. Kern, J. Yano and V. K. Yachandra: Nature **617** (2023) 629.*

The process of vision: Structure of ultrafast mammalian rhodopsin determined by time-resolved femtosecond crystallography

Vision starts by light hitting the back of our retina. Located in the rod cells of the retina, the protein rhodopsin absorbs a photon through its chromophore retinal. Rhodopsin, consisting of 348 amino acids and 7 α-helices folded inside the membrane of the rod discs, bears an 11-*cis* retinal located deep inside the core of the protein (Fig. 1(a)). The first rhodopsin structure in the resting state (dark state) was determined at the beginning of this millennium at SPring-8 [1], followed by two higher resolution structures [2,3]. The structure of rhodopsin, being a prototype of the highly druggable family of G protein-coupled receptors (GPCRs), in an activated state sheds light on some conserved features of the rest of the family. Numerous spectroscopy studies have shown that retinal binding proteins trigger their activity by the absorption of a photon followed by isomerization of the chromophore inducing the next steps of activation. The trigger is one of the fastest events in biology, happening in the femtosecond range for mammalian rhodopsin. The full intramolecular mechanism of rhodopsin activation is still unclear.

We studied the structures of early intermediates in the ultrafast picosecond range by capturing the conformation of rhodopsin 1, 10 and 100 ps after illumination, at room temperature, using serial crystallography in a pump-probe mode at SACLA and SwissFEL [4]. Rhodopsin microcrystals were initially optimized to grow small and in high density according to [2,3] but did not diffract to high enough resolution to refine the retinal conformation [5], at SACLA. A first hit (Fig. 1(b)) was found with low molecular-weight polyethylene glycol, often found to be successful with GPCRs. Crystal size optimization and large scale (microliters) production in lipidic cubic phase (LCP) (Fig. 1(c)) allowed in 2017 pilot diffraction tests at SACLA and LCLS suggesting the feasibility of time-resolved experiments.

In 2018, we eventually performed time-resolved femtosecond serial crystallography (TR-SFX) experiments at the SACLA and the SwissFEL. Rhodopsin microcrystals grown in the dark were delivered into the beam path of a pump laser at 480 nm, followed after exactly 100 ps by the X-ray pulse of the XFEL (Fig. 2(a)). Data were collected to a resolution beyond 2 Å under dim red light (Fig. 2(b)) at SACLA **BL3 EH2** (Fig. 2(c)). The pump laser at 480 nm, illuminated rhodopsin with a 100 fs-pulse and a repetition rate of 15 Hz. It was circularly polarized, had an orientation 90 degree to the XFEL beam and a focus size of 47–50 μm FWHM (80–85 μm $1/e^2$) (Fig. 2(a)).

We performed the control experiment that the ground state structures from cryo-crystallography studies [3] and from our SFX measurement were similar (rmsd less than 0.33 Å) [4]. Even in the two independent experiments, the electron density maps were quasi-identical and Fig. 3 displays the retinal chromophore binding pocket from the obtained rhodopsin structure. A minor but non-negligible domain of the rhodopsin crystal presenting a lattice translation was characterized and corrected before refinement [6].

The main signals obtained in the difference electron density (DED) maps after 100 ps were, as expected, associated with the isomerizing retinal event (Fig. 3(c)). Figure 3(d) shows the new bathorhodopsin model (in blue) at room temperature, 100 ps after illumination, built out of the extrapolated map (not shown) which displays a reconstructed electron density of photoactivated rhodopsin electron density taking into account the level of photoactivation. It shows a distorted (highly distorted at C7 and C14) all-*trans* retinal and gives insights into several features like the retinal isomerization in a "space-saving motion" inside the tight rhodopsin binding pocket; the compatibility with the mechanism of an aborted bicycle pedal isomerization mechanism with a large displacement of methyl C20 while the C19 keeps mostly in place (Fig. 3(d)); the observation of a displacement of the segment C8–C10 of the retinal polyene chain, inducing a displacement of the β-ionone ring towards a region of the receptor bundle typically involved in agonist interaction in the Class A receptors; the permanent

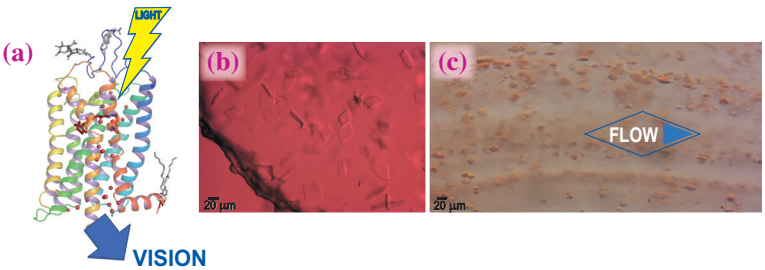

Fig. 1. Rhodopsin function, structure, and crystallization. **(a)** rhodopsin containing the red chromophore, 11 *cis*-retinal, which, absorbing a photon triggers the process of vision. **(b)** First rhodopsin crystal hit in an 80-nanoliters drop seen under dim red light. **(c)** Optimized rhodopsin crystals in microliters sample for TR-SFX.

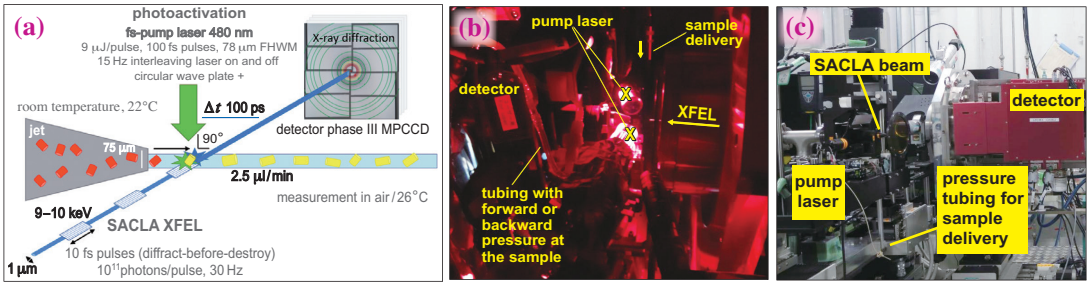

Fig. 2. TR-SFX experimental settings. **(a)** Overview of the experimental TR-SFX settings. **(b)** Picture of the TR-SFX stage in dim red light in an experiment having close settings (in the present experiment, we had only one pump laser output). **(c)** The sample stage of the SACLA BL3 EH2.

shift of the water molecule (Wat01) at the tip of the rotating methyl C20 (Fig. 3(c)) and belonging to the counterions (Glu 113 and Glu 181) H-bond network. It is interesting to observe that 1 ps after photoactivation (see details in [4]), more changes were observed than in the 100 ps time-delay. Several amino acids, even those a few helices turn away from the retinal, shifted of about half an angstrom in an anisotropic way towards the extracellular milieu, constituting a protein breathing motion due to the dissipation of excess energy. After 100 ps (Fig. 3 (c)), evanescent changes disappeared and the main rearrangements are located at the retinal and surrounding amino acids of the receptor bundle (Glu 122, Cys 110, Trp 265, Tyr 268) and the extracellular loop 2 (Cys 187, Tyr 191), highlighting the first amino acid involved in the first photoactivation step of vision. Molecular simulations and dynamics support our models.

This study does not only reveal the molecular trigger for vision and but investigate the early intramolecular mechanism in the process, that is, show the first molecular rearrangements after photon absorption [4]. More time-delays, from the nanosecond to the milliseconds are studied in order to follow the intramolecular mechanism of transduction of the light signal absorbed by retinal to the G protein partner transducin binding site located at the other end of the rhodopsin bundle, at the intracellular side of the rod cells.

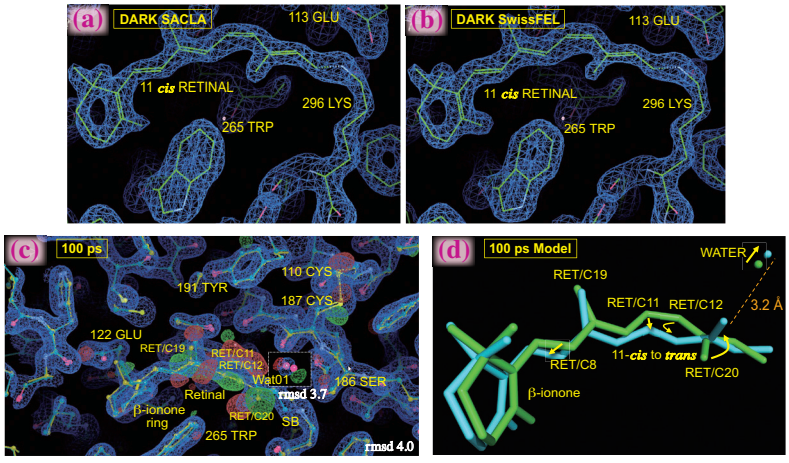

Fig. 3. Rhodopsin structures at the XFELs. **(a)** and **(b)** models of 11*cis*-retinal of the rhodopsin binding pocket (covalent Shiff base with Lys 296) in the dark state contoured with the $2F_O–F_C$ maps measured at SACLA and SwissFEL, respectively. **(c)** Difference map between 100 ps-illuminated state and the dark state shown at 4σ (for water Wat01 at 3.7σ). Colored with positive density in green and negative density in red. **(d)** Models of retinal from dark rhodopsin (in green) and 100 ps-photoactivated (cyan blue) with water Wat01 in a *spatio* temporal determination at the XFEL.

Matthew J. Rodrigues and Valerie Panneels*

Laboratory for Biomolecular Research,
Paul Scherrer Institute, Switzerland

*Email: valerie.panneels@psi.ch

References

[1] K. Palczewski *et al.*: Science **289** (2000) 739.
[2] T. Okada *et al.*: J. Mol. Biol. **342** (2004) 571.
[3] J. Li *et al.*: J. Mol. Biol. **343** (2004) 1409.
[4] *T. Gruhl, T. Weinert, M. J. Rodrigues, C. J. Milne, G. Ortolani, K. Nass, E. Nango, S. Sen, P. J. M. Johnson, C. Cirelli, A. Furrer, S. Mous, P. Skopintsev, D. James, F. Dworkowski, P. Båth, D. Kekilli, D. Ozerov, R. Tanaka, H. Glover, C. Bacellar, S. Brünle, C. M. Casadei, A. D. Diethelm, D. Gashi, G. Gotthard, R. Guixà-González, Y. Joti, V. Kabanova, G. Knopp, E. Lesca, P. Ma, I. Martiel, J. Mühle, S. Owada, F. Pamula, D. Sarabi, O. Tejero, C.-J. Tsai, N. Varma, A. Wach, S. Boutet, K. Tono, P. Nogly, X. Deupi, S. Iwata, R. Neutze, J. Standfuss, G. Schertler and V. Panneels: Nature **615** (2023) 939.*
[5] W. Wu *et al.*: Acta Crystallogr. F **71** (2015) 856.
[6] M. J. Rodrigues *et al.*: Acta Crystallogr. D **79** (2023) 224.

Mapping protein dynamics at high spatial resolution with temperature-jump X-ray crystallography

Time-resolved crystallography (TRX) is a powerful method for investigating protein conformational dynamics with high temporal and spatial resolutions [1]. In the early stages of TRX development, the technique focused on photoactive proteins in combination with photoexcitation as the reaction initiators. The applicability of TRX has been widened by incorporating techniques, such as photocaged ligands [2] and rapid "mix-and-inject" methods [3]. However, universally triggering protein dynamics in time-resolved structural studies remains challenging.

Recent multi-temperature crystallography experiments have demonstrated that modifying the temperature allows tuning of the conformational ensemble sampled at equilibrium, facilitating temperature-jump (T-jump) TRX experiments using infrared (IR) lasers [4]. In such experiments, a mid-IR laser excites the O–H stretching mode of water molecules, resulting in rapid heating of the sample. The proteins exhibit various conformations at different temperatures, with more high-energy states at elevated temperatures. This method has also been used to study the thermal denaturation of enzymes. However, previous studies lacked detailed time-resolved observations of the motions induced by rapid heating.

We applied the T-jump method as a reaction-induced method for TR serial femtosecond crystallography (TR-SFX) with X-ray free electron lasers (XFEL). Lysozyme microcrystals suspended in hydroxyethyl cellulose carrier media were transported from the injector to the intersecting area using an XFEL and a nanosecond IR laser (Fig. 1). In the interaction zone, the crystals were rapidly heated by the IR laser and then exposed by X-ray pulses from SACLA **BL2** at specific intervals after the IR laser heating (20 ns, 20 μs, and 200 μs). Algebraic tools leveraged from previous solution X-ray scattering experiments were used to detect the induction of a T-jump, which was corroborated by observations of unit cell thermal expansion and increased atomic displacements.

Our analysis of the experimental maps supports a rapid increase in the atomic displacement parameters (B-factors) within 20 ns after IR laser irradiation, which suggests an increase in harmonic motion due to heat transfer from the excited solvent to the protein. The uneven distribution of difference electron density features, which are especially noticeable at shorter pump-probe intervals (Fig. 2), implies that heat flows more readily into certain regions of the lysozyme molecule than into others. We also modeled high-energy conformations directly from the TR difference electron density maps and refined them against the extrapolated structure factor magnitudes (ESFMs). This analysis revealed motions such as rotamer flips on fast timescales, and larger motions, including correlated shifts of loops spanning multiple residues, on slower timescales. The most significant of these movements includes a short loop covering residues 97–100, which lies at the end of an α-helix adjacent to the active site and is known to be mobile during lysozyme hinge bending.

We performed T-jump SFX in the presence of chitobiose to assess whether our analysis could detect functional protein motion. This compound is an inhibitor of lysozyme and shifts the conformational equilibrium of the enzyme toward the more compact ‘closed’ state in which the two lobes of the enzyme clamp down on the carbohydrate in the active site. We observed that the difference electron density maps corresponding to 20 ns time delay were similar for both the apo- and chitobiose-bound datasets. However, for a time delay of 200 μs, the difference electron density maps calculated from the chitobiose-bound data did not indicate the dissipation of short amplitude motions into larger-scale conformational changes, as seen for the apo enzyme. Instead, they exhibited similarities with the maps corresponding to the 20 ns time delay. The inhibitor restricted larger movements, such as hinge bending related to substrate binding and catalysis, locking it in a ‘closed’ conformation. Therefore, its presence did not affect the initial rapid

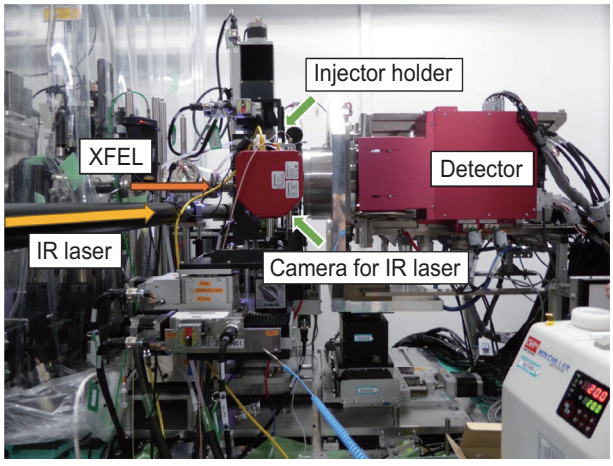

Fig. 1. Photograph of the T-jump TR-SFX experimental setup. The sample injector is installed behind the camera for IR laser detection.

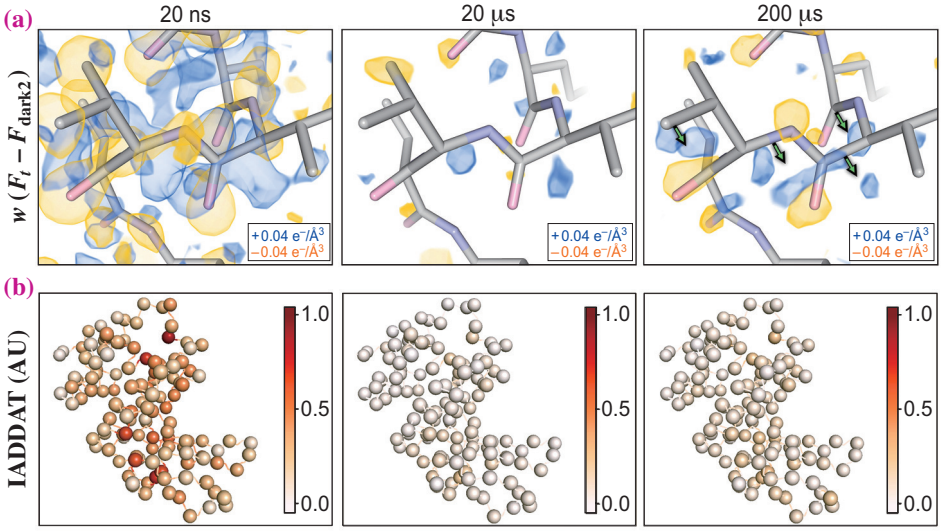

Fig. 2. Temporal evolution of the difference electron density observed during T-jump TR-SFX. **(a)** Comparison of weighted difference electron density maps for each pump-probe time delay, centered around residues 97–100. Maps were visualized at an absolute contour level of ±0.04 $e^-/Å^3$ alongside the corresponding refined models. Although the model coordinates appear stable across pump-probe time delays, difference maps reveal time-resolved changes in the T-jump induced signal, with evidence for coordinated motions (green arrows) apparent by 200 μs. **(b)** Integration of the absolute difference density above a noise threshold (IADDAT) was calculated as an average value per residue for each pump-probe time delay, then mapped onto Cα positions (spheres) of the respective model, and plotted as a function of the residue number. [5]

thermal movements through the enzyme, although it suppressed the changes attributed to microsecond functional motions (Fig. 3), probably shifting them to millisecond or longer timescales.

In this study, we revealed that rapid heating using a nanosecond-pulsed laser tuned to the mid-IR region excited the intrinsic dynamics of lysozyme crystals and demonstrated that this method is an effective perturbation for measuring protein conformational dynamics.

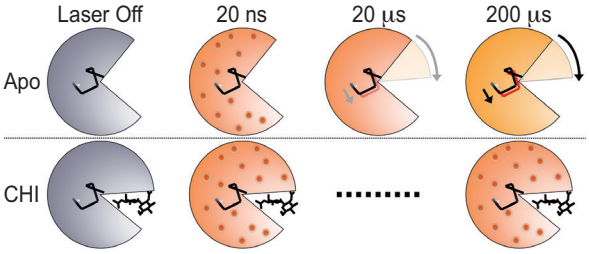

Fig. 3. Schema of the time-resolved conformational changes in the lysozyme after the T-jump. The schematic illustrates the closure of the active site cleft upon chitobiose binding, with subsequent representations of structural changes following the T-jump. For a time delay of 20 ns, atomic vibrations (red dots) occur in both the apo- and inhibitor-bound structures. These vibrations persist in the inhibitor-bound structure but dissipate into more complex motions in the apo-structure. [5]

Eriko Nango[a,b,*] and Michael C. Thompson[c]

[a] Institute of Multidisciplinary Research for Advanced Materials, Tohoku University
[b] RIKEN SPring-8 Center
[c] Department of Chemistry and Biochemistry, University of California, USA

*Email: eriko.nango.c4@tohoku.ac.jp

References

[1] U. K. Genick *et al.*: Science **275** (1997) 1471.
[2] T. Tosha *et al.*: Nat. Commun. **8** (2017) 1585.
[3] J. R. Stagno *et al.*: Nature **541** (2017) 242.
[4] D. A. Keedy *et al.*: eLife **7** (2018) e36307.
[5] *A. M. Wolff, E. Nango, I. D. Young, A. S. Brewster, M. Kubo, T. Nomura, M. Sugahara, S. Owada, B. A. Barad, K. Ito, A. Bhowmick, S. Carbajo, T. Hino, J. M. Holton, D. Im, L. J. O'Riordan, T. Tanaka, R. Tanaka, R. G. Sierra, F. Yumoto, K. Tono, S. Iwata, N. K. Sauter, J. S. Fraser, M. C. Thompson: Nat. Chem.* ***15*** *(2023) 1549.*

High resolution structure analysis of bacteriorhodopsin K intermediate

Bacteriorhodopsin (bR) of *Halobacterium salinarum* is a proton pumping membrane protein driven by light energy (Fig. 1(a)) [1]. bR contains a retinal chromophore with a long conjugated double bond. The retinal connects to Lys216 of bR via a Schiff base linkage and is converted to the 13-*cis* form via photoisomerization while it is in the all-*trans* form in the resting state (Fig. 1(b)). The K intermediate is the first intermediate generated immediately after retinal isomerization. The structural changes associated with K formation are limited to retinal and the surrounding residues. Therefore, the K structure can provide insights into the proton pump mechanism in terms of energy storage and propagation in photoactive proteins. However, despite their importance, many inconsistencies have been observed among the previously reported K structures, especially in the conformation of retinal and interactions with surrounding residues (Fig. 1(c)). Therefore, we performed high resolution X-ray crystallographic analysis of the K intermediate [2].

Large bR crystals (approximately 300×300×30 μm^3) were prepared using the lipidic cubic phase (LCP) method, and the LCP matrix around the crystals was removed using squalane [3]. Diffraction experiments were performed at SPring-8 **BL41XU**. The K intermediate accumulated in the crystals upon irradiation with green laser light (λ = 532 nm) at 100 K. The diffraction dataset containing the K intermediate was collected at 15 K using He gas cooling. An additional diffraction dataset for the ground state was subsequently collected from the identical crystals at 15 K, after regenerating the ground state by irradiating with red laser light (λ = 678 nm) at 100 K. The X-ray absorption dose for the each data set was suppressed to be 0.05 MGy, which is one third of the limit at 15 K [3]. Both datasets indicated a resolution of approximately 1.3 Å.

In the F_o(K+bR) – F_o(bR) difference Fourier map, strong densities were observed only around retinal (Fig. 2). The 13-*cis* retinal in the K intermediate adopts an S-shaped conformation. The largest discrepancies from previously reported K structures occurred at the positions of the C13, C14, and C20 atoms of retinal. Regarding the interaction between retinal and the surrounding residues, the side chain of Lys216, which is covalently bound to retinal, interacts with Asp85 and Thr89 in the K intermediate. Furthermore, the Nζ-H bond of the protonated Schiff base linkage interacts with Asp212 and a water molecule, W402. The hydrogen bonding between Nζ and W402 in the K intermediate suggests that W402 moves to the cytoplasmic side of the Schiff base linkage via the hydrogen bond at the transition to the next L intermediate in the photocycle of bR.

The non-covalent interaction (NCI) plot shows the reduced density gradient isosurface [4]. The plot for K was calculated from a hydrogen atom-added structure obtained by quantum mechanics/molecular mechanics (QM/MM) calculations and used to examine the interactions around the Schiff base linkage (Fig. 3). Bluish green surfaces indicating the presence of relatively strong interactions are observed between the amide-proton on Nζ of Lys216 and Oδ1 of Asp212 as well as between Nζ of Lys216 and W402, as suggested directly from the crystal structure. In addition, green surfaces indicating the presence of

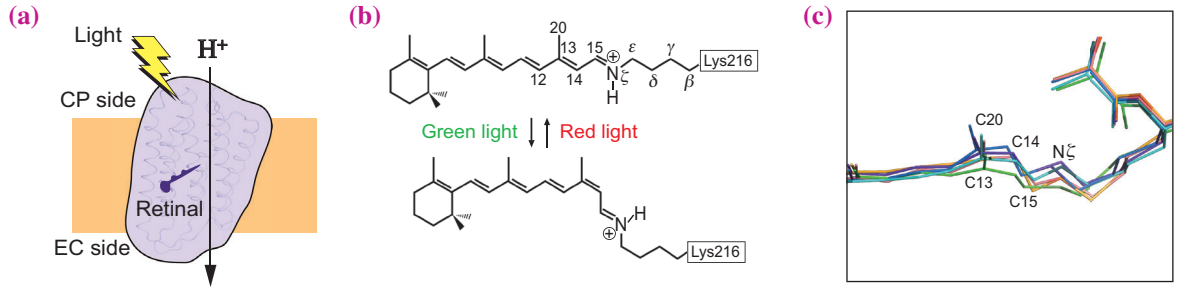

Fig. 1. Function of bR. (**a**) bR transports protons (H^+) from the cytoplasmic (CP) side to the extracellular (EC) side of the plasma membrane of *H. salinarum* using light energy. (**b**) All-*trans* retinal of bR in the resting state is converted to the 13-*cis* form by green light, while a back reaction is caused by red light at ~100 K. (**c**) Superimposition of retinal in various previously reported K structures. 1QK0, 1M0K, 1IXF, 6G7K, 6GA6 and 7Z0C are represented in green, yellow, cyan, dark blue, orange, and purple, respectively.

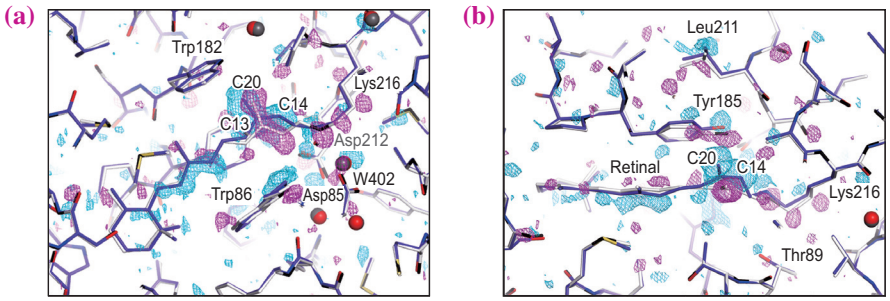

Fig. 2. Structural differences between the K intermediate and ground state. (**a**) The F(K+bR) – F(bR) map around retinal is represented by cyan (+3σ) and magenta (–3σ) meshes. The K structure is represented by violet sticks, while the ground state structure is superimposed as gray sticks. (**b**) View from the upper part of panel (a).

weak attractive interactions are observed between the methylene hydrogen atoms of Cε of Lys216 and the oxygen and hydrogen atoms of Thr89, as well as between Cε of Lys216 and Oδ1 of Asp85. These interactions are plausible stabilizing factors for the distorted conformation of retinal in the K intermediate.

The K structure in this study exhibited some differences from the recent time-resolved serial femtosecond crystallography (TR-SFX) K structures, such as the retinal conformation and water positions. In TR-SFX experiments, the contribution of multiphoton processes owing to the intense excitation laser pulses may pose a serious problem [5]. However, in this study, the K intermediate accumulated under light intensity as weak as sunlight by employing the cryo-trapping method. Therefore, multiphoton absorption could not occur. To further elucidate the proton pump mechanism of bR, the validity of the TR-SFX analyses with high-intensity pump lasers should be examined using integrated results, including those of this study.

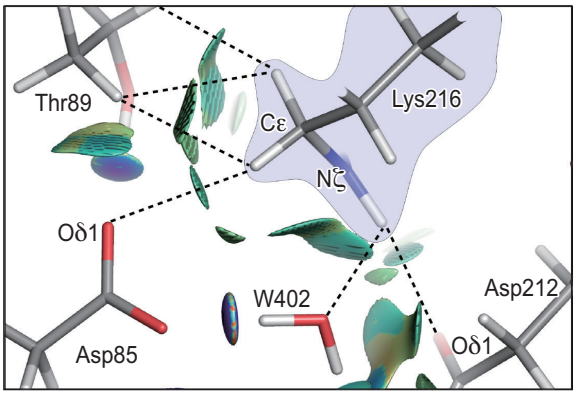

Fig. 3. NCI plot around the Schiff base linkage. The isosurface is colored according to a blue-green-red scheme, where blue, green, and red indicate attraction, very weak attraction, and repulsion, respectively.

Shoun Taguchi, Satomi Niwa and Kazuki Takeda*

Department of Chemistry, Kyoto University

*Email: ktakeda@kuchem.kyoto-u.ac.jp

References

[1] D. Oesterhelt and W. Stoeckenius: Nat. New Biol. **233** (1971) 149.
[2] *S. Taguchi, S. Niwa, H.-A. Dao, Y. Tanaka, R. Takeda, S. Fukai, K. Hasegawa and K. Takeda: Commun. Chem. **6** (2023) 190.*
[3] N. Hasegawa *et al.*: Sci. Rep. **8** (2018) 13123.
[4] E. R. Johnson *et al.*: J. Am. Chem. Soc. **132** (2010) 6498.
[5] D. Miller *et al.*: Nat. Commun. **11** (2020) 1240.

Identifying antibiotics based on structural differences in the conserved allostery from mitochondrial heme-copper oxidases

Antimicrobial resistance (AMR) is a global health problem [1]. Many efforts have been made to reduce the burden of AMR perils globally since 2013, yet threats from some species continue to rise regardless: drug-resistant *Neisseria gonorrhoeae* is one of five urgent threats [2]. Resistance to ceftriaxone, the last option for an empirical first-line antibiotic against *Neisseria gonorrhoeae* in most countries, has been reported and continues to emerge globally [3]. The gonococcal infection could become untreatable due to a high degree of AMR, which would increase serious complications: infertility, ectopic pregnancy, and increased transmission of HIV. The emergence of resistant pathogens to currently available antibiotics is very alarming; thus, the development of treatment options is imperative to tackle AMR. Therefore, the development of a novel mechanism and narrow-spectrum antibiotics is seriously required.

The respiratory chain has recently gained scientific attention as a target of antibiotics [4]. Heme-copper oxidases (HCOs) are terminal oxidases in the electron transfer chain and the essential enzymes in life, thereby being a prospective target of antibiotics. However, the structural similarity and substrate commonality with host proteins are risks for cross-reactivity. On this point, an allosteric inhibitor is a feasible choice to avoid cross-reactivity because allosteric sites are evolutionarily less conserved than orthosteric sites.

We identified a novel allosteric inhibitor of mammal HCO, mitochondrial cytochrome c oxidase (mtCcO), using a high-throughput screening. We determined the crystal structure of mtCcO complexed with the inhibitor solved at a resolution of 2.2 Å (X-ray diffraction data were collected at SPring-8 **BL26B1** using D-cha and SPACE) (Fig. 1) [5]. The inhibitor binding pocket was different from the binding site for molecular oxygen or cytochrome c, or the route for electron transfer pathway, proton pathway, or oxygen accessing channel (Fig. 2). But we could not conclude the inhibitory mechanism from the structure. To elucidate the allosteric inhibition mechanism, we performed molecular dynamics simulation and resonance Raman spectroscopy followed by stopped-flow spectroscopy. Taken together, we conclude that the inhibitor binding in the novel allosteric site of mtCcO obstructs the oxygen channel.

The allosteric site in mtCcO is on the surface of the core structure conserved in pathogenic bacteria, and it is covered by additional helices only in mammals (Fig. 3). We hypothesized that this additional helix in mtCcO makes the inhibition pockets distinct from bacterial HCOs. This structural difference will lead us to identify specific allosteric antibiotics with a narrow spectrum.

We used *E. coli* bo_3 ubiquinol oxidase (bo_3 UqO) to prove the conservation of the allostery as a model bacterial HCO. Firstly, we established a custom compound library by *in silico* screening from mtCcO inhibitors. We identified a specific and allosteric inhibitor for bo_3 UqO. We confirmed that the allosteric effect is even conserved in bo_3 UqO by cryo-EM analysis (Micrograph data were collected at SPring-8 **EM04CT**) (Fig. 3) and mutational analysis followed by stopped-flow analysis.

Then, we determined to tackle quinol-dependent NO reductase, qNOR, from a pathogenic bacteria. qNOR is a distant family member of HCO. The

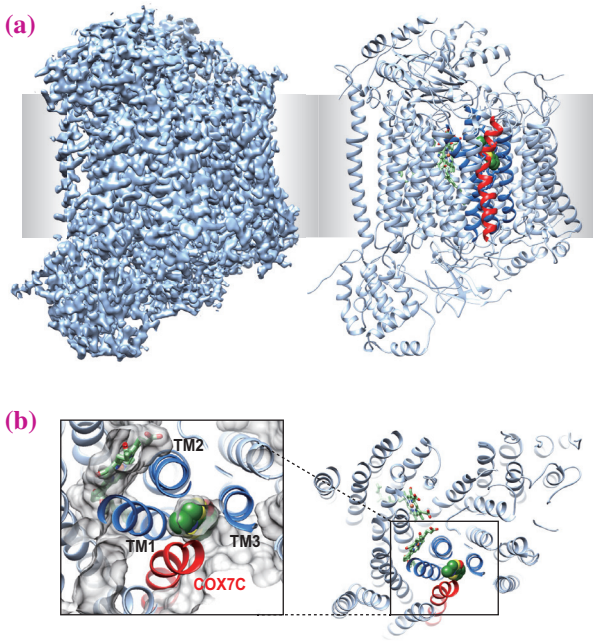

Fig. 1. The allosteric site for T113 is buried inside eukaryotic mtCcO. **(a)** X-ray structure of mtCcO with T113. The electron density map ($2Fo-Fc$), contoured at 1σ, is shown in the left. The ribbon model of mtCcO with T113 in sphere is shown in the right. T113 was covered by COX7C (red), hidden from the surface. **(b)** T113 was surrounded by 4 transmembrane helices (TM1-3, COX7C) and buried from the surface, viewed from the inter-membrane space. Protein molecular surface is shown as gray in the close-up view. Three helices of subunit I surrounding the allosteric site are shown as dark blue, the other helices of subunit I as pale blue, subunit COX7C in mtCcO is shown as red.

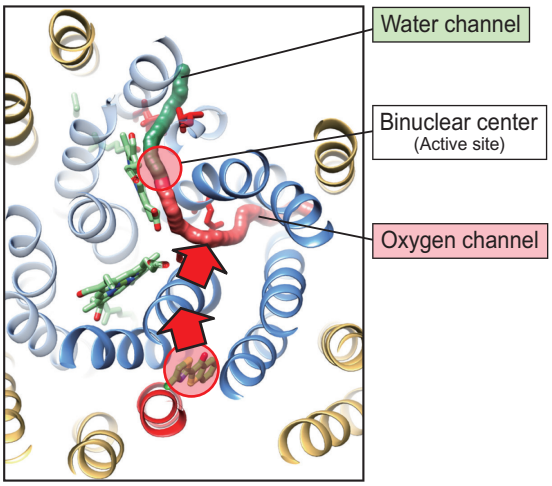

Fig. 2. Scheme of the allosteric inhibition mechanism of mtCcO. The inhibitor binding in the novel allosteric site obstructs the oxygen channel as domino effect. Helices of subunit I, are shown as blue, subunit COX7C is shown as red, and the other helices as yellow. Inhibitor is shown as a green stick.

spreading of multi-drug-resistant *Neisseria gonorrhoeae* is one of the most significant global health concerns. We performed a similar approach as bo_3 UqO and identified qNOR-specific allosteric inhibitors. Finally, we demonstrated the antimicrobial effect against a clinically isolated super-resistant *N. gonorrhoeae*.

In summary, we focused on the allosteric site on the surface of the conserved core structure of HCOs. Based on the difference in structure of the inhibitor binding site, which is covered by an additional subunit in mammals, we succeeded in identifying pathogenic bacterial HCO-specific inhibitors, which have therapeutic potential against AMR. Generally, the core structures of fundamental proteins, not only respiratory enzymes, have acquired additional subunits that modulate their function along molecular evolution. They could likely contain allostery at the boundary of the structures between eukaryotes and bacteria, making us expect that our approach can be applied to other therapeutic targets. Thus, in conclusion, this study will open fresh avenues in protein science and therapeutic development, especially for antibiotics with different mechanisms of action.

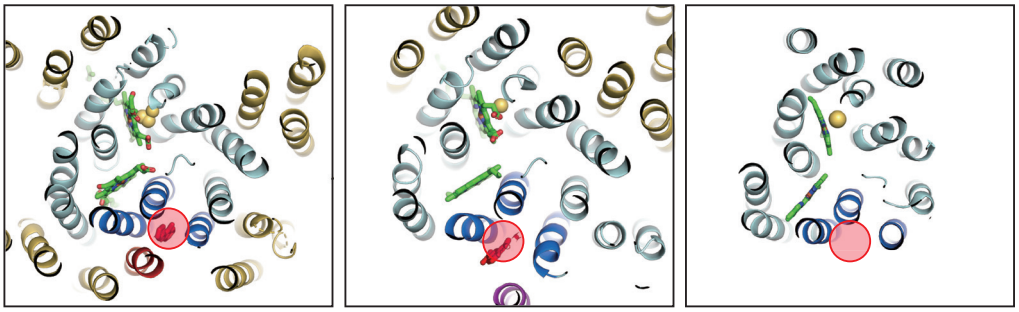

Fig. 3. The allosteric sites of mtCcO (left, pdb 7xmb, complex structure with an inhibitor) is buried by a eukaryotic-specific subunit, though those of *E. coli* bo_3 UqO (middle, pdb 7xmd, complex structure with an inhibitor) and *N. meningitidis* qNOR (right, pdb 6fwf) are opened up. Helices of subunit I, conserved subunit in HCOs, are shown as blue, subunit COX7C in mtCcO is shown as red, transmembrane helix 0 (TM0) of subunit I as purple, and the other helices as yellow. Inhibitors are shown as red stick, and the allosteric sites are shown as red circles.

Yasunori Shintani* and Yuya Nishida

Department of Molecular Pharmacology, National Cerebral and Cardiovascular Center

*Email: shintani.yasunori@ncvc.go.jp

References

[1] R. Laxminarayan *et al.*: Lancet Infect. Dis. **13** (2013) 1057.
[2] M. Unemo *et al.*: Lancet Microbe **5247** (2021) 3.
[3] M. Unemo *et al.*: Sex Health **16** (2019) 412.
[4] G. M. Cook *et al.*: Microbiol Spectr. **2** (2014) 1.
[5] *Y. Nishida, S. Yanagisawa, R. Morita, H. Shigematsu, K. Shinzawa-Itoh, H. Yuki, S. Ogasawara, K. Shimuta, T. Iwamoto, C. Nakabayashi, W. Matsumura, H. Kato, C. Gopalasingam, T. Nagao, T. Qaqorh, Y. Takahashi, S. Yamazaki, K. Kamiya, R. Harada, N. Mizuno, H. Takahashi, Y. Akeda, M. Ohnishi, Y. Ishii, T. Kumasaka, T. Murata, K. Muramoto, T. Tosha, Y. Shiro, T. Honma, Y. Shigeta, M. Kubo, S. Takashima, Y. Shintani: Nat. Commun.* ***13*** *(2022) 7591.*

De novo discovery and structural analysis of thiopeptide pseudo-natural products acting as TNIK kinase inhibitors

Despite the decades of impressive progress in drug discovery, natural products remain a major source of new therapeutics. Natural products have evolved to modulate protein functions in the biological milieu, and their structures are optimized for high metabolic stability, cell permeability, and other pharmacological properties. Therefore, harnessing natural product-like scaffolds in drug discovery is a promising strategy to generate high-quality lead compounds for medicinal chemistry campaigns.

To this end, we have previously *in vitro* reconstituted the biosynthesis of lactazole A, a thiopeptide natural product produced by *Streptomyces lactacystinaeus* (Fig. 1(a)) [1]. As with other ribosomally synthesized and post-translationally modified peptides [2], lactazole biosynthesis commences with the transcription and translation of the structural gene, which produces a precursor peptide. The five biosynthetic enzymes then catalyze multiple post-translational modifications, which include the formation of dehydroamino acids, azole heterocycles and peptide macrocyclization, in the precursor to furnish the mature natural product. We replicated this biosynthetic logic by using an *in vitro* translation system to express the precursor peptide and converted it to lactazole A by adding the biosynthetic enzymes to the translation mixture. We further discovered that the enzymes can accept structurally diverse precursor peptides and convert them to natural product analogs [1,3], which enabled us to construct a selection platform for *de novo* discovery of pseudo-natural products with biological activities of interest [4]. The platform combines *in vitro* lactazole biosynthesis with the mRNA display technology (Fig. 1(b)). To produce a library of thiopeptides, mRNA-barcoded LazA analogs are translated and converted into pseudo-natural lactazole analogs as described above. The resulting thiopeptide library can be subjected to a pulldown against an immobilized protein target.

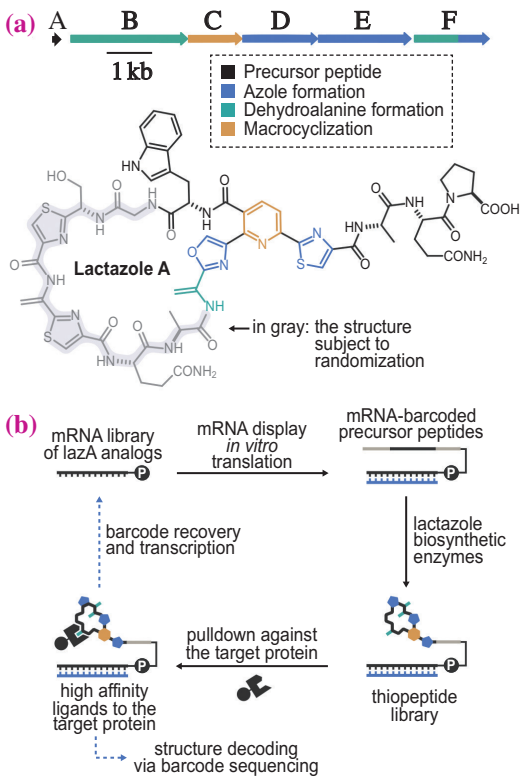

Fig. 1. **(a)** The biosynthetic gene cluster for lactazole A, the parent natural product, and its chemical structure. **(b)** An overview of the platform for the discovery of pseudo-natural product peptides with bioactivities against protein targets of choice.

In the proof-of-concept study [4], we utilized Traf2- and NCK-interacting kinase, TNIK, as the protein target. TNIK is involved in colorectal cancers and lung squamous cell carcinomas, and its inhibition is a confirmed therapeutic strategy, which makes this kinase an attractive drug target [5]. Here, we utilized the established selection platform to identify a series of thiopeptide inhibitors of TNIK, which resulted in the identification of 11 ligands with high affinities to the target protein (K_D ~ 1–60 nM). The compounds also acted as strong enzyme inhibitors, with two thiopeptides, TP1 and TP15 (Fig. 2(a)), demonstrating sub-μM IC_{50} values in a kinase inhibition assay. TP15 also underwent cell uptake, and inhibited TNIK in cell assays.

To understand the molecular basis of target engagement by the discovered compounds, we sought to conduct a structural analysis of the interactions. TNIK·TP1 and TNIK·AMPPNP·TP15 complexes were crystallized, and the X-ray diffraction data was collected at SPring-8 **BL32XU**, allowing us to solve the crystal structures to 2.1 and 2.3 Å resolution, respectively (Fig. 2(b)).

The analysis revealed that both TP1 and TP15 engage with the substrate-binding site of TNIK, and the substrate mimicry is particularly apparent for TP15. The Thr3–Ile4–Arg5 motif in TP15 resembles a prototypical TNIK substrate, and accordingly, Thr3 is positioned at the entrance to the P-site, Ile4 occupies a hydrophobic pocket that constitutes the P+1 site,

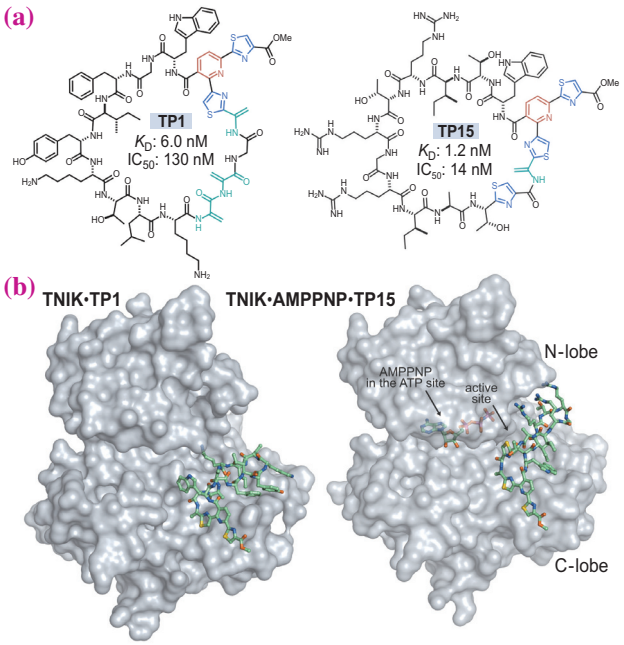

Fig. 2. Chemical structures of discovered thiopeptides **(a)** TP1 and TP15 and **(b)** their interaction with TNIK (pdb 7xzr and 7xzq).

and Arg5 makes ionic contacts with the αC-helix of TNIK (Fig. 3(a)). The phosphate transfer to the side-chain of TP15's Thr3 appears to be obstructed by the partially closed Gly-rich loop of the kinase, which dislocates the γ-phosphate of ATP and sterically occludes it from the substrate. The unique mechanism of enzyme inhibition seen in the TNIK·TP15 complex may serve as the basis for the development of a new type of peptidic kinase inhibitors.

The structures also revealed how multiple non-proteinogenic elements in TP1 and TP15 aid the thiopeptide folding. Both compounds adopt β-hairpin secondary structures featuring a β-turn facing the heteroaromatic scaffold, and the enzymatically installed post-translational modifications (azoles, dehydroalanines, and pyridines) appear to rigidify the fold. Despite similar secondary structures, TP1 and TP15 fold and interact with TNIK in distinct ways. TP15 adopts a "pyridine carbonyl out" conformation that, in combination with a nearby thiazole, helps with the antiparallel positioning of β-strands, whereas the "pyridine carbonyl in" in TP1 leads to a twisting of two adjacent dehydroalanines. As a result, although the aromatic scaffold is positioned similarly in the complexes, the relative strand orientations are inverted. In TP15, the amino acid occupying the P+1 pocket (Ile4) is located on the N-terminal strand, while in TP1, the analogous residue (Leu9) is on the C-terminal side.

Overall, the structures of TNIK·TP1 and TNIK·AMPPNP·TP15 complexes revealed how enzymatically installed non-proteinogenic elements facilitate diverse conformational landscapes of pseudo-natural thiopeptides. The obtained insights will be used to devise the next-generation selection platforms for rapid and efficient discovery of natural product-like structures for drug discovery applications.

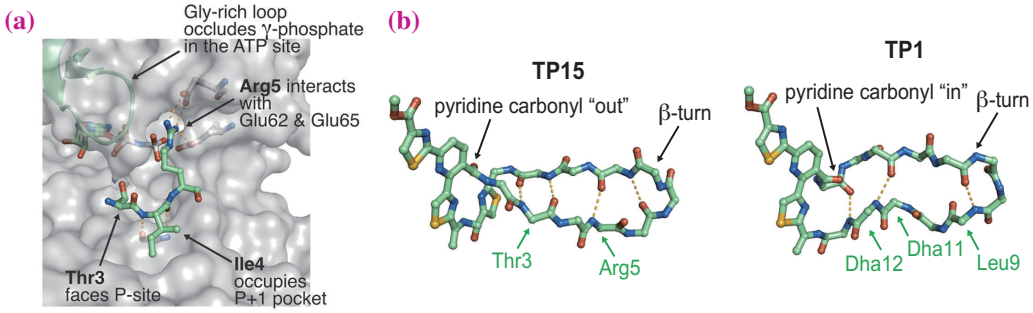

Fig. 3. **(a)** Important molecular interactions between TP15 and TNIK. Only the Thr3–Ile4–Arg5 motif of TP15 is shown. **(b)** Folding of TNIK-bound TP1 and TP15. The protein and amino acid side-chains of the thiopeptides are omitted for clarity. Dha: dehydroalanine.

Alexander A. Vinogradov[a,*], Yuki Goto[a,†] and Toru Sengoku[b]

[a] The University of Tokyo, Graduate School of Science
[b] Yokohama City University, Graduate School of Medicine

[†] Present address: Graduate School of Science, Kyoto University

*Email: vngrdv@g.ecc.u-tokyo.ac.jp

References

[1] A. A. Vinogradov *et al.*: Nat. Commun. **11** (2020) 2272.
[2] S. Hayashi *et al.*: Chem. Biol. **21** (2014) 679.
[3] A. A. Vinogradov *et al.*: J. Am. Chem. Soc. **142** (2020) 20329.
[4] *A. A. Vinogradov, Y. Zhang, K. Hamada, J. S. Chang, C. Okada, H. Nishimura, N. Terasaka, Y. Goto, K. Ogata, T. Sengoku, H. Onaka and H. Suga: J. Am. Chem. Soc.* ***144*** *(2022) 20332.*
[5] T. Yamada *et al.*: Cancer Sci. **108** (2017) 818.

Structural analysis of divalent cation block generated in the prokaryotic sodium channel

Divalent cation blocking was observed in important tetrameric cation channels. For example, magnesium ions block NMDA receptor currents in a voltage-dependent manner [1]. The pore domain of the tetrameric cation channels consists of two transmembrane helices, and a selectivity filter (SF) is located in the loop between them. The SF of the tetrameric cation channels is responsible for the selective permeation of cations. Functional analyses and simulations of NMDA receptors suggested that residues in the SF are involved in magnesium inhibition. However, the detailed molecular mechanism of divalent cation blocking of SFs is not yet fully understood. Prokaryotic Nav (BacNav) provide structural insights into tetrameric channels. NavAb is the most critical contributor of BacNav to the first full-length structure of Nav at atomic resolution [2]. NavAb current is not blocked by divalent cations. Therefore, reproducing the blocking on NavAb and its structural analysis would help elucidate the molecular mechanisms of divalent cation blocking. By introducing mutations into NavAb SF Leu176, we successfully reproduced the divalent cation-blocking effect of the NavAb (Fig. 1) [3].

Interestingly, the divalent cation-blocking mutations can be classified into two types. One is a mutation in a hydrophilic side chain residue, and the other is a mutation in a residue with a small side chain. In contrast, no inhibitory effect was observed for mutations in large side-chain residues in the side chain. We conducted a crystallographic structural analysis of these mutants using SPring-8 **BL32XU, BL41XU**, and **BL45XU** beamlines [3].

We determined the crystal structures of L176Q, L176G mutants, and wild-type channels with and without calcium ions at resolutions of approximately 3 Å (Fig. 2(a)). NavAb has three ion interaction sites in the SF: a high-energy-field site (SiteHFS), a center site (SiteCEN), and an inner site (SiteIN) (Fig. 2(b)). To evaluate electron density, we compared the difference maps between the structures of each mutant with and without calcium ions. In the ionic pathway of the wild-type channel, there was no difference in the density of the calcium ion condition subtracted from the electron density of the no calcium ion condition (Fig. 2(b)). In the L176Q mutant, significant increases in differential density were observed between SiteCEN and SiteIN and below SiteIN (Fig. 2(c)). These increased densities were due to calcium ions, which caused current inhibition. The carbonyl group of the L176Q side chain faces the center of the ion pathway. By comparing the electron densities of the L176Q and wild-type channels under the same ionic conditions, we found that the L176Q side chain was responsible for the increase in electron density below SiteIN (Fig. 2(c)). This suggests that the L176Q mutation can stabilize ions or water at this site more effectively than the wild-type channel can. Therefore, calcium ions were stacked at the center of the ion permeation pathway and blocked the current in the L176Q mutant. In the case of the

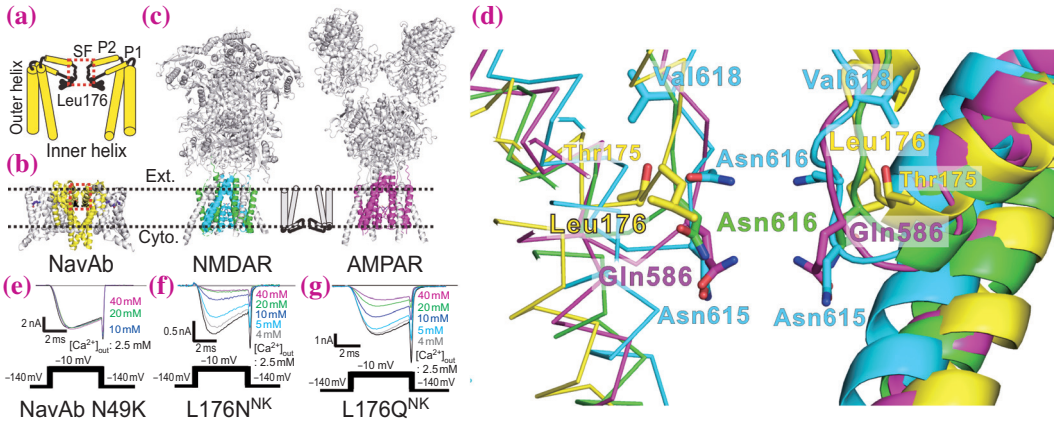

Fig. 1. **(a, b)** Schematic diagram and overall structure of NavAb channel (pdb code; 5yuc). The pore domain is colored yellow. The red dashed square indicates the SF. Leu176 is colored black. **(c)** Overall structures of NMDAR and AMPAR. The pore domain of NMDAR (pdb code; 4tlm) is colored green (NR1) and cyan (NR2B), and the pore domain of AMPAR (pdb code; 5wek) is colored magenta. **(d)** The pore domain of NavAb superimposed on that of NMDAR NR1 and NR2b subunit and AMPAR A2 subunit, respectively. **(e-g)** Representative current traces of NavAb N49K, N49K/L176N, and N49K/L176Q mutants.

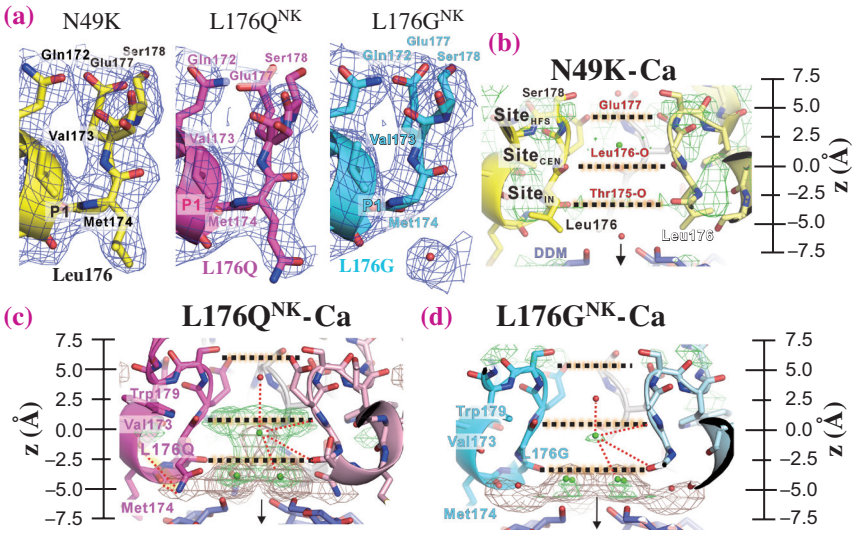

Fig. 2. **(a)** The electron density around residue 176 of the SF. The cartoon view and carbon atoms of NavAb wild-type channel, L176Q, and L176G mutants are colored yellow, magenta, and cyan, respectively. The blue mesh indicates the $2F_O - F_C$ electron density map contoured at 1σ. **(b-d)** Horizontal view of the SF of NavAb wild-type channel (b), L176Q (c), and L176G (d) mutants. Green mesh indicates the difference-electron density map contoured at 5σ of each mutant F_O in the calcium condition subtracted with that in the non-calcium condition. Brown mesh indicates the differential electron density map contoured at 5σ of each mutant F_O subtracted with wild-type channel F_O. The upside is the extracellular side.

L176G mutant, the differential density increased because the glycine mutation created an extra cavity at the interface between the SF and inner vestibule (Fig. 2(d)). The electron density of SiteIN in the L176G mutant was also more substantial than that of the wild-type NavAb under calcium ion conditions (Fig. 2(d)). This suggests that calcium ions are stacked around SiteIN and block the current in the L176G mutant.

The crystal structures of these mutants showed an increase in electron density derived from calcium ions at the bottom of the SF. Hydrophilic side chain mutations provide hydrogen bonds to molecules around SiteIN of the SF, allowing calcium ions to stack at SiteCEN (Fig. 3, middle). The small side-chain mutation of Leu176 creates extra cavities in which the original leucine side chains are located. Including additional water molecules allows divalent cations to interact with water molecules and block the entrance to the inner vestibule (Fig. 3, right), similar to hydrophilic mutations. We proceeded with a molecular dynamics (MD) simulation to analyze the detailed interaction between calcium ions and the mutated side chains of the L176Q and L176G mutants, and our hypothesis was confirmed. BacNavs are the most advanced channel groups, with well-organized structural analyses and simulations. Therefore, our results and methods of structural analysis and MD simulations are expected to play a meaningful role in the advanced analysis of the molecular mechanisms of tetrameric ion channels.

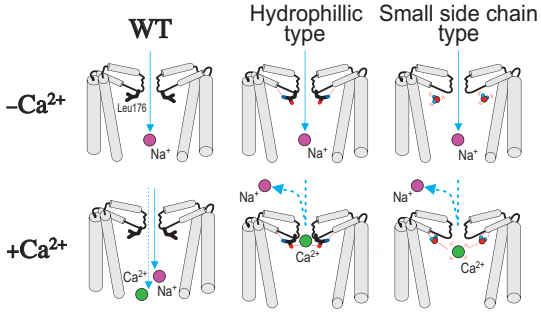

Fig. 3. The proposed molecular models of NavAb wild-type, L176Q, and L176G, respectively. Gray cylinders indicate the helices of the NavAb pore domain helices. Green and purple spheres indicate calcium and sodium ions, respectively.

Katsumasa Irie

Department of Biophysical Chemistry,
Wakayama Medical University

Email: kirie@wakayama-med.ac.jp

References

[1] M. L. Mayer *et al.*: Nature **309** (1984) 261.
[2] J. Payandeh *et al.*: Nature **475** (2011) 353.
[3] *K. Irie, Y. Oda, T. Sumikama, A. Oshima, Y. Fujiyoshi: Nat. Commun.* ***14*** *(2023) 4236.*

Structure of bifidobacterial sulfoglycosidase revealed the architecture for specific sugar recognition and breakdown of intestinal mucin glycan

Gut microbes have received increasing attention in recent years due to their significant impact on human health. Host animals absorb most of the nutrients in their food through the small intestine. Thus, the carbon sources for bacteria in the colon are poor. Therefore, gut bacteria compete for survival by equipping themselves with various enzymes that degrade food-derived non-digestible carbohydrates that are not absorbed by the host. In contrast, host animals provide nutritional sources for symbiotic microorganisms in another way. The mucus layer of the intestinal epithelium functions as a barrier against pathogens, and its main component, the glycoprotein mucin, serves as an energy source for symbiotic bacteria, helping to prevent the invasion of other microbes. The mucin glycans in the colon are frequently sulfated, and it has been shown that bacterial sulfatase, which hydrolyzes and detaches a sulfate from sugars, is involved in their degradation [1]. We discovered a sulfatase-independent degradation pathway for mucin glycans in *Bifidobacterium bifidum* [2]. Among the bifidobacteria known to elicit various beneficial effects in humans, *B. bifidum* is a prominent species because it contains a repertoire of extracellular glycoside hydrolases (GHs) that can cross-feed liberated sugars and increase the total abundance of *Bifidobacterium* [3]. The key enzyme in the sulfatase-independent degradation pathway is sulfoglycosidase (BbhII), which releases *N*-acetylglucosamine (GlcNAc)-6-sulfate (GlcNAc-6S) from mucin glycans (Fig. 1) [4]. The *in vivo* functions of BbhII in *B. bifidum*-administrated mice as well as in the feces of human infants were also demonstrated [2].

BbhII is a cell wall-anchored extracellular enzyme with a transmembrane region at the C-terminus, consisting of an N-terminal carbohydrate-binding module family 32 (CBM32) domain and a catalytic domain classified as GH family 20 (GH20) (Fig. 2). We solved the crystal structure of BbhII in complex with GlcNAc-6S at 1.65 Å resolution [2]. Diffraction data were collected at the structural biology beamline SPring-8 **BL26B2**, and a dataset from a selenomethionine-substituted crystal was used for phase determination.

The catalytic domain consists of a $(\beta/\alpha)_8$ barrel fold with GlcNAc-6S located at its center. GH20 enzymes use a substrate-assisted mechanism in which the *N*-acetyl group of the substrate acts as a nucleophile in the hydrolysis reaction. The *N*-acetyl moiety of GlcNAc-6S bound to the catalytic site is distorted, making its carbonyl group appropriate for glycosidic bond cleavage (Fig. 3(a)). The distorted *N*-acetyl moiety is supported by the side chains of Y637, D552, and three aromatic residues (W588, W607, and W685). As an acid/base catalyst, E553 forms a hydrogen bond with the O1 hydroxyl group of GlcNAc-6S to facilitate glycosidic bond cleavage. Unexpectedly, no basic residues (e.g., arginine or

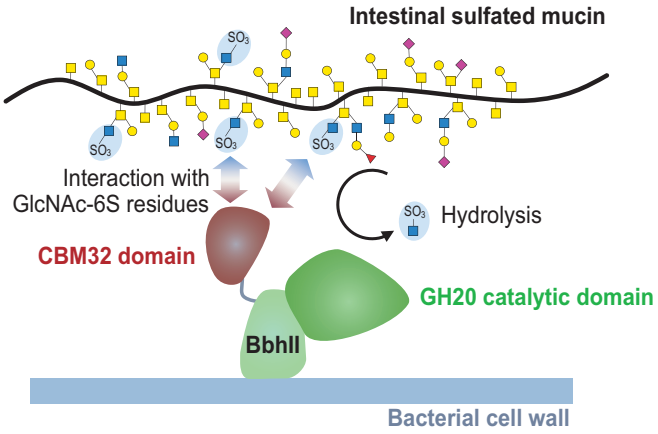

Fig.1. Schematic representation of the CBM-dependent breakdown strategy of mucin glycan by *B. bifidum*. The bacterium interacts with sulfated mucin glycans via the cell-surface-located carbohydrate-binding module family 32 (CBM32) domain of BbhII to initiate glycan degradation using a series of glycoside hydrolases.

lysine) are involved in the recognition of the 6-sulfate group of GlcNAc-6S. Q640, W651, and several water molecules formed hydrogen bonds with sulfate in the active site.

The CBM32 domain consists of a β-sandwich fold containing a Ca^{2+} ion, but the metal was not involved in the glycan binding (Fig. 2). GlcNAc-6S bound through a stacking interaction with the aromatic side chain of W183 and many hydrogen bonds with E62, N89, R95, S97, and N126 (Fig. 3(b)). Again, no basic residues were directly involved in sulfate group recognition. The K_d value toward GlcNAc-6S was 25 μM, indicating a stronger affinity than other CBM32 domains. Although binding to chitosan and β-galactoside has been reported for CBM32s, CBM32 in BbhII was the first to be shown to bind to sulfated glycans.

B. bifidum also contains many other glycosidases on its surface. These extracellular enzymes are expected to capture mucin glycans by CBMs present in the same polypeptide and efficiently release mono- and disaccharides from the glycans, as in the case of BbhII (Fig. 1). Our results provide molecular insights into how gut microbiota utilize carbohydrate-active enzymes to persist in the gut ecosystem, and how these pathways influence microbiome formation in healthy humans.

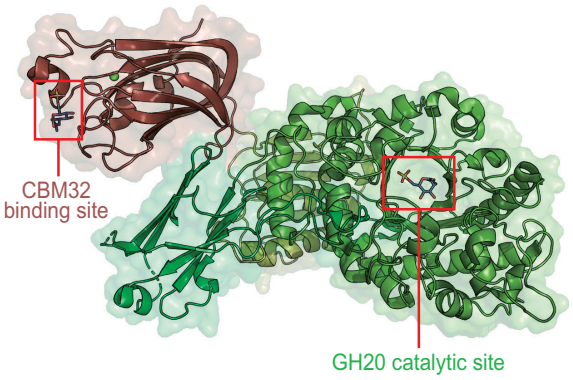

Fig. 2. Overall structure of BbhII. Two GlcNAc-6S-binding sites are indicated. Ca^{2+} bound to CBM32 is shown as a green sphere.

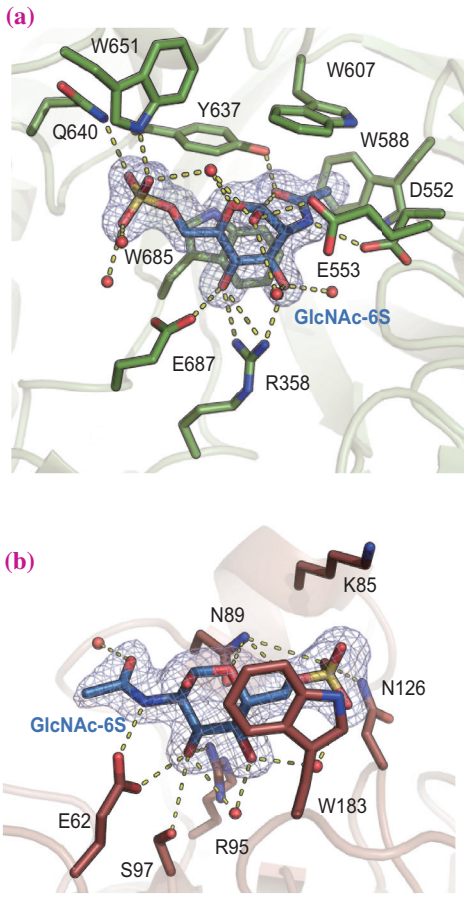

Fig. 3. GlcNAc-6S-binding sites of BbhII. **(a)** The catalytic site. **(b)** The binding site in CBM32.

Shinya Fushinobu[a,*], Toshihiko Katoh[b] and Toma Kashima[a]

[a] Department of Biotechnology, The University of Tokyo
[b] Graduate School of Biostudies, Kyoto University

*Email: asfushi@mail.ecc.u-tokyo.ac.jp

References

[1] A. S. Luis *et al.*: Nature **598** (2021) 332.
[2] *T. Katoh, C. Yamada, M. D. Wallace, A. Yoshida, A. Gotoh, M. Arai, T. Maeshibu, T. Kashima, A. Hagenbeek, M. N. Ojima, H. Takada, M. Sakanaka, H. Shimizu, K. Nishiyama, H. Ashida, J. Hirose, M. Suarez-Diez, M. Nishiyama, I. Kimura, K. A. Stubbs, S. Fushinobu, T. Katayama: Nat. Chem. Biol.* ***19*** *(2023) 778.*
[3] T. Katoh *et al.*: Microorganisms **8** (2020) 481.
[4] T. Katoh *et al.*: Biosci. Biotechnol. Biochem. **81** (2017) 2018.

Structural basis of the type IVb pilus-dependent transport for the colonization factor of *Vibrio cholerae*

Pathogenic bacteria utilize molecular machines called secretion systems to transport virulence-associated proteins to interact with and manipulate their host environment [1]. *Vibrio cholerae* secretes a cholera toxin (CT) through the type II secretion system (T2SS), leading to the development of severe diarrhea. The T2SS operates similarly to a piston, where a periplasmic proteinaceous filament, called endopilus (formerly known as a pseudopilus), extends and retracts repeatedly to expel the substrates from the cell. T2SS is evolutionally and structurally related to the type IV pilus (T4P) system. Some of T4P also function as a secretion system, transferring enzymes or colonization factors from the periplasm to the extracellular milieu. *V. cholerae* possesses a toxin-co-regulated pilus (TCP), which belongs to a subclass of T4P (T4bP) (Fig. 1(a)). This pilus is capable of transporting a soluble colonization factor, TcpF. TcpF is a bilobed protein comprising an N-terminal domain (NTD) and a C-terminal domain (CTD), and has an N-terminal flexible 25-residues extension [2]. Despite the important role of TcpF in the pathogenicity of *V. cholerae*, the mechanisms underlying TcpF secretion via T4bP remain unclear.

TCP consists of two structural components: the major pilin TcpA and the minor pilin TcpB (Figs. 1(b,c)). TcpA is arranged in a right-handed helical manner to form the main body of the TCP, whereas TcpB is located at the pilus tip and comprises three domains: pilin-like domain 1, beta-sheet domain 2, and β-sandwich-fold domain 3. TcpB forms a homotrimer by interacting with domains 2 and 3 and acts as the initiating complex for pilus formation [3]. Because TcpF is not secreted efficiently in a TCP-non-expressing strain lacking the *tcpA* gene, we hypothesized that TcpF interacts with one of the pilus subunits and is secreted upon pilus elongation. Isothermal titration calorimetry experiments showed that TcpF binds to TcpB, but not to TcpA. To clarify the interactions between TcpB and TcpF, we crystallized the complex and collected the diffraction data at SPring-8 **BL26B1**. The diffraction pattern of the TcpB–TcpF crystal was initially very poor at ~10.0 Å. However, the addition of sucrose to the reservoir solution and dehydration of the crystals resulted in a notable improvement in the resolution limit to ~4.0 Å. The initial phases were solved to a resolution of 4.05 Å by molecular replacement (MR) using the structures of TcpF and TcpB [4]. Three TcpF molecules were found above domain 3 of TcpB, forming a homotrimer shaped like a flower with three petals via interactions with the NTD (Fig. 1(d)). Overall, TcpB and TcpF formed a heterohexameric complex. Using native mass spectrometry and analytical ultracentrifugation experiments, we confirmed that this heterohexamer also exists in solution. Judging from the residual electron densities found at the clefts of the interface of each TcpB trimer, the N-terminal flexible extensions of TcpF molecules, rather than the NTDs and CTDs, are supposed to interact with the TcpB trimer. However, because of the low resolution of the data, it was not possible to model this interaction site.

To clarify the interaction between TcpB and the N-terminus of TcpF, we analyzed the structures of complexes formed between TcpB and the N-terminal TcpF (1–15) peptide. The diffraction data of these complexes at the highest resolution of 2.30 Å were obtained using BL26B1 [4]. We used the TcpB structure as an MR search model to solve the structures of the TcpB and TcpF (1–15) complexes. The N-terminal 11 residues of TcpF, from Phe1 to Val11, were responsible for its binding to the TcpB trimer (Fig. 2(a)). The N-terminal 5 residues of TcpF formed a type I β-turn structure like hook conformation stabilized by the pi–pi stacking of the Phe1–Tyr5 pair. Because Tyr5 is essential for TcpF secretion [2], this unique hook-like conformation seems to be important for its interaction with TcpB. We previously demonstrated that the N-terminal

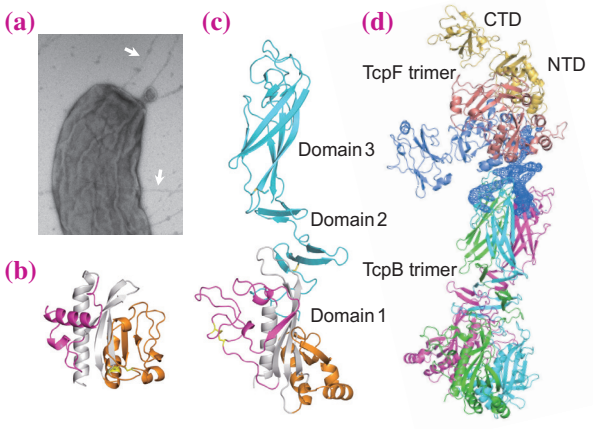

Fig. 1. The T4bP of *V. cholerae*. **(a)** Transmission electron micrograph of the pathogenic *V. cholerae* strain O395 forming TCP. **(b)** Crystal structure of the major pilin TcpA (PDB ID: 1oqv). **(c)** Crystal structure of the monomer of the minor pilin TcpB (PDB ID: 7w63). **(d)** Crystal structure of the TcpB–TcpF complex (PDB ID: 7w65). The omit map (blue, countered at 1.0σ) corresponding to the N-terminal portion of TcpF is depicted.

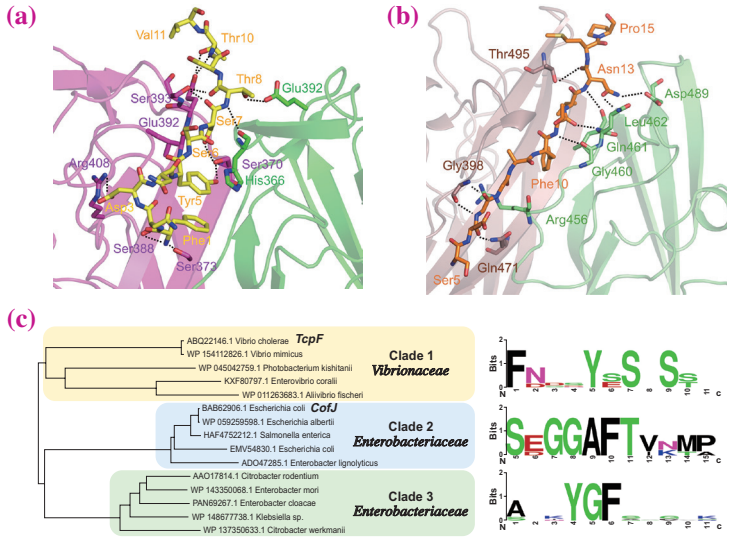

Fig. 2. Interaction between colonization factors and minor pilins in T4bP-expressing pathogenic bacteria. **(a)** Interactions between one TcpF (1–15) peptide (yellow) and two TcpB molecules (green and magenta) (PDB ID: 7w64). **(b)** Interactions between one CofJ (1–24) peptide (orange) and two CofB molecules (brown and lime green) (PDB ID: 5ypz). **(c)** Left panel: Phylogenetic tree of the colonization factor T4bP-SS in various pathogenic bacteria. Right panel: Sequence logo plots of the T4bP-SS in three clades.

region (Ser5–Pro15) of the secreted colonization factor CofJ binds to the minor pilin CofB of CFA/III and the T4bP of enterotoxigenic *Escherichia coli* (ETEC) (Fig. 2(b)) [5]. The aromatic residue Phe10 in the N-terminal region is essential for this interaction. Recognition of the aromatic amino acid in the colonization factor by the formation of a minor pilin trimer-dependent binding pocket is considered a common feature of the T4bP system. The colonization factor has an N-terminal segment containing approximately 10 residues, including important aromatic residues, named the T4bP secretion signal (T4bP-SS). We performed a phylogenetic analysis to compare the colonization factors of other pathogenic bacteria harboring T4bP and showed that T4bP-SS was divided into three clades, each with a characteristic motif containing aromatic residues (Fig. 2(c)). These results indicate that the minor pilins of each pathogenic bacterium may have evolved to recognize the T4bP-SS of its cognate colonization factor.

The structure of the TcpB–TcpF complex was refined using the TcpB–TcpF (1–15) structure to model the full length of TcpF, including T4bP-SS. We constructed an entire structural model of the TcpF–TCP complex, in which the TcpF trimer was found to be situated on the tip of TCP, using the TcpA filament model (Fig. 3) [4]. Based on these findings, we propose the hypothesis that the mechanism underlying TcpF secretion involves TCP elongation (Fig. 3) [4]. When TcpF binds to TcpB, TcpA assembles and the pilus elongates, simultaneously carrying TcpF through the TcpC secretin ring. Subsequently, TcpF separates from the TcpB trimer and is deposited near the bacterial cell. Alternatively, the TcpF trimer located at the TCP tip may bind to a putative receptor on intestinal epithelial cells.

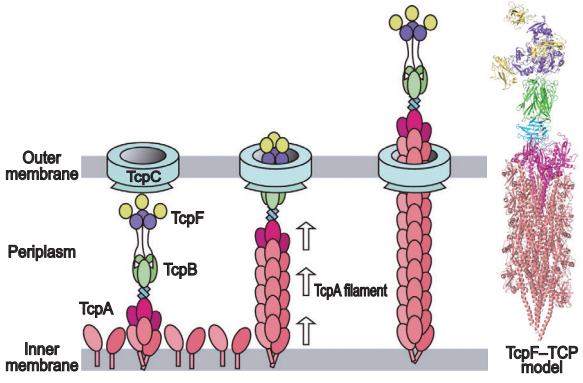

Fig. 3. A model depicting the transport of the colonization factor TcpF by TCP formation and elongation.

In recent years, there has been growing interest in anti-adhesive agents targeting bacterial adhesins and colonization factors. Because secreted colonization factors are critical for bacterial adhesion and colonization, the newly identified interactions between the minor pilin and the colonization factor T4bP-SS is an attractive target for the development of anti-adhesion agents against T4bP-expressing pathogenic bacteria, such as *V. cholerae* and ETEC.

Hiroya Oki[a,*], Kazuki Kawahara[b] and Shota Nakamura[a]

[a] Research Institute for Microbial Diseases, Osaka University
[b] Graduate School of Pharmaceutical Sciences, Osaka University

*Email: hirooki@gen-info.osaka-u.ac.jp

References

[1] T. R. D. Costa *et al.*: Nat. Rev. Microbiol. **13** (2015) 343.
[2] C. J. Megli *et al.*: J. Mol. Biol. **409** (2011) 146.
[3] M. Gutierrez-Rodarte *et al.*: J. Biol. Chem. **294** (2019) 15698.
[4] *H. Oki, K. Kawahara, M. Iimori, Y. Imoto, H. Nishiumi, T. Maruno, S. Uchiyama, Y. Muroga, A. Yoshida, T. Yoshida, T. Ohkubo, S. Matsuda, T. Iida and S. Nakamura: Sci. Adv.* ***8*** *(2022) eabo3013.*
[5] H. Oki *et al.*: Proc. Natl. Acad. Sci. USA **115** (2018) 7422.

Structural basis for the recognition of citrate synthase by the SCF^{Ucc1} ubiquitin ligase complex

Organisms capable of conducting the glyoxylate cycle can utilize acetate or fatty acids as a sole carbon source, producing glucose from acetyl-CoA through a sequence of reactions in the glyoxylate cycle, the TCA (tricarboxylic acid) cycle, and the gluconeogenic pathway. In the glyoxylate cycle, acetyl-CoA, derived from acetate or fatty acids, undergoes condensation with oxaloacetate (OAA) by citrate synthase to generate citrate. Our previous study demonstrated that Cit2, a citrate synthase in the glyoxylate cycle of *Saccharomyces cerevisiae*, is targeted for proteasomal degradation by the ubiquitin ligase complex SCF^{Ucc1} (Skp1–Cdc53–F-box protein Ucc1). Biochemical analyses revealed that OAA induces a conformational change in Cit2, inhibiting its recognition and ubiquitination by SCF^{Ucc1}. These findings suggested the existence of a positive feedback loop wherein higher amounts of gluconeogenic metabolites (e.g., acetyl-CoA and OAA) stabilize Cit2, further activating the glyoxylate cycle. In conjunction with cell biological analyses, we propose that SCF^{Ucc1}-mediated regulation of Cit2 acts as a metabolic switch for the glyoxylate cycle in response to changes in carbon source. However, the structural basis of how Ucc1, an F-box protein serving as a substrate recognition factor, discriminates the metabolite-dependent conformational change of Cit2 remained unclear.

To address this, we conducted an X-ray crystal structure analysis. Crystallization was performed for the Ucc1-Skp1 complex with Cit2 (Ucc1-Skp1-Cit2), Apo-Cit2, Cit2 in complex with OAA and CoA (Cit2-OAA-CoA), and Apo-Cit1. This study employs CoA instead of acetyl-CoA to prevent enzymatic reactions during crystallization. X-ray diffraction data were collected at SPring-8 **BL44XU**. Despite the absence of a homology structure for Ucc1 through sequence search, we successfully determined the initial phases of Ucc1-Skp1-Cit2 only using a Cit2 homology model for molecular replacement. Ultimately, we resolved the crystal structures of Ucc1-Skp1-Cit2, Apo-Cit2, Cit2-OAA-CoA, and Apo-Cit1 at resolutions of 2.30 Å, 2.39 Å, 1.48 Å, and 1.42 Å, respectively [1] (Fig. 1).

The Ucc1-Skp1-Cit2 structure comprises a Ucc1-Skp1 complex and a Cit2 dimer (Fig. 1(a)). Ucc1 features a typical F-box domain at its N terminus, while its substrate binding domain (SBD) adopts a unique structure. The interaction surface between Ucc1 and Cit2 involves complementary charged residues (Fig. 1(b)). The Apo-Cit2 structure consists of two Cit2 subunits, each containing large and small domains, with the ligand binding site situated between these domains (Fig. 1(c)). Apo-Cit2 lacks substrates OAA and acetyl-CoA in its open form, exposing its ligand

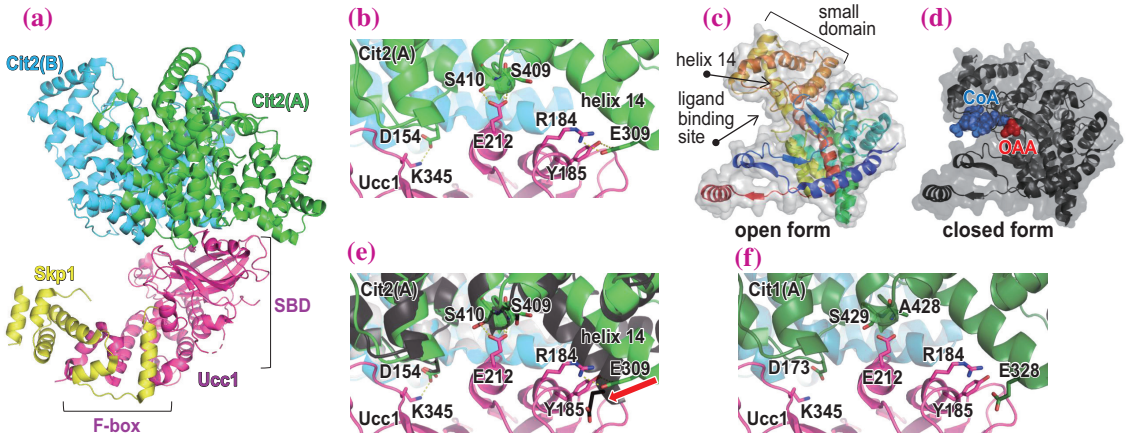

Fig. 1. Structural basis for the recognition mechanisms of citrate synthase by the Ucc1-Skp1 complex. **(a)** Overall structure of the Ucc1-Skp1-Cit2 complex. **(b)** Close-up view of the interaction between the Cit2 and Ucc1 in the Ucc1-Skp1-Cit2 complex. Critical hydrogen bonding residues are depicted as sticks. **(c)** Structure of subunit A in the ligand-free Cit2 (open form). Ribbon color-coded from blue to red (N- to C-terminus). **(d)** Structure of subunit A in Cit2 with OAA and CoA (closed form). **(e)** Superimposition of Cit2 closed form (black) on Cit2 in the Ucc1-Skp1-Cit2 complex. The red arrow indicates the movements of E309 in helix 14. **(f)** Predicted intermolecular contacts between Apo-Cit1 and Ucc1. Apo-Cit1 superimposed on Cit2 in the Ucc1-Skp1-Cit2 complex. Conserved amino acids predicted to form hydrogen bonds are shown as stick models.

binding sites to the solvent region. The structure of Apo-Cit2 closely resembles that of Cit2 in the Ucc1-Skp1-Cit2 complex. Additionally, we determined the crystal structure of Cit2-OAA-CoA, revealing a ligand-induced conformational change when OAA and CoA are present (Fig. 1(d)). This change involves the movement of the small domain to close the ligand binding site (closed form). The small domain of Cit2 contains E309, which interacts with R184 and Y185 in Ucc1. Therefore, such conformational changes may destruct these interactions. Indeed, mutant Cit2 E309A or Ucc1 R184A/Y185A substitutions result in reduced binding between them [1]. When the closed form of the Cit2 structure is superposed onto the Cit2 structure in the Ucc1-Skp1-Cit2 complex, helix 14, including E309 on Cit2, causes steric hindrance with Ucc1, (Fig. 1(e)). These results indicate that Ucc1 preferentially recognizes the open form, not the closed form of Cit2. Furthermore, these findings provide a structural basis for the previously proposed positive feedback loop in which a higher amount of gluconeogenic metabolites stabilizes Cit2 to activate the glyoxylate cycle [2] (Fig. 2(a)).

Recent advances in cell biology have unveiled factors hindering mitochondrial import, including the accumulation of reactive oxygen species associated with aging, mutations in mitochondrial DNA, and aggregated proteins linked to neurodegenerative diseases such as Alzheimer's disease and Parkinson's disease. The primary sequence of Cit2 shares over 75% identity with that of Cit1, a mitochondrial citrate synthase; indeed, the Apo-Cit2 structure was almost identical to the Apo-Cit1 structure (Fig. 1(f)). Additionally, the amino acid residues critical for Ucc1 binding in Cit2 are mostly conserved in Cit1. We hypothesized that SCF^{Ucc1} could also target non-imported Cit1, generated during mitochondrial import defects, for proteasomal degradation. Upon inhibiting mitochondrial import, non-imported Cit1 is recognized, ubiquitinated by SCF^{Ucc1}, and degraded by the proteasome [1]. Excessive accumulation of non-imported Cit1 induces ectopic citrate synthesis, causing an imbalance in sugar carbon flux, depletion in amino acid and nucleotide pools, and growth defects. All these results highlight SCF^{Ucc1} as a critical ubiquitin ligase controlling citrate metabolism (Fig. 2(b)).

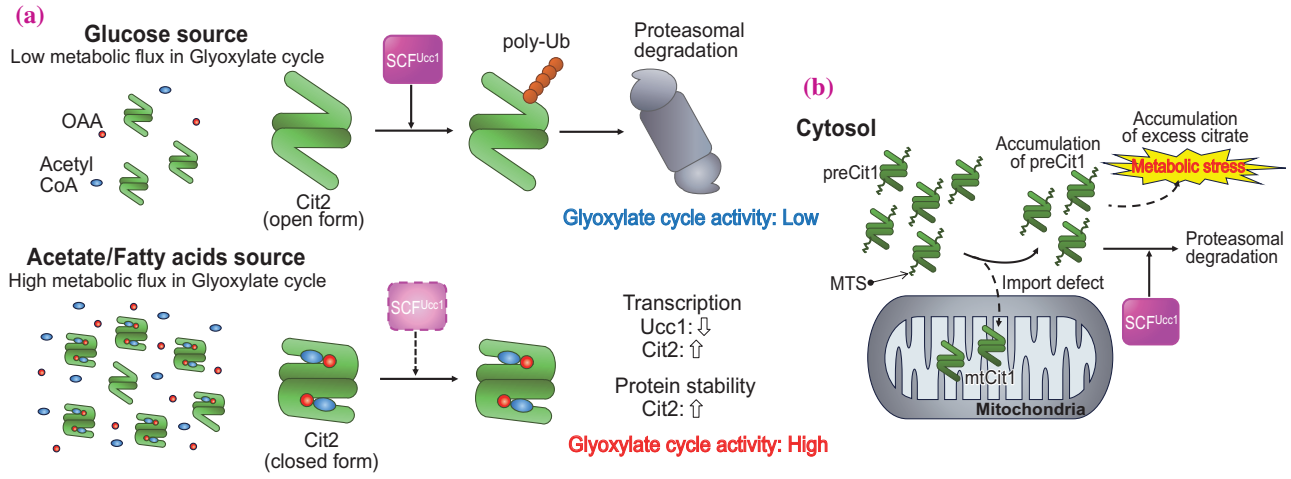

Fig. 2. Models illustrating the role of SCF^{Ucc1}. **(a)** SCF^{Ucc1}-mediated regulation of Cit2 in the modulation of metabolic flux. In acetate-grown cells, metabolites inhibit SCF^{Ucc1}-mediated ubiquitination of Cit2, activating the glyoxylate cycle to produce glucose through gluconeogenesis. **(b)** SCF^{Ucc1}-mediated degradation of mislocated Cit1 in the ectopic metabolic stress response.

Kazuya Nishio[a], Tsunehiro Mizushima[a] and Kunio Nakatsukasa[b,*]

[a] Department of Life Science, University of Hyogo
[b] Graduate School of Science, Nagoya City University

*Email: nakatsukasa@nsc.nagoya-cu.ac.jp

References

[1] *K. Nishio, T. Kawarasaki, Y. Sugiura, S. Matsumoto, A. Konoshima, Y. Takano, M. Hayashi, F. Okumura, T. Kamura, T. Mizushima, K. Nakatsukasa: Sci. Adv.* ***9*** *(2023) eadf1956.*
[2] K. Nakatsukasa *et al.*: Mol. Cell **59** (2015) 22.

Sweet/umami taste receptor-mediated chloride-sensation revealed by X-ray crystallographic analysis

Vertebrates sense organic nutrients in foods, such as sugars, amino acids, and nucleotides, by the sweet and umami receptors in the oral cavity. Taste sensation through these receptors promotes the intake of foods containing nutrients necessary for sustaining life. Sweet and umami receptors consist of taste receptor type 1 (T1r) proteins; the T1r2/T1r3 heterodimer serves as the sweet receptor, while T1r1/T1r3 serves as the umami receptor [1]. These receptors possess large extracellular domains that are responsible for the recognition of major taste substances, such as sugars and amino acids.

The mechanism by which these receptors recognize taste substances has long been unknown due to a lack of structural information. The most critical bottleneck in the structural analysis of these receptors is the preparation of protein samples. We previously found that the extracellular ligand-binding domain (LBD) of T1r2a/T1r3 from medaka fish was amenable to sample preparation by screening T1rs from various species [2]. The crystallographic structure of T1r2a/T1r3LBD was determined using SPring-8 **BL41XU** (Fig. 1(a)) [3]. The structure revealed the architecture of the ligand-binding sites in the receptor and the mechanism by which the receptor accommodated a wide array of amino acids at the binding sites. We also analyzed the structural difference between the amino acid-bound and ligand-free T1r2a/T1r3LBD by solution scattering using SPring-8 **BL45XU** and other equipment and found that the LBD undergoes a conformational change upon amino acid binding, likely inducing receptor responses resulting in taste sensation (Fig. 2) [2]. The crystal structure of medaka T1r2a/T1r3 is the sole structural information for T1rs reported to date and serves as a model for understanding T1r functions.

During the structural investigation of medaka T1r2a/T1r3LBD, we found the binding of an unknown substance in the vicinity of, but allosteric to, the amino acid binding site in the T1r3 subunit. The substance was most likely a chloride ion based on the coordination structure and distances (Fig. 1(a)). The effects of chloride on T1rs have never been investigated, although several examples have been reported for other receptors in the same protein family: class C G protein-coupled receptors (GPRCs). Therefore, we attempted to identify the chemical entity of the unknown substance, presumed to be a chloride ion, and examine its action on taste receptors [4].

First, all the chloride in the crystal of medaka T1r2a/T1r3LBD was replaced with bromide, and the diffraction data was collected using a wavelength of 0.9194 Å, close to the absorption edge of bromine, at BL41XU. The anomalous difference Fourier map derived from the data showed an eminent peak at the position where the presumed chloride ions were originally bound (Fig. 1(b)). These results indicate that the binding site was specific to halogen ions. Second, the diffraction data of the original crystal containing chloride was collected using a wavelength of 1.9 Å at BL41XU, as well as 2.7 Å at BL-1A at Photon Factory (Tsukuba, Japan). Although several kinds of light elements show similar levels of anomalous scattering,

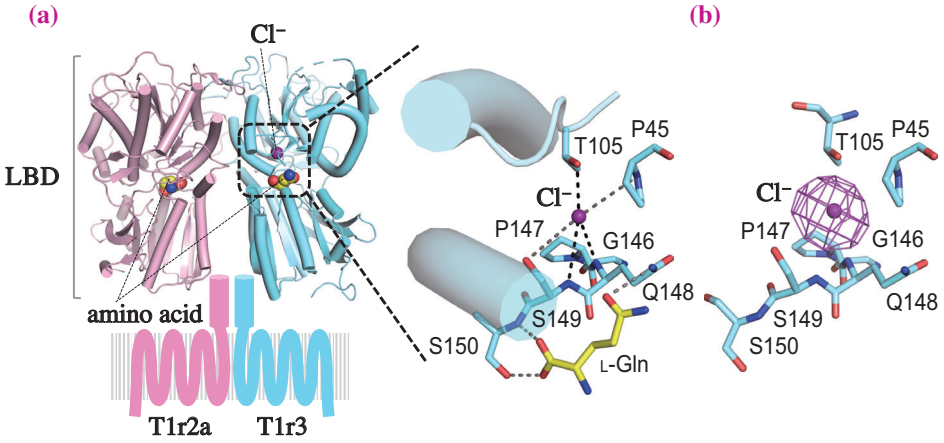

Fig. 1. The structures of the overall and the ligand-binding sites of T1r2a/T1r3 from medaka fish. **(a)** Schematic drawing of the overall structure of T1r2a/T1r3, in which the crystal structure of the ligand-binding domain (LBD) is shown (PDB ID 5X2M). The close-up view of the amino acid- and chloride ion-binding sites in T1r3 is shown in the right panel. **(b)** The anomalous difference Fourier map (5σ, magenta) derived from the diffraction data of the Br^--substituted crystal is overlaid to the chloride ion-binding site in T1r3.

as chloride ions are present at this wavelength, a noticeable anomalous difference in the Fourier peak was observed at the presumed position of the chloride ion, while the other peaks were observed at the positions of the sulfur atoms in the protein. With these data taken together, we conclude that the unknown element bound to T1r3 is a chloride ion. Using a binding assay, we confirmed that chloride binding to T1r3 occurs not only in crystals, but also in solution.

We have addressed the physiological relevance of chloride binding to T1r3. Biophysical analyses showed that chloride binding induced a conformational change in medaka T1r2a/T1r3LBD in a manner similar to that of an amino acid (Fig. 2). This is likely because both the amino acid- and chloride ion-binding sites are located close to the interface between the two T1r subunits, which are known to reorient upon agonist binding during the activation of other class C GPCRs (Fig. 1(a)). Therefore, the surrounding structures may be affected by the binding or dissociation of these substances. Notably, based on the structure and amino acid sequences, the chloride ion binding site is likely to be conserved among T1r3s in many species, including mammals such as humans and mice. Indeed, we examined taste nerve responses in mice and found that chloride application induced taste nerve responses mediated by T1rs. These results indicate that chloride ions evoke taste sensations through sweet and umami receptors.

It has been reported that humans perceive low-concentration table salt solutions to be sweet [5]. The concentration range of sodium chloride-induced sweet taste is reportedly lower than those inducing salty taste evoked by sodium ions, but matches with those inducing the conformational change of medaka T1r2a/T1r3LBD and taste nerve responses in mice by chloride ions. Therefore, chloride sensation via T1r may occur even in humans (Fig. 2). The finding of chloride ion binding in T1r3 observed by X-ray crystallography led to the presumption that the sweet and umami receptors play a role in salt taste sensation, which is important for its intake at an appropriate amount to maintain body fluid homeostasis, and thus for human health.

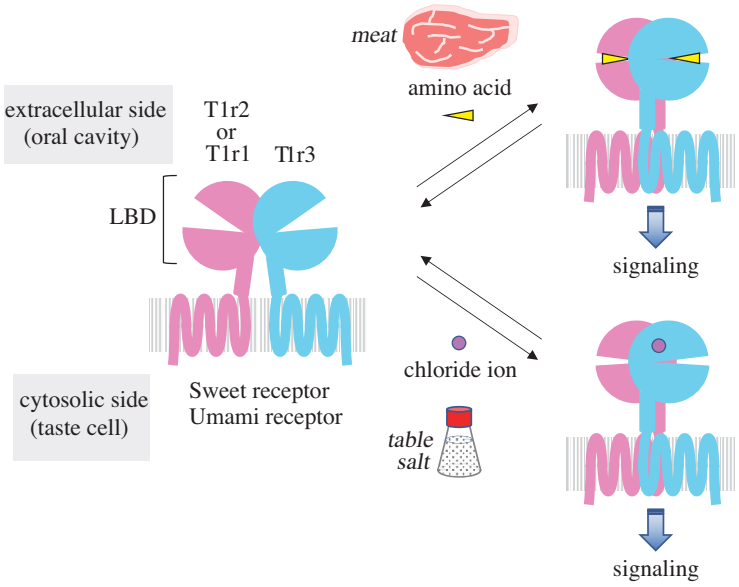

Fig. 2. Speculative mechanism of taste substance-induced responses by sweet and umami taste receptors. The schematic drawing shows the amino acid- (upper) and chloride ion- (lower) induced conformational change of the receptors and the resultant signal transductions.

Atsuko Yamashita

Faculty of Medicine, Dentistry
and Pharmaceutical Sciences, Okayama University

Email: a_yama@okayama-u.ac.jp

References

[1] R. Ahmad and J. E. Dalziel: Front. Pharmacol. **11** (2020) 587664.
[2] E. Nango *et al.*: Sci. Rep. **6** (2016) 25745.
[3] N. Nuemket, N. Yasui *et al.*: Nat. Commun. **8** (2017) 15530.
[4] *N. Atsumi, K. Yasumatsu, Y. Takashina, C. Ito, N. Yasui, R. F. Margolskee, A. Yamashita: eLife* ***12*** *(2023) e84291.*
[5] L. M. Bartoshuk *et al.*: Physiol. Behav. **21** (1978) 609.

Exploring the impact of whole-body vibration on bone metastasis and vascularization in a murine model of breast cancer

Breast cancer (BC) is the most prevalent cancer and primary cause of cancer-related fatalities among women worldwide, highlighting the urgency for effective interventions. Although advancements in early detection and treatment have enhanced survival rates, metastasis to distant organs, particularly bones, poses a significant challenge. Bone metastasis in BC often leads to osteolytic destruction, initiating a detrimental cycle of bone degradation and cancer progression. Despite patients with bone-only BC metastasis exhibit a more favorable prognosis than patients for whom metastasis is more extensive, the condition remains largely incurable, resulting in severe complications known as skeletal-related events. Current pharmacological interventions, such as bisphosphonates and denosumab, offer relief, but present long-term risks. Due to the mechanosensitivity of bone, exercise has been explored as a non-pharmacological approach; however, its applicability is hindered by the physical challenges faced by patients with BC. This study investigated whole-body vibration (WBV) as a potential passive exercise, demonstrating bone-anabolic responses without the risks associated with traditional exercise. Existing evidence supports WBV's efficacy in preserving bone health in various contexts, including childhood cancer survivors [1]. However, the specific effects on BC-induced bone loss remain unexplored. This study used mice with mammary tumors to assess the protective effects of WBV against metastatic BC-induced bone loss. In addition, this study examined the structure of the bone marrow vasculature in BC metastasis, considering its role in tumor progression and drug delivery. Employing synchrotron radiation-based computed tomography (SRCT, 2.74-μm cubic voxel) with vascular casting, our research aimed to provide valuable insights into the potential benefits of WBV in mitigating BC-induced bone loss and its impact on the associated bone marrow vasculature [2].

Eight-week-old female BALB/c mice were anesthetized, and 4T1 tumor cells were injected into the mammary fat pad. 4T1-bearing mice were assigned to two groups: those treated with Whole-Body Vibration (BC-WBV) and sham-treated controls (BC-Sham). Age-matched mice (intact) were sham-treated to assess the progression of bone loss induced by the 4T1 cell injection. The BC-WBV group experienced 20 min/day of vertical sine-wave vibration with a 0.3 g amplitude at 90 Hz for five days a week, concurrently with similar handling for BC-Sham and Intact mice, albeit without vibration exposure.

Three weeks after the onset of the vibration protocol, the mice were euthanized, and the right and left tibiae were harvested from the three groups for SRCT and H&E histology, whereas the subsets of BC-Sham and BC-WBV mice underwent vascular casting. Briefly, under isoflurane anesthesia, mice underwent laparotomy, followed by catheterization of the left ventricle and euthanization. The vascular bed was cast using a zirconium-based contrast agent (ZrCA), consisting of a mixture of agarose and colloidal ZrO_2 particles. The right tibia was then harvested and fixed in formalin.

The proximal metaphyseal portion of all specimens was scanned with a 17.95-keV X-ray at SPring-8 **BL20B2**. Calibration using K_2HPO_4 phantom solutions yielded the relation: $\mu = 7.58 \times BMD + 1.03$, where μ (cm^{-1}) is the linear absorption coefficient, proportional to the grayscale value of reconstructed bone image, and BMD (g/cm^3) is the bone mineral density. The vascular-cast specimens underwent additional scanning using an 18.05-keV X-ray, which enhanced the contrast of the blood vessels due to the sharp absorption jump of ZrCA. Therefore, selective visualization of vascular structures was possible by subtraction between a pair of 17.95- and 18.05-keV images [3]. Figure 1 shows the

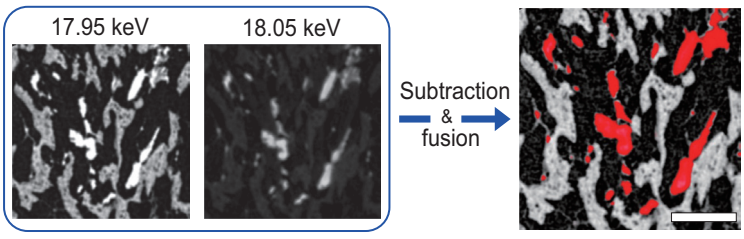

Fig. 1. Images reconstructed from scan data sets at 17.95 keV and 18.05 keV and their fusion via image subtraction, segmented into blood vessels (red) and trabecular bone (gray). Bar, 100 μm.

images of the tibial marrow region reconstructed from SRCT using 17.95- and 18.05-keV light and their fusion.

Histological H&E sections demonstrated metastatic lesions that extensively infiltrated the bone marrow cavity in both the BC-Sham and BC-WBV groups; however, a significant difference was found in the degree of bone destruction between the two groups. Figure 2 shows the cross-sectional bone reconstructions from the Intact, BC-Sham, and BC-WBV groups, and the bone structural indices and mean BMD of the three groups. Osteolytic bone deterioration in the BC-Sham group was characterized by a decrease in cortical bone thickness, trabecular bone volume fraction, trabecular bone thickness, trabecular number, and mean BMD in both the cortex and trabeculae. In contrast, no significant differences were found in bone features other than trabecular bone thickness between the BC-WBV and Intact groups, indicating the bone-protective effects of WBV.

Figure 3 shows three-dimensional reconstructions of the marrow vasculature and trabeculae, as well as the distribution of diameter-specific vascular volume fractions in BC-Sham and BC-WBV mice. On average, BC-WBV mice had smaller vessel diameters and spacing and a trend toward higher vessel numbers compared to BC-Sham mice. Furthermore, WBV shifted the distribution of diameter-specific vascular volume fractions toward smaller vessel diameters and decreased the heterogeneity of the marrow vessel diameter. Solid tumor vasculature is characterized by increased heterogeneity in vessel diameter, which causes not only low perfusion, but also heterogeneous perfusion, leading to regional tissue hypoxia. Hypoxia confers aggressive and metastatic phenotypes to tumors, and heterogeneous perfusion coupled with increased interstitial fluid pressure leads to inefficient delivery of antitumor drugs. Therefore, WBV may be effective against tumor growth and poor distribution of antitumor drugs [4].

In summary, WBV mitigates bone loss in BC bone metastasis, which may be partly due to the alteration of the marrow vasculature, which is favorable for reducing regional hypoxia in BC metastatic bone lesions. Further studies are needed to clarify the multiple actions of WBV on the bone, tumor, and marrow vasculature and how they contribute to bone protection in BC metastasis.

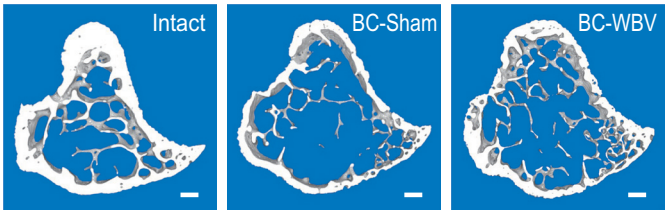

Bone structural indices and mineral density

	Intact (n = 5)	BC-Sham (n = 15)	BC-WBV (n = 13)
Cortical bone thickness (μm)	180.0 ± 4.0	99.8 ± 4.6##	117.2 ± 9.5*
Trabecular bone volume fraction (%)	6.82 ± 0.58	3.80 ± 0.46##	4.88 ± 0.55
Trabecular bone thickness (μm)	45.0 ± 0.8	33.3 ± 1.3#	33.5 ± 2.1#
Trabecular bone number density (mm^{-3})	1688 ± 272	1179 ± 195#	1575 ± 203*
Cortical bone mineral density (g/cm^3)	1.26 ± 0.03	1.13 ± 0.02##	1.18 ± 0.02**
Trabecular bone mineral density (g/cm^3)	1.01 ± 0.03	0.93 ± 0.01##	0.95 ± 0.01*

Data are presented as mean±SD. #P<0.05, ##P<0.01 *vs.* Intact; *P<0.05, **P<0.01 *vs.* BC-Sham.

Fig. 2. Reconstructions of proximal tibial diaphyseal bone from each of Intact, BC-Sham, and BC-WBV groups, binarized with a threshold of 0.5 g/cm^3 (top) and the summary of the bone structural indices and mineral density (bottom). Bar, 100 μm.

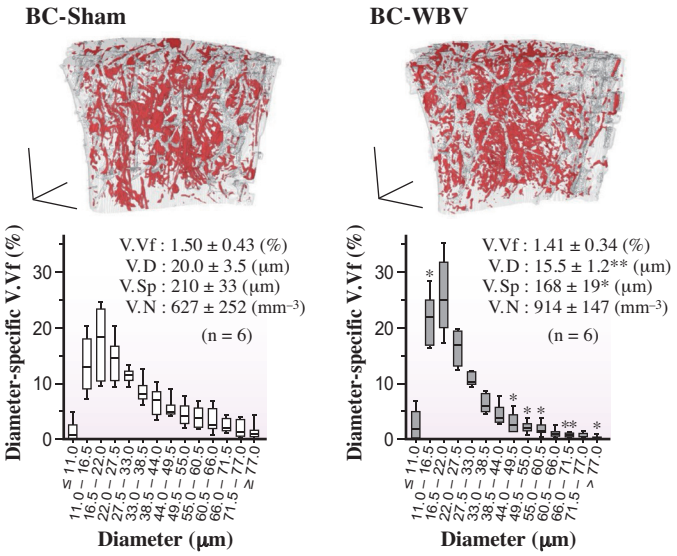

Fig. 3. Reconstructions of blood vessels and trabeculae (top) and boxplots of the diameter-specific vascular volume fraction (bottom) in the medullary region of proximal metaphyseal tibiae of BC-Sham and BC-WBV groups. V.Vf, vascular volume fractions; V.N, vessel number; V.Sp, vessel spacing; V.D, vessel diameter. The lengths of orthogonal line segments are all 0.5 mm. *P < 0.05, **P < 0.01 *vs.* BC-Sham.

Takeshi Matsumoto

Industrial and Social Sciences, Tokushima University

Email: t.matsumoto@tokushima-u.ac.jp

References

[1] R. J. Mogil *et al.*: JAMA Oncol. **2** (2016) 908.
[2] *T. Matsumoto and A. Mukohara: Calcif. Tissue Int.* ***111*** *(2022) 535.*
[3] T. Matsumoto *et al.*: Lab. Invest. **93** (2013) 1054.
[4] R. Lugano *et al.*: Cell Mol. Life Sci. **77** (2020) 1745.

Synchrotron stories: Illuminating the past through foraminiferal imaging

In the past two centuries, human activities have significantly impacted coastal regions, affecting vulnerable areas subjected to natural hydrographic changes and increasing anthropogenic pressures [1]. Rising atmospheric carbon dioxide levels (pCO_2) lead to ocean acidification (OA), as well as contribute to higher temperatures, increased water stratification, and the expansion of oxygen-depleted zones (hypoxia or deoxygenation), and results in the degrading of coastal benthic ecosystems.

To understand these changes' severity and potential outcomes, we turned to paleoenvironmental records, specifically marine sediment archives and their calcite microfossils. In our study, we used 3D reconstructions of foraminiferal shells, focusing on the species *Elphidium clavatum* in the Öresund region, a transition zone between the North Sea, Skagerrak, and the Baltic Sea, highly vulnerable to hydrographic changes and human impacts [1]. Foraminifera are single-celled microorganisms, often with a shell of calcite making them highly useful in environmental and climate reconstructions. Employing a synchrotron light-based μCT approach, we provide a historical context from the 1800s to the present day, offering insights into environmental changes through morphological patterns [2].

Detailing morphological changes based on synchrotron light-based μCT has only been used to a limited extent in micropaleontology; we are providing one of the very first μCT-based time series. We used foraminiferal samples from the study by Charrieau *et al.* [1], and we particularly focused on *Elphidium clavatum*, to unravel environmental changes in the Baltic Sea entrance over the past 200 years. This species is especially interesting since it dramatically changes its abundance over the investigated period. We carefully selected 16 sediment layers, each representing a snapshot in time, and chose a total of 124 foraminiferal specimens for detailed tomographic analysis.

To capture the intricate details of these microscopic specimens, we employed advanced imaging techniques at SPring-8 **BL47XU**. Synchrotron light-based μCT, with a voxel size of 0.5 μm and 1800 projections, provided unprecedented clarity in our 3D reconstructions. These images were then processed using open-source software Fiji and MeshLab (Fig. 1).

The challenging task of measuring the thickness of foraminiferal shells was tackled using a novel approach. Instead of traditional 2D image analyses which only use parts of the shell, we automatically computed the thickness of the entire shell from the image stack, using the BoneJ plugin in Fiji. This is a novel approach, not used before in micropaleontology. Moving beyond traditional analyses, we explored the relationships between the surface/volume ratio, pore density, and thickness from 3D reconstructions using MeshLab (Fig. 2). Pore patterns, a relatively unexplored aspect, were examined using a topological tool to estimate the number of pores throughout the entire shell.

Our analysis of 124 foraminiferal specimens revealed profound changes in foraminiferal abundance, reflecting the impact of natural shifts and anthropogenic pressures over the investigated time period. Long-term morphological trends in *Elphidium clavatum*, such as a ~28% decrease in shell average thickness and a ~91% increase in the number of pores, illustrate the pronounced change in coastal environments due to multiple stressors such as ocean acidification, deoxygenation, and warming (Fig. 3). Large variability in morphological patterns at the same age level indicates contrasting environmental conditions, while lower variability suggests stability.

Examining variations over the centuries, we noted

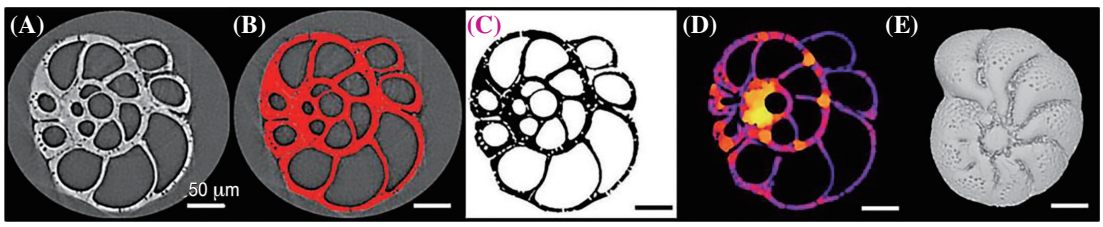

Fig. 1. Illustration of the stepwise image processing of a shell. **(A)** Visualization of raw images. **(B)** Segmentation. **(C)** Binary images resulting from the segmentation. **(D)** Thickness map generated by the BoneJ plugin. **(E)** 3D reconstruction of a shell.

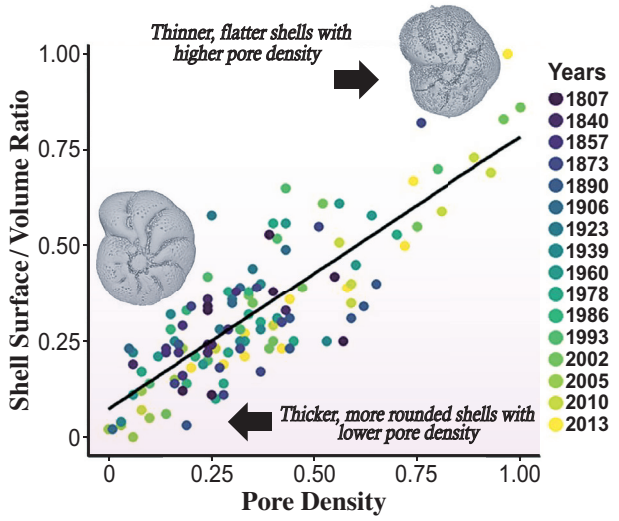

Fig. 2. Relationships between the shell surface/volume ratio and the pore density. Values adjusted between 0 and 1.

asynchronous changes between foraminiferal abundance and morphological patterns. In the early industrial period, despite stable foraminiferal abundances, pore density fluctuated broadly, indicating significant natural variations. From the 1940s, synchronous increases in both abundance and morphological variability suggest more pronounced seasonal environmental shifts and increased anthropogenic impact. In the early 21st century, a stable abundance alongside significant morphological variations signifies a persistent multi-stressor scenario. The large degree of morphological variability might be linked to maximizing the chances of species survival during more adverse conditions.

Our project not only underscores the significance of using a 3D time series of calcifying microfossils from geological archives to quantify the impacts of anthropogenic climate change and natural variability but also introduces an enhanced efficiency in 3D post-data analysis. The method is a valuable complement to traditional foraminiferal assemblage studies, providing a more detailed and nuanced understanding of the evolving dynamics in coastal environments. By decoding the intricate language of foraminiferal morphological changes, our study contributes critical insights into the effects of both human influence and natural forces on these delicate ecosystems, furthering our knowledge of the complex interactions shaping our coastal regions.

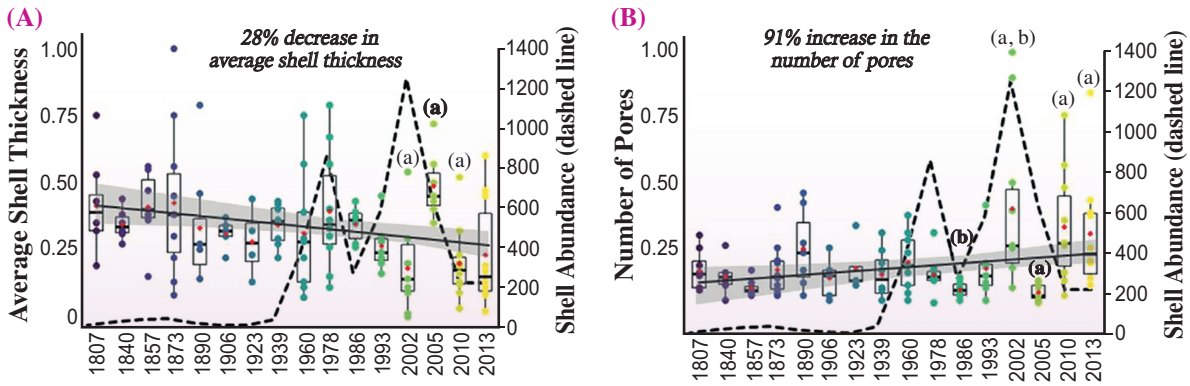

Fig. 3. 3D time series of the **(A)** Average thickness and **(B)** Number of pores. Boxplots are shown with colored individual data points per estimated year, the red diamond indicates the mean. The dashed line is the shells' abundance [2]. The morphological values (*y*-scale) are adjusted (0–1). The bold letters **(a, b)** indicate significant differences. A regression line (black line) with a 95% confidence interval (gray area) represents a significant long-term trend.

Helena L. Filipsson* and Constance Choquel

Department of Geology, Lund University, Sweden

*Email: Helena.Filipsson@geol.lu.se

References

[1] L. M. Charrieau *et al.*: Biogeosciences **16** (2019) 3835.
[2] *C. Choquel, D. Müter, S. Ni, B. Pirzamanbein, L. M. Charrieau, K. Hirose, Y. Seto, G. Schmiedl, H. L. Filipsson: Front. Earth Sci.* ***11*** *(2023) https://doi.org/10.3389/feart.2023.1120170*

Virtual osteohistology of paravian dinosaurs: from 2D to 3D perspective

Starting in 2016, a Japan-Slovak research platform in integrative paleobiology was established at SPring-8. This platform aims to utilize synchrotron radiation to detect information about the life of extinct organisms accessible in fossilized remains. Several pilot projects were carried out to test imaging technology at SPring-8 on different kinds of fossil objects such as individual bones of recently extinct giant birds of New Zealand and Madagascar (2016A1038) and of non-avialan and avialan dinosaurs from the Mesozoic of China (2018B1543), as well as objects more challenging for scanning, including high-density dinosaur eggs containing embryos (2017A1714, 2017B1755) and flattened fossils associated with soft tissues (2019B1381). Here, we demonstrate our first results referring to both the imaging quality and research achievements in studying dinosaur evolution.

Two major investigation approaches, invasive (or destructive) and non-invasive (non-destructive), have been used to access the inner structure of fossilized objects: skulls, individual bones, teeth, eggs, eggshells, mineralized soft tissues, and amber inclusions. The destructive approach was used by earlier paleontologists to make hidden anatomy available for study, for example, to assess the shapes of the inner cranial cavities, canals, and sinuses by sawing fossilized skulls. From a historical perspective, these studies can be seen as revolutionary in revealing unknown biological features that significantly influenced our understanding of less accessible morphology. Despite the invasive nature, those studies had inductive effects on the modernization of our views concerning the capacity of fossils to preserve much more than anatomic information. Thus, a semi-destructive approach is still broadly applied for making physical thin sections to investigate developmental events recorded in hard tissues.

Modern experimental approaches are expected to reduce invasive intervention to a minimum. They are required to possess enhanced functionalities for the accurate visualization of qualitative traits and quantitative characters in three dimensions on a micro- or nanoscale. It is mainly the quantitative aspect of the ancient tissue microstructure that is currently seen as a promising, but mostly underexplored, source of evolutionary information. This source provides the correlation interface for the reconstruction of biological phenomena such as ontogenic chronology [1], embryonic development [2], growth dynamics, metabolic rates, thermoregulation, physiological crises, sexual maturity, reproduction, and which may further facilitate progress in new disciplines: paleoproteomics and paleogenomics. X-ray imaging techniques turned out to be well-adapted and prospective for multiscale purposes of the paleobiological investigation. We claim that at SPring-8 **BL20B2** and **BL28B2**, combined with other imaging beamlines, provide an extraordinary experimental environment that makes SPring-8 one of the leading facilities suited for exploring new cellular and molecular frontiers of ancient life. As far as virtual osteology is concerned, we succeeded in imaging the 3D microstructure of 120 million-year-old bones with an exceptional histological resolution that is comparable to 2D physical thin sections (Fig. 1(a)). This histological quality resulted from the well-sized samples (preserved in volcanic rocks) and modulation of scanning parameters (reasonable X-ray energy, exposure time, and effective propagation distance) for reaching the voxel size between 1 and 2 microns. The

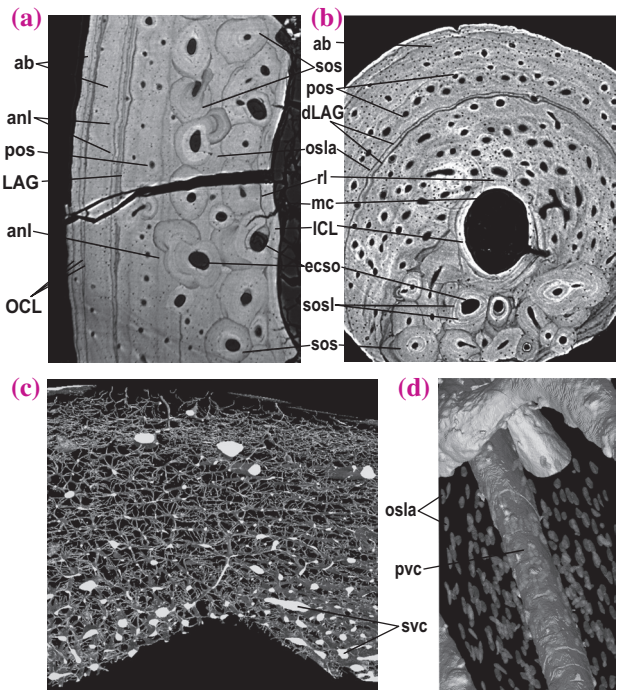

Fig. 1. (**a,b**) Virtual paleo-osteohistology of dinosaur bones (Paraves) approaching histological quality. (**c,d**) 3D-rendered vasculature and osteocyte lacunae of the extinct giant bird (Dinornithiformes). Abbreviations: ab, avascular bone; anl, annulus; dLAG, double ICL; ecso, expanded cavity with sos; inner circumferential layer; LAG, line of arrested growth; OCL, outer circumferential layer; osla, osteocyte lacuna; pos, primary osteon; rl, resorption line; sos, secondary osteon.

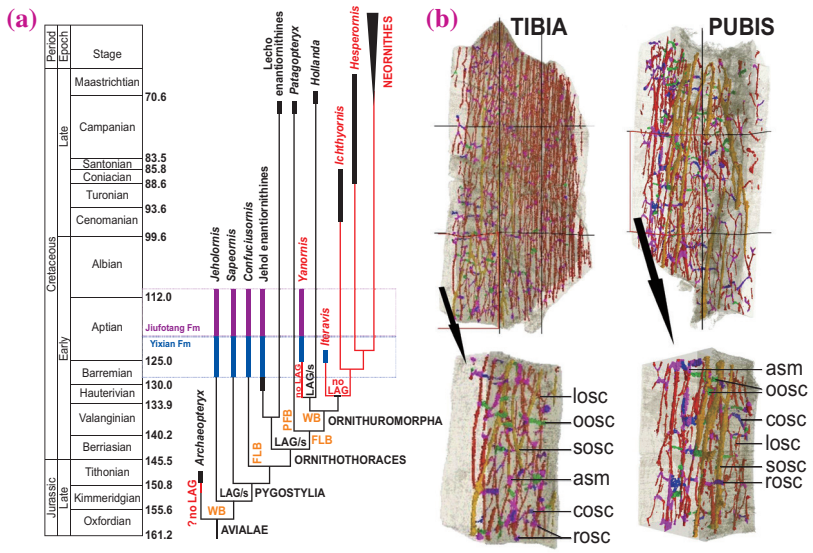

Fig. 2. (**a**) Simplified cladogram depicting the ornithuromorph lineages, in which rapid uninterrupted growth (red lines) evolved. (**b**) 3D-rendered vasculature models of the limb and pelvic bones of *Yanornis martini*. Abbreviations: asm; anastomosis; cosc, circumferential osc (in blue); FLB, fibrolamellar bone; LAG, line of arrested growth; losc, longitudinal osc (in red); oosc, oblique osc (in green); osc, osteonal canal; rosc, PFB, parallel-fibered bone; radial osc (in purple); sosc, secondary osc (in orange); WB, woven bone.

phase contrast modality enabled the reconstruction of complex vascularization in fossil and subfossil bones (Fig. 1(b)) with a high precision that is critical for further quantitative investigation.

Osteohistology of the long bones of extant amniotes usually indicates higher vascularization. Higher vascularization is typically associated with high metabolic activity and non-interrupted growth (Fig. 2(a)) in birds and mammals. In general, there is a direct correlation between metabolic rates and body temperature. We used bone vasculature variables as a proxy to determine growth rates and thermophysiology of the Mesozoic avialan dinosaur *Yanornis martini* (one of the oldest birds with non-interrupted growth) using 2D synchrotron osteohistological sections [3].

We found that *Yanornis* exhibits a dual pattern in growth rates between the pelvic bone (pubis) and the inferior limb bone (tibia) (Fig. 2(b)). Having plotted the extant ectothermic and endothermic proxies, based on vascular ratios, the estimated thermic values for *Yanornis* are aligned with those of marsupial and saurian taxa rather than with most of the endothermic taxa (birds and placentals), indicating a rather mesothermic thermophysiology. We further test this interpretation using 3D synchrotron-based data of *Yanornis*, the non-avialan dinosaur *Liaoningvenator* (Fig. 3), and extant amniotes (e.g., *Opisthocomus*, *Arvicola*) using enhanced analytical tools able to fragment the neurovascular complex by diameter and angulation of osteonal canals.

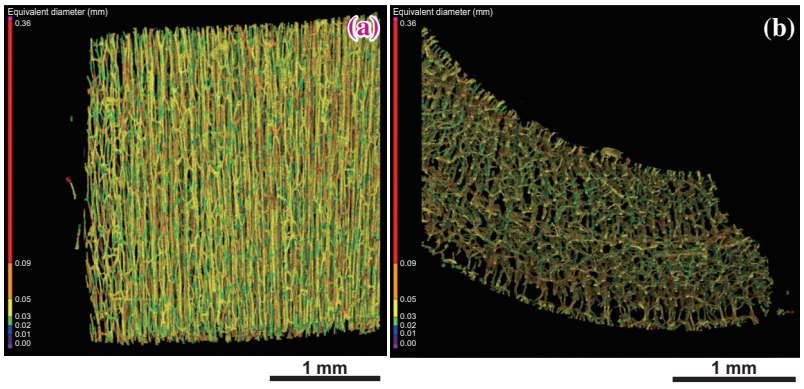

Fig. 3. Fragmentation of the bone neurovascular network by diameter in a paravian dinosaur. (**a**) Radial view. (**b**) Longitudinal view.

Martin Kundrát[a,*], Kentaro Uesugi[b] and Masato Hoshino[b]

[a] Center for Interdisciplinary Biosciences, Technology and Innovation Park, Pavol Jozef Šafárik University, Slovakia
[b] Japan Synchrotron Radiation Research Institute (JASRI)

*Email: martin.kundrat@upjs.sk

References

[1] C. Shen *et al.*: Historical Biol. **31** (2019) 253.
[2] M. Kundrát *et al.*: Current Biol. **30** (2020) 1.
[3] *Q. Monfroy, M. Kundrát, K. Uesugi and M. Hoshino: Historical Biol. **34** (2022) 1039.*

Investigating the micro-scale structures of macro-scale dinosaur bones using synchrotron radiation-based X-ray micro-tomography

Introduction

Understanding the biology of dinosaurs is facilitated by assessing the histological microstructures (HMSs) of fossilized bones. Synchrotron radiation-based X-ray micro-tomography (SXMT) was employed at SPring-8 **BL28B2** to visualize the HMSs of dinosaur bones through tomographic images [1].

Analyzing dinosaur bones

HMSs provide numerous insights into the growth rate, age, and physiology of vertebrate bones [2]. For example, a growing bone contains numerous vascular canals (less than 1 mm in diameter) that provide nutrients to the bone. A young bone also exhibits secondary osteons as sites for the deposition of new bone materials. Additionally, a long bone accumulates the lines called the lines of arrested growth (LAGs). Each LAG is much less than 0.1 mm in width and is deposited each year in most dinosaurs with irregular growth rates (Fig. 1). What is important about these HMSs is that they may be preserved in fossil bones. Therefore, they can be used to investigate the growth rate, age, and physiology of fossilized and extinct animals, including dinosaurs.

However, although the usefulness of HMSs in dinosaur research is unquestionable, there are limitations. In the traditional analytical technique to observe HMSs, samples must be cut and ground into thin sections (typically 0.03 mm thick) to be analyzed under a petrological microscope. Thus, this technique damages the samples and is difficult to apply to the specimens under conservation. This is where SXMT becomes very useful.

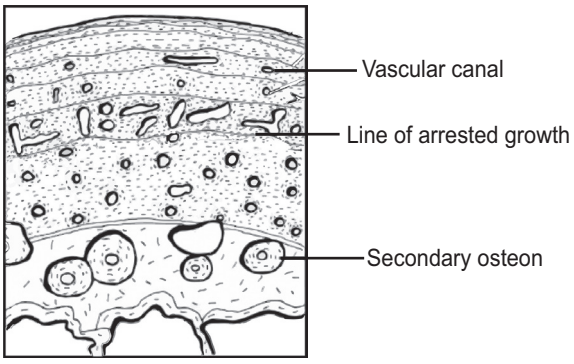

Fig. 1. Schematic of HMSs observed in a dinosaur bone (modified from Ref. 2).

Studying dinosaur growth at SPring-8

Using SXMT, HMSs in fossil bones can be visualized without damaging them. In the SXMT technique, an X-ray beam with a large flux and high coherence can penetrate dense and large fossilized bones and highlight subtle compositional differences in various HMSs. Previously, the capacity and advantages of SXMT at SPring-8 have not been thoroughly addressed. Therefore, this technique was applied to dinosaur limb bones to demonstrate its effectiveness.

In the study by Imai *et al.* two femora (thigh bones) of *Fukuiraptor* were used as samples. *Fukuiraptor* is a carnivorous dinosaur found in Fukui, Japan (Fig. 2) that lived approximately 120 million years ago, and the largest individual measured approximately 4.5 m in length [3]. Fossil bones assignable to *Fukuiraptor* are designated as natural treasures, making it difficult to conduct HMS studies using the traditional (destructive) technique. These dinosaur fossils are good candidates for SXMT. The BL28B2 was selected for the experiments because it has a large available field of view (~3 cm) and X-ray energy (~200 keV), which are ideal for large and dense dinosaur bones. The femora were approximately 20 cm long and 3 cm wide at their shafts. Special permission was granted to cut and grind these samples to compare the results of the traditional technique with those of SXMT.

For each experiment, approximately 20 tomographic images of the femoral shaft were acquired in each experiment. Figure 3 shows a comparison of the images obtained using traditional and SXMT techniques. Thin-section images obtained using the traditional technique exhibited vascular canals, numerous secondary osteons, and LAGs. Tomographic images captured using SXMT showed identical HMSs. On tomographic images, extensive distribution of vascular canals and many secondary osteons indicated that the femur was actively growing. Additionally, there were in total of four LAGs in the femur, suggesting that it belonged to a *Fukuiraptor* individual that was four years old at the time of death. Therefore, this study argues that at the age of four, *Fukuiraptor* was immature and its bones were still growing. These observations and arguments demonstrate the effectiveness of SXMT in HMS analyses of dinosaur bones.

Applications of SXMT to HMSs in fossil bones have only recently begun at SPring-8. The experiments were successful in that HMSs in *Fukuiraptor* femora were visualized without damaging the samples [1].

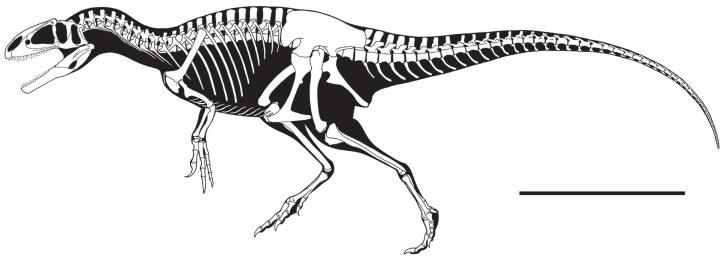

Fig. 2. Skeletal reconstruction of *Fukuiraptor kitadaniensis*. Scale bar = 1 m. Artwork by G. Masukawa.

The potential of this technique is not limited to evaluating dinosaur growth. For example, the pathways of the blood vessels within fossil bones that supply nutrients to particular tissues can be traced. Additionally, SXMT enables large-scale HMS analysis of multiple samples, in which numerous histological sections of numerous bones can be obtained. However, it is hoped that more researchers and students will apply this technique to their specimens to expand its potential. Numerous dinosaur species and types of HMS studies can be used to increase our understanding of these peculiar animals.

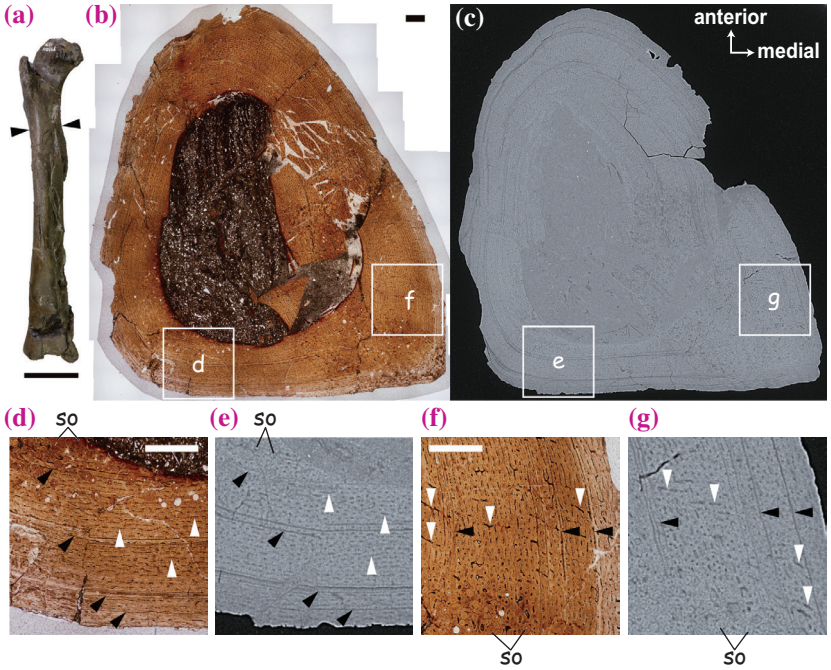

Fig. 3. Exterior **(a)**, transverse thin sections **(b, d, f)** and tomographic images **(c, e, g)** of the shaft of a *Fukuivenator* femur. Arrowheads in (a) indicate the level at which the thin section and tomographic images was obtained. Rectangles in (b) and (c) indicate areas magnified in d–g. Black arrowheads in (d–g) indicate LAGs. White arrowheads in (d), (e), (f), and (g) indicate vascular canals. Thin-section images and corresponding tomographic images are in the same scales. Abbreviations: so, secondary osteon. Scale bars = 20 mm for (a) and 1 mm for (b), (d), and (f).

Takuya Imai

Institute of Dinosaur Research, Fukui Prefectural University

Email: ti.star.gtw@gmail.com

References

[1] *T. Imai, S. Hattori, M. Hoshino and K. Uesugi: J. Synchrotron. Rad.* ***30*** *(2023) 627.*
[2] A. M. Bailleul *et al.*: PeerJ. **7** (2019) e7764.
[3] Y. Azuma and P. J. Currie: Can. J. Earth Sci. **37** (2000) 1735.

Impact of the U 5*f* states in the electronic structure of heavy-fermion superconductor UPd_2Al_3: Electronic structure study of $ThPd_2Al_3$

Actinides exhibit distinct physical properties. For example, a number of unconventional superconductors have been discovered among them and have attracted much attention. These characteristic physical properties originate from strongly correlated 5*f* states, which exhibit both localized and itinerant properties. UPd_2Al_3 is a typical uranium compound that exhibits an antiferromagnetic transition at T_N = 14 K and undergoes a transition into a superconducting state at $Tc = 2$ K [1]. To understand the 5*f* state, it is essential to observe its band structure and Fermi surface. Angle-resolved photoemission spectroscopy (ARPES) is a powerful experimental technique that allows experimental observation of the band structure and Fermi surfaces of materials [2]. In this study, the electronic structure of $ThPd_2Al_3$, a non-5*f* reference compound for UPd_2Al_3, was investigated by ARPES using soft X-rays from SPring-8 **BL23SU** to clarify the contribution of the U 5*f* state to UPd_2Al_3 [3]. The crystal structures of $ThPd_2Al_3$ and UPd_2Al_3 are shown in Fig. 1. Both compounds share a common hexagonal structure, with Th(U)–Pd and Al layers stacked alternately along the *c*-axis.

Figure 2 summarizes the band structure and Fermi surfaces of $ThPd_2Al_3$ obtained by ARPES: the ARPES spectrum of $ThPd_2Al_3$ measured along the Γ-K-M high symmetry line at $h\nu$ = 660 eV and the calculated band structure with the simulation of the ARPES spectra based on the band-structure calculation are shown in Figs. 2(a) and 2(b), respectively. The prominent dispersions at $E_B \geq 2.5$ eV are the contributions from the Pd 4*d* states, while the dispersive bands at $E_F \leq E_B \leq 2.5$ eV reflect the contributions mainly from other Al and Th states. The experimental band structure was well explained by band structure calculations. The Fermi surface map obtained by the integration of the ARPES spectra over 100 meV across E_F, the calculated Fermi surface with the simulation of the experimental Fermi surface map, and the three-dimensional shapes of the calculated Fermi surfaces are shown in Figs. 2(c,d) and 2(e), respectively. The Fermi surface of $ThPd_2Al_3$ was also well explained by band structure calculations.

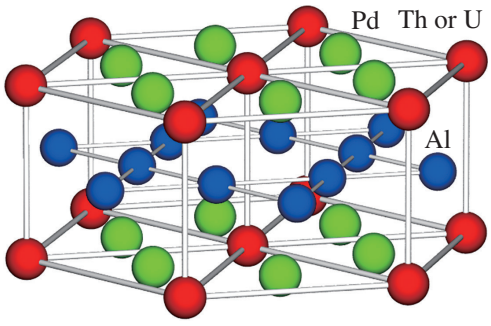

Fig. 1. Crystal structures of $ThPd_2Al_3$ and UPd_2Al_3.

Next, we compared the ARPES spectra of $ThPd_2Al_3$ and UPd_2Al_3 to reveal the contribution of the U 5*f* states to the electronic structure of UPd_2Al_3. Figures 3(a) and 3(b) show the experimental ARPES spectra of $ThPd_2Al_3$ and the corresponding calculated band structures, respectively. The color coding of the calculated bands represents the contributions from the Th 6*d* and Al 3*p* states. The experimental ARPES spectra are well explained by the band structure calculations, which suggest that the Fermi surface of $ThPd_2Al_3$ exhibits an enhanced Al 3*p* character. Figures 3(c) and 3(d) show the experimental ARPES spectra of UPd_2Al_3 recorded at $h\nu$ = 600 eV and the corresponding calculated band structure. The U 5*f* difference spectrum obtained by the resonant photoemission measurements and the calculated U 5*f* DOS are shown in the right panel of Fig. 3(c). The experimental energy dispersions of $ThPd_2Al_3$ and UPd_2Al_3 are very similar to each other, but the intensity of the energy dispersions distributed at $E_B = E_F - 1.2$ eV is enhanced in the spectra of UPd_2Al_3, which is the contribution from the U 5*f* states. The overall structure of the experimental spectra of UPd_2Al_3 was also explained by band structure calculations, although the details of each dispersion were not resolved experimentally. A comparison between the ARPES spectra of $ThPd_2Al_3$ and UPd_2Al_3 indicated that the U 5*f* states were strongly hybridized with the non-*f* dispersive bands, which corresponded to the calculated bands 15–18 for $ThPd_2Al_3$. These calculated bands have an enhanced contribution from the Al 3*p* states, suggesting that the U 5*f* states are strongly hybridized with the Al 3*p* states of UPd_2Al_3. This implies that the U 5*f* states form heavy quasi-particle bands with a strong three-dimensional character because the U–Pd and Al layers are stacked along the *c*-axis, as shown in Fig. 1. By contrast, the U 5*f* states have a strong electron correlation effect, and the U 5*f* states in UPd_2Al_3 have an incoherent peak distributed at approximately E_B = 0.2 – 1 eV as shown in the right panel of Fig. 3(c). Thus, the experimental bands near this binding energy can be attributed to

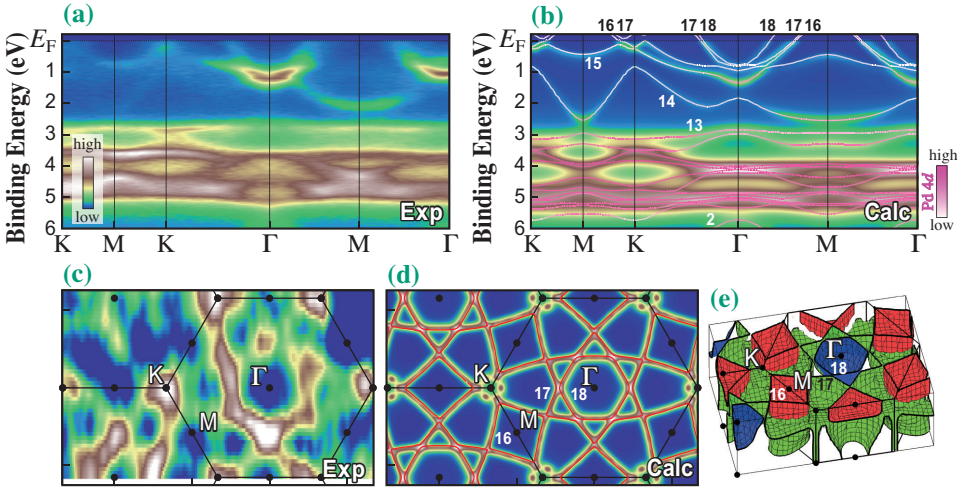

Fig. 2. Band structure and Fermi surface of $ThPd_2Al_3$ obtained by angle-resolved photoemission spectroscopy (ARPES).

an incoherent component. This is consistent with the dual nature of the U 5*f* states in UPd_2Al_3 as proposed theoretically, where superconductivity appears as a result of strong coupling between the heavy quasi-particle bands and the localized component of the U 5*f* states [4].

Accordingly, the Fermi surface and band structure of $ThPd_2Al_3$ obtained by ARPES were well explained by band structure calculations. A comparison between the ARPES spectra of $ThPd_2Al_3$ and UPd_2Al_3 suggests that the electronic structure of UPd_2Al_3 in the vicinity of E_F is dominated by enhanced U 5*f*-Al 3*p* hybridization, and the U 5*f* states form heavy quasi-particle bands with a strong three-dimensional character, which is responsible for the superconductivity of this compound.

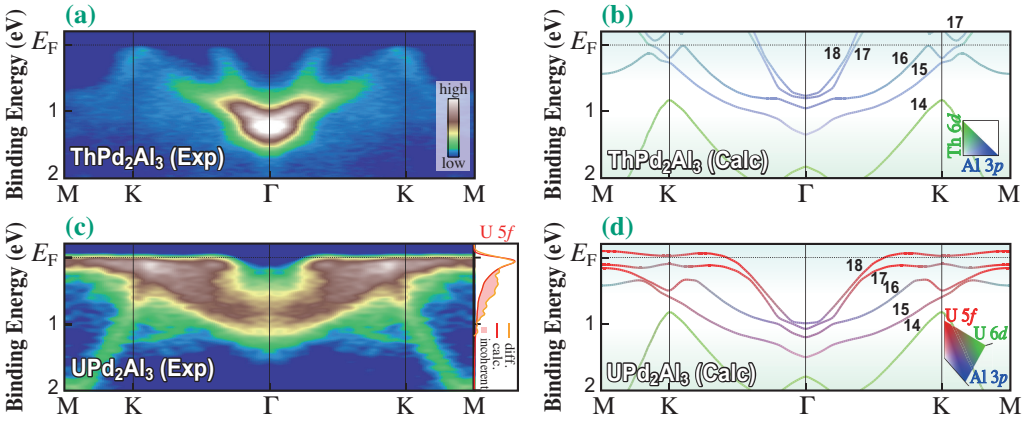

Fig. 3. Comparison between the ARPES spectra of $ThPd_2Al_3$ and UPd_2Al_3 and the result of the band structure calculations.

Shin-ichi Fujimori

Materials Sciences Research Center,
Japan Atomic Energy Agency

Email: fujimori@spring8.or.jp

References

[1] C. Geibel *et al.*: Z. Phys. B **84** (1991) 1.
[2] S. Fujimori *et al.*: J. Phys. Soc. Jpn. **85** (2016) 062001.
[3] *S. Fujimori, Y. Takeda, H. Yamagami, J. Pospíšil, E. Yamamoto and Y. Haga: Phys. Rev. B* ***105*** *(2022) 115128.*
[4] N. K. Sato *et al.*: Nature **410** (2001) 340.

Direct imaging of orbitals using hard X-ray photoelectron spectroscopy (HAXPES)

In the study of novel materials, the electronic structure is one of the most fundamental aspects needed to understand the emergence of interesting and exotic properties. One of the most direct approaches to experimentally access the electronic structure is photoelectron spectroscopy (PES). It is a very wide-spread and established technique, but as with any other spectroscopy, the interpretation of the spectra is not always straightforward and can be a significant challenge by itself.

In this context, Fadley and co-workers proposed already in the 1980's, a specific geometry for PES that would allow to directly image orbitals of free-standing atoms [1]. Such experiment would be capable of providing highly relevant information directly from the data, effectively bypassing the need for calculations. However, for solid state materials, the presence of scattering processes that the outgoing photoelectrons endure interferes so strongly with the desired signal that such PES technique has not been realized until now. Here, we show how we have successfully implemented such experiment using hard X-ray PES (HAXPES) [2].

Our work is performed at the HAXPES end-station of SPring-8 **BL12XU** (Taiwan Beamline). The end-station, which is part of the collaboration between the Max Planck Institute for Chemical Physics of Solids and the National Synchrotron Radiation Research Center (NSRRC), is equipped with two analyzers mounted perpendicular and parallel to the polarization of the incoming beam, making it highly suitable for studying the effects of polarization in HAXPES [3]. The parallel analyzer, in particular, corresponds to the geometry proposed by Fadley, see Fig. 1.

In order to experimentally test and realize the technique, the 5*d* transition metal oxide ReO_3 was chosen as a model compound. Multiple single crystalline samples were prepared in order to be able to reach all relevant crystalline orientations by rotating θ. The orientations were chosen with a certain redundancy in order to ensure that the effects observed corresponded to the orientation dependence and not to e.g. emission or incidence angle.

Figure 2 shows photoemission spectra of ReO_3 near the valence region. In order to compare the measured spectra at different orientations and angles, we normalized all spectra to a fully filled Re core level, Re 4*f*, at around 45 eV. This normalization criterium is key to nullify the undesired electron scattering effects including photoelectron diffraction.

The valence band spectra measured at different orientations after this normalization is shown in Figs. 3(a-c). We observe three features, A, B, and C, all of them presenting strong orientation dependences: In A, we observe almost a factor 3 in intensity changes depending on the orientation. C is, in orientations close to [001], a peak comparable to A or B, but closer to [110] or [111], it is a mere shoulder.

We study those changes by integrating first regions A and B, and plotting the anisotropic part of the integrated intensity. Figure 3(d) shows that the shape obtained from this integration matches nicely to the shape of a t_{2g} orbital as calculated from spherical harmonics, indicating the orbital character of these two valence band features. As for region C, we observe that the trends in B strongly affect its overall intensity. In order to integrate only the peak or shoulder C, we subtract a baseline starting from peak B to the background after C at around 10 eV. By plotting its anisotropic part (Fig. 3(e)), we obtain a very good match to the e_g orbital shape, which unveils the presence of e_g states at this deep region of the valence band.

Finally, our analysis procedure was validated with *ab initio* photoemission calculations using the state-of-the-art one step model [4], which includes specifically the geometry, the angle of incidence and the polarization of the light.

Our results provide a novel way to use HAXPES to identify in a very direct and visual manner the information about the electronic states of the studied

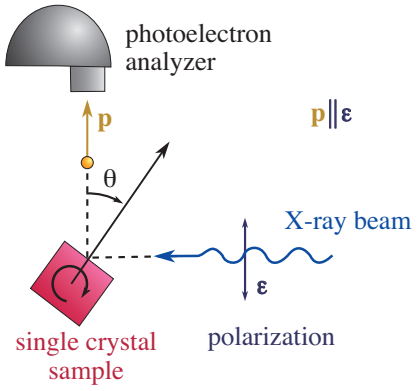

Fig. 1. Schematic representation of the experimental geometry. The photoelectrons detected by the analyzer have their momentum **p** parallel to the electrical field ε of the X-rays. The angle θ determines the orientation of the sample facing the analyzer.

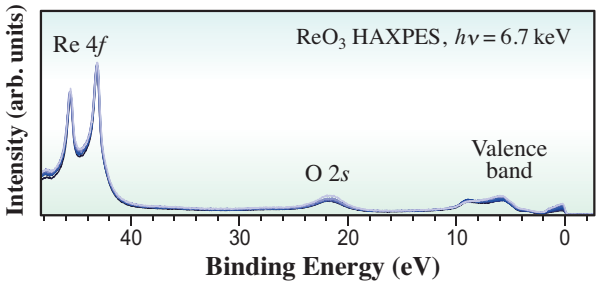

Fig. 2. Photoemission spectra of ReO_3 in a wide energy range encompassing the Re 4*f* core level used for the normalization and the valence band, where the orientation dependence is studied.

materials without needing to rely on theoretical calculations. This is especially promising for strongly correlated materials, where *ab initio* theoretical methods are often unreliable due to the complexity arising from many-body interactions. Our technique is complementary to other variants of PES such as ARPES, as well as to other direct orbital imaging methods such as *s*-NIXS [5]. Our HAXPES technique can be applied to a wide range of single crystalline systems, from thin films to bulk materials, thereby opening up new opportunities also for the field of applied research.

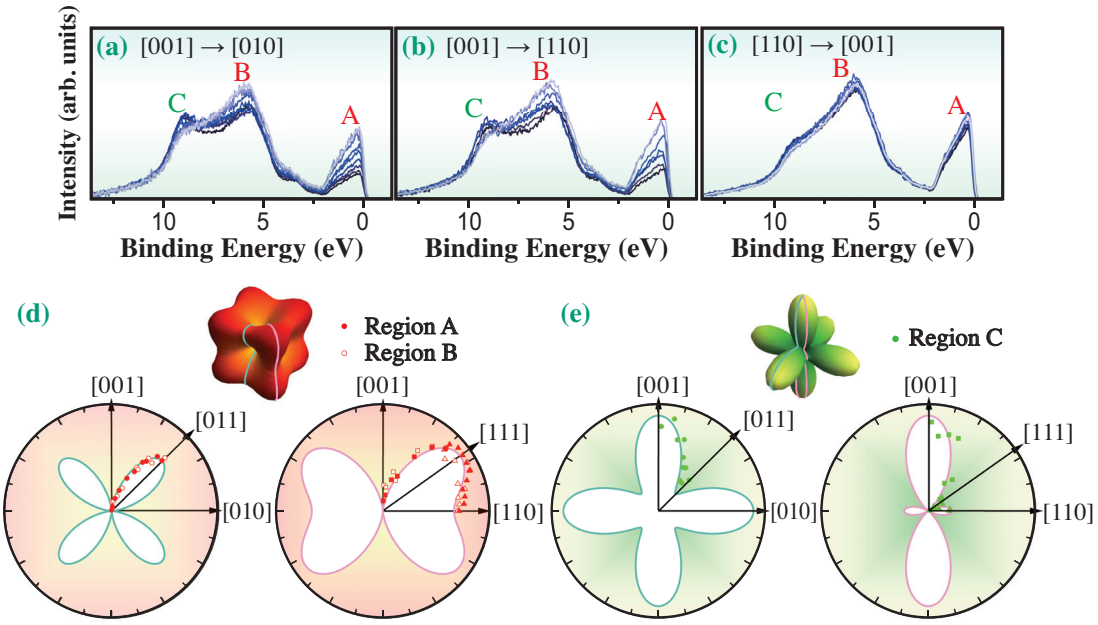

Fig. 3. **(a-c)** Valence band spectra taken at multiple orientations of ReO_3 by measuring multiple samples with different orientations and changing the angle θ. The spectra have been normalized to the integrated intensity of the Re 4*f* core level. **(d)** Polar plot of the anisotropic part of the integrated intensity of regions A (–0.5 to 2 eV) and B (2 eV to 7.5 eV), together with the theoretical t_{2g} line shape. **(e)** Polar plot of the anisotropic part of the integrated intensity of feature C, together with the theoretical e_g line shape.

Daisuke Takegami* and Liu Hao Tjeng

Max Planck Institute for Chemical Physics of Solids, Dresden, Germany

*Email: Daisuke.Takegami@cpfs.mpg.de

References

[1] S. M. Goldberg *et al.*: J. Electron Spectrosc. Relat. Phenom. **21** (1981) 285.
[2] *D. Takegami, L. Nicolaï, Y. Utsumi, A. Meléndez-Sans, D. A. Balatsky, C.-A. Knight, C. Dalton, S.-L. Huang, C.-S. Chen, L. Zhao, A. C. Komarek, Y.-F. Liao, K.-D. Tsuei, J. Minár and L. H. Tjeng: Phys. Rev. Res.* ***4*** *(2022) 033108.*
[3] D. Takegami *et al.*: Phys. Rev. B **99** (2019) 165101.
[4] H. Ebert *et al.*: Rep. Prog. Phys. **74** (2011) 096501.
[5] H. Yavaş *et al.*: Nat. Phys. **15** (2019) 559.

Micromagnetic understanding of evolutions of antiferromagnetic domains in NiO

Magnetic materials generally form magnetic domains to reduce the total energy of the system [1]. While magnetic domains in ferromagnets have been extensively studied for both fundamental and technological importance, those in antiferromagnets have not been investigated as much. In the recently emerging antiferromagnetic spintronics [2], antiferromagnetic domain formations and its dynamics are becoming implicit questions and are key to elucidate the antiferromagnetic behaviors in response to various extraneous fields such as magnetic field, spin orbit torque [3], and electric field. Since antiferromagnets do not have spontaneous magnetization, the magnetocrystalline anisotropy and magnetoelastic energies often dominate over the negligible magnetostatic energy, which bring about the domain formations and evolutions in completely different manner than those of ferromagnets. Therefore, one often experiences a difficulty to simulate antiferromagnets with conventional micromagnetic simulation packages (e.g., OOMMF, mumax^3, etc.) primarily designed for ferromagnets.

In this study, we experimentally investigate formations and evolutions of antiferromagnetic domains in NiO (001) of a bulk single crystal, which is an archetypical collinear antiferromagnet, with a strong external magnetic field. By implementing the crystallographic continuity into the magnetic energy calculations, we then establish a unique micromagnetic simulation algorithm for the antiferromagnetic NiO and understand the domain formations and evolutions.

NiO shows a rock-salt structure above the Néel temperature T_N = 523 K and it sustains a slight rhombohedral distortion in one of the <111> directions below T_N. In the antiferromagnetic phase, there are two different magnetic anisotropies due to the crystalline symmetry. One is a strong magnetic *easy-plane* anisotropy lying on a {111} plane which is strongly coupled with the rhombohedral distortion and promotes the so-called *T*-domain (Fig. 1). The other is a weak three-fold *in-plane* anisotropy in the <11$\bar{2}$> directions in the {111} plane which promotes the so-called *S*-domain. Therefore, one *T*-domain always contains a few of the three *S*-domain. Combination of these magnetic anisotropies results in 12 different orientations of Néel vectors in *T*- and *S*-domain. Here, we label a *T*-domain associated with (111) as T_1 and *S*-domain with [$\bar{2}$11] as **S**$_1$ and so on as indicated in Fig. 1.

Since *T*-domain always associates with the rhombohedral distortion, crystallographic continuity is the most important consideration to construct the micromagnetic structure. Considering the rhombohedral symmetry, the boundaries in the same symmetry are classified by colors for each *T*-domain unit-cell as shown in Fig. 1. With this classification, connection between *T*-domain unit-cells is preferentially made with the same color boundary.

For the micromagnetic simulations, we consider the four different potential energies involved for the stabilization of the ground state which are associated with (1) the *boundary connections* (U_B), (2) the *T-domain connections* (U_T), (3) the *S-domain connections* (U_S), and (4) the *Zeeman energy* (U_Z). The *boundary connections* consider increase of the potential energy if a connection between different color boundaries is made. For the *T-domain connections*, the potential energy increases when neighboring *T*-domains are discrepant. Similarly, for the *S-domain connections*, the potential energy increases when neighboring *S*-domains are discrepant. The *Zeeman energy* characterizes the Néel vector orientation with respect to the external magnetic field.

Figure 2 shows the X-ray magnetic linear dichroism photoemission electron microscopy (XMLD-PEEM) images and the ones constructed by the micromagnetic simulation of a virgin (001) surface of a cleaved NiO before applying external magnetic field. The XMLD-PEEM images were taken by *p*-polarized X-ray beam incident with photon energies at the oxygen *K*-edge and the Ni L_2-edge at SPring-8 **BL17SU**. Figures 2(a) and 2(c) essentially reflect the *T*-domain and *S*-domain patterns, respectively. The pattern with the O *K*-edge is found to be very sharp and shows only one contrast. On the other hand, the pattern with Ni L_2-edge is more complex with more than two contrasts. We first construct the *T*-domain pattern by minimizing $\Sigma_x^n \Sigma_y^n \Sigma_{t=0}^1 U_B$ and reproduce the one experimentally obtained. As one can see in Fig. 2(b), the reproduced *T*-domain pattern

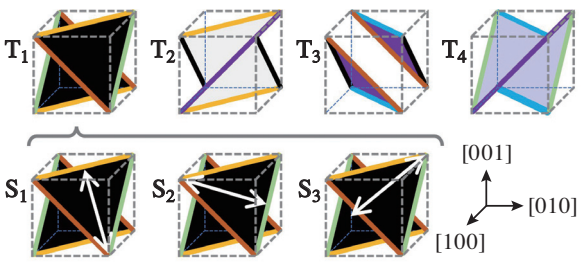

Fig. 1. Easy-plane orientations of *T*-domains and the easy axes of the *S*-domains.

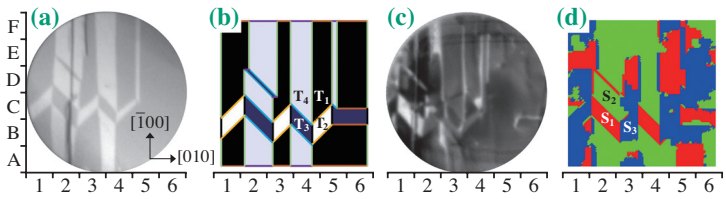

Fig. 2. XMLD-PEEM images taken with the photon energy at the O *K*-edge **(a)** and Ni L_2-edge **(c)** which respectively represent *T*-domain and *S*-domain patterns. The reproduced *T*-domain **(b)** and *S*-domain pattern **(d)** by the micromagnetic simulation.

has no discrepancies on the boundary connections. Most importantly, it almost completely reproduces the detailed domain structures seen in Fig. 2(a). One can see even the small details in the locations: C-5, D-3, and E-2 in Fig. 2(a) are perfectly reproduced. The contrast with Ni L_2-edge is more complex and does not directly accord with the simulated *S*-domain pattern (Figs. 2(c) and 2(d)). For the meanwhile, we start from these initial *T*- and *S*-domain patterns and investigate antiferromagnetic domain evolutions after applying external magnetic fields.

Starting from the initial state shown in Fig. 2, we take XMLD-PEEM images after a magnetic field application and analyze them with the corresponding *T*-domain and *S*-domain patterns reproduced by the simulation. The results are displayed in Fig. 3.

The *T*-domain patterns observed by the O *K*-edge are almost kept the same after the field is applied in either [010] or [100] direction (Figs. 3(a-c)). The simulations reproduce the pattern very well (Figs. 3(f-h)) which are essentially unchanged under the magnetic fields. The experimental observations and the simulation results can be explained by the *Zeeman energy* term U_Z. The system can minimize U_{tot} by switching *S*-domain without changing *T*-domains, leading to the invariant *T*-domain pattern. The same arguments apply to the [100] field.

Remarkable changes in the domain patterns are observed when the magnetic field is applied in [$\bar{1}$10] and [$\bar{1}\bar{1}$0] directions. As seen in Fig. 3(d), the change in the *T*-domain pattern taken after the [$\bar{1}$10] field application is quite dramatic. The longitudinal domains disappear, and the diagonal domains expand along the field direction, which are perfectly reproduced by the simulation (Fig. 3(i)).

In summary, we experimentally investigate and numerically simulate evolutions of antiferromagnetic domains in a cleaved NiO (001) under magnetic fields. First, we clearly observed, by the XMLD-PEEM, the antiferromagnetic domain evolutions with a strong magnetic field and its behavior strongly depending on the magnetic field direction. Second, by considering the appropriate potential energy factors taking into account the crystallographic symmetry as well as relevant magnetic energies, we established a unique micromagnetic simulation algorithm to reproduce details of the experimentally observed antiferromagnetic domain evolutions [4].

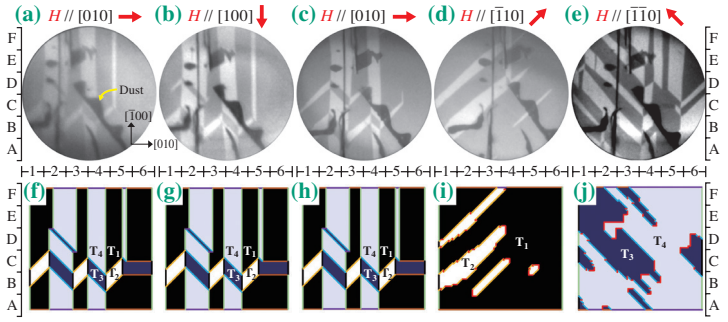

Fig. 3. **(a-e)** XMLD-PEEM images taken with the photon energy at the O *K*-edge after each magnetic field application. **(f-j)** Corresponding *T*-domain patterns reproduced by the simulations. The red boundaries indicate the discrepancy boundary connection, i.e., connection between different color boundaries. The alphabet-number coordinate system is referenced to specify a location.

Takahiro Moriyama

Department of Materials Physics, Nagoya University

Email: moriyama.takahiro.a4@f.mail.nagoya-u.ac.jp

References

[1] S. Chikazumi: Physics of Ferromagnetism (OUP Oxford, New York, 2009).
[2] V. Baltz *et al.*: Rev. Mod. Phys. **90** (2018) 015005.
[3] T. Moriyama *et al.*: Sci. Rep. **8** (2018) 14167.
[4] *T. Moriyama, L. Sánchez-Tejerina, K. Oda, T. Ohkochi, M. Kimata, Y. Shiota, H. Nojiri, G. Finocchio and T. Ono: Phys. Rev. Mater. 7 (2023) 054401.*

Ultrafast subpicosecond magnetization of a two-dimensional ferromagnet

Controlling the magnetization of ferromagnets on a subpicosecond (sub-ps) timescale is highly desirable, although challenging, because it enables the operation of new ultralow-power spin-based electronic devices at THz frequencies [1,2], which are beyond the limitations of the present CMOS circuitry. To date, ultrafast spin dynamics studies have generally employed femto-second (fs)-pulse lasers with strong fluences to excite magnetic materials [2]. When the photon energy coincides with a resonant transition between different bands, the laser pulses excite carriers into *d*- or *f*-orbital spin-polarized bands, causing instant magnetization enhancement. However, unlike optical pumping, electrical gating, the basic operation in CMOS, cannot significantly change the carrier density or cause band-to-band transitions in the ultrafast timescale.

In this study, we demonstrate a new scheme for sub-ps magnetization manipulation, called wavefunction (WF) engineering, which requires no change in the total carrier density, using the quantum well (QW) structure of a ferromagnetic semiconductor (FMS) (In,Fe)As [3]. FMSs are alloy semiconductors doped with a significant amount of magnetic elements (several %; Mn, Fe, etc.) that play the role of local spins. These local spins (*d* electrons) strongly couple to itinerant carriers (*s* or *p* electrons) via *s,p-d* exchange interactions, which mainly contribute to the establishment of ferromagnetism in FMSs. Among the various FMSs, (In,Fe)As stands out as the first carrier-induced n-type FMS, where electron carriers possess coherence lengths as long as 40 nm [3]. The sample examined in our study consists of (In,Fe)As (10 nm, 8% Fe)/InAs (5 nm)/AlSb (300 nm)/AlAs (5 nm)/GaAs grown on a semi-insulating (SI) GaAs (001) substrate via molecular beam epitaxy (Fig. 1(a)). In this structure, the electron carrier WFs are extended throughout and well confined in the top bilayer (Fig. 1(b)). The magnetic properties of this bilayer QW, such as the Curie temperature (T_C), are determined by the spatial overlap between the WFs and local spins (Fe) [3]. Thus, by controlling the WF peak position and shape, the magnetic properties of (In,Fe)As/InAs QWs can be effectively changed without pumping additional carriers into the system.

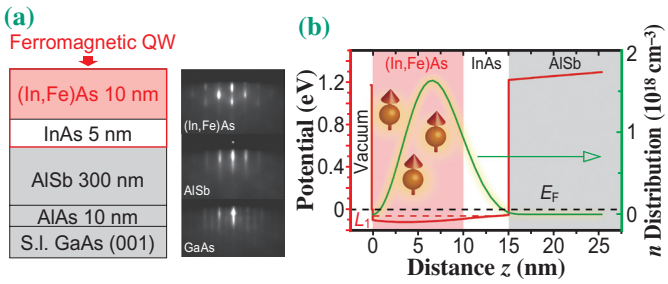

Fig. 1. **(a)** Schematic of the sample structure. **(b)** Conduction band bottom profile (red curve) and electron carrier distribution (green-yellowish curve) in the (In,Fe)As/InAs QW.

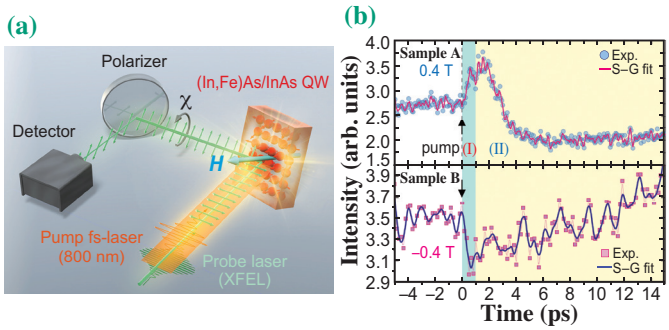

Fig. 2. **(a)** Pump-probe measurement setup. **(b)** Time evolution of XFEL intensity for samples A (top) and B (bottom), which reflects the rapid change in the magnetization **M**. Circle and square: raw data; lines: data smoothened using a Savitzky–Golay (S–G) filter.

To study the spin dynamics in the (In,Fe)As/InAs QW, we conducted pump-probe measurements at SACLA **BL1**. We used a fs-pulse laser (wavelength = 793 nm; pulse width = 30 fs) to excite the *s,p*-electron bath close to the Fermi surface. To probe the magnetization of the (In,Fe)As/InAs QWs, we conducted X-ray magneto-optical Kerr effect measurements, using a linearly polarized X-ray free electron laser (XFEL) beam with an energy of 52 eV, which resonates with the *M* absorption edge of Fe [4]. As illustrated in Fig. 2(a), the Kerr rotation angle, θ_K, of the XFEL beam after being reflected from the (In,Fe)As/InAs sample was experimentally determined using rotating analyzer ellipsometry. For the time-resolved measurements, the analyzer angle was fixed, and the detected XFEL intensity provides a measure of θ_K with time. Upon pumping sample A with the infrared laser pulse, the detected XFEL intensity instantly increased (from 2.8 to 3.4) on a timescale of 600 fs (region I), and then slowly saturated and decreased in the next several ps (region II) (top panel, Fig. 2(b)). These results indicate sub-ps enhancement of the magnetization **M** of the (In,Fe)As/InAs QW in sample A. For comparison, similar experiments were conducted on sample B, where **M** points in the opposite direction (bottom panel, Fig. 2(b)). The opposite signs of the

changes in the XFEL intensities for samples A and B prove that the changes originate from the evolution of the magnetization **M** of the (In,Fe)As/InAs QW. The observation of the ultrafast magnetization of the (In,Fe)As/InAs QW (~600 fs) is the first sub-ps enhancement of **M** of an FMS ever reported [5].

Next, we discuss the mechanism of the sub-ps magnetization. Upon the arrival of the pump laser pulse, photoelectrons and photoholes are instantly generated (~1 fs), which have an exponentially decreasing distribution from the surface toward the substrate side (right panel, Fig. 3(a)). However, these photoelectrons reside in bands 1.1 eV higher than the conduction band bottom and thus cannot instantly interact with the Fe spins and cause the sub-ps magnetization. Owing to the density gradient along the *z*-axis, these photocarriers start diffusing toward the substrate side, which is much faster for the photoelectrons than for the photoholes because of their higher mobility and higher temperature excited by the pump laser. Consequently, there are more photoholes at the surface and more photoelectrons at the substrate side, and an electric field pointing from the surface to the substrate side rapidly builds up over time. This is called the photo-Dember field. In the (In,Fe)As/InAs QW, the photo-Dember field likely pushes the 2D electron WF toward the top (In,Fe)As layer, leading to enhanced magnetization in the QW. Our numerical calculations confirm this scenario. As shown in Fig. 3(b), the deviation between the local densities of the photoelectrons $N_{pe}(z,t)$ and photoholes $N_{ph}(z,t)$ rapidly increased at every time step of 100 fs. Consequently, over time, the (In,Fe)As/InAs QW potential deepened at the center of the (In,Fe)As layer (see Fig. 3(c)), causing a redistribution of the 2D electron carriers, $N_{2D}(z,t)$, in the (In,Fe)As region (Fig. 3(d)) and a consequent enhancement of T_C from 17 to 31 K (Fig. 3(e)) [5].

The ability to control the magnetization of a magnetic material on the sub-ps timescale is a remarkable feature of a ferromagnetic QW, utilizing the high coherency of itinerant carriers. Schemes for controlling the carrier WFs are not limited to optical pumping, and this control can also be performed by applying a gate voltage to the transistor structures. The electrical control of ferromagnetism using WF engineering may potentially lead to ultrafast and scalable electronic devices in the future.

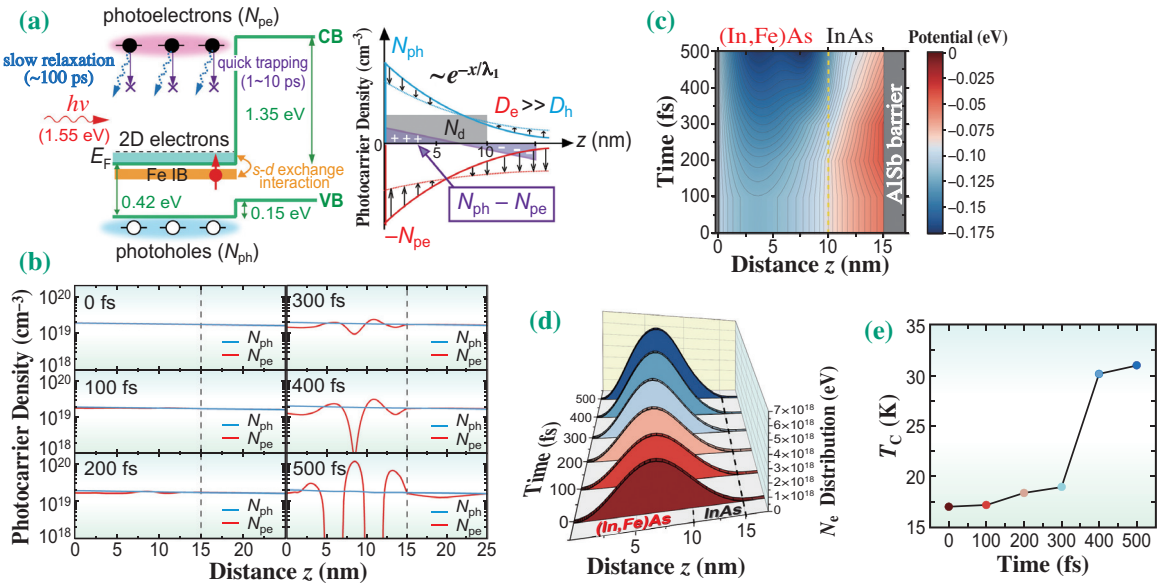

Fig. 3. **(a)** Generation and redistribution of photocarriers (holes, electrons), which build up a photo-Dember electric field. Our calculations confirmed the ultrafast (sub-ps) redistribution of **(b)** the photocarriers, **(c)** potential profile, **(d)** 2D electron density distribution, and **(e)** T_C of the (In,Fe)As/InAs QW.

Le Duc Anh*, Masaki Kobayashi and Masaaki Tanaka

Department of Electrical Engineering and Information Systems,
The University of Tokyo
Center for Spintronics Research Network (CSRN),
The University of Tokyo

*Email: anh@cryst.t.u-tokyo.ac.jp

References

[1] I. Žutić *et al.*: Rev. Mod. Phys. **76** (2004) 323.
[2] A. Kirilyuk *et al.*: Rev. Mod. Phys. **82** (2010) 2731.
[3] L. D. Anh *et al.*: Phys. Rev. B **92** (2015) 161201(R).
[4] Sh. Yamamoto *et al.*: Phys. Rev. B **89** (2014) 064423.
[5] *L. D. Anh, M. Kobayashi, T. Takeda, K. Araki, R. Okano, T. Sumi, M. Horio, K. Yamamoto, Y. Kubota, S. Owada, M. Yabashi, I. Matsuda, and M. Tanaka: Adv. Mater.* ***35*** *(2023) 2301347.*

Dislocations faster than transverse speed of sound

Dislocation motions in crystals cause ductile materials to deform or fail in response to their surroundings. As such, dislocation dynamics are essential to understand the mechanical properties of materials. The maximum speed at which dislocations can travel has long been thought to be limited by the transverse sound speed of the crystal, because their self-energy and stress diverge as the dislocations approach those velocities [1]. However, recent theories and molecular dynamics simulations suggest that dislocations can move faster than these limiting velocities if they are created at such high speeds [1,2]. Experimental observations of dislocations moving faster than the sound speed would deepen the knowledge of how crystals deform under extreme conditions, as high-speed deformation mechanisms differ from conventional plasticity.

In this study, we coupled the XFEL and the high-energy laser available at SACLA **BL3 EH5** [3]. We irradiated the high-energy laser onto our single-crystal diamond samples to drive strong shock-waves. We cut the diamonds along two different orientations to enable our shocks to propagate along the [100] and [110] directions to examine the orientational dependence of the shock response. We estimate the peak shock stresses in diamond to be 184 ± 16 GPa and 92 ± 15 GPa for the [100] and [110] shock directions, respectively. The unfocused XFEL beam generated at SACLA probed the diamond samples during shock compression, visualizing the dynamics of the shock-induced deformations as they occurred. We placed a lithium fluoride (LiF) crystal at ~11 cm downstream from the diamond sample to collect the transmitted X-rays as color centers in the LiF. The distribution of the color centers can be read by using a confocal laser microscope, allowing us to observe the X-ray intensity map [4]. While our X-ray images exhibit some phase-contrast effects because of the small characteristic sizes of the features formed in the diamonds under shock-deformations, we call our measurements as X-ray radiography because of the short distance between the sample and LiF detector, and to distinguish from phase-contrast imaging set-ups used for laser-shock experiments at XFELs.

A representative X-ray radiograph image of diamond shocked along [110] orientation is shown in Fig. 1(b) [5]. Our X-ray radiography visualized the elastic and plastic shock wavefronts traversing the sample from the bottom to the top of the image. Behind the plastic shock wavefront, we observed phase contrast caused by stacking faults traversing the diamond along the {111} slip planes of diamond.

When an edge of a stacking fault is within a crystal (i.e., not at a grain boundary or crystal surface), the edge is a partial dislocation. Thus, the observed stacking faults reaching to the plastic wavefront indicate that partial dislocations are present at the plastic wavefront, though the dislocations themselves are too small to be resolved by our measurements with ~1 μm spatial resolution [4]. The observed

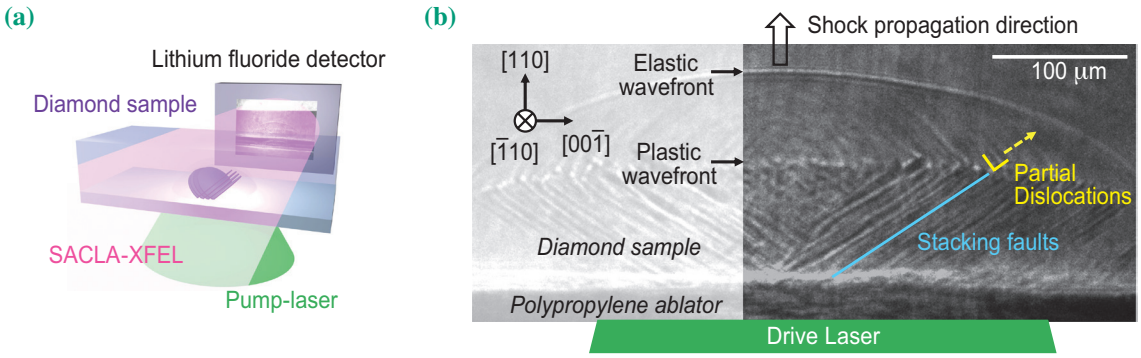

Fig. 1. **(a)** The dynamic X-ray radiography for laser-shock experiments at SACLA BL3 EH5. **(b)** An X-ray radiograph image of single-crystal diamond shocked along [110] orientation taken at 12 ns after the pump-laser irradiation. The two shock wavefronts corresponding to the elastic and plastic wavefronts and the shock induced stacking faults diagonally propagating the diamond behind the plastic wavefront are visualized. The stacking faults (eye guided by the light blue line) appear along the {111} slip planes of diamond.

stacking faults appear as continuous lines with no significant kinks, indicating these partial dislocations are traveling with the plastic wavefront from the diamond surface. By changing the time difference between the laser-pump and XFEL-probe, we took snapshots of the deformation dynamics to determine the velocities of the propagating partial dislocations (i.e., the velocities of the stacking fault extension). The observed dislocation velocities are shown in Fig. 2 along with the three sound wave velocities of diamond. Because of its structural anisotropy, diamond has two transverse sound wave speeds (c_2 and c_3) in addition to a longitudinal sound speed (c_1). These sound speeds define a supersonic regime, two transonic regimes, and a subsonic regime, as indicated in Fig. 2. Our measurements show that the velocities of the partial dislocations for the [100]-shock and [110]-shock both fall in the 1st transonic regime, which is the first experimental evidence of dislocations propagating faster than a transverse sound speed in a real-crystal.

To summarize, we used the XFEL-based dynamic X-ray radiography technique to indirectly observe transonic partial dislocation propagations in diamond under a high-strain rate shock deformation. As most current models for high-strain rate deformations assume transonic or supersonic dislocations to be prohibited, our results provide new insights to refine these models. This will now open a new field of crystal plasticity – experimentally exploring the physics that describes dislocation motion at these ultrafast velocities. The findings from this work will help to refine and validate models that are essential to understand the behavior of ultrafast materials science, of planetary impact and geology, and of high-energy density physics, among others.

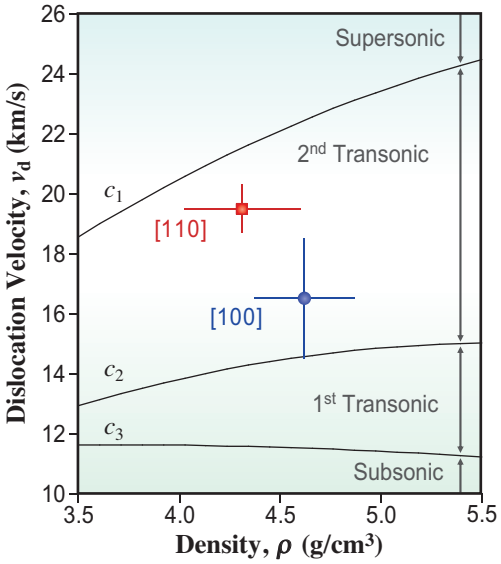

Fig. 2. Measured dislocation velocities as a function of the diamond's material density. The blue circle and red square represent the results for the [100] and [110] shock directions, respectively. The black curves are the longitudinal sound velocity (c_1) and two transverse sound velocities (c_2 and c_3) of diamond propagating along [110] direction.

Kento Katagiri[a,b,c,d,e,*], Leora E. Dresselhaus-Marais[c,d,e] and Norimasa Ozaki[a,b]

[a] Graduate School of Engineering, Osaka University
[b] Institute of Laser Engineering, Osaka University
[c] Department of Materials Science & Engineering, Stanford University, USA
[d] SLAC National Accelerator Laboratory, USA
[e] PULSE Institute, Stanford University, USA

*Email: kentok@stanford.edu

References

[1] D. N. Blaschke *et al.*: Phys. Rev. B **108** (2023) 224102.
[2] P. Gumbsch *et al.*: Science **283** (1999) 965.
[3] Y. Inubushi *et al.*: Appl. Sci. **10** (2020) 2224.
[4] T. Pikuz *et al.*: Matter Rad. Extremes **3** (2018) 197.
[5] *K. Katagiri, T. Pikuz, L. Fang, B. Albertazzi, S. Egashira, Y. Inubushi, G. Kamimura, R. Kodama, M. Koenig, B. Kozioziemski, G. Masaoka, K. Miyanishi, H. Nakamura, M. Ota, G. Rigon, Y. Sakawa, T. Sano, F. Schoofs, Z. J. Smith, K. Sueda, T. Togashi, T. Vinci, Y. Wang, M. Yabashi, T. Yabuuchi, L. E. Dresselhaus-Marais, N. Ozaki: Science* ***382*** *(2023) 69.*

Real-space observation of ligand holes in $SrFeO_3$

An anomalously high valence state of a transition-metal element sometimes shows up in oxide compounds. In such systems, holes tend to occupy mainly the ligand *p* orbitals, giving rise to interesting physical properties such as superconductivity in cuprates and rich magnetic phases in ferrates.

$SrFeO_3$ is an archetypal tetravalent ferrate compound, in which, at least formally, four electrons occupy the Fe 3*d* orbitals. It forms the perovskite-type structure with the cubic space group $Pm\bar{3}m$ (Fig. 1(a)) and exhibits metallic conductivity [1]. The local symmetry at the Fe site is $m\bar{3}m$. Each Fe atom is surrounded by an O_6 regular octahedron without Jahn-Teller distortion, where the 3*d* orbitals are split into the lower-lying triplet (t_{2g}) and the higher-lying doublet (e_g). The high-spin state of $3d^4$ corresponds to the $t_{2g}^3 e_g^1$ electron configuration, which causes some anisotropy in the valence electron density. However, previous X-ray photoelectron spectroscopy and X-ray absorption spectroscopy measurements suggest that the ground state consists of mixed $3d^4$ and $3d^5\underline{L}$ ($\underline{L}$: ligand hole) states [2,3]. In the extreme limit of the $3d^5\underline{L}$ state, the electron density around the Fe site should be spherical because of the $t_{2g}^3 e_g^2$ electron configuration.

Although the ligand holes in the crystal have been observed by spectroscopy measurements [2,3], no one has ever seen where the ligand holes exist in real space. To observe the spatial distribution of the holes, the measurement with high-wavevector (Q) resolution is indispensable. In this study, we observe the valence electron density distribution of $SrFeO_3$ by electron density analysis using state-of-the-art synchrotron X-ray diffraction (XRD).

XRD experiments were performed at SPring-8 **BL02B1**. A He-gas-blowing device was employed to cool the crystal to 30 K. The X-ray wavelength was $\lambda = 0.31020$ Å. A two-dimensional detector CdTe PILATUS, which had a dynamic range of ~10^7, was used to record the diffraction pattern. The intensities of Bragg reflections with the interplane distance $d > 0.28$ Å were collected. A core differential Fourier synthesis (CDFS) method [4] was used to extract the valence electron density distribution around each atomic site. [Kr], [Ar], and [He] type electron configurations were regarded as core electrons for Sr, Fe, and O atoms, respectively.

Figure 1(b) shows the valence electron density distribution of $SrFeO_3$ at 30 K. No valence electron density larger than $3e$/Å^3 is observed around the Sr site, which is consistent with the Sr^{2+} ($5s^0$) state. In contrast, valence electrons are observed around the Fe and O sites, as shown by yellow iso-density surfaces. An orange iso-density surface for higher electron distribution is observed only around the Fe site, which is clearly distinct from a sphere: there are six hollow holes toward the six ligand oxygens.

To quantify the anisotropy of the valence electron density $\rho(\boldsymbol{r})$ around the Fe site, the density at a distance r = 0.2 Å from the Fe nucleus is shown by a color map on a sphere (Fig. 2(a)). The maximum and minimum electron densities are present along the <111> and <100> axes, respectively. Figures 2(b) and 2(c) show surface color maps of $\rho(\theta,\phi)$ for the calculated electron density considering the high-spin $3d^4$ and $3d^5$ states for an isolated Fe ion, respectively. In the case of $3d^4$, we assume that an

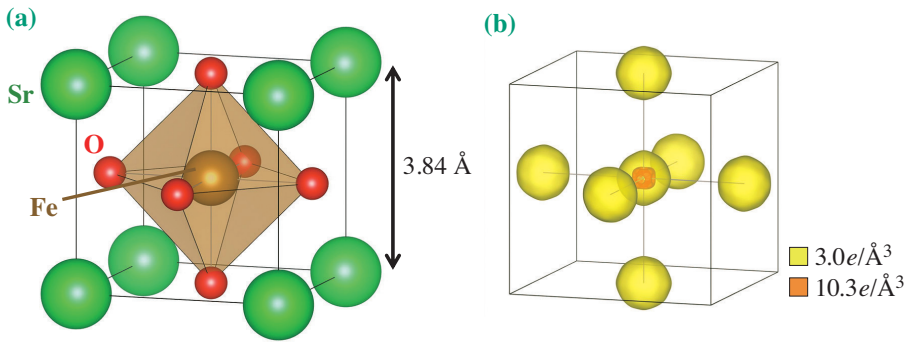

Fig. 1. **(a)** Crystal structure and **(b)** valence electron density distribution of $SrFeO_3$ at 30 K. Yellow and orange iso-density surfaces show electron-density levels of 3.0 and 10.3e/Å^3, respectively.

electron occupies each e_g orbital with a probability of 1/2. A clear anisotropy is observed in the $3d^4$ state, in contrast to the completely isotropic electron density in the $3d^5$ state. By comparing the CDFS results and simulations, the number of Fe 3*d* electrons is estimated to be N_e = 4.64(8), which is consistent with the previous reports of X-ray absorption spectroscopy measurement (N_e = 4.7) [3].

Since the corresponding valence of Fe obtained by the CDFS analysis was 3.36(8), the oxygen valence is estimated to be –1.79(3), which deviates from the ideal closed-shell value of –2. That is, the valence electron density distribution around the O site should not be isotropic. Figure 2(d) shows a color map of the electron density $\rho(\theta,\phi)$ at a distance r = 0.40 Å from the O nucleus, obtained from the CDFS analysis. The observed $\rho(\theta,\phi)$ has some anisotropy, which differs from the isotropic behavior of an ideal O^{2-} ion (Fig. 2(e)). While the highest electron density exists toward the surrounding four Sr atoms, the lowest electron density is observed in the [100] direction toward Fe. These results suggest the existence of ligand holes accommodated in the O $2p_\sigma$ — Fe 3*d* antibonding σ* orbital. The distribution of ligand holes around the O site was captured for the first time by the CDFS analysis [5].

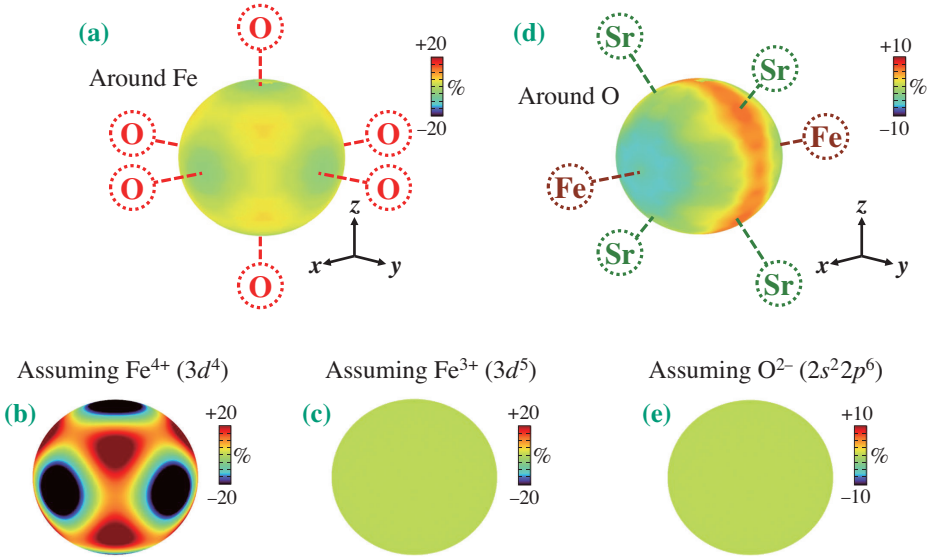

Fig. 2. Color map of the electron density **(a)** at a distance r = 0.2 Å from the Fe nucleus and **(b)** at a distance r = 0.4 Å from the O nucleus. Color maps of the calculated direction dependence of electron density for the **(c)** Fe^{4+} $3d^4$, **(d)** Fe^{3+} $3d^5$ and **(e)** O^{2-} $2s^2sp^6$ states assuming isolated Fe and O atoms. The color bar scale is represented by $\frac{[\rho(\theta,\phi)-N_e/4\pi]}{N_e/4\pi}\times 100(\%)$. N_e is the number of valence electrons.

Shunsuke Kitou* and Taka-hisa Arima

Department of Advanced Materials Science,
The University of Tokyo

*Email: kitou@edu.k.u-tokyo.ac.jp

References

[1] J. B. MacChesney *et al.*: J. Chem. Phys. **43** (1965) 1907.
[2] M. Abbate *et al.*: Phys. Rev. B **65** (2002) 165120.
[3] A. E. Bocquet *et al.*: Phys. Rev. B **45** (1992) 1561.
[4] S. Kitou *et al.*: Phys. Rev. Res. **2** (2020) 033503.
[5] *S. Kitou, M. Gen, Y. Nakamura, K. Sugimoto, Y. Tokunaga, S. Ishiwata and T. Arima: Adv. Sci.* ***10*** *(2023) 2302839.*

Bayesian framework for analyzing adsorption processes observed via time-resolved X-ray diffraction

In recent years, data-driven methods have attracted considerable attention in the field of materials science. One representative method is Bayesian inference, which estimates the posterior probability distribution of parameters $\boldsymbol{\theta}$ from experimental data $\boldsymbol{D}$ as $p(\boldsymbol{\theta}|\boldsymbol{D})$. Conventional nonlinear least-squares fitting corresponds to point estimation; however, Bayesian inference estimates the probability distribution of possible parameter values, thereby enabling the evaluation of the estimation accuracy based on the shape and width of the distribution. We can also naturally incorporate knowledge already known from previous research into Bayesian inference as a prior probability distribution. Furthermore, Bayesian inference enables the selection of the most plausible model among possible models, such as fitting functions, by evaluating the posterior probability $p(M|\boldsymbol{D})$ for each model M. By replacing conventional nonlinear least-squares fitting with Bayesian inference, the amount of information extracted from experimental data increases considerably, leading to a better understanding of materials.

Nagata and Tokuda developed the Bayesian framework for analyzing multipeak spectra [1,2]. In materials science, this method has been utilized to analyze synchrotron radiation X-ray spectra [3]. Previous studies focused on one-dimensional spectra, whereas we established a Bayesian framework for multiple spectra, such as time-series spectra. We demonstrate the effectiveness of our framework by investigating the gas-adsorption process observed via time-resolved X-ray diffraction (Tr-XRD) [4].

We selected a typical metal-organic framework as a sample, a nanoporous Cu coordination polymer $[\{Cu_2(pzdc)_2(pyz)\}_n$ (pzdc = pyrazine-2,3-dicarboxylate; pyz = pyrazine)] (CPL-1). The Ar gas adsorption process was observed using Tr-XRD at SPring-8 **BL02B2**. XRD patterns were measured continuously from $t = 0$ with an exposure time of 0.333 s. During the measurements, Ar gas molecules were injected into the sample cell at $t = 6.327$ s (t_s). We focused on the 031 reflection and analyzed the XRD patterns from 7.70° to 8.22°.

Conventional analysis based on nonlinear least-squares fitting has several limitations. Because of the poor signal-to-noise ratio of the Tr-XRD data, conventional analysis substitutes t_s for the adsorption start time (t_0). A time lag inevitably exists between the gas injection and start of adsorption, leading to a misunderstanding of the adsorption dynamics. In addition, evaluating time-evolution models describing the time variation of the diffraction peaks throughout the adsorption process is difficult; thus, a model must be determined prior to analysis, even when several model candidates exist. We aim to overcome these problems using Bayesian inference.

Figures 1(a-c) show the color maps of the observed Tr-XRD patterns and estimated results using

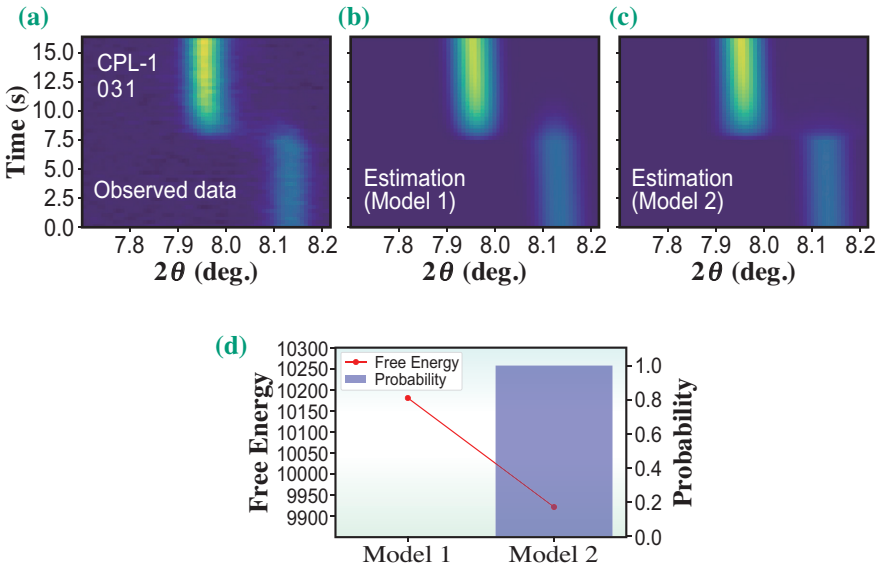

Fig. 1. **(a-c)** Color maps of the observed time-resolved X-ray diffraction patterns and estimated results with Model 1 and Model 2. **(d)** Comparison between Bayes free energies of Model 1 and Model 2. The realization probability of each model is also shown. [5]

Table 1. Time-evolution models

	Model 1	Model 2
Peak area	KJMA equation	KJMA equation
Peak position	Linear	Linear
Peak width	Constant	Exponential

Model 1 and Model 2, i.e., the different time-evolution models in Table 1. Both models appeared to have good qualitative agreement with the observed data. To quantify the realization probability of each model, we calculated $p(M|\boldsymbol{D})$ using the Bayes free energy, as shown in Fig. 1(d). Because the Bayes free energy of Model 2 was approximately 300 lower than that of Model 1, $p(M = 2|\boldsymbol{D})$ was almost equal to 1. Therefore, the Bayesian model selection suggested that Model 2 is considerably better than Model 1.

Based on the selected model (Model 2), we obtained the posterior probability distributions of t_0 and the rate constant (κ), as shown in Fig. 2. Using one standard deviation (1σ) of each distribution as a measure of accuracy, the adsorption start time was estimated to be t_0 = 7.4461 ± 0.0287 s. The accuracy was one order of magnitude greater than that of the conventional analysis (~0.333 s). The probability distribution also indicated that the probability of t_0 and t_s matching was almost zero, implying that the value of t_0 deviated significantly from t_s in this experiment. Because conventional analysis substitutes t_s for t_0, such a large time lag leads to a misunderstanding of the adsorption dynamics. The rate constant was estimated to be κ = 0.6192 ± 0.0235 1/s, whereas it was estimated to be κ = 0.1535 1/s in the conventional analysis. We consider this difference to be owing to the time lag between t_s and t_0.

In this study, we established a Bayesian framework for analyzing the adsorption processes and demonstrated the effectiveness of our framework by investigating the Ar gas adsorption process of CPL-1. Bayesian analysis enables the selection of the most plausible model on the basis of the experimental data. The posterior probability distribution represents a more accurate estimation than the conventional analysis. Our framework can be applied to other dynamic processes, such as chemical reactions, by modifying the time-evolution models. Hence, Bayesian analysis is expected to be utilized in various areas of materials science research.

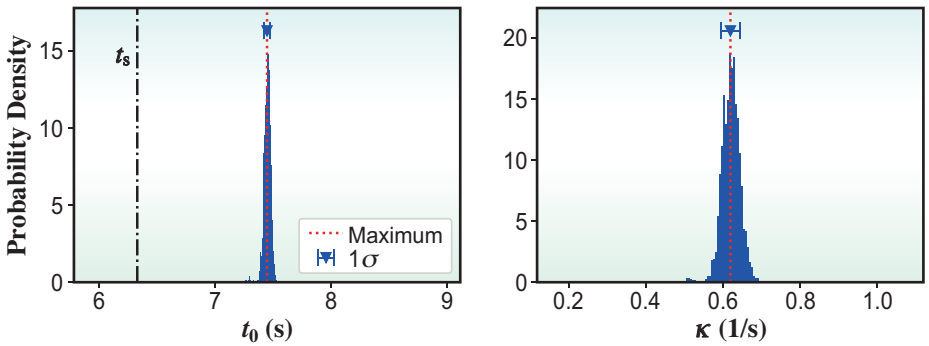

Fig. 2. Posterior probability distributions of the adsorption start time (t_0) and rate constant (κ). The dotted line and error bar correspond to the maximum and one standard deviation (1σ) of the distribution, respectively, and the dash-dotted line denotes the gas-shot time (t_s). [5]

Yuichi Yokoyama[a,*], Shogo Kawaguchi[a] and Masaichiro Mizumaki[a,b]

[a] Japan Synchrotron Radiation Research Institute (JASRI)
[b] Faculty of Science, Kumamoto University

*Email: y.yokoyama@spring8.or.jp

References

[1] K. Nagata *et al.*: Neural Networks **28** (2012) 82.
[2] S. Tokuda *et al.*: J. Phys. Soc. Jpn. **86** (2017) 024001.
[3] Y. Yokoyama *et al.*: J. Phys. Soc. Jpn. **90** (2021) 034703.
[4] *Y. Yokoyama, S. Kawaguchi, and M. Mizumaki.: Sci. Rep.* ***13*** *(2023) 14349.*
[5] Y. Yokoyama: Nihon Kessho Gakkaishi **65** (2023) 218.

Visualization of fast oxygen deintercalation reaction using time-resolved X-ray diffraction

Elucidating the mechanisms behind chemical reactions is a key challenge in materials chemistry as it facilitates the creation of compounds with desired structures or optimization of reactions for functional uses. However, reactions in solid-state crystalline compounds are poorly understood as compared to molecular reactions. This is partly because solid-state reactions generally require high temperatures, making the *in situ* monitoring of these reactions relatively difficult. Inhomogeneous reactions derived from the differences in surface and bulk states, as well as the existence of numerous atoms in crystals, also hinder precise analyses of reactions in solid states. Development of *in situ* measurement techniques is necessary to achieve the rational design of solid-state compounds and their reactions.

In situ X-ray diffraction (XRD) is a powerful tool for monitoring reactions in bulk materials, and the recent development of synchrotron X-rays has facilitated access to high-resolution data within a short time window. Time-resolved synchrotron XRD measurements have been used to investigate many reactions in crystalline phases, such as hydrothermal reactions, gas absorption, and solid-gas catalytic reactions. However, the development of a time-resolved XRD measurement of a solid–gas reaction that can precisely reveal the structural evolution on a sub-second scale remains a challenge. When the time scale of the measurement increases, intermediate phases can be captured with a shorter lifetime. This affords further prospects to optimize the reactions and/or synthesize metastable structures.

This study focused on the Ruddlesden–Popper layered perovskite $Sr_3Fe_2O_{7-\delta}$, which has recently attracted attention as a high-performance oxygen storage material. A reversible topochemical redox reaction has been observed between $Sr_3Fe_2O_{7-\delta}$ ($\delta \approx 0.4$) and $Sr_3Fe_2O_6$ (δ = 1.0) under O_2 and H_2 at 773 K. The perovskite also exhibits excellent performance as an environmental catalyst material. Previously, we revealed that Pd loading dramatically promotes the oxygen release rate and decreases the release temperature under H_2 flow on $Sr_3Fe_2O_{7-\delta}$ ($\delta \sim 0.4$); however, the reaction pathways and structural evolution during the reduction remain unelucidated.

Therefore, we aimed to observe the actual reduction steps of $Sr_3Fe_2O_{7-\delta}$ by H_2 gas and the deintercalation of oxygen at SPring-8 **BL02B2** (Fig. 1). During the measurements, a capillary into which a powder sample was introduced was connected to a gas atmosphere control device. This apparatus was originally developed for the *in situ* observation of the structure of gas absorption and release of coordination polymer complexes [3]. We visualized the solid–gas reaction pathways by synchronizing the gas introduction and XRD measurements [4].

To improve the reproducibility of the reaction, the sample was subjected to multiple redox cycles at 700°C as a pretreatment. The sample in the oxidation state was then set at 500°C in vacuum, and H_2 gas was introduced 3 s after the start of the time-resolved XRD measurement. The XRD patterns near the main peaks obtained at intervals of 100 ms are shown in Figs. 2(a) and 2(b). The horizontal and vertical axes correspond to time and diffraction angle (2θ), respectively. Measurements were performed for pristine $Sr_3Fe_2O_{6.6}$ and Pd-loaded $Sr_3Fe_2O_{6.6}$. In the case of both samples, the peaks shifted to the low-angle side immediately after the introduction of H_2, indicating that the reaction proceeded because of the introduction of the gas. The reaction took approximately 30 s to complete for the unsupported sample; however, for the Pd-supported sample, the reaction was remarkably accelerated and completed within a few seconds.

More importantly, the peak shifted continuously for the unloaded sample, whereas a discontinuous jump in the peak was observed for the Pd-loaded sample. This implies that a first-order phase transition of the structure occurred in the Pd-loaded sample,

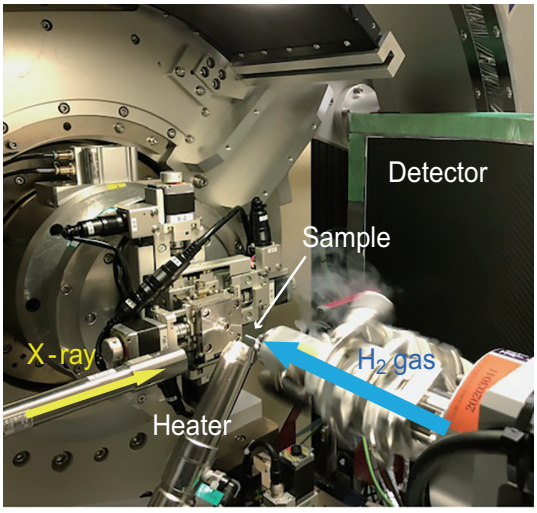

Fig. 1. Experimental setup around the sample at SPring-8 BL02B2.

whereas the structure relaxed continuously (second-order phase transition-like) in the pristine sample. This indicates that the reduction rate at the surface is slower than the diffusion of oxide ions in the bulk, and the structure is continuously relaxed at each stage of reduction in the unsupported material. Meanwhile, in the Pd-loaded sample, the reduction rate at the surface is dramatically accelerated, and the structural relaxation cannot keep pace with the reduction. Therefore, in the Pd-loaded sample, the compound was reduced to $Sr_3Fe_2O_6$ before the structural relaxation was completed, and a first-order phase transition to the stable phase was considered to have occurred. As expected, a dynamic intermediate phase, $Sr_3Fe_2O_6$ with random oxygen defects (Fig. 2(e)) appeared before the phase transition.

In this study, owing to advances in measurement techniques, we successfully captured rapid phenomena that were previously impossible to observe. Elucidation of the reaction pathway in $Sr_3Fe_2O_{7-\delta}$ is important for establishing design guidelines for future oxygen storage catalysts. Furthermore, the fact that the reaction pathway can be manipulated by surface modification is important for future exploration of materials. In other words, the reaction pathway may be selected by the surface modification of inorganic solids, just as the reaction pathway can be selected using functional groups in organic reactions. In the present reaction, we ultimately obtained the same phase despite changing the reaction pathway because of the high reaction temperatures involved. However, we anticipate that the selective synthesis of metastable phases that are inaccessible by ordinary reactions will be realizable in the future via the appropriate selection of reaction systems and temperatures.

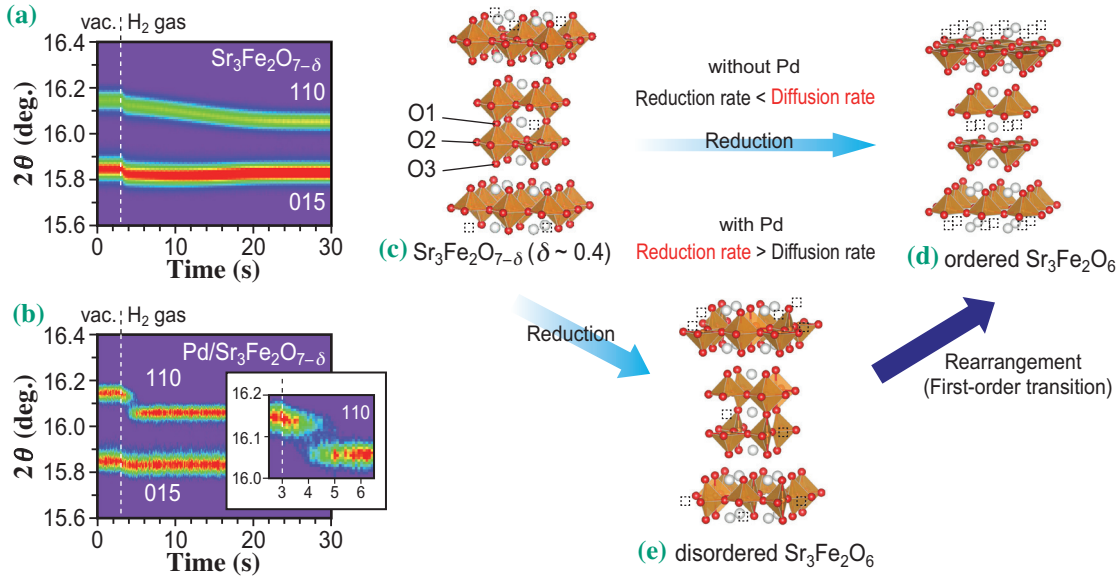

Fig. 2. Time-resolved XRD patterns for the reduction of **(a)** $Sr_3Fe_2O_{7-\delta}$ and **(b)** $Pd/Sr_3Fe_2O_{7-\delta}$ [4]. Structures of **(c)** $Sr_3Fe_2O_{6.6}$, **(d)** ordered $Sr_3Fe_2O_6$, **(e)** disordered $Sr_3Fe_2O_6$.

Takafumi Yamamoto

Laboratory for Materials and Structures,
Tokyo Institute of Technology

Email: yama@msl.titech.ac.jp

References

[1] Y. Tsujimoto *et al.*: Nature **450** (2007) 1062.
[2] M. A. Hayward and M. J. Rosseinsky: Nature **450** (2007) 960.
[3] S. Kawaguchi *et al.*: J. Synchrotron Rad. **27** (2020) 616.
[4] *T. Yamamoto, S. Kawaguchi, T. Kosuge, A. Sugai, N. Tsunoda, Y. Kumagai, K. Beppu, T. Ohmi, T. Nagase, K. Higashi, K. Kato, K. Nitta, T. Uruga, S. Yamazoe, F. Oba, T. Tanaka, M. Azuma and S. Hosokawa: Adv. Sci.* ***10*** *(2023) 2301876.*

Transcription of atomic scale screw dislocation of silicon carbide crystal to X-ray vortex wave field

Various spiral structures are ubiquitously observed in nature, such as in DNAs, which comprise two chains that form a double helix. In industrial functional materials, such as silicon carbide (SiC) crystals used in high-power electronic devices, the density of threading screw dislocations (TSDs) must be reduced to achieve the desired performance [1]. Therefore, an efficient method is required to precisely measure the density of TSDs on SiC crystals.

We devised a method to transcribe the atomic-scale structure of screw dislocations in an X-ray vortex wave field in the reciprocal space. X-ray vortices are ideal phase markers with phase anomalies of 2π or multiples of 2π phase ambiguity with a complete zero intensity at the center [2,3], and can be used for novel dichroism, quantum communications, or even super-resolution imaging (refer to [2]). The formation of the X-ray vortex wave field was confirmed by an X-ray simulation in the kinematical diffraction regime, where the severe multiple diffraction effect was minimized, and was verified using a SiC crystal as reported in [4]. These results provide a novel direction for the development of crystal X-ray optical components.

Conventionally, the evaluation of crystalline dislocations in a large field of view has been performed using X-ray topography, which is unsuitable for a quantitative discussion of the lattice plane around the dislocations. To overcome this problem, we propose a method of X-ray two-beam topography, by which we can determine the phase at the detector plane that is directly related to the deformation of the lattice planes around dislocations. The measurement was performed in the kinematical diffraction regime with a relatively large offset angle from the Bragg peak to overcome the X-ray multiple diffraction effect inside the crystal. This simplified the computer simulations for calculating the phase shift by the Bragg reflection around the TSDs. Our method will be useful because of the relaxed sample size constraint, with a field of view of up to the millimeter scale, of bulk crystalline specimens and will play a complementary role to other high spatial resolution measurements, such as transmission electron microscopy and Bragg coherent diffractive imaging.

For the two-beam topography experiment, we utilized a large and thick bulk 4H–SiC wafer with dimensions of $10\times10\times0.2$ mm^3 containing TSDs. Low-energy electron-channeling contrast images were captured on one of the TSDs under the focused condition, where a spiral pattern was clearly observed (Fig. 1(a)). The X-ray topograph shows that the core of the TSD appears dark under Bragg conditions. We performed a simulation in the kinematical diffraction regime of the Bragg-reflected X-ray wave field downstream of a SiC crystal containing a TSD, as shown in Fig. 1(b). The simulated result showed destructive interference of the Bragg-reflected beam and the generation of an X-ray vortex wave field in reciprocal space (Fig. 1(b)).

To measure the phase distribution in the reflected wave downstream of a SiC crystal, we constructed an X-ray wavefront-dividing interferometer using 7.71 keV X-rays at an undulator beamline, SPring-8 **BL29XUL**, where an X-ray beam is one-dimensionally focused in the vertical direction. X-rays passed through a 10-μm-width slit at the focal plane, which worked as a stable source. We used a parabolic mirror in the transport channel of BL29XUL. The wavefront-dividing two-beam X-ray interferometer was realized with a diamond prism at L_2 = 44.3 m from the slit, which refracted a part of the wave field in the vertical direction.

One of the wave fields irradiates an offset position from the center of the TSD and works as a reference wave. This wave field was approximated as a plane wave, whereas the other wave field irradiated the center of the TSD and received a specific phase shift (Fig. 2). The grazing incidence angle on the prism was set to be approximately 17° to realize the refraction angle of $\Delta\theta_r$ = 38 μrad and the interference fringe spacing of $d_f = \lambda/\Delta\theta_r$ = 4.2 μm, resolvable by our X-ray image sensor. The distance between the prism and crystal was L_3 = 3.6 m to realize the width of the interference region, $L_3\Delta\theta_r$ = 140 μm, large enough to

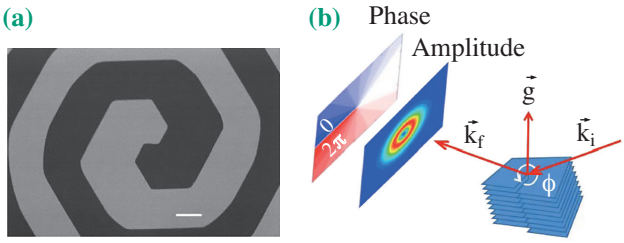

Fig. 1. **(a)** Low-energy electron channeling contrast image of one of the TSDs, where a spiral pattern is clearly observed. The scale bar is 1 μm. **(b)** Summary of the kinematical diffraction simulation. k_i & k_f are incident & exit waves and ϕ is the azimuthal angle around TSD on SiC (0004) plane. The calculated amplitude and phase of the X-ray Bragg reflected wave field from the crystal are shown on the left, exhibiting a donut intensity profile and a spiral phase distribution with a phase jump of 2π.

cover the lattice planes around the TSD.

On the other hand, the Bragg reflection of the SiC crystal occurred in the horizontal direction (Fig. 2). Interferograms are recorded by setting the crystal at an off-Bragg condition of $\Delta\theta$ = 10″, with the measured reflectivity of 5.5% compared to the Bragg peak. Under these conditions, multiple diffraction effects were negligible.

Interferograms obtained using this setup are shown in Fig. 3(a). The bright lines of interferogram bridging the dark line showed two Y-shaped fork patterns with reversed orientations, separated by the amount of shear of $L_4\Delta\theta_r$ (see Fig. 2). This indicates that an X-ray vortex with a topological charge of one was formed in the Bragg reflected wave field. This agrees well with the simulation results for the kinematical diffraction regime shown in Fig. 3(b). In addition, it shows that our two-beam topography enabled us to quantitatively derive the phase shift by Bragg reflection from the areas around the TSD, as predicted by our simulation. Special attention should be paid to the darkened and brightened areas on the fringes, indicated by the upper and lower green dotted lines in Fig. 3(a), extending upward and downwards from the image center, respectively, which likely contain the contributions of basal plane dislocations. The dark centers of the vortices are contained around the image center.

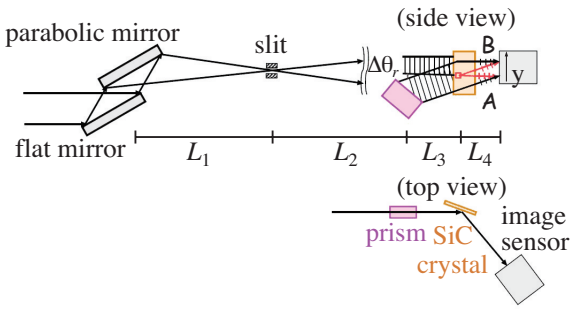

Fig. 2. Schematic diagram of a wave-front dividing two-beam interferometer with a diamond prism splitter. The interference fringes are formed at the overlap of X-rays due to the refraction angle $\Delta\theta_r$ by the prism. The images of TSDs in the interferogram are formed at positions A and B.

Most of the TSDs were accompanied by basal-plane dislocations within the sample.

In conclusion, we proved that the two-beam topography method enables the detection of threading screw dislocations in a large field of view, and we predict that it will play an important role in clarifying the distribution and network of these dislocations and finding methods to significantly reduce them in the near future.

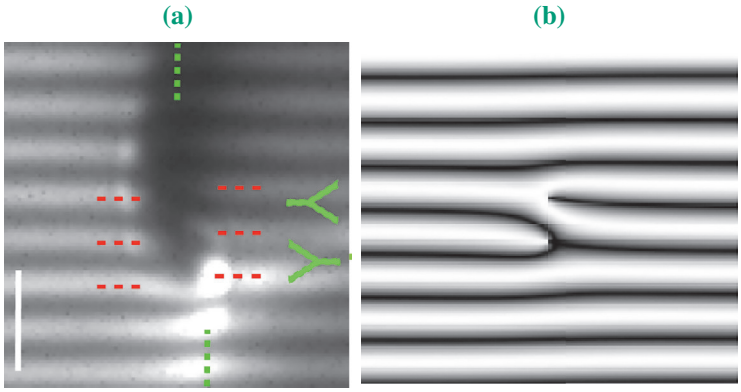

Fig. 3. **(a)** Interferograms obtained at off-Bragg condition with offset angle of $\Delta\theta$ = 10″. Two Y-shaped fork patterns bridging the dark line, near the image center, were observed with reversed orientations and with the separation of the amount of shear. This dark area contains the contributions of the dark center of vortices. Upper and lower green dotted lines are likely related to basal plane dislocations. The exposure time is 20 s and the scale bar is 10 μm. **(b)** Simulated interferogram in the kinematical diffraction regime.

Yoshiki Kohmura[a,*] and Kenji Ohwada[b]

[a] RIKEN SPring-8 Center
[b] Synchrotron Radiation Research Center, National Institutes for Quantum Science and Technology (QST)

*Email: yoshiki.kohmura@riken.jp

References

[1] H. Yamaguchi and H. Matsuhata: J. Electron. Mater. **39** (2010) 715.
[2] Y. Kohmura *et al.*: Opt. Express **28** (2020) 24115.
[3] Y. Kohmura: SPring-8/SACLA Research Frontiers 2020, p. 50.
[4] *Y. Kohmura, K. Ohwada, N. Kakiuchi, K. Sawada, T. Kaneko, J. Mizuki, M. Mizumaki, T. Watanuki and T. Ishikawa: Phys. Rev. Res.* ***5*** *(2023) L012043.*

Revealing microscopic origin of ultralow lattice thermal conductivity in thermoelectric InTe using inelastic X-ray scattering technique

In the pursuit of advancing technology in fields such as thermal management in electronics, thermal barrier coatings, and thermoelectric (TE) energy conversion, materials with intrinsically low thermal conductivity play a pivotal role. Among these, TE materials require low lattice thermal conductivity (κ_L) to achieve high TE performance, as characterized by the figure of merit (zT). In this context, understanding the microscopic origin of intrinsically low κ_L is crucial for designing efficient materials. Rattlers and lone pair electrons are the two "textbook" concepts developed for understanding intrinsically low thermal conductivity. Each concept has been extensively studied and plays a fundamental role not only in the thermoelectric field but also broadly in condensed matter physics and solid state chemistry. While rattling atoms introduce localized vibration modes [1], lone pair electrons usually induce anharmonicity and lattice distortion. Recent attention has turned to materials combining both rattlers and lone pair electrons with TlSe-type compounds emerging as promising TE materials with intrinsically low κ_L. Among these compounds, the simple crystal structure of InTe exhibits a κ_L approaching the so-called glass limit (~0.3 $Wm^{-1}K^{-1}$) at high temperatures [2] despite its relatively light mass compared with Tl-related analogs, and the detailed origin of the ultralow κ_L remains unknown. In this study, we combined inelastic X-ray/neutron scattering, anharmonic phonon calculations, and quantitative chemical bonding analysis to investigate soft transverse phonons in InTe [3]. Dominated by significant In^{1+} z rattling motions, these phonons exhibit remarkable stiffening upon heating, stemming from a giant anharmonicity rooted in the strong lone pair expression tendency. This tendency, along with unstable antibonding states induced by covalency between delocalized In^{1+} $5s^2$ lone pair electrons and Te $5p$ states, contributes to the material's intrinsically low lattice thermal conductivity. Additionally, we elucidate the weak temperature-dependent lattice thermal conductivity at higher temperatures by correlating it with the observed intense stiffening of anharmonic In^{1+} z phonons and a concurrent decrease in phonon scattering strength.

InTe single crystals were grown by the vertical Bridgman method, where the phase purity was confirmed by Rietveld refinements of synchrotron powder X-ray diffraction data at 90 and 300 K collected at SPring-8 **BL44B2**. The inelastic X-ray scattering (IXS) experiments on a InTe single crystal were performed at the RIKEN Quantum NanoDynamics, SPring-8 **BL43LXU** [4,5], a cutting-edge momentum-resolved inelastic X-ray scattering spectrometer, offering unique access to very small single-crystal samples, with, in the present case, a probed sample volume of <0.1 mm)^3. This was particularly valuable for this study due to the small single-domain size induced by the brittle nature of InTe crystals. Si (11 11 11) backscattering was employed at an incident energy of 21.747 keV, with an instrument energy resolution of approximately 1.3 meV. To facilitate parallel data collection, a two-dimensional analyzer array was employed, allowing simultaneous measurements at 28 distinct momentum transfers. The IXS measurements were performed at 50, 100, 200, 300, 500, and 700 K.

To probe the anharmonic phonon modes in InTe, we first conducted theoretical atomic dynamics simulations by combining *ab initio* molecular dynamics

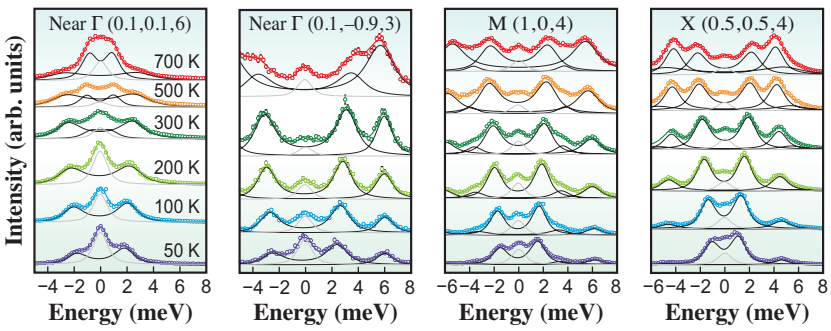

Fig. 1. The temperature dependence of the IXS spectra at Q points of near Γ (0.1,0.1,6), near Γ (0.1,–0.9,3), M (1,0,4), and X (0.5,0.5,4) for probing low-energy (In^{1+} z)-related transverse modes of near ΓO1, near ΓO2, MA1, and XA1, respectively. Open circles and lines with colors represent the IXS spectra and the fits with damped harmonic oscillators, respectively. The black (gray) lines represent the fits to the inelastic (elastic) intensity.

with the temperature-dependent effective potential technique (TDEP). The very large mode Grüneisen parameters as well as the highly-anharmonic frozen phonon potential energy curves reveal giant phonon anharmonicity of low-lying optical and transverse acoustic modes ΓO1, ΓO2, MA1, XA1, and ZO1 dominated by In^{1+} *z* vibrations. To experimentally elucidate these low-lying anharmonic modes, we conducted IXS measurements using carefully selected **Q** points of (0.1,0.1,6), (0.1,–0.9,3), (1,0,4), and (0.5,0.5,4). **Q** points of (0.1,0.1,6) and (0.1,–0.9,3) were used to probe the near ΓO1 and ΓO2 optical modes close to the Brillouin zone center, whereas (1,0,4) and (0.5,0.5,4) were adopted to measure the XA1 and MA1 transverse modes at the zone boundary. The IXS spectra exhibit distinct peaks described by damped harmonic oscillators (Fig. 1). The low-energy phonon dispersion at 300 K aligns well with TDEP simulations (Fig. 2(a)), considering an ideal defect-free structure.

We then explored the temperature dependence of the low-energy phonon modes. Notably, we found that phonon modes such as near ΓO1, near ΓO2, XA1, and MA1 exhibit an anomalously strong stiffening trend with increasing temperature, contrary to the typical softening observed in high-energy phonons with lattice expansion at elevated temperatures (Figs. 2(b,c)). This stiffening, consistent with the inelastic neutron scattering data, is accurately captured by TDEP simulations. The stiffening of rattling modes, commonly observed in rattling systems, is attributed to the rattler's larger thermal motion exploring steeper walls of anharmonic potential surfaces at higher temperatures. In this study, this stiffening behavior has an electronic origin, stemming from the stabilizing effect of lone-pair-induced occupied antibonding states with larger In^{1+} *z* thermal motions. Additionally, the low-energy (In^{1+} *z*)-related modes exhibit clear broadening as temperature rises, in line with significant anharmonic In^{1+} *z* thermal motions.

The momentum-resolved inelastic X-ray scattering data collected at BL43LXU in this research is remarkable as it reveals for the first time the low-energy anharmonic In^{1+} *z* rattling phonon modes as the microscopic origin of the ultralow lattice thermal conductivity in InTe. This comprehensive study not only uncovers the correlation between lone pair electrons on rattlers and lattice anharmonicity but also provides insights into the unique phonon dynamics contributing to ultralow κ_L in InTe. The covalency-driven instability of antibonding states results in highly anharmonic phonon modes, contributing to the exceptional thermal properties of InTe. The combination of experimental techniques and theoretical insights showcased in this study exemplifies a holistic approach to unraveling the complexities of materials at the atomic level, paving the way for designing efficient materials for TE application.

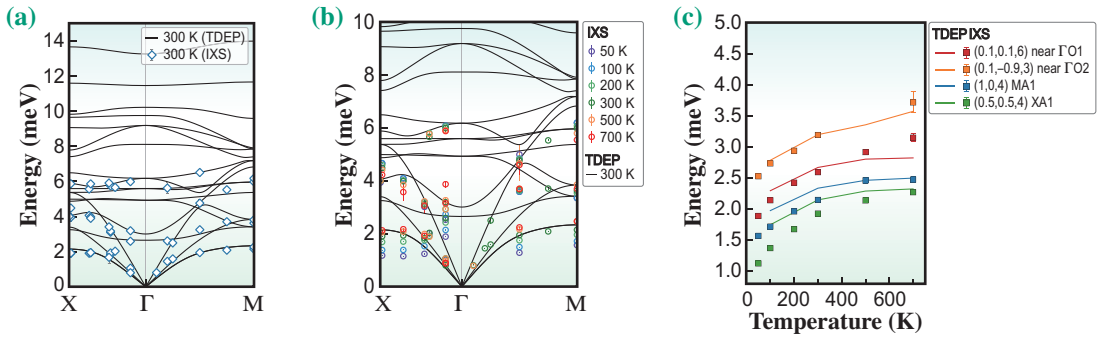

Fig. 2. (**a**) Measured low-energy phonon dispersions by IXS in comparison with the TDEP simulation of InTe at 300 K. (**b**) Measured low-energy phonon dispersions by IXS of InTe at 50, 100, 200, 300, 500, and 700 K. (**c**) Temperature dependence of phonon energies of the low-energy modes at (0.1,0.1,6), (0.1,–0.9,3), (1,0,4), and (0.5,0.5,4).

Jiawei Zhang[a,b,*] and Bo B. Iversen[a]

[a] Center for Integrated Materials Research, Department of Chemistry and iNANO, Aarhus University, Denmark
[b] State Key Laboratory of High Performance Ceramics and Superfine Microstructure, CAS, China

*Email: jiaweizhang@mail.sic.ac.cn

References

[1] M. Christensen *et al.*: Nat. Mater. **7** (2008) 811.
[2] J. Zhang *et al.*: Nat. Commun. **12** (2021) 6709.
[3] *J. Zhang, D. Ishikawa, M. M. Koza, E. Nishibori, L. Song, A. Q. R. Baron, B. B. Iversen: Angew. Chem. Int. Ed.* ***62*** *(2023) e202218458.*
[4] A. Q. R. Baron: SPring-8 Information **15** (2010) 14.
[5] A. Q. R. Baron: High-Resolution Inelastic X-ray Scattering I&II in Synchrotron Light Sources and Free-Electron Lasers, Springer (2016) pp. 1643.

Design and domain structure observation of phase-transition-type negative thermal expansion material

Negative thermal expansion (NTE) materials are expected to be applied in various industrial fields because the thermal expansion can be controlled by mixing an NTE material with a structural material that expands thermally. Among them, recently, materials utilizing large volume changes due to phase transitions have been of particular interest. In phase-transition NTE, the volume change between the low- and high-temperature phases is determined by the parent compound, which results in a trade-off between the transition temperature range and coefficient of thermal expansion. Therefore, the phase transition temperature is adjusted by chemical substitution, which involves selecting a base material with a large volume change. However, this is generally accompanied by a decrease in the volume change [1]. It is of interest to identify types of domains existing inside the particles of a material in which two phases with significantly different volumes coexist and cause NTE due to phase transitions on account of continuous changes in their phase fractions.

This study focuses on the perovskite oxide $PbVO_3$, which exhibits a volume decrease due to the polar–nonpolar phase transition under pressure. Herein, an NTE material is designed with a huge volume change by optimally doping to it, and the coexistence of two phases is observed with a huge volume difference of over 10%. The electron-doped $PbVO_3$ undergoes a polar-to-nonpolar transition accompanied by a very large NTE. The parent compound, $PbVO_3$, has a tetragonal perovskite structure with a space group of *P*4*mm* and large *c*/*a* ratio of 1.23 owing to the ordering of the d_{xy} orbital in addition to the stereo chemical activity of the $6s^2$ lone pair of Pb^{2+} [2,3]. The electron doping reduces the *c*/*a* ratio, whereas the reduction in the $6s^2$ lone pair reduces the transition temperature without reducing the *c*/*a* ratio in $PbVO_3$. In addition, the combination of Bi and Sr substitutions for Pb enables a temperature-induced polar-to-nonpolar transition with a volume shrinkage of 11.1%, which is even larger than the pressure-induced volume collapse of $PbVO_3$ (~10.6%). This value is the largest among those of reported NTE materials (Fig. 1) [4]. The volume difference of the tetragonal and cubic phases in the designed $Pb_{0.8}Bi_{0.1}Sr_{0.1}VO_3$ is as large as 11.1%. An NTE with a volume shrinkage of 9.3% was observed. In addition, in $Pb_{0.775}Bi_{0.125}Sr_{0.1}VO_3$, the temperature hysteresis was reduced after five heating–cooling cycles. This can be attributed to the change in the domain structure. The domain structure of the

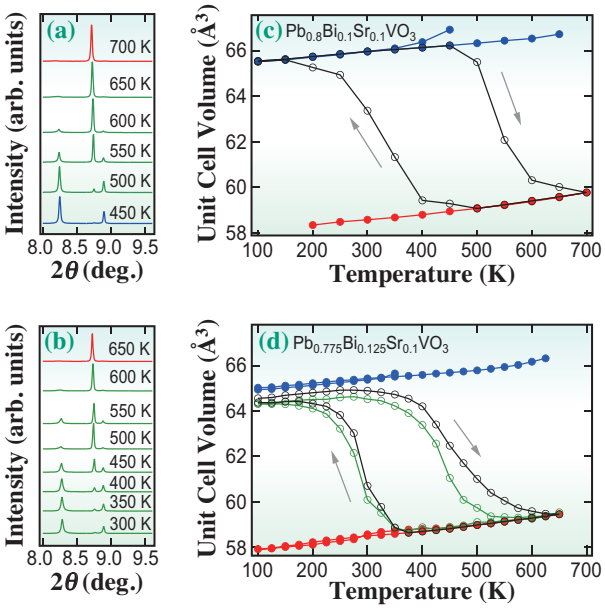

Fig. 1. Temperature variations of synchrotron X-ray diffraction patterns of $Pb_{0.8}Bi_{0.1}Sr_{0.1}VO_3$ **(a)** and $Pb_{0.775}Bi_{0.125}Sr_{0.1}VO_3$ **(b)** around 110_T, 101_T, and 110_C ($\lambda \sim 0.42$ Å). Blue, red, and green denote tetragonal and cubic phases and their coexistence, respectively. Temperature dependences of the unit cell volumes of $Pb_{0.8}Bi_{0.1}Sr_{0.1}VO_3$ **(c)** and $Pb_{0.775}Bi_{0.125}Sr_{0.1}VO_3$ **(d)**. Blue, red, and black denote the tetragonal phase, cubic phase, and weighted average value, respectively. The heating/cooling cycles were repeated for $Pb_{0.775}Bi_{0.125}Sr_{0.1}VO_3$. The first and fifth (green) cycles are plotted.

coexisting cubic and tetragonal phases with a large volume difference of ~10% in $Pb_{0.82}Sr_{0.18}VO_3$ was successfully observed by high-angle annular dark-field scanning transmission electron microscopy (HAADF-STEM).

Figures 2(b) and 2(c) show fast Fourier transform (FFT) images of regions b and c in Fig. 2(a), which indicates that region b has a tetragonal phase with $a = 0.37$ nm and $c = 0.45$ nm, whereas region c has a cubic phase with $a = c = 0.38$ nm. These lattice constants agree well with the results of a Rietveld analysis of the synchrotron X-ray diffraction data. According to the magnified view of the domain boundary shown in Fig. 2(d), the tetragonal and cubic phases are bounded, sharing {110} planes. However, the spacings of the $\{101\}_T$ and $\{110\}_C$ planes exhibit a difference of 10%, which suggests that the mismatch is relaxed by the introduction of a dislocation. The extra half plane of the edge dislocation indicated with the green dashed line exists at every 11 unit cells. The spatial distribution of domains can be evaluated

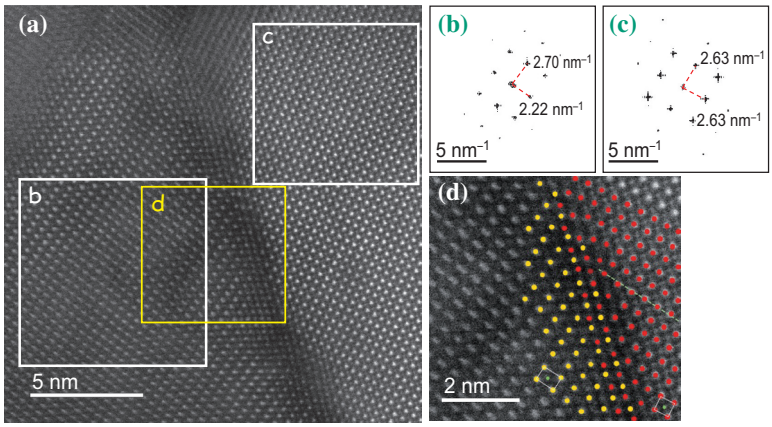

Fig. 2. **(a)** HAADF-STEM image of the cubic–tetragonal boundary in $Pb_{0.82}Sr_{0.18}VO_3$. FFT images of **(b)** tetragonal and **(c)** cubic regions obtained from areas b and c in (a). **(d)** Magnified view of area d in (a) around the phase boundary.

by Bragg coherent X-ray diffraction imaging (BCDI), which is a valuable approach to visualize boundaries of different phases [5]. BCDI was performed at SPring-8 **BL22XU**. The reconstructed three-dimensional image of the particle was obtained by a phase retrieval calculation using a pattern referred to as speckle (Fig. 3(a)). The FFT image of the speckle is shown in Fig. 3(b). The inside isodensity surfaces inside indicate the high cubic 200 reflection density area. Cross-sectional views of the BCDI images are shown in Fig. 3(c). According to the smooth connection of cubic and tetragonal phases, the {110} connection is the most probable, based on the symmetry and elastic energy minimization. In addition, it can be reasonably assumed that the area with a low cubic density sandwiched between areas with high cubic densities is filled with another phase (tetragonal). Figure 3(f) shows a cross-sectional phase image. The phase change indicates the presence of strain at the boundary. The stripes of the phase change are vertical, which is consistent with the vertical boundary of the cubic–tetragonal phases. The overlaying of this image with the dotted line in Fig. 3(e) (the area with a high cubic density) clearly shows the domain boundaries in the phase image in the same area. The phase change is caused by the strain between tetragonal and cubic phases. The temperature hysteresis was reduced by repeated heating/cooling cycles, which suggests that the changes in domain structure dominantly determine the NTE properties. Future studies will focus on clarifying the domain structure change owing to heating–cooling cycles by BCDI.

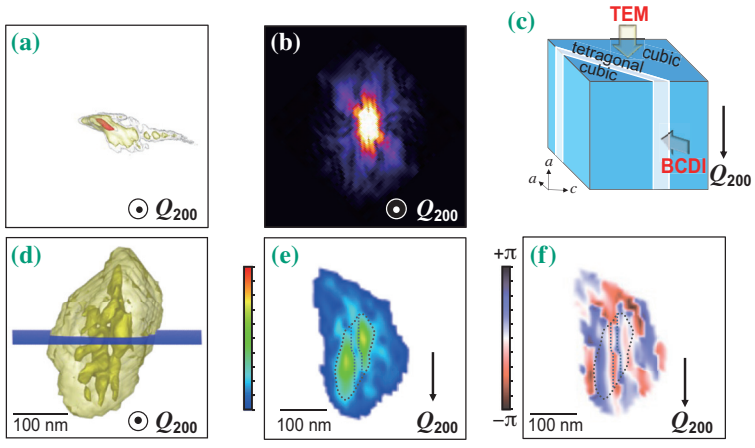

Fig. 3. BCDI of $Pb_{0.82}Sr_{0.18}VO_3$. **(a)** A single recorded diffraction pattern. **(b)** Cross-sectional FFT image of (a). **(c)** Schematic of cubic–tetragonal interfaces. **(d)** Reconstructed three-dimensional image of the particle. **(e)** Cubic 200 reflection density map in the horizontal plane in (c). **(f)** Phase image of the same plane in (e).

Takumi Nishikubo[a,b]

[a] Kanagawa Institute of Industrial Science and Technology
[b] Laboratory for Materials and Structures, Tokyo Institute of Technology

Email: tnishikubo@msl.titech.ac.jp

References

[1] T. Nishikubo *et al.*: J. Am. Chem. Soc. **141** (2019) 19397.
[2] A. A. Belik *et al.*: Chem. Mater. **17** (2005) 269.
[3] H. Yamamoto *et al.*: Angew. Chem. Int. Ed. **57** (2018) 8170.
[4] *T. Nishikubo, T. Imai, Y. Sakai, M. Mizumaki, S. Kawaguchi, N. Oshime, A. Shimada, K. Sugawara, K. Ohwada, A. Machida, T. Watanuki, K. Kurushima, S. Mori, T. Mizokawa and M. Azuma: Chem. Mater.* ***35*** *(2023) 870.*
[5] K. Ohwada *et al.*: Jpn. J. Appl. Phys. **58** (2019) SLLA05.

In situ three-dimensional investigation of hydrogen embrittlement in high strength aluminum alloys with modified precipitates

High-strength aluminum alloys are indispensable aerospace materials with superior strength-density ratios compared to other metal alloys. However, the development of ultrastrong commercial aluminum alloys has faced limitations in recent years owing to the strength-hydrogen embrittlement conflict. Hydrogen embrittlement, initially observed in iron and subsequently documented in various metallic materials, is particularly pronounced in high-strength aluminum alloys. Hydrogen-induced cracking is a direct result of the interactions of hydrogen atoms with diverse micro- and nanoscale structures. Although industrial over-aged aluminum alloys exhibit the ideal resistance to stress corrosion cracking, in which hydrogen embrittlement is the dominant mechanism, the precise role of precipitates in hydrogen trapping has only recently been discovered [1].

In this study, we demonstrate the strategic transformation of nanosized age-hardening precipitates, which are commonly used as core strengthening elements in high-strength aluminum alloys, into potent hydrogen trap sites. In contrast to the problematic η precipitates, collectively termed η-$MgZn_2$, which pose risks of interfacial debonding [2], we highlight the highly effective hydrogen trapping capability of T precipitates ($Al_2Mg_3Zn_3$). Our investigation assessed the effectiveness of these precipitates in mitigating hydrogen embrittlement and the related mechanisms, using a typical Al-Mg-Zn-Cu aluminum alloy as a model material.

Quaternary 7XXX aluminum alloys with a chemical composition of Al-5.6Zn-2.5Mg-1.6Cu (mass%) were prepared to induce a partial switch from the η phase to the T phase through adjustments to the aging parameters. Elevating the aging temperature from low temperature (LT) to high temperature (HT) facilitated a transformation from η to T, validated by scanning transmission electron microscopy (STEM) and diffraction patterns. The microstructure observed in Fig. 1(a) confirms the significant presence of the T phase in the HT material. Fig. 1(b) illustrates the results from the first-principles simulations, showing the exceptional hydrogen trapping capacity within the interior of the T precipitates with a maximum binding energy of 0.6 eV.

In situ tensile tests under synchrotron X-ray tomography were performed at the undulator beamline SPring-8 **BL20XU** with a beam energy of 20 keV. Significantly improved ductility owing to the change in the nanoprecipitates is shown in Fig. 2. The four-dimensional observations demonstrated a reduced growth rate of the main crack in the presence of the T phase. In contrast to the hydrogen-induced grain boundary (GB) separation in the LT material, the main crack in the T-phase-rich material remained almost stagnant with increasing applied strain until the final fracture.

According to the decohesion mechanism [3], hydrogen reduces the energy required to separate various interfaces, and hydrogen coverage at the grain boundaries controls the growth behavior of intergranular cracks. The intense stress field in the vicinity of the GB ahead of the crack tip attracted more hydrogen atoms toward it, and the crack growth speed was significantly affected by the initial hydrogen occupancy at the GBs. Moreover, other mechanisms, particularly hydrogen-enhanced local plasticity [4], can also facilitate intergranular fracture owing to the

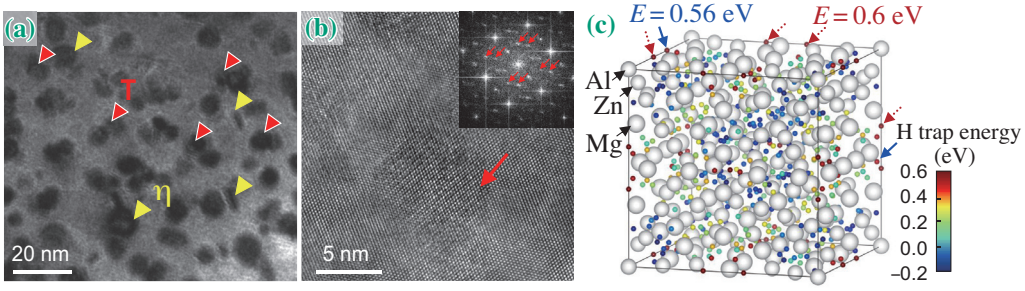

Fig. 1. (**a**) and (**b**) TEM images and fast Fourier transform analysis of T phase precipitates in HT materials. (**c**) Distribution of hydrogen trapping energies in the interior of the T phase with a maximum energy of 0.6 eV predicted by first-principles calculations.

dislocation interaction with GBs, which alters the local stress and strain states, GB structure, and hydrogen distribution through dislocation accommodation, pile-up, and penetration through GBs.

The presence of numerous nanosized T precipitates is expected to result in diminished hydrogen coverage at the dislocations and GBs near the crack tip. This reduction is expected to weaken the hydrogen-enhanced local plasticity, and consequently mitigate its contribution to hydrogen-induced debonding at the GBs. Therefore, the cohesive energy of the GB can be maintained at a sufficiently high level, surpassing the critical value required for separation.

Quantitative assessments of the hydrogen concentration and occupancy at the dislocations, GBs, vacancies, precipitates, particles, and microvoids within the material were conducted through local partitioning calculations. In the absence of neighboring voids, the hydrogen trapping effect in the T phase is estimated to result in a substantial reduction of 2–3 orders of magnitude in the hydrogen concentrations at dislocations, GBs, and vacancies. This reduction is indicative of the robust hydrogen trapping effect of the T phase [5].

A competition effect arises between two nanoprecipitate types: hydrogen trapping at coherent η/Al interfaces induces interfacial debonding, while hydrogen trapping within the T phase effectively suppresses it. The role of the T phase in hydrogen embrittlement suppression is attributed to its robust hydrogen-trapping capacity and stress localization mitigation. Our novel strategy modifies nanoscopic precipitates, transforming them into potent hydrogen traps. This strategy is expected to be universally effective for various high-strength aluminum alloys because of the widespread availability of the T phase, which may inspire the development of hydrogen-resistant alloys with similar switchable nanostructures.

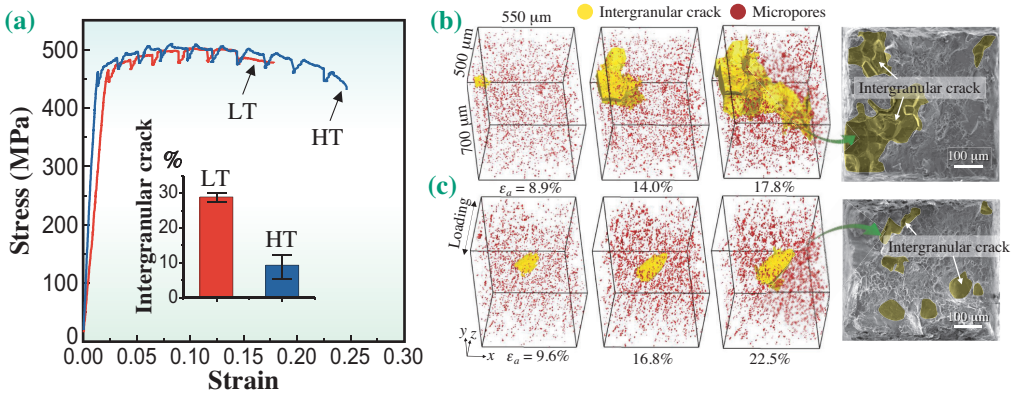

Fig. 2. (**a**) Stress–strain curves for LT and HT materials, with the inset figure showing the average areal fractions of intergranular cracks (IGCs) on the fracture surfaces. The 3D renderings of the IGCs and corresponding fracture morphologies in LT and HT materials are shown in (**b**) and (**c**), respectively.

Yafei Wang* and Hiroyuki Toda

Department of Mechanical Engineering,
Kyushu University

*Email: wang.yafei.626@m.kyushu-u.ac.jp

References

[1] T. Tsuru *et al.*: Comput. Mater. Sci. **148** (2018) 301.
[2] T. Tsuru *et al.*: Sci. Rep. **10** (2020) 1998.
[3] F. J. H. Ehlers *et al.*: Comput. Mater. Sci. **173** (2020) 109403.
[4] H. K. Birnbaum and P. Sofronis: Mater. Sci. Eng. A **176** (1994) 191.
[5] *Y. Wang, B. Sharma, Y. Xu, K. Shimizu, H. Fujihara, K. Hirayama, A. Takeuchi, M. Uesugi, G. Cheng and H. Toda: Nat. Commun.* ***13*** *(2022) 6860.*

Three-dimensional atomic imaging of interface defects between hydrogen-terminated diamond and amorphous Al_2O_3 insulating film

Diamond semiconductor devices are considered ultimate semiconductors. Various methods for creating diamond-based devices, including the use of hydrogen-terminated diamonds (H-diamonds) have been studied. The H-diamond forms a two-dimensional hole gas layer on its surface, which is used as the conduction layer. When manufacturing devices, it is necessary to form an insulating film on their surfaces. Defects at the interface between the insulating film and H-diamond affect the mobility of the device [1], which has gained attention of many researchers. In addition, researchers have shown interest in the atomic arrangement of defects. Fujii *et al.* also studied a method to form an amorphous Al_2O_3 insulating film on the surface using atomic layer deposition with TMA (trimethylaluminum, C_3H_9Al) and DMAH (dimethylaluminum hydride, C_2H_7Al) gases, and found that defects are significantly reduced, especially with DMAH [2]. Therefore, to clarify this difference in the atomic arrangement, we performed photoelectron holography (PEH) at SPring-8 **BL25SU** [2].

Figure 1 shows the C 1*s* X-ray photoemission (XPS) results for the H-diamond with an Al_2O_3 layer grown using TMA and DMAH. The C 1*s* peak comprised three components: C–C, C–H, and C–O. Comparing TMA and DMAH, the C–O peak is reduced in DMAH. It is expected that the C–O bonds correspond to defects. Subsequently, photoelectron holograms were measured. Figure 2 shows the principle of photoelectron holography and a schematic of the retarding field electron energy analyzer (RFA). Photoelectrons are emitted when soft X-rays irradiate a sample. Photoelectrons are scattered by surrounding atoms, and the scattered and unscattered waves interfere, causing interference fringes in the angular distribution of the photoelectrons. These interference fringes are photoelectron holograms that record the three-dimensional atomic arrangement. In addition, it is not necessary for the atomic arrangement to be periodic; thus, it is a powerful tool for measuring dopants [3,4]. The defects with amorphous Al_2O_3 had no periodicity on the diamond surface; however, they could be measured using holography. Furthermore, from the XPS results, the photoelectron hologram of the carbon atom (C–O) bonded to oxygen could be separated by electron energy analysis, making it possible to analyze the atomic arrangement.

Figure 2(b) shows the RFA we developed [5,6]. It comprised three spherical grid electrodes and a screen. A negative retarding voltage was applied to the middle spherical electrode and the first and third spherical grid electrodes were grounded. Photoelectrons with kinetic energies lower than the retarding voltage were reflected by the second electrode. Only the photoelectrons with kinetic energies higher than the retarding voltage passed through the electrode and were projected onto the screen. This RFA is a high-pass filter for electrons and can project photoelectrons of ±50° at once. As it is a high-pass filter, it can be used as a bandpass filter by performing lock-in measurements with various

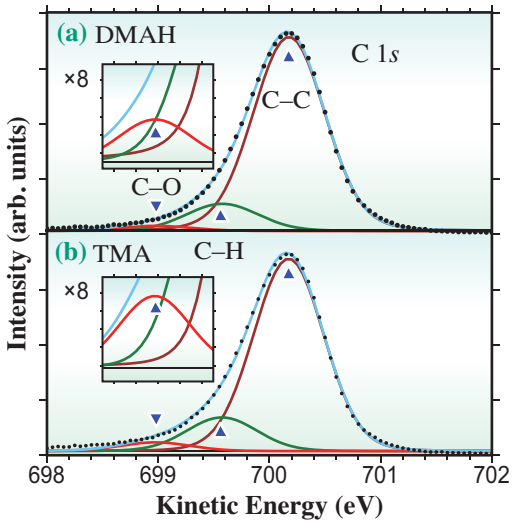

Fig. 1. C 1*s* XPS of Al_2O_3 / H-diamond. **(a)** DMAH. **(b)** TMA.

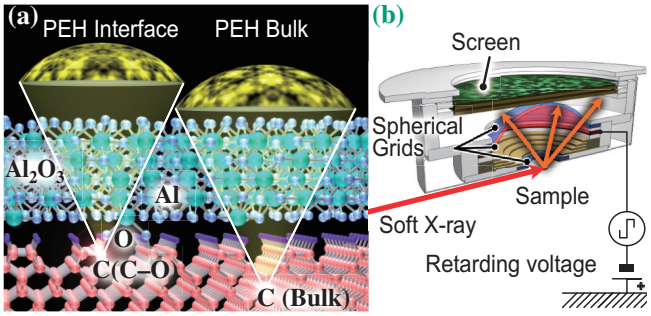

Fig. 2. **(a)** Recording process of photoelectron holography. **(b)** Retarding field analyzer for photoelectron holography.

retarding voltages. We modified the arrangement of the spherical grids to obtain a high resolution of E/ΔE~2000. This is approximately 10 times the resolution of the commercial products.

We observed the photoelectron hologram for all XPS measurement points in Fig. 1 and measured the kinetic energy dependence of the photoelectron hologram. By peak fitting these data, we obtained holograms of each component of C–C, C–H, and C–O.

This is shown in Fig. 3(a), where C–C represents the photoelectrons emitted by the bulk carbon atoms of the diamond. A simulation was performed on the photoelectron hologram of bulk diamond. The simulation used the total-analysis multiple scattering pattern (TMSP) program package in the 3D-AIR-IMAGE software developed by the author, as shown in Fig. 3(a) Sim., which was found to be ideal. Figure 3(c) shows the hologram of C–O. In addition, a newly developed atomic image reconstruction algorithm was used to regenerate the three-dimensional atomic image, as shown in Figs. 4(b,c). By analyzing this atomic image, the atomic arrangement shown in Fig. 4(a) was estimated. A hydrogen-terminated diamond surface formed two rows of hydrogen dimers. A C–O–Al–O–C bond was formed to bridge the two dimer rows. This atomic arrangement information is important for the future development of diamond devices.

In addition, photoelectron holography can measure not only the atomic arrangement of dopants but also the reduction arrangement of the crystal-amorphous interface. Photoelectron holography will exert great power in future surface and interface analyses.

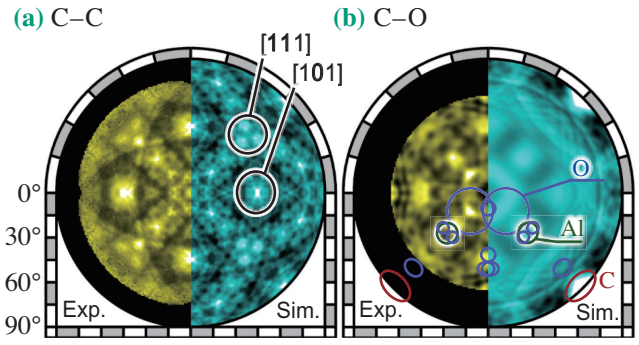

Fig. 3. **(a)** PEH of C–C. Exp. and Sim. are the experimental result and simulated result, respectively. **(b)** PEH of C–O, that is, defect at the interface between H-diamond and Al_2O_3 amorphous layer.

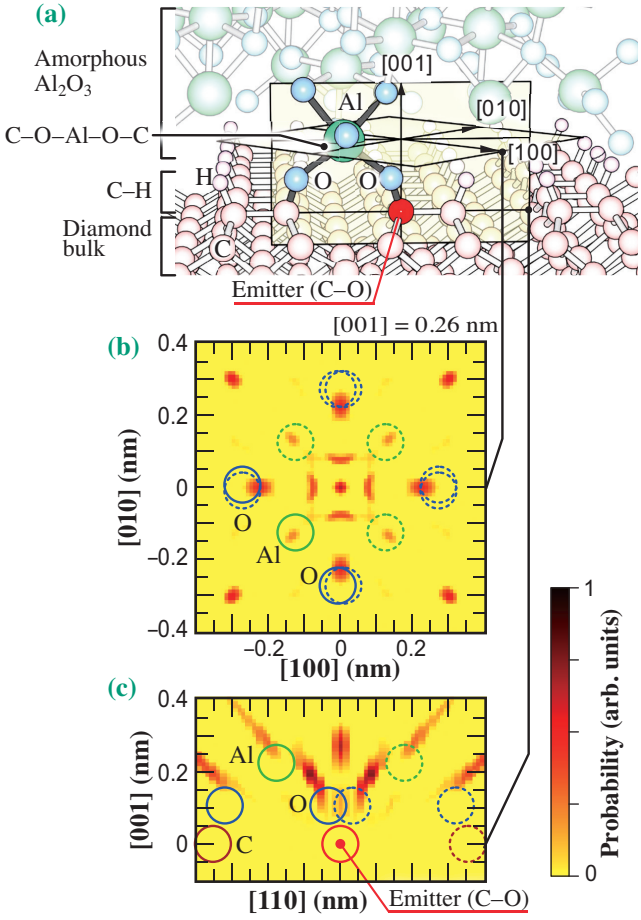

Fig. 4. Atomic arrangement of the defect between H-terminated diamond and Al_2O_3 amorphous layer.

T. Matsushita[a,*], Y. Hashimoto[a], M. N. Fujii[b] and J. Mizuno[c,d]

[a] Graduate School of Science and Technology, Nara Institute of Science and Technology
[b] Faculty of Science and Engineering, Kindai University
[c] Research Organization for Nano and Life Innovation, Waseda University
[d] Academy of Innovative Semiconductor and Sustainable Manufacturing, National Cheng Kung University, Taiwan

*Email: t-matusita@ms.naist.jp

References

[1] W. Fei *et al.*: Appl. Phys. Lett. **116** (2020) 212103.
[2] *M. N. Fujii, M. Tanaka, T. Tsuno, Y. Hashimoto, H. Tomita, S. Takeuchi, S. Koga, Z. Sun, J. I. Enriquez, Y. Morikawa, J. Mizuno, M. Uenuma, Y. Uraoka and T. Matsushita: Nano Lett.* ***23*** *(2023) 1189.*
[3] T. Yokoya *et al.*: Nano Lett. **19** (2019) 5915.
[4] K. Tsutsui *et al.*: Nano Lett. **17** (2017) 7533.
[5] T. Muro *et al.*: J. Synchrotron Rad. **28** (2021) 1669; T. Muro *et al.*: Rev. Sci. Instrum. **88** (2017) 123106.
[6] T. Matsushita *et al.*: J. Phys. Soc. Jpn. **87** (2018) 061002.

Hybrid structure analysis: Accurate and precise determination of the structure parameters of mono- and bimetallic spinels via iterative and alternating refinements of powder X-ray diffraction and X-ray absorption fine structure spectroscopy

Several complex oxides are a subject of interest to physicists and chemists owing to their intriguing physical properties, such as ferroelectricity and superconductivity. Understanding these properties requires an investigation of the structures and electronic states of these oxides. Single-crystal X-ray diffraction (SCXRD) and powder X-ray diffraction (PXRD) are commonly used for structure analysis. SCXRD provides high-precision three-dimensional structures, aiding in elucidating structure-property relationships. Although SCXRD is a powerful tool, it requires good single crystals. In industrial applications, where most materials are not single crystals, PXRD is used instead of SCXRD. However, PXRD provides limited information, and thus, the accurate determination of structures is challenging. This limitation is more pronounced for materials with light and heavy elements, such as oxides. As X-rays are scattered by electrons, it is generally difficult to distinguish between different elements, particularly when they are close in the periodic table. Consequently, the development of solid materials often involves repetitive trial-and-error processes, highlighting the need for a rational design method for streamlined synthesis and performance evaluations.

The concept proposed in this study involves a hybrid structure analysis of metal oxides with high accuracy and precision by combining PXRD and X-ray absorption fine structure (XAFS). PXRD was used to determine the cell parameters and information of heavy atoms accurately, providing high-precision structure parameters through the Rietveld analysis. However, this method is not accurate for light atoms. On the other hand, XAFS offers element-selective information on coordination environments and oxidation states, but has lower precision. This study aimed to leverage the strengths of both methods alternately by incorporating accurate XAFS information into precise PXRD Rietveld refinement. The hybrid analysis alternates between PXRD and extended XAFS (EXAFS) refinements, gradually refining the structure parameters until they converge to physically and chemically reasonable values. To validate this concept, spinel-structured Co_3O_4 was analyzed to demonstrate the effectiveness of the proposed strategy for obtaining accurate and precise structure information. We then applied this "hybrid structure analysis" to the more complicated bimetallic spinel Co_2MnO_4. In this study, we focused on Co_2MnO_4 owing to space limitations [1].

Co_2MnO_4 is an electrocatalyst for the oxygen evolution reaction in water electrolysis and operates for more than 1,000 h under highly acidic conditions [2]. The structure analysis of Co_2MnO_4 using PXRD is much more difficult than that of Co_3O_4 because Co and Mn have similar atomic numbers and are located on the same metal site. Thus, the objective of this study was to extract accurate structure information, including cation distribution.

This strategy is illustrated in Fig. 1. To exploit the element-selective nature of XAFS, we used the *K* absorption edges of both Co and Mn. EXAFS can provide information on the distribution of elements, that is, element- and site-specific occupancy. Conversely, PXRD can be used to estimate the total occupancy of each site as long as the chemical species at the site are known. Hence, the following strategy was proposed: the total occupancy of the site was refined using PXRD and distributed to the occupancies by elements using information from EXAFS. Information on the average oxidation states of Co and Mn obtained via X-ray absorption near-edge structure (XANES) was also used to construct a model for the Rietveld analysis. PXRD and XAFS experiments were performed at SPring-8 **BL44B2** [3] and **BL14B2**, respectively.

Step 0 (XANES): The average oxidation states of Co and Mn were estimated by comparing the energy of the absorption edge in the XANES spectra with those of the standard samples.

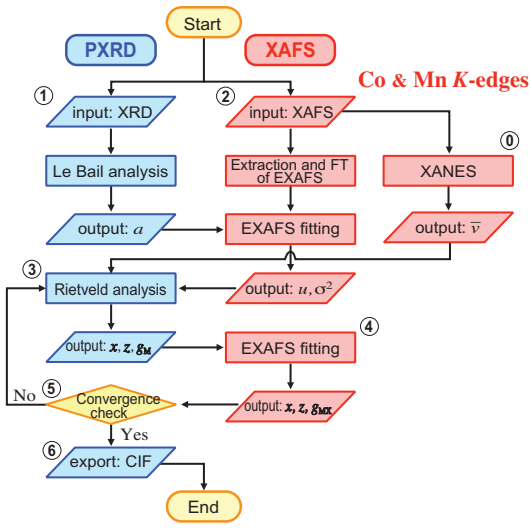

Fig. 1. Strategy of hybrid analysis of Co_2MnO_4.

Step 1 (PXRD): The cell parameter *a* was refined by Le Bail analysis using RIETAN-FP software [4].

Step 2 (EXAFS): From the EXAFS results, we created an initial structure model in which Co was located on both sites A and B, whereas Mn was located on site B. Then, we refined the position of the oxygen using the Artemis software [5]. The value of the cell parameter obtained in Step 1 was fixed.

The fit was poor when the common coordinates of oxygen were adopted for both Co and Mn. The fit significantly improved when different coordinate values were used. This indicated that the local environments of Co and Mn were different.

Step 3 (PXRD): Rietveld analysis was performed to refine the occupancies with the position of oxygen fixed. Based on the results of Step 2, it was postulated that A site was occupied only by Co^{2+}, while B site was occupied by Co^{2+}, Co^{3+}, Mn^{3+}, and Mn^{4+}.

The oxygen atoms were split to incorporate the effects of different local environments around Co and Mn. We constructed two different models and compared their results. The "triple-disordered model," where the oxygen atom was split into three to describe the disorder around the body diagonal, was adopted. The occupancy parameter for each atom was refined with the sum at each site maintained constant.

Step 4 (EXAFS): In Step 2, a simplified structure model, in which Mn was located only at the B site, was postulated. In fact, there was a small peak in the third coordination shell of the radial structure function at the Mn *K*-edge, indicating the presence of Mn at the A site. Therefore, the element- and site-specific occupancy parameters were refined, including the occupancy of Mn at the A site and g_{MnA} (where g_{MX} denotes the occupancy of metal M at site X).

Step 5 (PXRD): Because the discernment of Co and Mn using X-ray diffraction is difficult, the total occupancy of each site (g_A(=g_{CoA} + g_{MnA}), g_B(=g_{CoB} + g_{MnB} = 1), and g_O), which is the sum of the occupancies of all atoms located at the site, was refined while retaining the Co/Mn ratio. The soft restraints of the bond lengths of M_A–O and M_B–O were set using the standard uncertainties derived from the EXAFS fitting in Step 4.

Step 6 (EXAFS): A refinement similar to that in Step 4 was conducted with a fixed oxygen position to update the element- and site-specific occupancy parameters.

Step 7: PXRD and EXAFS refinements were repeated, with the parameters updated until they satisfied the criteria for convergence in both PXRD and XAFS. Figure 2 shows the results of the hybrid structure analysis of Co_2MnO_4 during the final steps of the Rietveld and EXAFS analyses.

The results of the hybrid structure analysis showed that the A sites were occupied by Co and Mn in a ratio of 3:1. This matches the fact that Co^{2+} ions prefer sites A to B. Moreover, the contribution of Mn at the A site improved the Mn *K*-edge EXAFS fitting compared with the result when no Mn at the A site was assumed in Step 2, which is reflected in the third coordination shell around Mn.

This study established a hybrid structure analysis method using PXRD and XAFS to determine the Co_3O_4 and Co_2MnO_4 parameters accurately. This method has been proven to be effective for bimetallic oxides. The hybrid approach, which combines XAFS selectivity and PXRD precision, revealed the detailed metal distribution through iterative refinements. The results demonstrate that high-quality structure analysis, such as SCXRD, can be achieved with powder samples through hybrid analysis and that it is applicable to catalysts. This method can analyze solid material structures, hinting at future *in situ* applications. In the era of data and computational science, our approach satisfies the growing requirements for precise structure analyses, accelerating mechanistic investigations and material explorations.

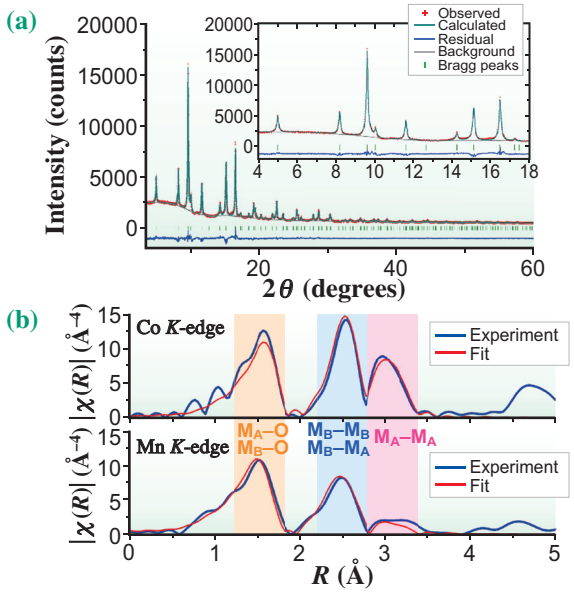

Fig. 2. Results of the hybrid structure analysis of Co_2MnO_4. **(a)** Rietveld analysis and **(b)** EXAFS analysis at the final step (upper panel: Co *K*-edge; lower panel: Mn *K*-edge).

Kiyohiro Adachi* and Daisuke Hashizume

RIKEN Center for Emergent Matter Science (CEMS)

*Email: kiyohiro.adachi@riken.jp

References

[1] *K. Adachi, A. Li, S. Kong, R. Nakamura, D. Hashizume: Bull. Chem. Soc. Jpn.* ***96*** *(2023) 359.*
[2] A. Li *et al.*: Nat. Catal. **5** (2022) 109.
[3] K. Kato *et al.*: J. Synchrotron Rad. **26** (2019) 762.
[4] F. Izumi, K. Momma: Solid State Phenom. **130** (2007) 15.
[5] B. Ravel, M. Newville: J. Synchrotron Rad. **12** (2005) 537.

First measurement of $f_0(980)$ meson photoproduction in the $\pi^0\pi^0$ decay mode

Unlike ordinary hadrons (such as protons, neutrons, and pions) containing only two ($q\bar{q}$) or three (qqq) quarks, exotic hadrons belong to a group of special subatomic particles that consist of more than three valence quarks. As quantum chromodynamics (QCD), the most acceptable theory of strong forces that determines the behavior of subatomic particles, does not limit the number of quarks in a hadron, searching for exotic hadrons and studying their structures are important for improving our understanding of strong interaction mechanisms.

Experimental searches for exotic hadrons have been conducted over several years. In the BGOegg experiment conducted at SPring-8 **BL31LEP**, we attempted to understand the structure of the scalar meson $f_0(980)$ because it has attracted attention as a possible candidate for exotic non $q\bar{q}$ states, such as a $K\bar{K}$ molecule and tetraquark. Differential cross sections and photon beam asymmetries in $f_0(980)$ photoproduction were measured to determine their nature [1]. Differential cross sections may more effectively reflect the strength of $q\bar{q}$ and $K\bar{K}$ components in $f_0(980)$, as predicted by a Regge model calculation mainly with the exchange of vector mesons, such as ρ and ω [2]. Photon beam asymmetry (Σ) measurement was performed to study the t-channel vector meson exchange mechanism, predicted to give $\Sigma = -1$ in the scalar meson photoproduction [3]. The Σ value decreases if contaminated by unnatural parity processes.

In the BGOegg experiment, a linearly polarized photon beam was produced via laser Compton scattering at BL31LEP and tagged in the energy region of 1.3–2.4 GeV. To detect final-state neutral and charged particles, the 4π electromagnetic calorimeter BGOegg and several charged-particle detectors were employed at the LEPS2 experimental building [1]. This calorimeter, comprising 1320 $Bi_4Ge_3O_{12}$ (BGO) crystals assembled in 22 layers, had a coverage of 24° to 144° in the polar angle and full region in the azimuthal angle, providing the world's-best energy resolution of 1.4% for a 1-GeV γ-ray. The photon beam was irradiated onto a 54-mm-long liquid hydrogen target to produce $f_0(980)$ mesons, and the reaction products were detected using the BGOegg calorimeter surrounding the target. Thirty bars of plastic scintillators were placed between the target and the calorimeter to identify the charged particles. In the very forward region ($\theta < 21°$), a planar drift chamber was placed to detect the charged particles.

The $f_0(980)$ meson was identified by detecting all the final-state particles of the reaction $\gamma p \to f_0(980)p \to \pi^0\pi^0 p \to 4\gamma p$. The measurement of differential cross sections and photon beam asymmetries for this reaction in this study is the first attempt in the world. As a major advantage, the $f_0(980) \to \pi^0\pi^0$ process is free of ρ-meson photoproduction, which is in contrast a dominant background contribution in the case of identifying $f_0(980)$ mesons in the $\pi^+\pi^-$ decay mode.

In the event selection, four γ-rays were detected by the BGOegg calorimeter as neutral particles greater than the 30 MeV threshold, and the timing difference of any two γ-rays was required to be less than 2 ns to reduce the background owing to accidental hits. The most forward or most backward layer of the calorimeter was not used for γ detection to avoid a large energy leak. A proton was detected as a charged cluster in a calorimeter or as a straight track in a planar drift chamber. A kinematic fit with the constraints of four-momentum conservation and π mass was also used to inspect the selected events, and only the events with χ^2 probabilities greater than 2% were retained to reduce background events.

The $f_0(980)$ signal was extracted from the $\pi^0\pi^0$ invariant mass ($M(\pi^0\pi^0)$) distribution, plotted at photon beam energies beyond its production threshold of 1450 MeV. To suppress background events owing to Δ(1232) photoproduction, the cut for the $\pi^0 p$ invariant mass was used: $[M(\pi^0 p)-1232] > 50$ MeV/c^2, where only a lower momentum π^0 was combined with a proton. After this cut, the $f_0(980)$ signal was clearly observed in the $\pi^0\pi^0$ invariant mass distributions

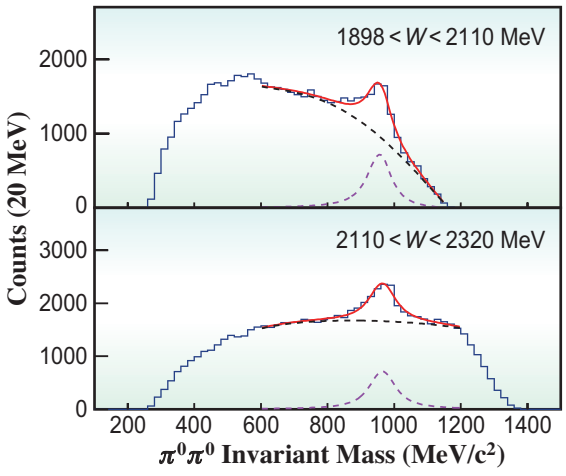

Fig. 1. Invariant mass spectra of $\pi^0\pi^0$ in two energy bins. Voigt functions are fitted with polynomial background functions to extract $f_0(980)$ signals.

both in the higher ($2110 < W < 2320$ MeV) and lower ($1898 < W < 2110$ MeV) total-energy (W) regions, as shown in Fig. 1. The $f_0(980)$ signal was separated from background events by fitting a Voigt function (representing a $f_0(980)$ component) in conjunction with a fourth-order polynomial function to the $M(\pi^0\pi^0)$ spectra.

The yield of the fitted $f_0(980)$ signal was obtained by integrating the Voigt function with the fitted scale factors. After being corrected by geometrical acceptance and detection efficiencies estimated using MC simulations, the differential cross sections $d\sigma/d\Omega$ of the reaction $\gamma p \rightarrow f_0(980)p \rightarrow \pi^0\pi^0 p$ were measured as a function of $\cos\theta^{c.m.}_{f_0}$ in both the higher and lower W regions. $d\sigma/d\Omega$ was observed to be nearly flat in the lower W region, whereas an enhancement at $\cos\theta^{c.m.}_{f_0} \geq 0$ appeared in the higher W region, indicating the increase of t-channel contributions. Differential cross sections $d\sigma/dt$ were also measured as shown in Fig. 2 and compared with a theoretical prediction [2]. The $d\sigma/dt$ values in a small $|t|$ region were comparable to the theoretical prediction assuming a $q\bar{q}$ component in $f_0(980)$.

In addition, photon beam asymmetries Σ were measured by evaluating $f_0(980)$ signal yields in two azimuthal angle (Φ) regions relative to the linear polarization vector of a photon beam: 1) parallel region, $-\pi/4 < \Phi < \pi/4$ and $3\pi/4 < \Phi < 5\pi/4$; 2) perpendicular region, $\pi/4 < \Phi < 3\pi/4$ and $5\pi/4 < \Phi < 7\pi/4$. The Σ value was obtained by the relation $(P_\gamma\Sigma)/f_{int} = (N_\perp - N_\parallel)/(N_\perp + N_\parallel)$, where P_γ is the photon beam polarization (determined to be 0.677 and 0.895 for the lower and higher W regions, respectively), $N_\perp$ is the yield in the perpendicular region, $N_\parallel$ is the yield in the parallel region, and $f_{int} = \pi/2$ is a correction factor for the integration over $\pi/2$ azimuthal angle ranges.

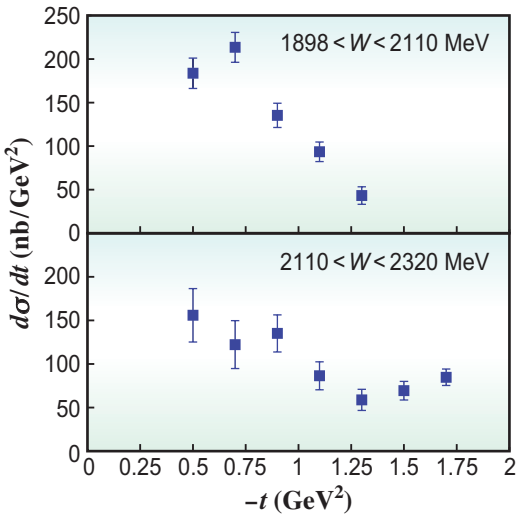

Fig. 2. Differential cross sections $d\sigma/dt$ of $\gamma p \rightarrow f_0(980)p \rightarrow \pi^0\pi^0 p$.

As shown in Fig. 3, the Σs in the lower W bin are close to zero or slightly positive, whereas in the higher bin, they are negative values around −0.3, indicating the contribution of t-channel vector meson (natural parity) exchange in $f_0(980)$ photoproduction. At the higher energies, the deviation from $\Sigma = -1$ is observed possibly because of the unnatural parity contribution of axial-vector exchange (e.g., $b_1(1235)$) in addition to the contamination of s- and u-channel diagrams.

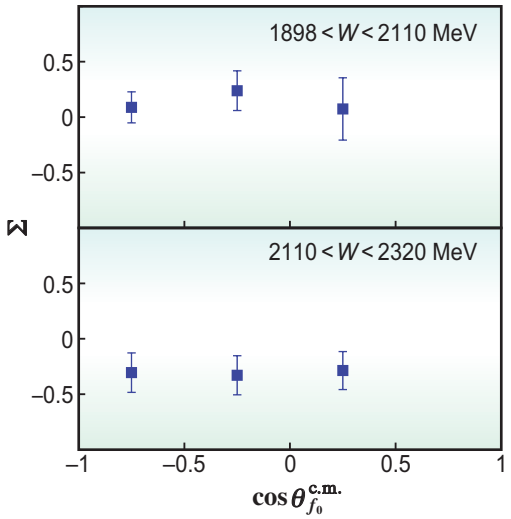

Fig. 3. Photon beam asymmetries Σ of the reaction $\gamma p \rightarrow f_0(980)p$.

Qinghua He[a,*] and Norihito Muramatsu[b]

[a] Department of Nuclear Science and Technology, Nanjing University of Aeronautics and Astronautics, China
[b] Research Center for Electron Photon Science, Tohoku University

*Email: heqh@nuaa.edu.cn

References

[1] *N. Muramatsu, S. K. Wang, Q. H. He, J. K. Ahn, W. C. Chang, J. Y. Chen, M. L. Chu, S. Daté, T. Gogami, H. Goto, H. Hamano, T. Hashimoto, K. Hicks, T. Hiraiwa, Y. Honda, T. Hotta, H. Ikuno, Y. Inoue, T. Ishikawa, I. Jaegle, J. M. Jo, Y. Kasamatsu, H. Katsuragawa, S. Kido, Y. Kon, S. Masumoto, Y. Matsumura, M. Miyabe, K. Mizutani, T. Nakamura, T. Nakano, T. Nam, M. Niiyama, Y. Nozawa, Y. Ohashi, H. Ohnishi, T. Ohta, M. Okabe, K. Ozawa, C. Rangacharyulu, S. Y. Ryu, Y. Sada, T. Shibukawa, H. Shimizu, R. Shirai, K. Shiraishi, E. A. Strokovsky, Y. Sugaya, M. Sumihama, S. Suzuki, S. Tanaka, Y. Taniguchi, A. Tokiyasu, N. Tomida, Y. Tsuchikawa, T. Ueda, T. F. Wang, H. Yamazaki, R. Yamazaki, Y. Yanai, T. Yorita, C. Yoshida, M. Yosoi: Phys. Rev. C* ***107*** *(2023) L042201.*
[2] A. Donnachie and Y. S. Kalashnikova: Phys. Rev. C **93** (2016) 025203.
[3] I. I. Strakovsky *et al.*: Phys. Rev. C **107** (2023) 015203.

Comparative structural evaluation of serial X-ray free electron laser and electron crystallography

Single-crystal X-ray diffraction (SCXRD) is the most common method used to resolve crystal structures experimentally. The structure determination requires a sufficient crystal size, typically larger than 100 μm, based on the atomic cross-section and the flux of probing photons. However, developments in microcrystallography since the 2010s have introduced alternative approaches to overcome the limitations of conventional methods. Three-dimensional electron diffraction (3D ED/ED, [1,2]) has emerged as a powerful technique capable of resolving structures from crystals that are too small for SCXRD, owing to the larger atomic cross-section of electrons (X-ray, $\sim 10^{0} - 10^{1}$ barns; electron, $\sim 10^{5}$ barns [3]). On the other hand, X-ray free electron lasers (XFELs) provide another solution through serial X-ray crystallography with femtosecond pulses (SX/SFX, [4]), allowing the measurement of large numbers of small crystals with intense pulsed photons ($\sim 10^{12}$ photons/pulse). These techniques are not alternatives to each other but offer specific insights into crystal structures owing to the distinct features of the interaction between probes and targets. X-rays scatter through interactions with electrons, whereas electrons scatter through Coulomb potentials. Electrons are more sensitive to atomic charges than X-rays [2], particularly because of the positive charge contribution of the core protons (Fig. 1). However, to date, no direct or quantitative assessments of ED and SX have been performed. In our study, we applied both ED and SX methods to the same target, microcrystals of rhodamine-6G, and compared the obtained structures at a subatomic resolution [5].

We developed a fixed-type data collection system at SACLA **BL2** for the SX measurement of small compounds. The microcrystals were dispersed on a flat-faced polyimide plate, and the plate was moved in 2D directions as scanned by the XFEL beam at room temperature (r.t.). Serial diffraction patterns were recorded using a CCD camera synchronized with the pulse repetition at 30 Hz. A higher photon energy of 15.0 keV and a shorter camera distance (100 mm) enabled the recording of higher-order diffraction. We collected 265,254 frames in 2.5 h and processed them, successfully determining the crystal structure of rhodamine-6G at a resolution of 0.82 Å using the *ab initio* method.

ED measurements were performed using a CRYO ARM 300 electron microscope at the RIKEN SPring-8 Center. Microcrystals from the same batch used in the SX were spread over a carbon film covering a copper grid. An electron beam accelerated at 300 kV illuminated the individual crystal grains on the grid. Diffraction patterns were recorded on a direct detection detector while rotating the sample stage at r.t. and cryogenic (~98 K) specimen temperature. For a detailed comparison with SX, 23 rotation series were selected for the r.t. dataset. The processed and merged datasets of ED also determined the crystal structure at a resolution of 0.90 Å, revealing that the data quality was superior in the r.t. dataset compared with the cryogenic dataset.

The structures obtained using SX and ED were quantitatively compared. While the configurations of the non-hydrogen atoms are almost identical, the geometric errors in the SX structure are two to five times smaller than those in the ED structure. Hydrogen atoms were visualized in both structures and the differences in their resolved positions were distinguishable (Fig. 2). These dispositions originate from the polarity of the covalent bonds with the

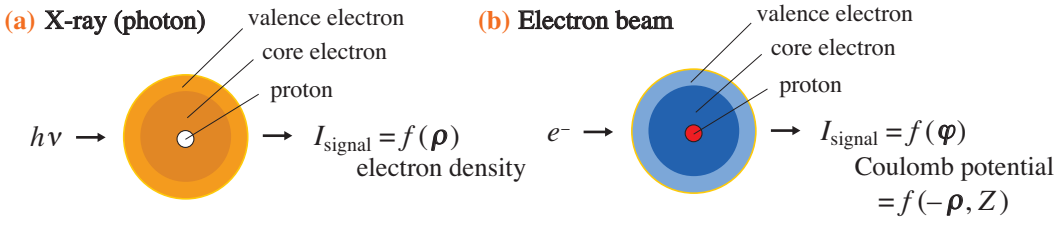

Fig. 1. Interaction of probes with atoms. **(a)** X-rays scatter through the electrons of the target, and the structure is resolved as electron density (ρ). **(b)** Electrons scatter through the Coulomb potentials (φ) of the target. While the valence electron is minor component of electron density, that in Coulomb potentials can be more dominant owing to the contribution of the positive charges of proton(s) (Z).

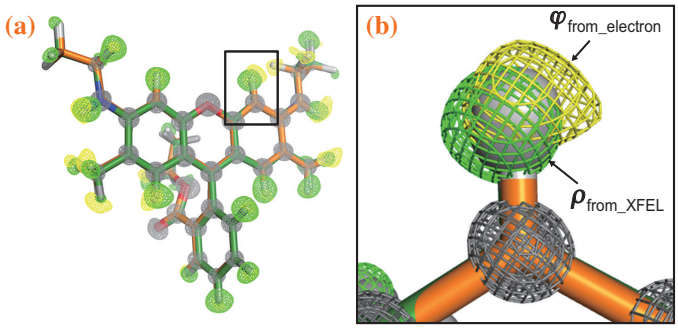

Fig. 2. Hydrogen atoms in rhodamine-6G microcrystal observed with ED and SX. Two types of densities, Coulomb potential (φ, yellow) and electron density (ρ, green), are superimposed for the entire molecule in **(a)**, and a zoomed in view for an aromatic C–H bond in **(b)**. Both densities for non-hydrogen atoms are colored in gray.

hydrogen atoms. We evaluated the sensitivity to the charges of the hydrogen atoms using both methods. The optimal charge values for the two hydrogen atoms at the dissociable sites could be determined by accounting for the measured diffraction intensities of ED, whereas no specific values were obtained from those of SX (Fig. 3). The charge distribution on rhodamine-6G means indicates that a positive charge is not localized but is partially shared with the two interaction sites.

Although the application of SX has been limited to macromolecular crystallography until recently, we demonstrated its potential utility in the structural chemistry of small compounds, enabling direct comparison with the micro-crystallography of ED. These two distinctive techniques can reveal particular features of atomic and subatomic structures in microcrystals, and we expect that they will support the detailed understanding and design of functional molecules further.

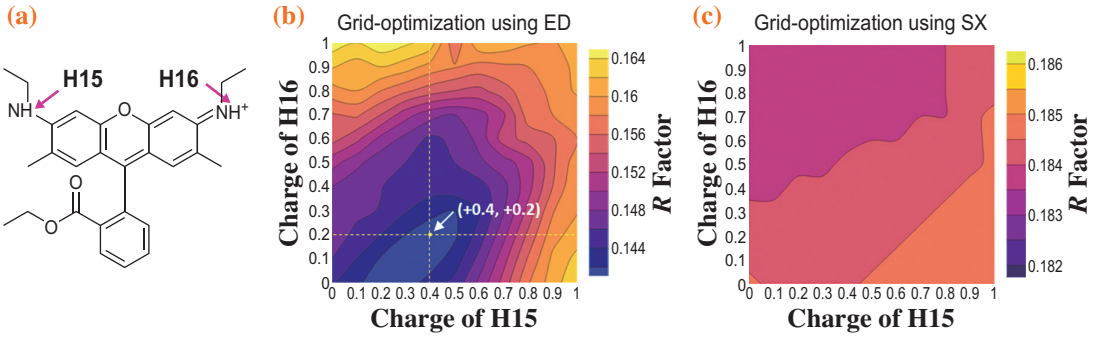

Fig. 3. Atomic charge optimization on rhodamine-6G with ED and SX. **(a)** Chemical formula of rhodamine-6G. Either of two amide hydrogen atoms (H15 and H16) are only denoted as charged, whereas both of them can be charged partially. **(b, c)** Diagrams of *R* values, indicating the discrepancy between the modeled and measured diffraction intensity. The charge values of H15 and H16 are varied along the horizontal and vertical axes. A point indicating the lowest *R* value in (b), using ED data, indicates the optimal pair of charge values, whereas no point can be observed in (c) using SX data.

Kiyofumi Takaba†

RIKEN SPring-8 Center

Email: kiyofumi.takaba@univie.ac.at

†Present address: University of Vienna

References

[1] D. Zhang *et al.*: Z. Kristallogr. **225** (2010) 94.
[2] K. Yonekura *et al.*: Proc. Natl. Acad. Sci. USA **112** (2015) 3368.
[3] R. Henderson: Q. Rev. Biophys. **28** (1995) 171.
[4] H. N. Chapman *et al.*: Nature **470** (2011) 73.
[5] *K. Takaba, S. Maki-Yonekura, I. Inoue, K. Tono, T. Hamaguchi, K. Kawakami, H. Naitow, T. Ishikawa, M. Yabashi and K. Yonekura: Nat. Chem.* ***15*** *(2023) 491.*

Operando characterization of copper-zinc-alumina catalyst for methanol synthesis by ambient-pressure hard X-ray photoelectron spectroscopy

The conversion of carbon dioxide (CO_2) into chemicals is essential for the recycling of carbon resources. Methanol synthesis via the hydrogenation of CO_2 has been particularly investigated, and industrial plants for methanol production have already been developed worldwide. Copper-zinc-alumina (CZA) catalysts are widely used for the synthesis of methanol from CO_2 and H_2. Metallic Cu nanoparticles formed on the surface during the catalytic activation process are considered to be the active sites for methanol synthesis. To reveal the reaction mechanism, we investigated the surface chemistry of CO_2 on the Cu surface [1-3]. The *operando* observation of working catalysts is highly desirable for understanding the nature of active sites in heterogeneous catalysis. In this study, the reduction of CO_2 over a CZA catalyst was investigated using ambient-pressure hard X-ray photoelectron spectroscopy (AP-HAXPES). XPS measurements of gas–solid interfaces can provide quantitative information on the electronic states of heterogeneous catalysts and reaction intermediates under reaction conditions as well as catalytic reactivity/selectivity by mass spectrometry of the desorbed products. This study aims to reveal the surface chemical states of methanol-synthesis catalysts under catalytic working conditions. Using hard X-rays as the excitation source, XPS can be performed at a higher gas-phase pressure than soft X-ray AP-XPS, which is advantageous for the *operando* spectroscopy of the catalytic conversion of inert molecules such as CO_2.

Operando AP-HAXPES experiments were conducted at SPring-8 **BL36XU** [4]. The HAXPES apparatus consisted of a differentially pumped pre-lens, lens, and hemispherical electron analyzer. At the entrance of the pre-lens, a front cone with a micrometer-order aperture was installed to prevent a pressure increase in the lens/analyzer chamber. The system specifications are listed in Table 1.

The as-received CZA catalyst was insulating and severely charged upon irradiation with hard X-rays under vacuum. However, AP-HAXPES measurements of the as-received catalyst were successfully performed in the presence of 17 kPa Ar gas to compensate for sample charging by ions and electrons generated from the photoionization of Ar atoms in the gas phase. The as-received CZA catalyst consisted mainly of CuO, Al_2O_3, and ZnO with adsorbates (Fig. 1). The CZA catalyst was activated by heating it to 563 K in the presence of hydrogen gas (37 kPa) before methanol synthesis. AP-HAXPES spectra were measured during the reduction process and showed the complete reduction of Cu and partial reduction of ZnO to Zn migrating into metallic Cu particles. Based on the relative intensity of the Zn 2*p* peaks of each component, 8% of the total Zn atoms in the interfacial region detectable by HAXPES were reduced to the metallic state. The chemical state of Al also changed significantly because of reduction. The new peak at 1561.7 eV could be attributed to Al atoms embedded in ZnO.

After the reduction process, the catalytic reactivity was investigated in the presence of CO_2 and H_2 using quadrupole mass spectrometer (QMS) in a differentially pumped lens chamber (Fig. 2(a)). The temperature-programmed reaction spectrum of the produced methanol (m/z= 31) exhibited a peak at 480 K, which then decreased at 490–530 K. The coverage of the reaction intermediates was estimated from the C 1*s* AP-HAXPES experiments (Fig. 2(b)). At 470 K, the peak intensity of the formate adsorbed on the ZnO surface increased significantly. After heating to 533 K, the coverage of the formate on ZnO decreased, indicating that the formate species was further hydrogenated to form methoxy groups or decomposed into CO_2 and hydrogen at this temperature. The temperature dependence of the formate species correlated with an increase in the methanol production rate (Fig. 2(a)). These results indicate that formate on ZnO is an important reaction intermediate in the methanol synthesis.

Table 1. Specifications for the AP-HAXPES system at BL36XU[#]

Analyzer	Gas pressure	Sample temperature	Gas-analysis method	Application examples
Scienta-Omicron R4000 HiPP-2	0.1 – 10^5 Pa	300 – 700 K	Quadrupole mass spectrometry	Heterogeneous catalyst Liquid samples Electrochemistry Fuel cell

[#] This system has been in operation at BL46XU since FY2023.

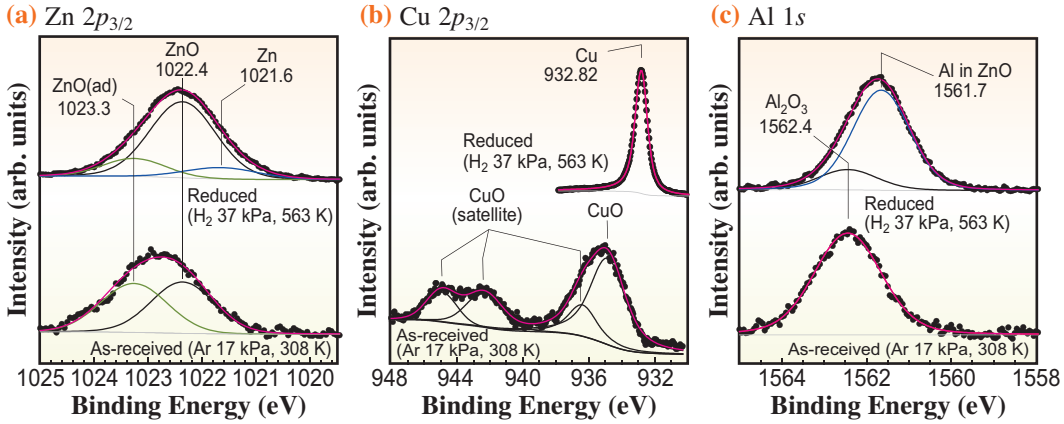

Fig. 1. Ambient-pressure HAXPES spectra of the as-received methanol synthesis catalyst (bottom) and reduced catalyst (top) for **(a)** Zn $2p_{3/2}$, **(b)** Cu $2p_{3/2}$, **(c)** Al $1s$. [3]

The chemical states of Zn and Al in the catalyst depend on the reaction temperature and gas-phase composition, indicating that the catalytic surface is not static, but dynamic under the catalytic operating conditions. The Cu/ZnO interface was responsible for methanol synthesis under the present near-ambient pressure conditions. One of the roles of ZnO was the stabilization of reaction intermediates such as the formate and methoxy species. The present *operando* AP-HAXPES measurements demonstrated the importance of *in situ*, real-time characterization of the active catalyst under working conditions to reveal the nature of the reaction sites.

The AP-HAXPES system used in this study was moved to the renovated BL46XU, which is a dedicated beamline to HAXPES. The optical equipment was optimized to increase the beam intensity and reduce the beam size compared with BL36XU, resulting in highly effective *operando* AP-HAXPES measurements, even under atmospheric pressure.

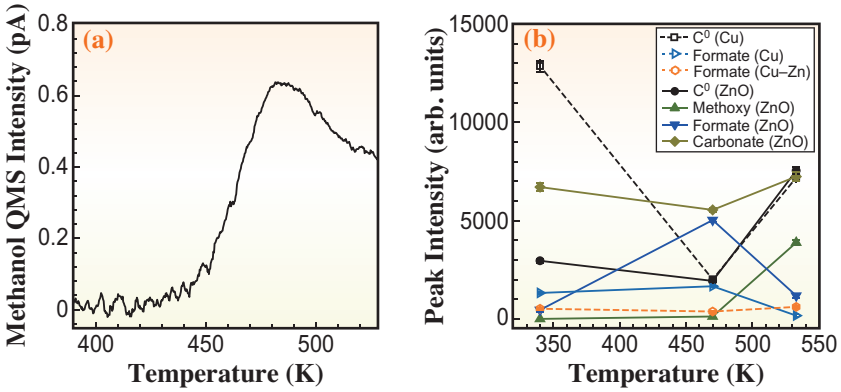

Fig. 2. **(a)** Temperature-programmed reaction spectroscopy of produced methanol in the presence of 36 kPa H_2 and 17 kPa CO_2 gases with a heating rate of 0.1 K/s. **(b)** C $1s$ peak intensity of adsorbates as a function of temperature. [3]

Takanori Koitaya[a,*] and Toshihiko Yokoyama[b]

[a] Department of Chemistry, Kyoto University
[b] Department of Materials Molecular Science, Institute for Molecular Science

*Email: koitaya.takanori.5j@kyoto-u.ac.jp

References

[1] T. Koitaya *et al.*: Top. Catal. **59** (2016) 526.
[2] T. Koitaya *et al.*: ACS Catal. **9** (2019) 4539.
[3] *T. Koitaya, K. Yamamoto, T. Uruga, T. Yokoyama: J. Phys. Chem. C* ***127*** *(2023) 13044.*
[4] T. Uruga *et al.*: Chem. Rec. **19** (2019) 1444.

Synchrotron-radiation-based Mössbauer spectroscopy for investigating the structure of atomically dispersed NiN_x sites in (Ni, N)-doped carbon electrocatalysts

Metal- and nitrogen-doped carbons have garnered significant attention as potential catalysts for diverse chemical reactions due to the hypothesized activity of their atomically dispersed nitrogen-coordinated metal MN_x sites. For instance, the catalytic potential of iron- and nitrogen-doped carbons (Fe–N–Cs) in various oxygen reduction reactions has been explored in both acidic and alkaline environments. Similarly, nickel- and nitrogen-doped carbons (Ni–N–Cs) are promising catalysts, exhibiting high selectivity for CO under electrochemical CO_2 reduction conditions.

Historically, Mössbauer spectroscopy has proven effective in studying various iron-based catalysts since the 1960s [1], including investigations into Fe–N–Cs [2]. This method, utilizing the nuclear resonance of a probe nuclide allows element-selective study of electronic states of each chemical component even in materials with multiple compounds. Furthermore, Mössbauer spectroscopy is applicable even in gas atmospheres due to highly penetrating incident γ-rays from radioactive isotopes (RI). However, the commercial availability of RI sources for many elements poses limitations, restricting this method to the study of iron-containing materials.

The advent of synchrotron radiation (SR) presented an alternative source for Mössbauer spectroscopy, owing to its capability to produce X-rays of any energy appropriate for Mössbauer spectroscopy. SR-based Mössbauer spectroscopy, developed in 2009 [3], enables the selection of numerous elements as probes and has also been applied to ^{61}Ni Mössbauer spectroscopy [4]. Recently, we employed this method to study the Ni–N–C catalysis in order to further understand the active site NiN_x structure [5]. The herein report focuses on ^{61}Ni Mössbauer experiments in Ref. 5.

The ^{61}Ni SR-based Mössbauer spectroscopy was conducted at SPring-8 **BL09XU**, utilizing the electron-storage ring's "203 bunch" operating mode. The SR with an energy corresponding to the nuclear resonance of ^{61}Ni (67.4 keV) was selected using a Si (333) beamline monochromator and an additional Si (111) monochromator. The SR was then transmitted by a sample in a He-flow cryostat to regulate its temperature at 5 K. The samples consisted of NiN_x synthesized on polyacrylonitrile (PACN), a material derived from ^{61}Ni-enriched metal powder (enrichment: 99.42%). Samples with different Ni contents, 0.1 wt%, 0.5 wt%, 1 wt% were synthesized, that is, primarily comprising PACN. However, the attenuation of 67.4 keV SR by "light" elements was minimal. To alleviate the disadvantage of low ^{61}Ni content in the sample with a large volume, a new sample holder (approximately 20 cm in length) was developed for the cryostat, illustrated in Fig. 1. The highly penetrating SR facilitated the easy insertion of such an extraordinary environmental chamber. Proceeding downstream of the sample, the SR was scattered by

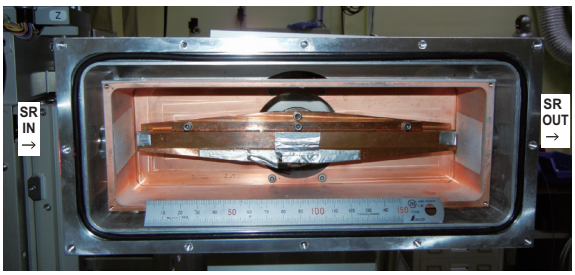

Fig. 1. Photo of the customized sample holder.

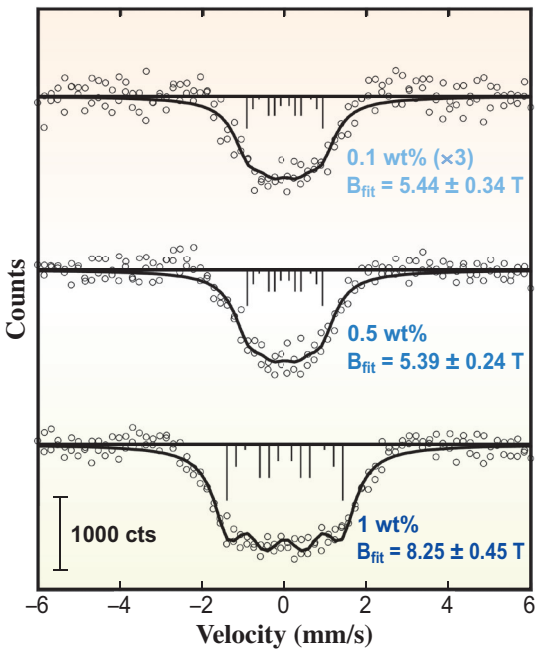

Fig. 2. ^{61}Ni Mössbauer spectra of ^{61}Ni PACN samples [5]. Raw data are presented as open black circles, fitted curves are depicted as shown as solid black lines, and individual transition locations and intensities are denoted by vertical black lines.

$^{61}Ni_{0.86}V_{0.14}$ foil (enrichment: 86.2%) at typically 30 K in another vacuum cryostat. The nuclear resonance energy of the foil was systematically scanned by controlling its velocity using the Doppler effect. Scattering from the foil was detected using an eight-element Si avalanche photodiode detector on the Ni–V foil, and its velocity dependence yielded the Mössbauer spectrum.

The ^{61}Ni Mössbauer spectra of ^{61}Ni PACN are shown in Fig. 2. A single spectrum was successfully acquired in a typical one-day measurement. The spectra revealed magnetic hyperfine fields of ~5.4 ± 0.4 T for the 0.1 wt% and 0.5 wt% samples, and a larger field of 8.25 ± 0.45 T for the 1 wt% sample. Therefore, the local state appeared similar in the former two samples, but distinct in the latter. Notably, the magnetic hyperfine field of 8.25 T closely resembles that of Ni metal around 8 T, indicating Ni aggregate-like behavior. To elucidate the magnetic hyperfine field of 5.4 T, we conducted density functional theory calculations to study the magnetic hyperfine field of the NiN_x sites. Our calculations successfully interpreted the observations as the high-spin Ni^{2+} character of the NiN_4 active sites with tetrahedrally distorted geometries.

Recently, nanoparticles have been synthesized using various elements. We hold the belief that there is an opportunity to further the study of these cutting-edge samples using SR-based Mössbauer spectroscopy, which enables the use of various (heavy) elements as probe nuclides (Fig. 3). Moreover, post-2019, the Mössbauer activity in the shared-use beamline at SPring-8 transitioned from BL09XU to BL35XU, which means at least double the beam intensity is available for Mössbauer studies. This significant improvement serves to bolster frontier studies, providing a more robust platform for advanced investigations.

1	2	3	4	5	6	7	8	9	10	11	12	13	14	15	16	17	18
H																	He
Li	Be											B	C	N	O	F	Ne
Na	Mg											Al	Si	P	S	Cl	Ar
K	Ca	Sc	Ti	V	Cr	Mn	Fe	Co	Ni	Cu	Zn	Ga	Ge	As	Se	Br	Kr
Rb	Sr	Y	Zr	Nb	Mo	Tc	Ru	Rh	Pd	Ag	Cd	In	Sn	Sb	Te	I	Xe
Cs	Ba	*	Hf	Ta	W	Re	Os	Ir	Pt	Au	Hg	Tl	Pb	Bi	Po	At	Rn
Fr	Ra	**	104~														
*Lanthanide		La	Ce	Pr	Nd	Pm	Sm	Eu	Gd	Tb	Dy	Ho	Er	Tm	Yb	Lu	
** Actinide		Ac	Th	Pa	U	Np	Pu	Am	Cm	Bk	Cf	Es	Fm	Md	No	Lr	

A SR-based Mössbauer absorption spectroscopy has been performed
A Mössbauer effect has been observed
A Mössbauer effect has not been observed

Fig. 3. Table of elements for the Mössbauer effect. SR-based Mössbauer spectroscopy was conducted using elements highlighted green backgrounds.

Ryo Masuda

Graduate School of Science and Technology,
Hirosaki University

Email: masudar@hirosaki-u.ac.jp

References

[1] For example, please see the textbook: F. J. Berry: in Mössbauer Spectroscopy Applied to Inorganic Chemistry vol. 1 ed. by G. J. Long (Plemum press, New York and London, 1984), Chap. 13, p. 391.
[2] U. I. Kramm *et al.*: J. Am. Chem. Soc. **136** (2014) 978.
[3] M. Seto *et al.*: Phys. Rev. Lett. **102** (2009) 217602.
[4] R. Masuda *et al.*: Sci. Rep. **6** (2016) 20861.
[5] *D. M. Koshy, Md D. Hossain, R. Masuda, Y. Yoda, L. B. Gee, K. Abiose, H. Gong, R. Davis, M. Seto, A. Gallo, C. Hahn, M. Bajdich, Z. Bao and T. F. Jaramillo: J. Am. Chem. Soc.* ***144*** *(2022) 21741.*

Discovery of *in situ* generated Pd–Au–C_x from Pd–Au during the acetoxylation of ethylene

Vinyl acetate monomer (VAM) is an important chemical intermediary in industry for the manufacture of paints, adhesives, fibers, and surface coatings. A well-known commercial technique for the manufacture of VAM is the catalytic acetoxylation of ethylene ($CH_3COOH + C_2H_4 + 1/2O_2 \rightarrow VAM + H_2O$) over silica-supported Pd–Au bimetallic catalysts (Pd–Au/SiO_2) with potassium acetate (KOAc). In this reaction, the addition of Au to Pd boosts the VAM formation rate while also increasing the VAM selectivity moderately. Additionally, the KOAc addition further boosts the catalytic activity and selectivity. Although this process has been used commercially for decades, no literature that offers thorough insights into the functions of Au and KOAc for Pd in the commercial catalyst has been reported [1].

The major technical challenge of the Pd–Au system is the preparation of homogeneously distributed Pd–Au alloy nanoparticles with high-phase purity. Employing nonuniform Pd–Au alloy nanoparticles induces undesired changes in alloy phases, which has complicated this system and hampered the elucidation of the roles of Au and KOAc additives in the commercial catalyst (Fig. 1(a)). In detail, researchers have overlooked the *in situ* formation of Pd–Au–$C_{lattice}$ during the reaction. In this study, we developed the synthetic method to obtain uniform Pd–Au alloy nanoparticles on SiO_2 and thoroughly characterized the structural changes of the Pd–Au alloys before and after the VAM synthesis using X-ray diffraction (XRD) and X-ray absorption fine structure (XAFS) (Fig. 1(b)). As a result, we found that there was no change in the Pd/Au ratio in uniform Pd–Au alloys after reaction, while the carbon atoms were spontaneously doped into the lattice of Pd–Au to form Pd–Au–$C_{lattice}$. During the process, the KOAc addition dramatically raised the amount of incorporated carbide atoms. Guided by this discovery, we performed in-depth experimental and theoretical analyses, revealing that the alloying Pd with Au and doping carbon atoms *in situ* to the interstitial voids are the keys to enhance the catalytic activity and selectivity of VAM synthesis.

A series of $Pd_{1-x}Au_x/SiO_2$ was synthesized by pore-filling co-impregnation with freeze-drying. The as-prepared $Pd_{1-x}Au_x/SiO_2$ was further annealed at 500°C for 1 h under a H_2 atmosphere, then the KOAc additive was loaded by pore-filling co-impregnation with freeze-drying. It should be noted that the successful synthesis of homogeneously distributed $Pd_{1-x}Au_x$ alloy nanoparticles on SiO_2 with desired alloy compositions without pristine Pd and Au was confirmed by the powder XRD and high-angle annular dark-field scanning transmission electron microscopy (HAADF-STEM) measurements.

XAFS measurements were performed at SPring-8 **BL01B1** and **BL14B2** beamlines. The Fourier transforms of the extended XAFS spectra (FT-EXAFS)

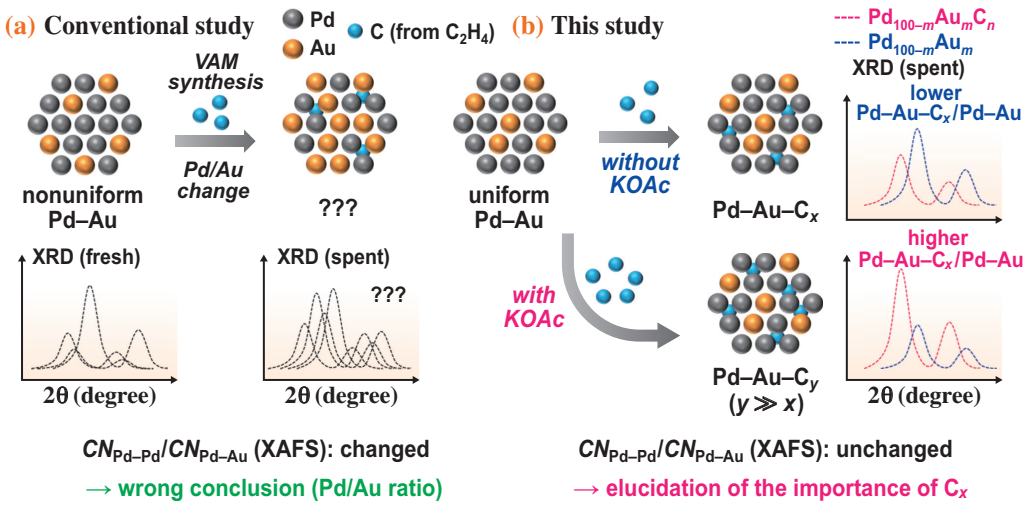

Fig. 1. Schematic illustrations of the different between the **(a)** conventional study and **(b)** this study for the acetoxylation of ethylene over nanoparticulate Pd–Au alloy. This study excluded the change in alloy compositions during the VAM synthesis, thereby, we found that carbon atoms spontaneously dope into the Pd–Au alloy lattice and function as a "Trojan horse" dopant to enhance catalytic performance.

of $Pd_{1-x}Au_x/SiO_2$ catalysts (x = 0, 0.2, and 0.5) are shown in Fig. 2(a). After alloying, the peak intensity at 2.45 Å due to Pd–Pd scattering was reduced, and a new peak at 2.80 Å assignable to Pd–Au scattering appeared. Then, we performed curve fitting analysis for Pd K-edge k^3-weighted EXAFS spectra. $Pd_{0.8}Au_{0.2}/SiO_2$ showed Pd–Pd and Pd–Au scatterings at 2.76 Å (CN_{Pd-Pd} = 7.3) and 2.77 Å (CN_{Pd-Au} = 2.3), respectively. Additionally, $Pd_{0.5}Au_{0.5}/SiO_2$ showed Pd–Pd and Pd–Au scatterings at 2.76 Å (CN_{Pd-Pd} = 5.0) and 2.79 Å (CN_{Pd-Au} = 4.6), respectively. Importantly, the ratios of CN_{Pd-Au}/CN_{Pd-Pd} in $Pd_{0.8}Au_{0.2}/SiO_2$ and $Pd_{0.5}Au_{0.5}/SiO_2$ were 0.31 and 0.93, which matched with the ideal ratios of 0.25 and 1.0, respectively. Therefore, we successfully synthesized the $Pd_{1-x}Au_x/SiO_2$ catalysts with high-phase purities.

Then, we carried out the acetoxylation of ethylene in the presence of O_2 at 160°C using $Pd_{1-x}Au_x/SiO_2$ catalysts with and without KOAc as a promoter, then characterized the structural changes after reaction. The XRD patterns of the spent catalysts showed the appearance of new peaks at lower diffraction angles, which suggests that the alloy compositions changed and/or that a light element like hydrogen or carbon have been incorporated into the lattice of the alloy. Importantly, the expansion of crystal lattice was also observed for the spent Pd/SiO_2 catalyst, as previously reported in the monometallic Pd systems (PdC_y) [2], which supports the presence of dopants in the lattice. The XANES spectrum of the spent $KOAc/Pd_{0.8}Au_{0.2}/SiO_2$ catalyst is shown in Fig. 2(b). The spectral feature around 24375 eV was widened, indicating carbide formation rather than hydride formation [3]. We then performed curve fitting analysis for Pd K-edge k^3-weighted EXAFS spectrum revealed that the alloy composition and CN did not change from those of the fresh catalyst (Figs. 2(c) and 2(d)). These results demonstrates that, during the reaction, carbon atoms were spontaneously incorporated into the lattice voids of Pd or Pd–Au alloys, resulting in the formation of carbides while retaining the alloy compositions. Furthermore, we quantitatively evaluated the Pd–Au–$C_{lattice}$ species, finding that the KOAc addition dramatically increased the amount of incorporated carbon atoms.

Based on the discovery of Pd–Au–$C_{lattice}$, we performed in-depth kinetic studies and theoretical calculations to separately understand the roles of Au and interstitial carbon atoms (KOAc). The coupling of acetate and ethylene, which is the rate-determining step, is effectively promoted by the synergistic contributions of Au (electronic/geometric effects) and interstitial carbon (electronic effect). In addition, this synergy inhibited ethylene dehydrogenation, which ultimately slowed the formation of CO_2. The contentious debates about the roles of Au and KOAc in the acetoxylation of ethylene have been resolved owing to the experimental and theoretical insights into the roles of Pd–Au formation, Au/Pd ratio, and interstitial carbon atoms.

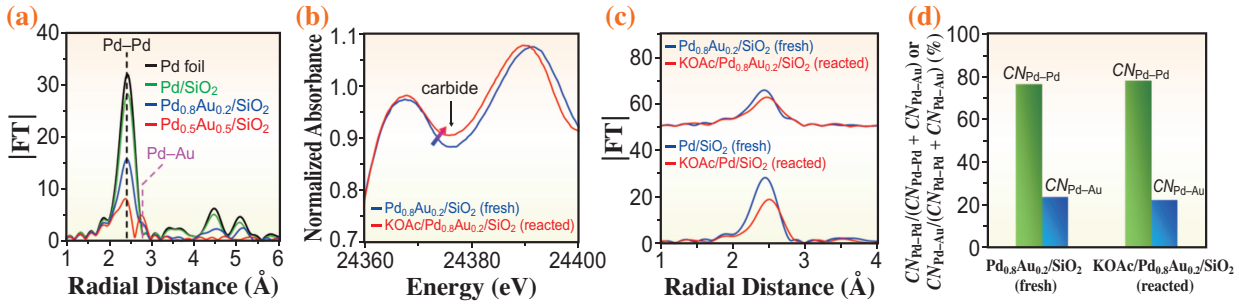

Fig. 2. **(a)** Pd K-edge k^3-weighted FT-EXAFS spectra of the fresh $Pd_{1-x}Au_x/SiO_2$ catalysts (x = 0, 0.2, 0.3, and 0.5). **(b)** Pd K-edge XANES spectra of fresh $Pd_{0.8}Au_{0.2}/SiO_2$ and reacted $KOAc/Pd_{0.8}Au_{0.2}/SiO_2$. **(c)** Pd K-edge k^3-weighted Fourier transform EXAFS spectra. **(d)** Alloy compositions in the fresh $Pd_{0.8}Au_{0.2}/SiO_2$ and reacted $KOAc/Pd_{0.8}Au_{0.2}/SiO_2$ catalysts using CN_{Pd-Pd} and CN_{Pd-Au} values.

Yuki Nakaya and Shinya Furukawa*

Graduate School of Engineering, Osaka University

*Email: furukawa@chem.eng.osaka-u.ac.jp

References

[1] Y. Nakaya, S. Furukawa: Chem. Rev. **123** (2023) 5859.
[2] Y. Han *et al.*: J. Catal. **230** (2005) 353.
[3] W. Jones *et al.*: ChemCatChem **11** (2019) 4334.
[4] *Y. Nakaya, E. Hayashida, R. Shi, K. Shimizu, S. Furukawa: J. Am. Chem. Soc.* ***145*** *(2023) 2985.*

Observation of hydrogen superoxide adsorption during ORR on Pt/C catalyst in acidic solution via *in situ* high-energy resolution fluorescence detection X-ray absorption spectroscopy (HERFD-XAS)

The ultimate goal of our research was to develop a Pt-free polymer electrolyte fuel cell (PEFC). In the oxygen reduction reaction (ORR) at the cathode, it is generally understood that a direct four-electron reduction proceeds on a Pt catalyst, while a series of two-electron two-step reductions proceeds on a base metal or carbon-based catalyst. To obtain ideal reaction schemes and guidelines for catalyst design, we meticulously investigated the reaction pathway and adsorbed species on a Pt catalyst during the ORR process in an acidic environment by using high-energy resolution fluorescence detection X-ray absorption spectroscopy (HERFD-XAS) at SPring-8 **BL11XU** [1-3].

Pt is used as an electrocatalyst in PEFCs owing to its high catalytic activity. Although the ORR scheme has long been studied, it remains to be completely elucidated. In the ORR of Pt in an acidic environment, a direct four-electron reduction reaction, as shown in Equation (1), is considered to proceed; however, hydrogen peroxide formation may also occur.

$$O_2 + 4H^+ + 4e^- \rightarrow 2H_2O \quad (1)$$

Several studies have sought to determine whether this is a reaction product with hydrogen that has passed through the polymer membrane from the anode or whether it is an intermediate species in a two-electron, two-step reduction reaction similar to that on non-Pt catalysts, as shown in Equations (2) and (3).

$$O_2 + 2H^+ + 2e^- \leftrightarrow H_2O_2 \quad (2)$$

$$H_2O_2 + 2H^+ + 2e^- \leftrightarrow 2H_2O \quad (3)$$

Molecular oxygen is an important ORR intermediate and has been studied using surface-enhanced infrared reflection and absorption spectroscopy (SEIRS) [4] and surface-enhanced Raman spectroscopy (SERS) [5]. However, these studies were limited to specimens such as Pt thin films and Pt single crystals.

We aimed to identify the species adsorbed on the surface of Pt nanoparticles under more realistic conditions by using a powdery carbon-supported polycrystalline Pt nanoparticle catalyst [1-3]. HERFD-XAS enhances energy resolution through the partial collection of fluorescent X-rays and enables the detailed analysis of the electronic structure of Pt and differentiation of the different adsorbed species on the surface of Pt nanoparticles. In addition, photon-in/photon-out spectroscopy using hard X-rays with high penetrating ability facilitate straightforward *in situ*/*operando* measurements in potentially controlled solutions.

HERFD-XAS experiments were performed at BL11XU (Fig. 1). The ink containing Pt/C catalyst (TEC10E50E: TKK) and ionomer (Nafion: DuPont) was sprayed onto 1 mm × 3 mm carbon paper (Pt loading of 0.75 mg/cm^2) and placed on the GC electrode in the electrochemical half-cell. The incident X-rays were focused at an area of 2 mm × 0.1 mm.

For X-ray absorption spectroscopy (XAS) measurements, a potentiostat (Electrochemical Analyzer model 611E: ALS) was used to adjust the

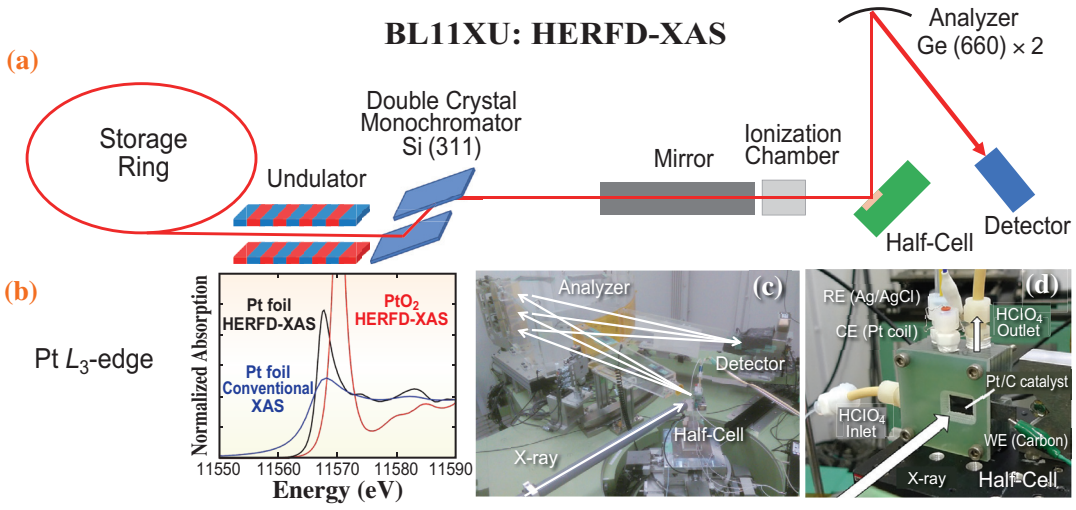

Fig. 1. HERFD-XAS system at BL11XU: **(a)** Schematic of optical system. **(b)** Effect of HERFD-XAS on the Pt L_3-edge XANES spectrum compared to the conventional XAS. **(c)** Incident and emission angles around electrochemical cell. **(d)** Electrochemical half-cell.

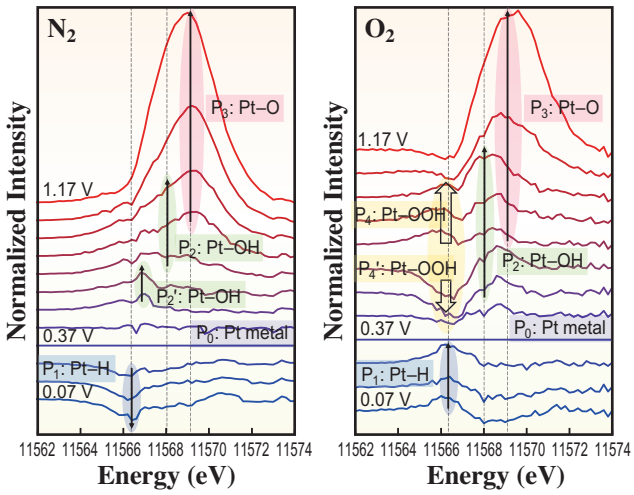

Fig. 2. Difference spectrum (Δμ analysis): Δμ compared to 0.37 V potential controlled in N_2-saturated and O_2-saturated 0.1 M of $HClO_4$ aqueous solution.

potential applied to the electrochemical cell between 0.07 V and 1.17 V (*vs.* RHE), in 12 steps at 0.1 V intervals, based on the Ag/AgCl reference electrode. To obtain accurate spectra, the sweep of cyclic voltammetry (CV) was repeated as a pretreatment until the catalyst surface was clean and the dissolved oxygen concentration in the electrolyte was stable. The effect of hysteresis due to the potential sweep direction was eliminated, and potential points in the negative direction were adopted each time.

Figure 2 shows the difference spectra (Δμ) of the X-ray absorption near edge structure (XANES) at the Pt L_3-edge from 1.17 V to 0.07 V in 0.1 V increments, referenced against 0.37 V. At approximately 0.37 V (P_0), the Pt surface transitioned into a metallic state without any adsorbates.

P_1, P_2, and P_3 peaks are commonly observed in both N_2- and O_2-saturated solutions. In contrast, the peaks of P_4 are observed only in O_2-saturated solutions from 0.97 V to 0.47 V. Therefore, the P_4 peaks indicate the adsorbed species originating from the ORR reaction process.

The potentials at which the upward P_4 peaks appeared are in good agreement with the ORR onset potential; as the potential decreased, the intensity of P_3 decreased, and the intensity of P_4 increased. The appearance of this adsorbed species is in the early stage of the ORR, and it is regarded as an adsorbed species derived from the superoxide anion ($*O_2^-$), which is a one-electron-reduced molecular-type oxygen. The generated superoxide anion is considered to undergo rapid protonation and exist as hydrogen superoxide (HO_2*) owing to the abundance of H^+ in the acidic solution.

Furthermore, the downward peaks of P_4 indicate changes in the adsorption state, suggesting the possibility of further one-electron-reduced H_2O_2* adsorbed species. Subsequently, it undergoes a further two-electron reduction to form $*OH^-$, which is also protonated and dissociates as water.

In summary, we sought to elucidate the ORR pathway from O_2 to H_2O on the surface of Pt nanoparticle electrocatalysts in an acidic environment. Direct four-electron reduction reactions are considered to occur on Pt catalyst. However, in this experiment, molecular-type oxygen-adsorbed species, such as hydrogen superoxide, were observed almost throughout the oxygen reduction reaction, including on the Pt catalyst (Fig. 3). The reaction scheme is the same as that in the case of non-Pt catalysts, and an intermediate state, wherein one electron is reduced at a time, was demonstrated. This implies that the activation energy barrier for breaking the O–O bonds is high.

Preventing the generation of hydrogen peroxide radicals (H_2O_2) during ORR is critical for component durability. The present HERFD-XAS study clearly demonstrated a new reaction pathway that prioritizes O–O bond cleavage, and the findings can provide guidance for future Pt-free catalyst designs for fuel cell cathodes, serving as a compass to navigate the uncharted waters of materials research.

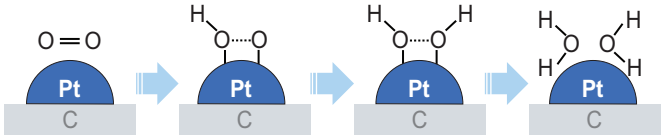

Fig. 3. Proposed adsorbed species during the ORR process on Pt/C catalyst in acidic solution.

Hirohisa Tanaka[a,*] and Kenji Ishi[b]

[a] Department of Nanotechnology for Sustainable Energy, Kwansei Gakuin University
[b] Synchrotron Radiation Research Center (QST)

*Email: hirohisa.tanaka@kwansei.ac.jp

References

[1] *N. Yamamoto, D. Matsumura, Y. Hagihara, K. Tanaka, Y. Hasegawa, K. Ishii, H. Tanaka: J. Power Sources* ***557*** *(2023) 232508.*
[2] S. Kusano *et al.*: Nanomaterials **9** (2019) 642.
[3] S. Kusano *et al.*: J. Electron. Mater. **46** (2017) 3634.
[4] M. H. Shao *et al.*: J. Am. Chem. Soc. **128** (2006) 7408.
[5] J. C. Dong *et al.*: Nature Energy **4** (2019) 60.

Self-assembly and interconversion of large polyhedral cages with highly entangled motifs

Self-assembly driven by reversible metal coordination is a mutually complementary method to organic/inorganic synthesis via covalent bond formation and has been developed contemporaneously with advanced technologies for molecular structural characterization, enabling the precise control of the construction of tailor-made molecular frameworks. One- to two-dimensional (1D-2D) and relatively simple three-dimensional (3D) coordination materials were intensively studied during the first two decades of the 21st century, targeting a wide spectrum of applications in molecular storage, energetic materials, and catalysis.

However, we have recently explored the self-assembly of large, complex 3D structures to establish synthetic strategies similar to those adopted in the formation of natural complicated molecules including proteins. Initially, we focused on metal–acetylene π-coordination using conventional coordination elements such as nitrogen-containing heterocycles and oxygen donors (Fig. 1(a)). As summarized in our recent review [1], acetylene π-coordination frequently appears in small organometallic compounds and host-guest systems, but its binding energy is typically too weak for the stabilization of larger assemblies. Therefore, we discovered that the cooperative ability of acetylene π-coordination is applicable to the discrete self-assembly of complex nanostructures, supported by its high structural flexibility and diversity.

After the serendipitous discovery of the smallest $(M_3L_2)_2$ cage (M = Cu(I), Ag(I)), this method was extended to the construction of a series of polyhedral molecular cages $(M_3L_2)_n$ based on hierarchically oligomerized M_3L_2 subunits (n = 4,6) [2]. *Small-to-large* interconversion to a 5-nm-class cubic cage (n = 8, Mw: 18,768, except for the free counter anions) was developed by combining the current method with an anion-exchange protocol that strengthens the stability of the M_3L_2 subunit electrostatically capturing the nitrate anion (Fig. 1(b)) [3].

In this study, this strategy was applied to *large-to-large* interconversion of polyhedral cages [4]. After additional anion exchange of the $(Ag_3L_2)_8$ cube using tetrabutylammonium nitrate in a nitroimethane-d_3 solution, platelet crystals were experimentally obtained via a vapor-diffusion protocol at low temperature. We examined several types of protocols at SPring-8 **BL26B1** and **BL41XU** to realize single-crystal X-ray analysis of relatively fragile crystals, partly because of the large structure of the main framework providing porous regions inside and outside. Finally, helical scanning (~200 μm) of the platelet crystals introduced into a borosilicate glass capillary enabled us to obtain acceptable diffraction data on the reduction of radiation damage.

The obtained $Ag_{21}L_{12}$ cage (Mw: 14,585) was revealed to have the concave framework (~4.0 × 4.0 × 3.2 nm^3) topologically transformed from the $(M_3L_2)_6$ prism (Fig. 2(a)), which was also supported by ^{1}H, ^{13}C, 2D nuclear magnetic resonance spectroscopy (NMR) studies in solution and atomic force microscopy imaging. The numbers of vertices (v = 21), edges (e = 33), and faces (f = 14) followed Euler's polyhedron formula ($v - e + f = 2$), exhibiting a concave tetrakaidecahedral structure. Formally, this polyhedron was formed via the insertion of three nitrate–silver–nitrate triads into all three lateral edges of the truncated prism shape, as observed for the $(M_3L_2)_6$ prism. In addition, the structure of the $Ag_{13}L_8$ concave decahedron (v, e, f = 13, 21, 10), as a modified form of the $(M_3L_2)_4$ tetrahedron (Fig. 2(b)), was also determined by X-ray analysis by merging two diffraction data sets to compensate for the rapid degradation of the crystals.

Importantly, the current assemblies based on flexible cooperative acetylene coordination afforded a series of unprecedented 3D structural motifs (Fig. 3) that are related to emerging molecular entanglements [5]. First, the smallest $(M_3L_2)_2$ cage exhibited an entangled θ-shape topology composed of two interlocked (connected via acetylene coordination) cage-like components. Second, the $(M_3L_2)_n$ polyhedra (n = 4,6,8) included entangled motifs resembling a trefoil knot

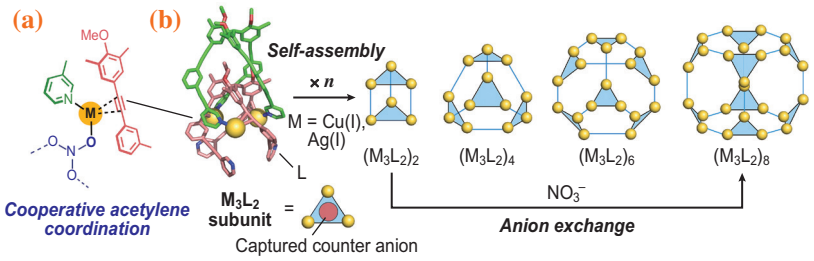

Fig. 1. **(a,b)** Self-assembly of the $(M_3L_2)_n$ polyhedral cages based on cooperative acetylene coordination.

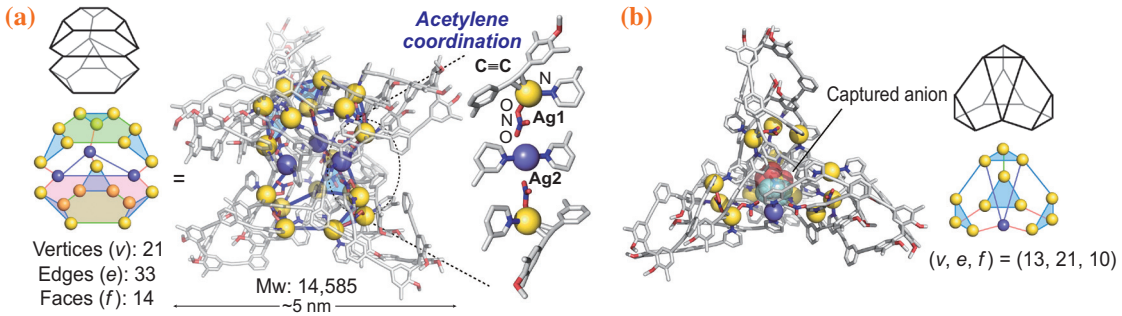

Fig. 2. Single crystal X-ray structures of **(a)** $Ag_{21}L_{12}$ and **(b)** $Ag_{13}L_8$ concave polyhedra.

and Solomon link, on each face of the polyhedra. Each assembly forms a complicated but well-ordered 3D structure (Fig. 3(a)) with an inner cavity capturing the anions and a topologically chiral character, which can be controlled by accumulating small chiral groups on its surface [1]. Furthermore, the current $Ag_{21}L_{12}$ and $Ag_{13}L_8$ cages also exhibit unique 'edited' structures: Solomon link-like motifs dissociated in the $Ag_{21}L_{12}$ framework, while its trefoil knot-like motifs are maintained (Figs. 3(b,c)). In addition, in $Ag_{13}L_8$, a trefoil motif dissociated during the maintenance of the three neighboring motifs (Fig. 3(d)). Such an interconversion may be applied as a prototype for the skeletal editing of large and complex polyhedral structures, inducing new properties and functions.

3D entanglements have recently attracted considerable attention, not only as substructures in some natural proteins, but also as fascinating motifs in artificial nano-to-macro-scale functional materials. The establishment of synthetic strategies is an essential step in the elucidation of potential physical and chemical properties for applications in stimuli-responsive molecular containers, molecular machines, and other hierarchically manufactured functional materials. We also emphasize that the precise design of future complex materials requires appropriate structural characterization utilizing emerging methodologies and techniques, including those offered by the next-generation facilities at SPring-8/SACLA.

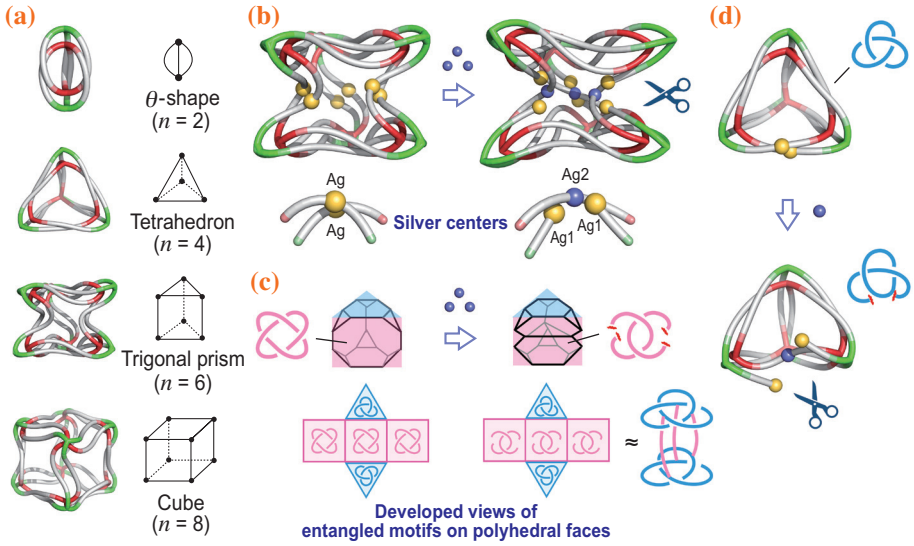

Fig. 3. **(a)** 3D entangled structures of the $(M_3L_2)_n$ cages (n = 2,4,6,8). Acetylene coordination connecting each component is omitted for clarity. **(b-d)** Partial modification of the entangled motifs in the $Ag_{21}L_{12}$ and $Ag_{13}L_8$ concave polyhedral frameworks.

Yuya Domoto[a,*] and Makoto Fujita[b,c]

[a] Division of Molecular Science, Gunma University
[b] Tokyo College, UTIAS, The University of Tokyo
[c] Division of Advanced Molecular Science, National Institutes of Natural Sciences

*Email: domoto@gunma-u.ac.jp

References

[1] Y. Domoto, M. Fujita: Coord. Chem. Rev. **466** (2022) 214605.
[2] Y. Domoto *et al.*: Angew. Chem. Int. Ed. **59** (2020) 3450.
[3] Y. Domoto *et al.*: J. Am. Chem. Soc. **143** (2021) 8578.
[4] *Y. Domoto, M. Abe, G. R. Genov, Z. Yu, M. Fujita: Angew. Chem. Int. Ed.* ***62*** *(2023) e202303714.*
[5] S. T. Hyde, M. E. Evans: Proc. Natl. Acad. Sci. USA **119** (2022) e2110345118.

Near-dimensionally invariable high-capacity positive electrode material

The development of high-capacity and long-life batteries is a key challenge for attaining a sustainable energy society. Lithium insertion materials are used as electrode materials in lithium-ion batteries. Reversible lithium extraction/re-insertion reactions with topotactic phase transitions have been achieved, coupled with cationic redox reactions of 3*d*-transition metal ions for these electrode materials [1]. Electrochemical lithium insertion/extraction generally alters the crystal structures of electrode materials, including volume changes, which induce strain. This leads to mechanical fractures, including the formation of cracks inside the particles. The fracture of lithium insertion materials due to mechanical strain results in the loss of electrical contacts in composite electrodes, and thus, a reduction in the reversible capacity during electrochemical cycles. Moreover, the electrode materials cannot be isolated in composite electrodes, which can be difficult to control, especially in the all-solid-state batteries that are currently being developed for advanced battery systems. Therefore, the discovery of materials that can reversibly insert/extract large quantities of charge carriers (Li^+), that is, high capacity, with inherent dimensional stability during cycles is indispensable.

In this study, lithium-excess vanadium oxides with disordered rock salt structures are examined as high-capacity and long-life positive electrode materials. X-ray diffraction data of as-prepared $Li_{8/7}Ti_{2/7}V_{4/7}O_2$ are shown in Fig. 1(a). The crystal structure of the sample was defined as a typical layered structure (space group; $R\bar{3}m$), which was isostructural with the $LiCoO_2$ and $LiNiO_2$ [2] used for practical lithium-ion batteries. However, the insufficient reversibility of the Li-storage properties in the as-prepared sample was noted; therefore, a nanosized material with a shorter Li-migration path in the host structures was prepared by mechanical milling. Material synthesis via mechanical milling typically results in the formation of nanosized materials with high symmetry, and cation disordered rock salt oxides (space group; $Fm\bar{3}m$) with low crystallinity can be obtained. In the case of $Li_{8/7}Ti_{2/7}V_{4/7}O_2$, the original layered structure was lost and a nanosized rock salt oxide with low crystallinity (<10 nm) was obtained after milling, as shown in Fig. 1(a). The nanosized sample showed a large reversible capacity of 300 mA·h·g^{-1} at room temperature (Fig. 1(b)) and delivered good capacity retention for the initial 20 cycles. However, an abrupt degradation in capacity retention was observed after 30 cycles (Fig. 1(c)) when 1 M $LiPF_6$ in ethylene carbonate and dimethyl carbonate (EC/DMC), a conventional electrolyte used for practical battery applications, was used as the electrolyte. In contrast, excellent capacity retention was attained using a concentrated electrolyte solution of lithium bis(fluorosulfonyl)amide (LiFSA) and dimethyl carbonate (DMC), LiFSA:DMC = 1:1.1 in molar ratio [3]. Additionally, a reversible capacity of >260 mA·h·g^{-1} was achieved after the 100-cycle test at 30 mA·g^{-1}, as shown in Figs. 1(b,c). The improved capacity retention with a concentrated electrolyte solution originated from the suppression of vanadium dissolution and deterioration of the metallic lithium electrode [4].

To further study the reaction mechanisms of nanosized $Li_{8/7-x}Ti_{2/7}V_{4/7}O_2$, the structural changes during the electrochemical cycles were examined using *in situ* XRD studies. *In situ* XRD data and changes in the 200 peak profiles are shown in Fig. 2. Although the peak height systematically decreased with charging, the peak position remained invariable during electrochemical cycling.

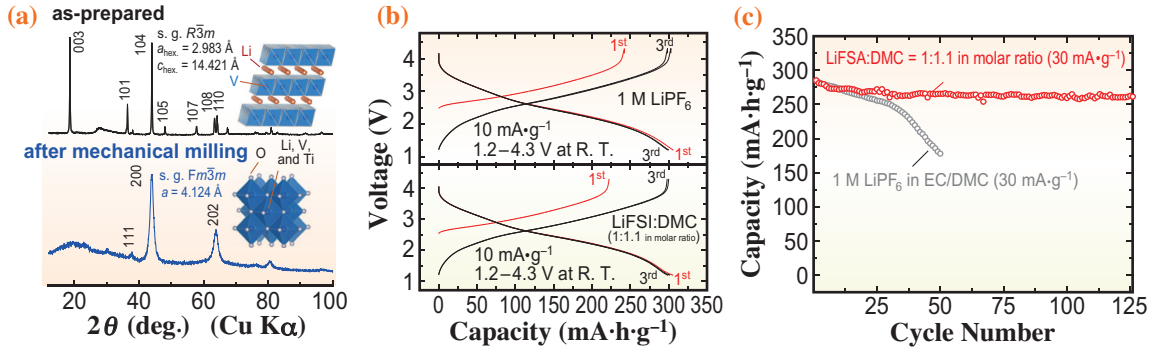

Fig.1. **(a)** XRD patterns of as-prepared and nanosized $Li_{8/7}Ti_{2/7}V_{4/7}O_2$. **(b,c)** Electrode performance of nanosized $Li_{8/7}Ti_{2/7}V_{4/7}O_2$ in different electrolyte solutions.

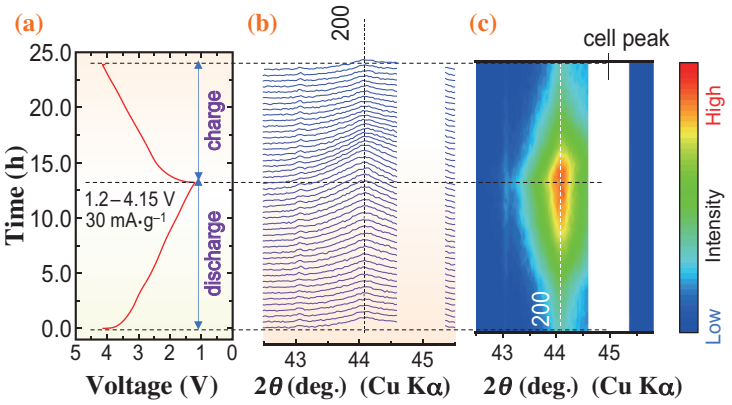

Fig. 2. **(a)** Charge/discharge curves of nanosized $Li_{8/7-x}Ti_{2/7}V_{4/7}O_2$ during *in situ* XRD measurement, **(b)** corresponding *in situ* XRD patterns for the 200 diffraction lines, and **(c)** a contour plot of XRD patterns.

Bulk and local structural changes in the nanosized $Li_{8/7-x}Ti_{2/7}V_{4/7}O_2$ during electrochemical cycling were also studied using high-energy X-ray total scattering (Fig. 3). The findings can be summarized as follows: (1) reversible V migration between octahedral and tetrahedral sites with cycling and (2) partial formation of the amorphous phase upon charging. Although V ions migrated into neighboring face-shared tetrahedral sites upon charging, these processes were reversible, and destruction of the phase was not observed [4].

In general, the unit cell volume of Li-insertion materials decreased upon charging because of the oxidation of transition-metal ions coupled with an increase in effective nuclear charge. The enrichment of vacant sites (an increase in free volume) also resulted in lattice contraction. However, the migration of cations, as observed in Fig. 3, strongly influenced the volume-change trend. The migration of V ions into smaller tetrahedral sites inevitably increased the repulsive interactions between V and O ions, resulting in the expansion of the crystal lattice. Such an expansion of the lattice would be partially canceled out by the volume decrease associated with the increase in the free volume by Li extraction as two competing factors. When shrinkage and expansion were well balanced, dimensional stability was retained, leading to a near-dimensionally invariable character, as observed in $Li_{8/7-x}Ti_{2/7}V_{4/7}O_2$. Furthermore, highly reversible Li storage for $Li_{8/7}Ti_{2/7}V_{4/7}O_2$ with no capacity fading over 400 cycles was achieved using a sulfide-based solid electrolyte [4]. This study demonstrates an example of an electrode/electrolyte couple that produces high-capacity and long-life batteries, including operation with solid electrolytes, associated with a unique structural phase transition, that is, invariant volume change during cycling.

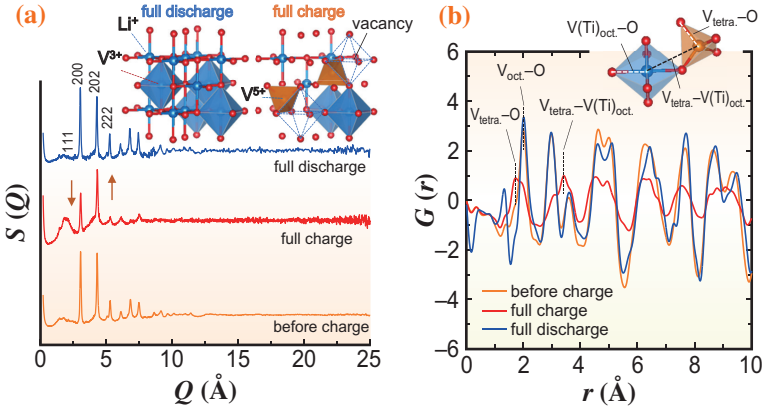

Fig. 3. **(a)** Structure factors of nanosized $Li_{8/7-x}Ti_{2/7}V_{4/7}O_2$ with different charging conditions using high-energy X-ray ($E = 61.4$ keV) at room temperature, from which **(b)** X-ray pair distribution functions were obtained. Schematic illustrations of crystal structures for charged and discharged $Li_{8/7-x}Ti_{2/7}V_{4/7}O_2$ are also shown. The synchrotron radiation experiments were performed at SPring-8 **BL04B2**.

Naoaki Yabuuchi[a,*], Satoshi Hiroi[b] and Koji Ohara[b]

[a] Department of Chemistry and Life Science, Yokohama National University
[b] Faculty of Materials for Energy, Shimane University

*Email: yabuuchi-naoaki-pw@ynu.ac.jp

References

[1] M. S. Whittingham: Chem. Rev. **114** (2014) 11414.
[2] N. Ikeda *et al.*: J. Mater. Chem. A **9** (2021) 15963.
[3] J. Wang *et al.*: Nat. Commun. **7** (2016) 12032.
[4] *I. Konuma, D. Goonetilleke, N. Sharma, T. Miyuki, S. Hiroi, K. Ohara, Y. Yamakawa, Y. Morino, H. B. Rajendra, T. Ishigaki, N. Yabuuchi: Nat. Mater.* ***22*** *(2023) 225.*

Catalytic properties of surface-exposed silver nanoclusters within a ring-shaped metal oxide

Noble-metal nanoclusters have attracted increasing interest in various fields owing to their unique properties that depend on their structures and electronic states. In addition, the exposed metal surfaces of metal nanoclusters provide a significant opportunity to impart unique catalytic properties. Silver (Ag) nanoclusters and nanoparticles supported on metal-oxide supports exhibit cooperative reactivity, leading to various catalytic molecular transformations [1]. However, the exposed reactive surfaces of metal nanoclusters can easily lead to undesirable agglomeration, hindering the development of structurally well-defined metal nanoclusters with exposed metal surfaces and/or interfaces.

Polyoxometalates (POMs) are anionic metal-oxide clusters with diverse structures and properties [2]. Recently, we developed a synthetic method for stable Ag nanoclusters using lacunary POMs, which acts as a stabilizing ligand owing to some deficient sites from the parent POM structure [3]. Due to the unique acidity/basicity, redox properties, and photochemical properties of POMs, POM-stabilized Ag nanoclusters have substantial potential in various applications that differ from those of nanoclusters stabilized by organic ligands or conventional metal-oxide supports. In this study, we utilized a rigid and bulky POM $[P_8W_{48}O_{184}]^{40-}$ (**P8W48**) with a cavity of ~1 nm in diameter for the sequential synthesis of surface-exposed Ag nanoclusters. This led to unprecedented catalytic properties owing to the exposed Ag surface and cooperative reactivity of Ag nanoclusters and POMs (Fig. 1) [4].

By reacting the tetra-*n*-butylammonium (TBA) salt of **P8W48** with silver acetate in acetone, 16 Ag^+ ions were accumulated within the cavity of **P8W48** to form **Ag16**. Then, we reacted **Ag16** with silver acetate in *N,N*-dimethylformamide as a solvent and a mild reducing reagent. The yellow reaction mixture turned brown, indicating the formation of Ag nanoclusters. X-ray crystallographic analysis was performed at SPring-8 **BL02B1** (λ = 0.4132 Å, 100 K), which revealed the formation of a $\{Ag_{30}\}$ nanocluster within the cavity of **P8W48** (**Ag30**), wherein 30 Ag atoms existed in a distorted body-centered cubic arrangement (Figs. 2(a,b)). Furthermore, by reacting **Ag30** with a reducing reagent (i.e., $TBABH_4$ or H_2 gas), another $\{Ag_{30}\}$ nanocluster was successfully obtained within the cavity of **P8W48** (**Ag30'**), wherein 26 of the 30 Ag atoms were arranged in a face-centered cubic structure (Figs. 2(c,d)). Elemental analysis, acid–base titration, and X-ray photoelectron spectroscopy showed

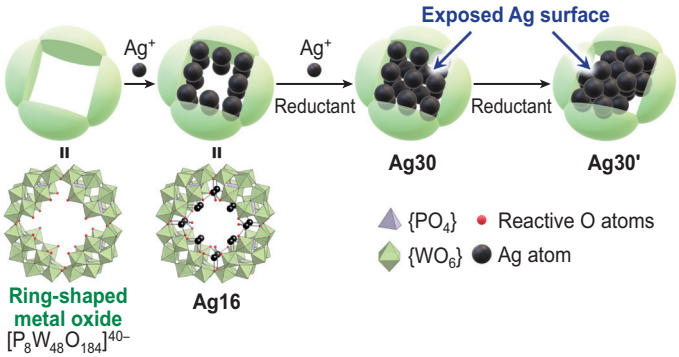

Fig. 1. Schematic of the sequential synthesis of surface-exposed Ag nanoclusters within ring-shaped POMs.

that the total charges of the $\{Ag_{30}\}$ nanoclusters of **Ag30** and **Ag30'** were +22 $\{Ag_{30}\}^{22+}$ and +16 $\{Ag_{30}\}^{16+}$, respectively. These results showed that the reduction of the $\{Ag_{30}\}^{22+}$ nanoclusters of **Ag30** led to the structural transformation of **Ag30** and **Ag30'**. Notably, both **Ag30** and **Ag30'** possessed exposed Ag surfaces at the apertures of the ring-shaped $\{P_8W_{48}\}$ framework, making them attractive molecular catalysts.

Ag30' exhibited excellent catalytic activity for the selective reduction of nitrobenzene to aniline using H_2 as a reductant under mild reaction conditions (60°C, 4 atm H_2 pressure) compared with the conditions using typical Ag catalysts on metal-oxide supports (>100°C, >10 atm H_2 pressure). However, the $\{Ag_{27}\}$ nanocluster

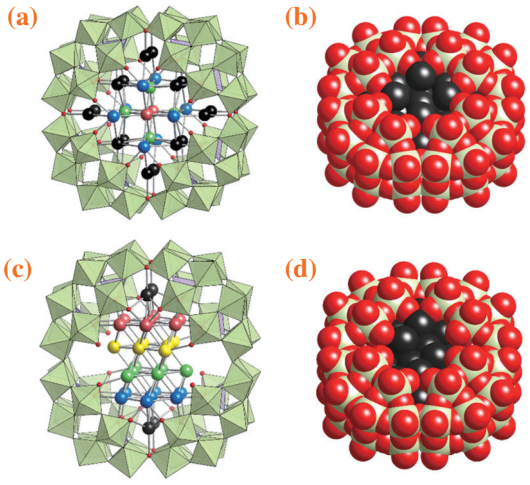

Fig. 2. Crystallographic structures of the anionic part of **(a,b) Ag30** (i.e., $[\{Ag_{30}\}^{22+}(P_8W_{48}O_{184})]^{18-}$) and **(c,d) Ag30'** (i.e., $[\{Ag_{30}\}^{16+}(P_8W_{48}O_{184})]^{24-}$) in the **(a,c)** polyhedral and **(b,d)** spacefill models. Green octahedron, $\{WO_6\}$; purple tetrahedron, $\{PO_4\}$; black, cyan, yellow, lime, and magenta balls, Ag atoms; red ball, oxygen atom.

completely covered by POMs[3] or polyvinylpyrrolidone (PVP)-coated Ag nanoparticles (Ag/PVP, 5 nm) hardly showed any catalytic activity. These results showed that the unique catalytic activity of **Ag30'** originated from its exposed Ag surface. Furthermore, this catalytic system could be applied to the selective reduction of various nitroarenes to their corresponding anilines (Fig. 3(b)). These results revealed the unique catalytic properties of **Ag30'**, which differ from those of typical Ag nanoparticle catalysts.

To further investigate the structure and electronic state of **Ag30'** after the catalytic reactions, we performed Ag *K*-edge X-ray absorption fine structure (XAFS) measurements at SPring-8 **BL01B1**. The *k*-space extended XAFS (EXAFS) oscillation pattern of **Ag30'** after the catalytic reaction showed no significant difference from that of **Ag30'** in the solid state, indicating that **Ag30'** maintained its structure during the catalytic reaction (Fig. 3(c)). Additionally, the X-ray absorption near-edge structure (XANES) spectrum of **Ag30'** after the catalytic reaction was compared with the XANES spectra of the original **Ag30'** and Ag foil, which showed that the $\{Ag_{30}\}$ nanocluster was further reduced due to its reaction with H_2 (Fig. 3(d)). Deuteride (D^-) species were not observed in the ^2H NMR study of the reaction solution of **Ag30'** and D_2 gas, revealing that a molecular H_2 dissociated into two protons and two electrons over **Ag30',** which were stored in the **P8W48** frameworks and $\{Ag_{30}\}$ nanoclusters of **Ag30'**, respectively.

In conclusion, we synthesized atomically precise $\{Ag_{30}\}$ nanoclusters within the cavity of a ring-shaped POM (i.e., $[P_8W_{48}O_{184}]^{40-}$), which possessed exposed Ag surfaces and interfaces with metal oxides. These $\{Ag_{30}\}$ nanoclusters exhibited high stability despite their exposed Ag surfaces, showing notable catalytic activity for the selective reduction of organic substrates using H_2 as a reductant under mild reaction conditions. We envisage that this method can be applied to the synthesis of various surface-exposed metal nanoclusters, which will promote investigations into the unique properties and applications of metal nanoclusters.

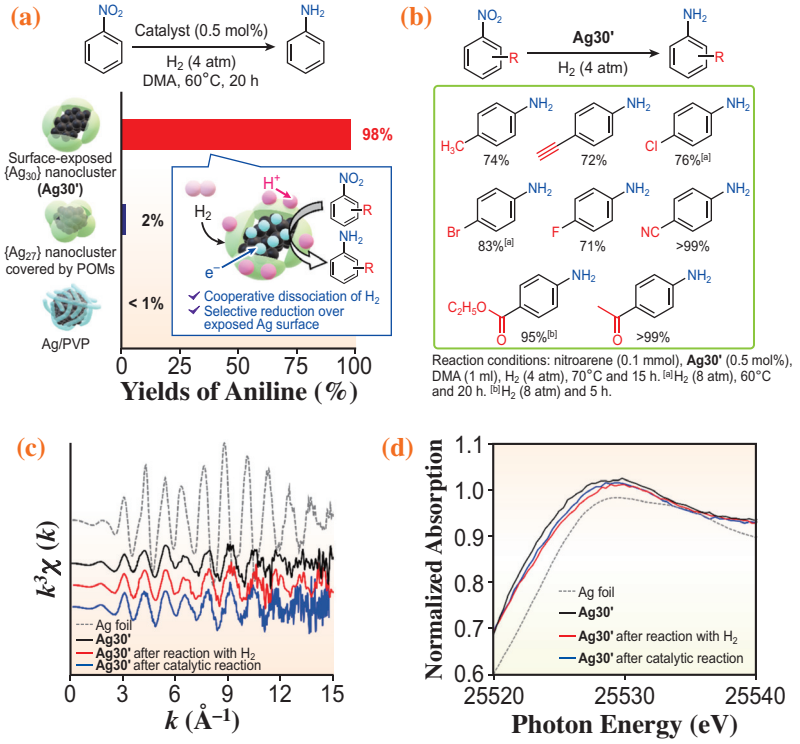

Fig. 3. **(a)** Catalytic activity and **(b)** substrate scope of the catalytic reduction of nitroarenes using **Ag30'**. **(c)** *k*-space EXAFS spectra and **(d)** XANES spectra of **Ag30'** before and after reacting with H_2 (4 atm, 60°C) in *N*,*N*-dimethylacetamide.

Kentaro Yonesato and Kosuke Suzuki*

Department of Applied Chemistry, The University of Tokyo

*Email: ksuzuki@appchem.t.u-tokyo.ac.jp

References

[1] X.-Y. Dong *et al.*: Catal. Sci. Technol. **5** (2015) 2554.
[2] M. T. Pope: Heteropoly and Isopoly Oxometalates (Springer, 1983).
[3] K. Yonesato *et al.*: J. Am. Chem. Soc. **141** (2019) 19550.
[4] *K. Yonesato, D. Yanai, S. Yamazoe, D. Yokogawa, T. Kikuchi, K. Yamaguchi, K. Suzuki: Nat. Chem.* ***15*** *(2023) 940.*

Mechanical properties and structures under the deformation of thiophene copolymers with cyclic siloxane units

Polymer-based electronic devices have attractive features such as low fabrication cost, low weight, and diverse form design. Controlling the mechanical modulus and elongation at break expands the utility of conjugated polymers when developing flexible and stretchable devices. Flexibility and stretchability are achieved in wearable devices that follow the stretching of the human skin with a low mechanical modulus, high elongation, and elastic recovery. However, because conjugated polymers consist of rigid aromatic rings, their fragility is a challenge. Researchers have focused on achieving flexibility in conjugated polymers using various approaches; for example, composites of rubber components and block copolymers with flexible segments have been proposed.

Although polythiophenes have garnered significant attention as semiconductive materials for hole transport, polythiophenes without side chains lack solubility in conventional organic solvents as well as processability using painting and heat-melting methods. Substitution of alkyl side chains into thiophene rings has been suggested in order to improve their solubility and processability, as well as to achieve higher electronic conductivities through self-assembly and crystallization involving side chains. Thus, we focused on the effects of polythiophene side chains and introduced flexible dimethylsiloxane groups into these side chains. We previously reported the flexibility of polythiophenes with disiloxane side chains [1].

Herein, we focus on random copolymers with 3-dodecyl-thiophene (3DDT) and thiophenes, including cyclic siloxanes, as flexible side chains (3CSiT or 3tetraCSiT), as shown in Fig. 1 [2]. Self-standing P(3DDT-3CSiT) films were prepared via the formation of cross-links. P(3DDT-3CSiT) films containing the acid generator TsOCH were prepared using a casting method. Acid_anneal and Acid_melt films were prepared under different thermal heating conditions. In contrast, the Melt_tetra films inherently possessed cross-linking points without any thermal treatment because the four-armed cross-linker unit 3tetraCSiT was involved in the polymerization process. A Melt_tetra film was also prepared by hot-pressing owing to the low solubility of P(3DDT-3tetraCSiT) in organic solvents. To compare the structural and mechanical properties, a Noacid film without the acid generator was also prepared.

The mechanical properties of the prepared polythiophene films were investigated via tensile tests. The strain-stress curves are shown in Fig. 2. Compared to P3DDT without cyclic siloxane moieties, the Young's modulus and tensile strength of the Noacid film decreased, whereas its strain at break reached 300%. The Noacid film exhibited crystallinity similar to that of P3DDT. Therefore, the higher strain at break can be attributed to the flexible cyclic siloxane side chains. Moreover, the formation of crosslinkers in the Acid_melt and Acid_anneal films provided larger modulus and lower strain at break than those of the Noacid films. The difference in crystallinity between the Acid_melt and Acid_anneal films caused the slightly larger modulus for the Acid_anneal films than for the Acid_melt films. The mechanical properties of the Melt_tetra film were similar to those of the Acid_anneal

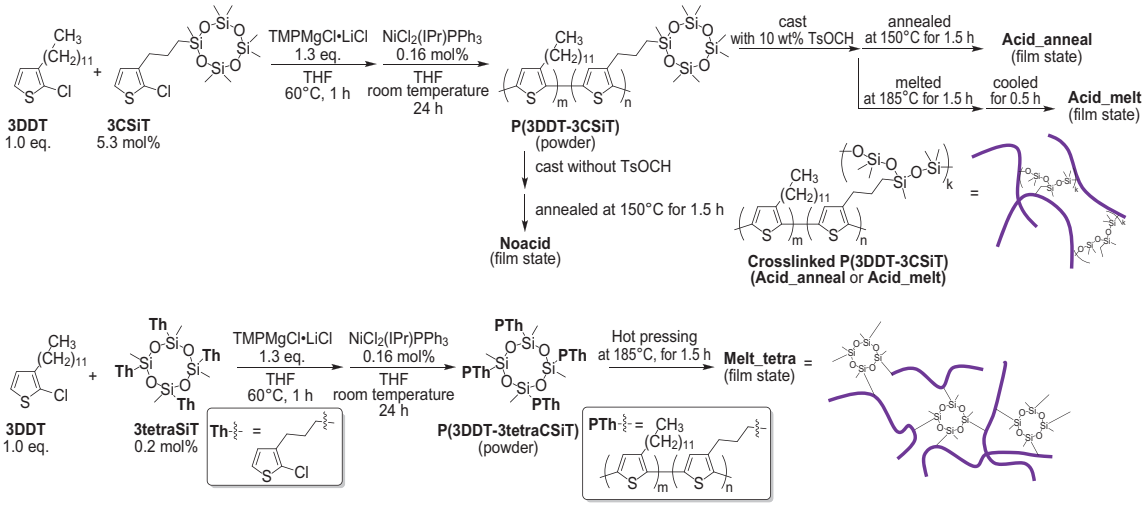

Fig. 1. Scheme of crosslinked polythiophenes syntheses.

and Acid_melt films due to the crosslinking of the tetra-substituted cyclic siloxane in the Melt_tetra film.

Cyclic tensile tests were performed to evaluate the elastic recovery of the cross-linked polythiophenes. The strain recovery ratio (R_{50}) was calculated from the strain values before and after unloading. The R_{50} values of the Noacid, Acid_anneal, and Acid_melt films were 80%, 87%, and 91%, respectively. The Acid_melt film exhibited the largest elastic recovery ratio because of its cross-linking and low crystallinity. The Acid_anneal film had a lower crystallinity than did the Acid_melt film, which enhances plastic deformation. In contrast, R_{50} for the Melt_tetra film was 84%, which was higher than that of the Noacid film and lower than those of the Acid_anneal and Acid_melt films.

Next, we focused on the effects of cross-linking on elastic recovery and structural deformation and performed X-ray diffraction measurements under cyclic tensile deformation using SPring-8 **BL03XU** [3]. The changes in the degree of crystallite orientation under loading and after unloading were analyzed using the diffraction of the (100) plane, as shown in Fig. 3. These measurements were performed for the Noacid, Acid_anneal, and Melt_tetra films because their crystallinities were sufficient to evaluate the crystallite orientation under deformation. For the films without stress, the diffraction of the (100) plane was observed as Debye-Scherrer rings at 0 MPa, as shown in Fig. 3(c). Thus, before stress was applied, the crystallites were randomly oriented. As the stress increased, the diffraction ring gradually changed to an arc in the meridian direction. Changes in the Hermann orientation degrees of the films are shown in Fig. 3(b). The crystallite orientation of the Noacid film increased when the loading strain was greater than 50% and decreased after unloading. However, for strains of less than 50%, the orientation gradually increased through repeated loading and unloading. The degree of orientation did not decrease after unloading. These results suggest that when the Noacid film was drawn, the film involved necking, and yielding deformations occurred under strains less than 50%. In addition, after the necking was completed, the film was drawn homogeneously after elongation at a strain greater than 50%. Therefore, the correlation between the strain and the orientation degree of the Noacid film was linear at strain values larger than 50%. The orientation degrees of the Acid_anneal film with high crystallinity and cross-links exhibited the highest repeatability with loading strains, as shown in Fig. 3. For the Melt_tetra film, the orientation degree of the crystallites exhibited higher repeatability when the strain was less than 40% compared with that of the Noacid film. However, the orientation degrees at strains greater than 40% were dispersed because of localized deformation under loading strain. These results coincide with the degree of cross-linking of the tetra-substituted cyclic siloxane moieties.

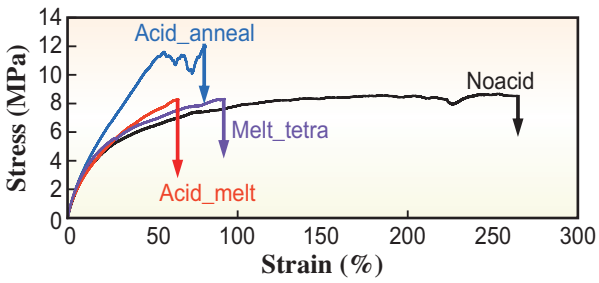

Fig. 2. Stress-strain curves of synthesized thiophene copolymers.

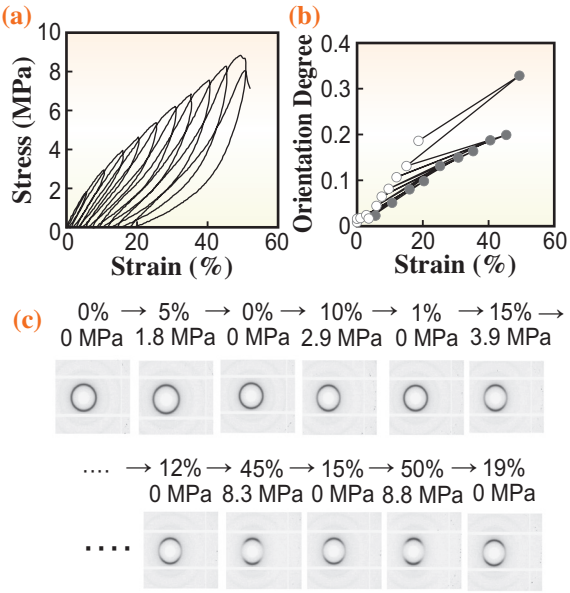

Fig. 3. **(a)** Stress-strain curves, **(b)** orientation degrees, **(c)** 2D X-ray diffraction images of Acid_anneal in *in situ* X-ray diffraction pattern measurements under cyclic tensile tests.

Takuya Matsumoto* and Takashi Nishino

Department of Chemical Science & Engineering,
Kobe University

*Email: matsumoto0521@person.kobe-u.ac.jp

References

[1] J. Shen *et al.*: Macromol. Chem. Phys. **218** (2017) 1700197.
[2] *T. Matsumoto, M. Kashimoto, C. Kubota, S. Horike, K. Ishida, A. Mori and T. Nishino: Polym. Chem. **13** (2022) 5536.*
[3] H. Masunaga *et al.*: Polym. J. **43** (2011) 471.

Direct observation of hydration and dehydration behaviors of poly(*N*-isopropylacrylamide) on silica beads through infrared spectroscopy

Stimuli-responsive polymers have attracted attention for several decades as functional materials in the field of materials chemistry. In particular, poly(*N*-isopropylacrylamide) (PNIPAAm) has been extensively studied owing to its remarkable temperature-dependent hydrophobicity and conformational alterations. PNIPAAm exhibits hydration and dehydration phenomena below and above its lower critical solution temperature (LCST) of 32°C, resulting in a conformational transition, referred to as the coil-globule transition (Fig. 1(a)). This transition induces expansion and contraction of the PNIPAAm chain. These thermally modulated modifications of the properties of PNIPAAm have significant applications in various biomedical fields, such as temperature-modulated bioseparation induced by temperature-modulated hydrophobic interactions (Fig. 1(b)) [1,2].

To investigate the PNIPAAm hydration behavior, infrared (IR) spectroscopy has proven to be a highly effective approach for examining the chemical environment of PNIPAAm functional groups. Changes in the amide bands of the IR spectrum during heating provided valuable insights into the variations in hydrogen bonding between the C=O and N–H bonds. Furthermore, the presence of hydrogen bonds between most carbonyl groups and water molecules in the hydrated coiled state at low temperatures, as well as the formation of intrachain and interchain cross-linkages through hydrogen bonding between C=O and N–H groups in the dehydrated globular state at high temperatures, can be inferred from IR spectroscopy. However, characterizing grafted PNIPAAm on base materials presents challenges compared to PNIPAAm in aqueous solution or bulk form because of the relatively small amount of grafted PNIPAAm compared to the base materials, resulting in weak signals from the grafted PNIPAAm.

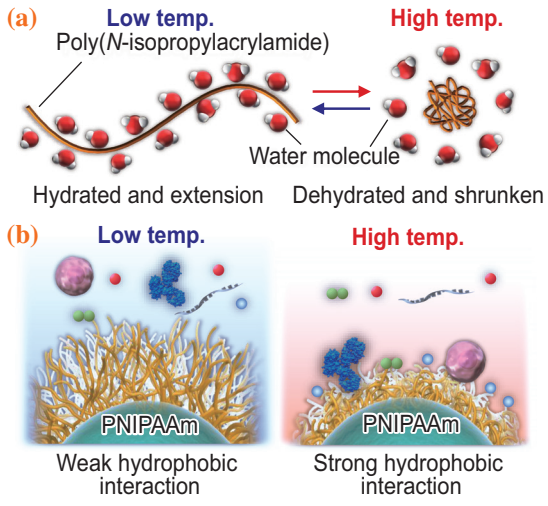

Fig. 1. Thermoresponsive polymer poly(*N*-isopropylacrylamide) and its application in temperature-responsive chromatography. **(a)** Thermoresponsive polymer PNIPAAm properties. **(b)** Concept of temperature modulated bio-separation using PNIPAAm with temperature-modulated hydrophobic interaction.

To address this issue, IR spectroscopy was performed at the IR beamline, SPring-8 **BL43IR**. The high brilliance of infrared synchrotron radiation is an advantage of SPring-8, and its ability to focus light on small areas using an infrared microscope can be applied to BL43IR. PNIPAAm modified silica beads were prepared by silane coupling reaction for modifying the atom transfer radical polymerization (ATRP) initiator on silica beads and subsequent of ATRP of PNIPAAm [3]. The hydration behavior of the PNIPAAm brush on the silica beads with changes in relative humidity and temperature was observed by IR spectroscopy of the IR beamline BL43IR at the SPring-8 synchrotron facility [3].

The FT-IR spectrum of the grafted PNIPAAm on the silica beads was observed by changing the humidity at 10°C to investigate the hydration behavior of PNIPAAm (Fig. 2). The height of the broad peak increased with increasing relative humidity (Fig. 2(a)). This broad peak was attributed to the O–H stretching of the water molecules. Generally, PNIPAAm hydrates at 10°C; thus, the grafted PNIPAAm on silica beads absorbed water molecules from humidified air, resulting in an increased absorbance at 3700–3000 cm^{-1} with higher relative humidity.

We investigated the changes in the FT-IR spectrum containing the peaks of the amide I and II bonds as the relative humidity varied (Fig. 2(b)). The PNIPAAm-grafted beads exhibited peak shifts with increasing relative humidity. In particular, with increasing relative humidity, the amide I and II peaks, attributed to C=O stretching and N–H bending vibrations, shifted to lower and higher frequencies, respectively. These peak shifts were attributed to the hydration of PNIPAAm. The C=O of PNIPAAm forms hydrogen bonds with the neighboring N–H and water. Thus, C=O acts as an acceptor of hydrogen bonds. On the contrary, the N–H group acts as a hydrogen bond donor. With increasing relative humidity, the quantity of water surrounding PNIPAAm increased, resulting in an increased number

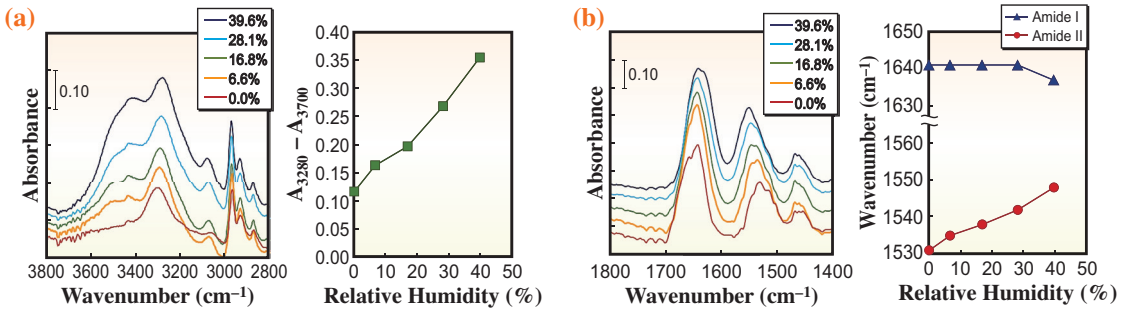

Fig. 2. FT-IR spectrum of the prepared PNIPAAm-grafted beads at a relative humidity of 10°C, **(a)** showcasing the absorbance difference ($A_{3280}-A_{3700}$) and **(b)** the peak shifts of amide I and II with changing temperature.

of hydrogen bonds within the PNIPAAm amide bond. Consequently, amide I (C=O) and amide II (N–H) experienced shifts toward lower and higher frequencies, respectively, indicating the hydration of PNIPAAm owing to elevated humidity levels.

Temperature-dependent IR spectral changes were observed at a relative humidity of 39.9% (Fig. 3). A significant change in the IR spectrum with temperature was observed at 3700–3000 cm^{-1} and 1800–1400 cm^{-1} (Fig. 3(a)). At 3700–3000 cm^{-1}, the intensity of the broad peaks decreased with increasing temperature because of temperature-dependent hydration and dehydration. With increasing temperature, PNIPAAm was dehydrated, significantly changing the IR spectrum from 3700 to 3000 cm^{-1}.

A notable shift in the peaks corresponding to amide I and II was observed between 1800 to 1400 cm^{-1} as the temperature increased (Fig. 3(b)). This shift was attributed to the temperature-dependent formation of hydrogen bonds involving the carbonyl bonds of PNIPAAm, particularly at relatively high humidity levels. At 10°C, PNIPAAm formed hydrogen bonds with water. The C=O group of PNIPAAm formed hydrogen bonds with both water molecules and adjacent N–H groups, resulting in a shift toward lower frequencies in the amide I peak. In contrast, the N–H group formed hydrogen bonds with water, and the number of hydrogen bonds decreased with increasing temperature. Thus, the amide II peak shifts to a higher frequency with increasing temperature. Additionally, conformational changes in PNIPAAm induce temperature influence the C–N stretching vibrations of amide II. Increasing the temperature caused a significant peak shift for amides I and II.

These results suggest that the hydration and dehydration behaviors of the grafted PNIPAAm on the silica beads can be observed using FT-IR spectrometry by controlling the humidity and temperature. These findings have practical applications for the design of biomedical materials utilizing PNIPAAm.

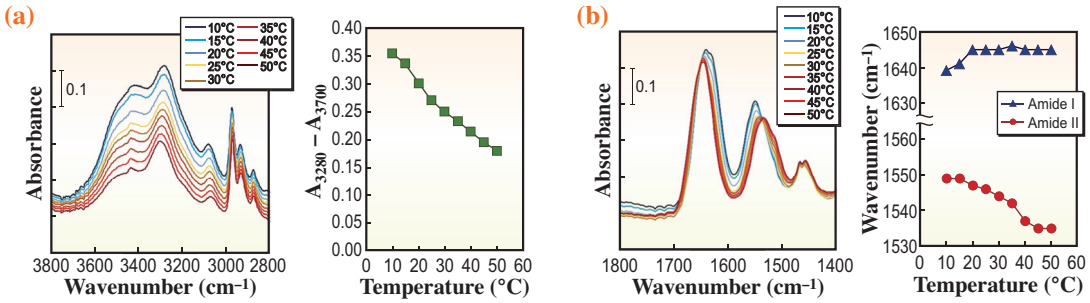

Fig. 3. FT-IR spectrum of the prepared PNIPAAm-grafted beads at various temperature at relative humidity of 39.9%, **(a)** showcasing the absorbance difference ($A_{3280}-A_{3700}$) and **(b)** the peak shifts of amide I and II with changing temperature.

Kenichi Nagase[a,b]

[a] Graduate School of Biomedical and Health Sciences, Hiroshima University
[b] Faculty of Pharmacy, Keio University

Email: nagase@hiroshima-u.ac.jp

References

[1] K. Nagase *et al.*: Biomaterials **153** (2018) 27.
[2] K. Nagase: Adv. Colloid Interface Sci. **295** (2021) 102487.
[3] *K. Nagase, J. Matsuda, A. Takeuchi, Y. Ikemoto: Surf. Interfaces* ***40*** *(2023) 103058.*

Curved post-garnet phase boundary and its implications for mantle dynamics

Recent seismic tomography studies have revealed that slabs stagnate at 660–1000 km depths in many subduction zones [1] and that plumes from the lowermost mantle become invisible at a depth above 1000 km [2]. One explanation for this is that a phase transition below the 660-km discontinuity decelerates slab subduction and accelerates plume upwelling in the upper part of the lower mantle. To achieve this, the sign of the Clapeyron slope must change with temperature because a positive Clapeyron slope enhances mantle convection (plume acceleration), whereas a negative slope impedes it (slab stagnation).

Garnet, a major mantle mineral, transforms into a bridgmanite-bearing assemblage at a depth of ~700 km. This is called the post-garnet transition and only occurs in the upper part of the lower mantle. Thus, determining the Clapeyron slope of the post-garnet transition is essential for understanding the dynamics of the upper part of the lower mantle.

The most accurate and precise method to determine the Clapeyron slope of a mineral phase transition is *in situ* X-ray diffraction with a multianvil press. Our recent studies highlighted two potential problems in accurately and precisely determining phase boundaries, namely the pressure change during heating and the sluggish kinetics of the investigated phase transitions [3,4]. An inevitable rapid pressure change upon heating hampers the accurate determination of the transition pressures. Although phase stability must be determined by observing pairs of normal and reversed reactions, this has not been confirmed in most previous studies. Thus, most previous studies have misinterpreted the phase relationships.

In this study, we have rigorously determined the boundary of the post-garnet transition in $Mg_3Al_2Si_3O_{12}$ (pyrope to bridgmanite+corundum transition), a major component of garnet, was determined using multianvil techniques combined with *in situ* X-ray diffraction using the Kawai-type multianvil press SPEED-Mk.II at SPring-8 **BL04B1** [5]. The strategy for establishing the phase boundary was as follows: (1) phase stability was continuously determined from the lowest temperature applied after sufficient annealing to release most deviatoric stresses, avoiding substantial pressure changes during phase identification; (2) the low- (pyrope) and high-pressure (bridgmanite + corundum) phases always coexisted during the experiments to monitor the direction of the reaction; and (3) the peak intensity change with time was monitored using X-ray diffraction patterns of the sample taken under the same conditions to identify a stable phase (Fig. 1). These experimental treatments resulted in a precise and accurate phase identification without rapid pressure changes or sluggish kinetics.

The phase relations in the $Mg_3Al_2Si_3O_{12}$ system were determined at 25.5–26.5 GPa and 1350–2100 K (Fig. 2). The transition pressure changed nonlinearly with increasing temperature, resulting in a downward boundary shape. The Clapeyron slope

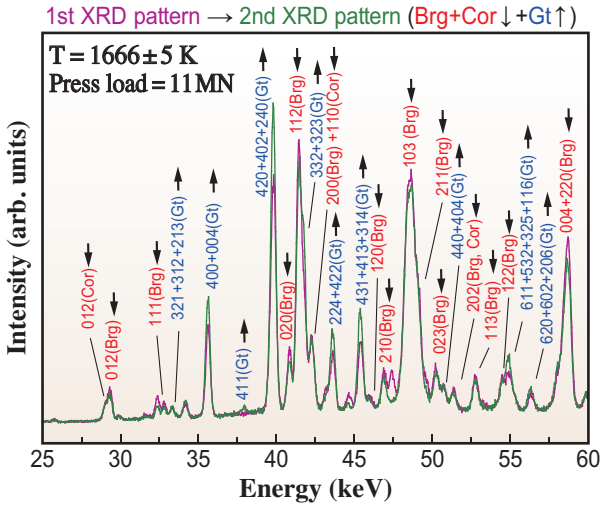

Fig. 1. An example of the accurate determination of phase stability between garnet (Gt) and bridgmanite (Brg) plus corundum (Cor) at 25.93(5) GPa and 1666 K. The Gt peaks are stronger in the second diffraction (green) than in the first (purple), whereas those of Brg and Cor are weaker, indicating that Gt is stable.

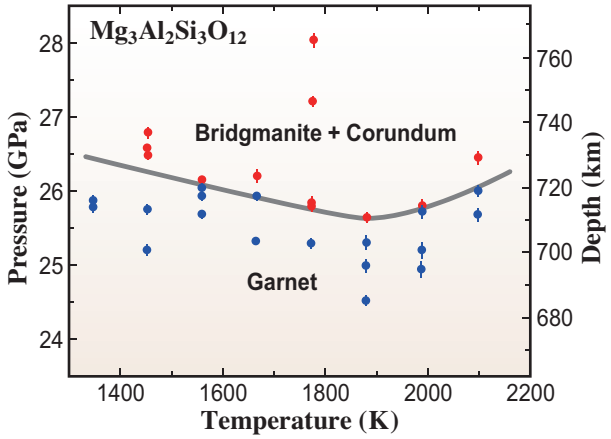

Fig. 2. Phase relations of the post-garnet transition in $Mg_3Al_2Si_3O_{12}$. The blue and red circles indicate the stable phases of garnet and bridgmanite plus corundum, respectively.

had a negative value of –1.5 MPa/K at 1400–1800 K, and a positive value of +2.5 MPa/K at 1900–2100 K. A change in the slope from positive to negative was first discovered during the phase transitions of mantle minerals. The Clapeyron slope is defined as the ratio of the entropy change (ΔS_{tr}) to the volume change (ΔV_{tr}) associated with the phase transition: $dP/dT = \Delta S_{tr}/\Delta V_{tr}$. As ΔV_{tr} is negative and only changes slightly with temperature, ΔS_{tr} is essential in forming the nonlinear boundary. Based on previously reported heat capacity data, we proposed an increase in the pyrope heat capacity at >1300 K. This can be explained by the possible disorder among the crystallographic sites in the $^{VIII}Mg_3{}^{VI}Al_2{}^{IV}Si_3O_{12}$ pyrope, as in the $^{VIII}Mg_3{}^{VI}[Mg,Si]^{IV}Si_3O_{12}$ majorite.

The curved post-garnet boundary explains the dynamics in the upper part of the lower mantle. In a cold subducting region, the post-garnet boundary has a negative slope (Fig. 3), which could stagnate a slab or decelerate the slab motion after crossing the 660-km discontinuity. This may result in a tomographic snapshot of the apparent slab stagnation below the 660-km discontinuity [1]. Slabs stagnating below the 660-km discontinuity are further promoted to subduct into deeper regions after being heated by the surrounding mantle because the Clapeyron slope of the post-garnet transition approaches zero with an increase in the average temperature (Fig. 3). In a hot upwelling region, the post-garnet boundary has a positive slope, which can accelerate plume upwelling (Fig. 3), resulting in plume thinning and reduced visibility in seismic tomography. This scenario may explain why tomographic images show indistinct plume traces below a depth of 1000 km [2]. The two types of seismic observations of slab stagnation and plume upwelling can be consistently interpreted based on the curved boundary of the post-garnet transition.

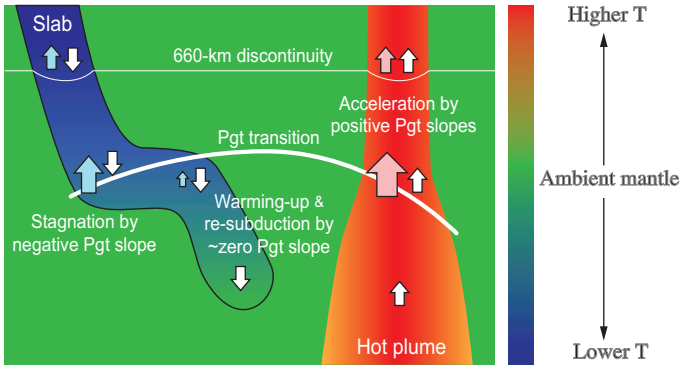

Fig. 3. Mantle dynamics in the upper part of the lower mantle controlled by phase transitions. The bold solid line is the post-garnet (Pgt) transition boundary determined in this study. Blue arrows show the positive buoyancies in a slab caused by the negative slopes of the post-spinel and Pgt transitions. Pink arrows indicate the positive buoyancies in a plume by the positive slopes of the Pgt transition. The main phase transition in a plume around a depth of 660-km is the Pgt transition. The arrow sizes express buoyancy magnitudes.

Takayuki Ishii[a,*] and Tomoo Katsura[b]

[a] Institute for Planetary Materials, Okayama University
[b] Bayerisches Geoinstitut, University of Bayreuth, Germany

*Email: takayuki.ishii@okayama-u.ac.jp

References

[1] Y. Fukao and M. Obayashi: J. Geophys. Res. Solid Earth **118** (2013) 5920.
[2] M. L. Rudolph *et al.*: Science **350** (2015) 1349.
[3] T. Ishii *et al.*: Nat. Geosci. **12** (2019) 869.
[4] A. Chanyshev *et al.*: Nature **601** (2022) 69.
[5] *T. Ishii, D. J. Frost, E. J. Kim, A. Chanyshev, K. Nishida, B. Wang, R. Ban, J. Xu, J. Liu, X. Su, Y. Higo, Y. Tange, H.-K. Mao and T. Katsura: Nat. Geosci.* ***16*** *(2023) 828.*

Measuring the electrical resistivity of liquid iron to 1.4 Mbar

Molten iron (Fe) is the dominant component of terrestrial cores, and its electrical and thermal conductivities control the dynamics and evolution of terrestrial bodies. Numerous theoretical predictions have been made regarding the electrical and magnetic properties of dense liquid Fe. However, experimental data on the electrical resistivity (the inverse of the electrical conductivity) of liquid Fe at high pressures are sparse compared to those on solid phases (e.g., [1]). Because of the high fluidity and chemical reactivity of molten Fe, it is difficult to conduct experiments in a high-pressure apparatus while maintaining the geometry and purity of the Fe sample. The resistivity of liquid Fe can currently be found in experimental data up to 51 GPa and 2900 K [1], although the pressure-temperature (*P*–*T*) conditions and data accuracy are not sufficient.

In this study [2], we determined the electrical resistivity of liquid Fe in the pressure range 42–135 GPa using a diamond anvil cell (DAC) combined with two novel techniques. The first, called the sapphire capsule method, is a resistance measurement technique for a liquid Fe sample encapsulated by a sapphire single crystal in a DAC combined with a laser and an internal resistance hybrid heating system. This technique aims to keep the geometry of the Fe sample unchanged during melting and minimize the temperature gradient inside the sample. The instantaneous resistance detection method (Fig. 1) seeks to detect the liquid Fe resistance prior to sample geometry changes by simultaneously measuring the electrical resistance, temperature, and X-ray diffraction (XRD) of Fe melted instantaneously via a single high-power laser shot. A total of nine separate runs using either of these methods were performed at SPring-8 **BL10XU**.

The sapphire capsule method was used in three separate runs conducted at approximately 40 GPa and 70 GPa. In a run, we compressed the sapphire-encapsulated Fe sample to 44 GPa at 300 K and then performed simultaneous high *P*–*T* resistance and XRD measurements to determine melting conditions. At the melting temperature of 2460 K at about 40 GPa, the resistance jump across melting was 21.7%. After temperature quenching, the sample resistance showed the same value as that before heating, and no additional XRD peaks other than those of Fe and sapphire were detected. Importantly, we did not observe any changes in the sample geometry under a microscope after melting. These facts guarantee that

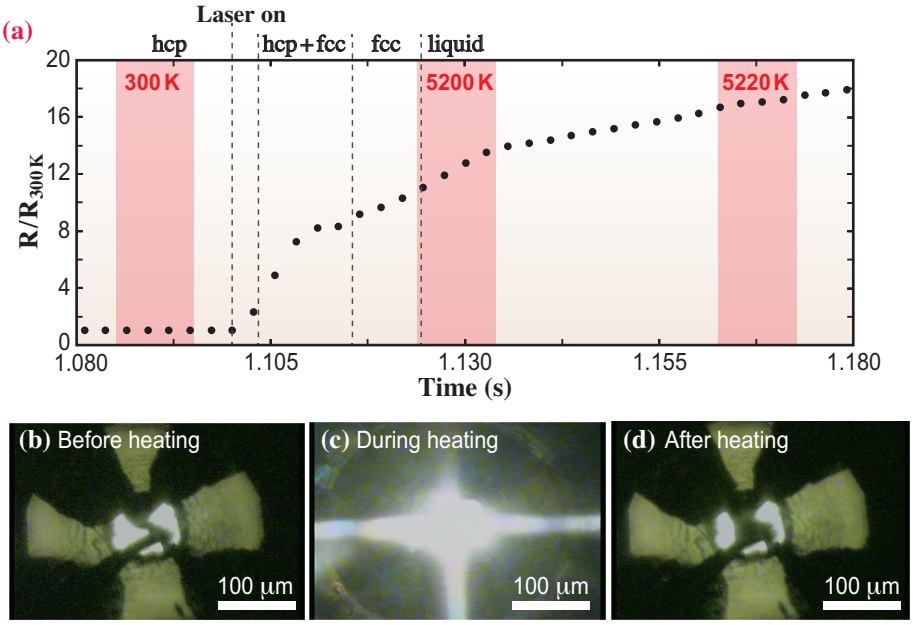

Fig. 1. Instantaneous resistance detection method: **(a)** Representative time (*t*) series of temperature and normalized resistance data obtained in a run, in which the maximum *P*–*T* condition was 107 GPa and 5200 K. The Fe phase(s) is/are identified from XRD measurements every 1 ms. Red rectangles indicate time windows for temperature measurements with 10 ms of exposure time. **(b)-(d)** Photos of a sample chamber viewed through a diamond anvil before, during, and after laser heating.

there was no change in the sample geometry during melting and no chemical contamination from the surroundings during the heating experiment.

An instantaneous resistance detection method was used to perform six separate runs at 135 GPa. The core of this method is high-speed simultaneous measurements of XRD in 1 ms, sample resistance in 2.25 ms, and temperature in 10 ms. Double-sided laser heating was used to melt the Fe sample during the synchronized data acquisition. Figure 1 shows the representative experimental data for which we started heating at 61 GPa. High-power laser shot heating began approximately 1.102 s after the start of synchronized data acquisition, resulting in *P*–*T* conditions of 105 GPa and 5200 K at t = 1.125 s, which are much higher than the melting point of Fe (Fig. 1(a)). The measured resistance responded to temperature changes by turning the laser beam on: a jump in the resistance at the beginning of heating (t > 1.102 s) and a gradual increase during melting (t > 1.125 s). We confirmed Fe melting by the disappearance of the XRD peaks of Fe at t = 1.125 s and simultaneously obtained its resistance at the same time. We considered these resistance data as the resistance of liquid Fe at 105 GPa and 5200 K, considering that the sample deformation and chemical reaction had not yet occurred at this time. The sample geometry changed after laser heating for approximately 3 s (Figs. 1(b-d)). Similar to the aforementioned run, we obtained the electrical resistance of liquid Fe within 1 ms of melting at 42, 49, 65, 79, and 135 GPa.

The obtained liquid Fe resistance data are converted to its high *P*–*T* resistivity, which provides the experimentally constrained resistivity of liquid Fe to more than two times higher pressures than in previous experiments (Fig. 2). For Mars and smaller terrestrial bodies in our solar system, the resistivity of liquid Fe at their core conditions is about 120 μΩ·cm, which is the lower limit of the core resistivity (note that the cores should contain some impurity elements that increase the resistivity). On the other hand, for the Earth and probably Venus, the lower limit of their liquid core resistivity is less than 80 μΩ·cm. Such a nonlinear pressure dependence on the resistivity of liquid Fe must be considered when estimating the conductivity of planetary metallic cores.

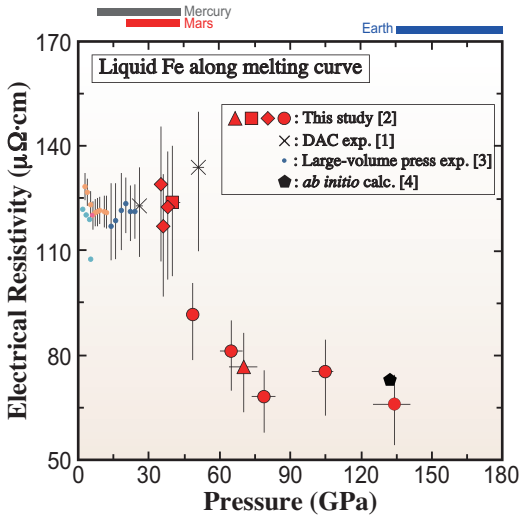

Fig. 2. The resistivity of liquid Fe along the melting curve. Red symbols represent values from this study [2], smaller circles depict the experimentally determined resistivities of liquid Fe in a large volume press [3], crosses indicate data from our previous study [1], pentagon indicate data from an *ab initio* calculation [4]. Color bars at the top of the figure show the pressure ranges of the cores of the Earth, Mars, and Mercury.

Kenji Ohta

Department of Earth and Planetary Sciences,
Tokyo Institute of Technology

Email: k-ohta@geo.titech.ac.jp

References

[1] K. Ohta *et al.*: Nature **534** (2016) 95.
[2] *K. Ohta, S. Suehiro, S. I. Kawaguchi, Y. Okuda, T. Wakamatsu, K. Hirose, Y. Ohishi, M. Kodama, S. Hirai, S. Azuma: Phys. Rev. Lett.* ***130*** *(2023) 266301.*
[3] W. Yong *et al.*: Geophys. Res. Lett. **46** (2019) 11065.
[4] J.-A. Korell *et al.*: Phys. Rev. Lett. **122** (2019) 086601.

Fe^{3+}-rich oxidizing magma formed by Fe^{2+} redox disproportionation under high pressure

The valence state of iron oxides (Fe^{2+} and Fe^{3+}) in the mantle of terrestrial planets significantly affects the oxidation state of the mantle. This is because iron is the most abundant multi-valence state element in the mantle of terrestrial planets. Oxygen fugacity is controlled by the exchange reaction between Fe^{2+} and Fe^{3+} (i.e., $2FeO + O_2 = Fe_2O_3$); therefore, the valence state of the iron oxides determines the oxidation state of the mantle. Because volcanic gas compositions change substantially depending on the oxidation state of the mantle, constraining the valence state of iron oxides in the mantle is a quite important issue for understanding the atmospheric composition of terrestrial planets and perhaps planetary habitability.

Previous geological constraints on the oxidation state of the Earth's mantle inferred from the Ce anomaly of zircons suggest that the Earth's mantle was already oxidized close to the present level 4 billion years ago [1]. This has been profoundly challenging to the canonical model of the oxidation state of the early Earth's mantle because of the equilibration between the metallic core and the silicate mantle during its formation. The redox disproportionation of Fe^{2+} in a molten mantle (hereafter magma ocean) under high pressures has been proposed to explain the oxidation of the early Earth's mantle [2]. This mechanism produces Fe^{3+} and metallic iron (Fe^0) from Fe^{2+} (i.e., $3Fe^{2+} \rightarrow 2Fe^{3+} + Fe^0$). After removing Fe^0 from the metallic core, the $Fe^{3+}/(Fe^{2+} + Fe^{3+})$ ratio of the magma ocean increases and becomes more oxidizing than in the initial state. The redox disproportionation of Fe^{2+} in silicate melts was recently confirmed at pressures above 10 GPa [3]. However, determining the $Fe^{3+}/(Fe^{2+} + Fe^{3+})$ ratio of silicate melt equilibrating with metallic iron under the Earth's magma ocean conditions (peridotitic melt under high-pressure conditions >27 GPa) remains unconstrained and technically challenging due to its high-liquidus (completely molten) temperatures (>2400°C).

We optimized the cell assembly for high-pressure melting experiments and successfully melted peridotite samples under metal-saturated conditions up to 28 GPa [4] (Fig. 1). The $Fe^{3+}/(Fe^{2+} + Fe^{3+})$ ratio of the silicate portion of the recovered samples was determined using X-ray absorption near-edge structure (XANES) measurements at SPring-8 **BL27SU**. The XANES spectra of the quenched samples showed a remarkable change at pressures between 15 and 28 GPa (Fig. 2), suggesting that the $Fe^{3+}/(Fe^{2+} + Fe^{3+})$ ratio changes significantly under different pressure conditions. We found that the calculated $Fe^{3+}/(Fe^{2+} + Fe^{3+})$ ratio of the quenched silicate melts from the XANES spectra increased from 0.13 to 0.52 with pressure (Fig. 3). These values are approximately one order of magnitude higher than the $Fe^{3+}/(Fe^{2+} + Fe^{3+})$ ratio of the Earth's upper mantle. These results suggest that the surface of the Earth's magma ocean after removing metallic iron into the core should be highly oxidizing, perhaps more than in the present state.

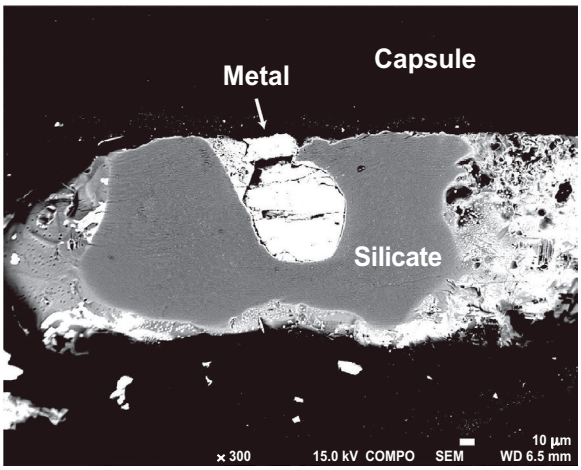

Fig. 1. The back-scattered electron image of the quenched sample at 28 GPa and 2600°C. The spheric metal surrounded by silicate indicates both phases were completely molten.

The oxidation state of the surface of the Earth's magma ocean having an $Fe^{3+}/(Fe^{2+} + Fe^{3+})$ ratio of 0.2–0.5 would have created highly oxidizing conditions, more so than at present. However, the estimated oxygen fugacity of such a magma ocean around 4–7 log-units above the iron-wüstite buffer is partially consistent with those estimated for the Earth's upper mantle 4.0–4.4 billion years ago based on zircon records [1] within their analytical uncertainties. To explain the discrepancy in the oxidation state between the magma ocean and the present Earth's upper mantle, we propose that metallic iron in late accreting impactors after the formation of the Earth may have reduced the Earth's mantle [4].

The positive relationship between the pressure and redox disproportionation of Fe^{2+} in the magma provides another unique insight into the origin of the difference in the oxidation states of terrestrial planets and their atmospheric compositions, particularly during their formation. More specifically, Moon- or Mars-sized rocky bodies may have a relatively reduced

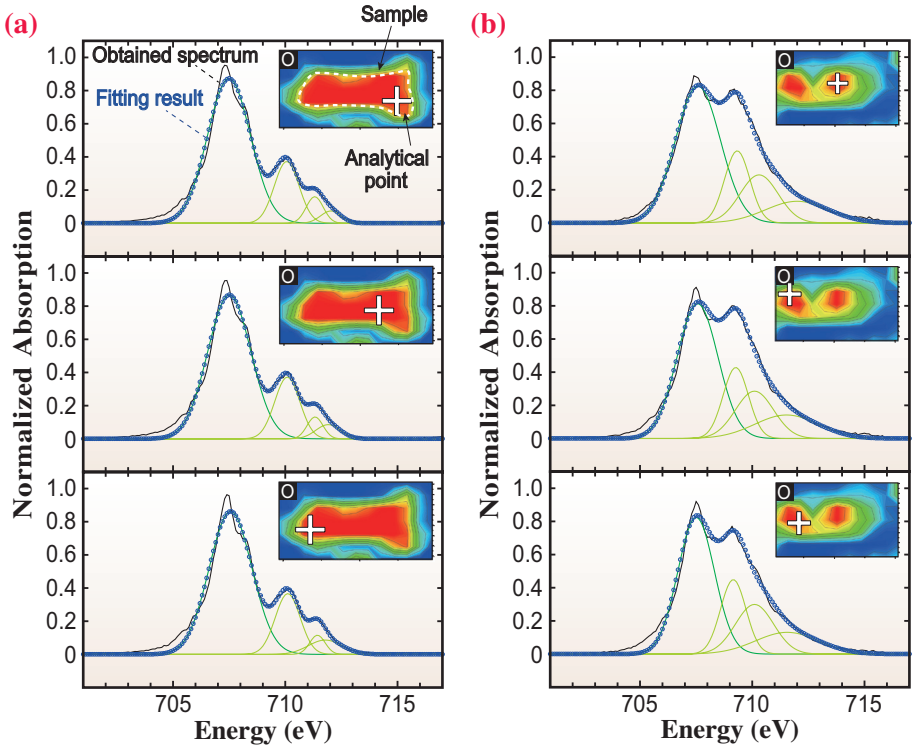

Fig. 2. Comparison of obtained XANES spectra of the silicate part of the recovered sample between **(a)** 15 GPa and **(b)** 28 GPa. The $Fe^{3+}/(Fe^{2+} + Fe^{3+})$ ratio was calculated from the area ratio of the first green-colored peak around 707 eV to all of the peaks. The inset of each figure shows an oxygen XRF map and analytical point indicated by **+**.

mantle and an atmosphere enriched in CH_4 and CO if the mantle is equilibrated with a metallic core. When a planet grows larger than Mars, the mantle may be significantly oxidized, and the atmospheric composition becomes rich in CO_2 and SO_2 [5]. The relationship between planetary size and atmospheric composition indicated in this study can be tested by future observations of exoplanetary atmospheres, particularly around young planets that likely have atmospheres equilibrated with the magma ocean.

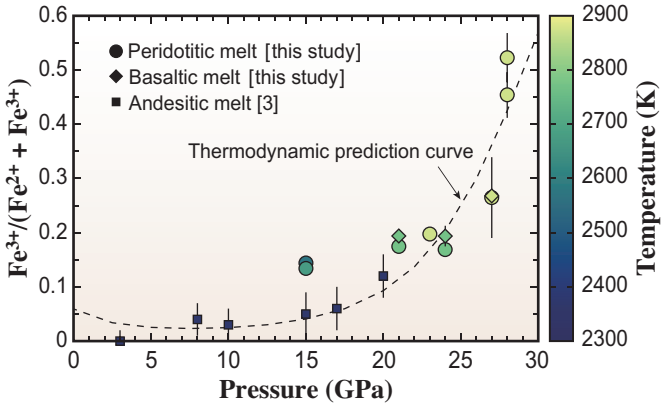

Fig. 3. Calculated $Fe^{3+}/(Fe^{2+} + Fe^{3+})$ ratio of quenched silicate melts equilibrating with metallic iron from XANES spectra. Data of andesitic melt were taken from [3]. The dashed curve indicates thermodynamic prediction based on experimental data [4]. At pressures above 20 GPa, Fe^{3+} in the melt is more stabilized than Fe^{2+}, and the $Fe^{3+}/(Fe^{2+} + Fe^{3+})$ ratio rapidly increases with pressure.

Hideharu Kuwahara[a,*] and Ryoichi Nakada[b]

[a] Geodynamics Research Center, Ehime University
[b] Kochi Institute for Core Sample Research, Institute for Extra-cutting-edge Science and Technology Avant-garde Research (X-star), Japan Agency for Marine-Earth Science and Technology (JAMSTEC)

*Email: kuwahara.hideharu.vd@sci.ehime-u.ac.jp

References

[1] D. Trail *et al.*: Nature **480** (2011) 79.
[2] M. M. Hirschmann: Earth Planet. Sci. Lett. **341-344** (2012) 48.
[3] K. Armstrong *et al.*: Science **365** (2019) 903.
[4] *H. Kuwahara, R. Nakada, S. Kadoya, T. Yoshino and T. Irifune: Nat. Geosci.* ***16*** *(2023) 461.*
[5] F. Gaillard and B. Scaillet: Earth Planet. Sci. Lett. **403** (2014) 307.

Density deficit of the Earth's inner core revealed by a multi-megabar rhenium primary pressure scale

The interiors of the Earth and the planets are environments of extreme pressure. These pressures can be estimated by determining the density distribution inside the planets and assuming hydrostatic equilibrium, with, e.g., the pressure at the center of the Earth calculated to be 365 GPa. Meanwhile, seismological observations are used to create models of the Earth's interior, such as the Preliminary Reference Earth Model (PREM) [1] which tell us the density (ρ) and the compressional (v_p) and shear (v_s) wave velocities as a function of depth based on how acoustic (seismological) waves propagate through the planet. We can then understand the interior of the Earth by generating high pressure in the laboratory, determining the density and sound velocity of materials under high pressure, and comparing these physical properties with the seismic model. Thus, the accurate determination of pressure in laboratory experiments is essential for understanding planetary interiors, as well as for studying the physical properties of materials under high pressure. The value of the pressure in high-pressure experiments is determined using an equation of state (pressure scale) that relates the density of a standard material and the physical pressure. Therefore, the development of an appropriate pressure scale has long been a fundamental and important challenge in high pressure science.

Most of the pressure scales commonly used in previous studies are based on the Rankine–Hugoniot curve and theoretical calculations. However, there are inconsistencies among those scales, due to the assumptions and extrapolations in the correction methods, with inconsistencies that can be as large to 40% at the Earth's core pressures. This situation makes it difficult to accurately determine pressures in high-pressure experiments and then to discuss the interior of the Earth quantitatively. For this reason, determination of absolute pressure in high-pressure experiments without assumptions and extrapolations, a primary pressure scale, has been desired. Zha *et al.* [2] demonstrated that a primary pressure scale could be determined by three physical properties of materials, v_p, v_s, and ρ, which could be measured independently under high pressure. However, due to the difficulty of measuring sound velocity under extreme pressures, primary pressure scales have been based on measurements over limited pressure ranges that do not extend to the extreme pressures of the Earth's core.

In this work [3], we determined v_p, v_s, and ρ of the rhenium metal up to a density ρ of 30.24 g/cm^3 using inelastic X-ray scattering (IXS) at SPring-8 **BL43LXU** [4]. This was made possible by sustained technical development and extensive experience with DAC measurements over the last decade, including sophisticated optics [5], and the strong X-ray source at BL43LXU. Even so, signal rates small, were only ~0.025 cps at the highest pressure. Figure 1 shows a typical spectrum collected at the highest ρ of 30.24 g/cm^3 corresponding to 230 GPa. We identified the IXS peaks for the longitudinal acoustic (LA) and

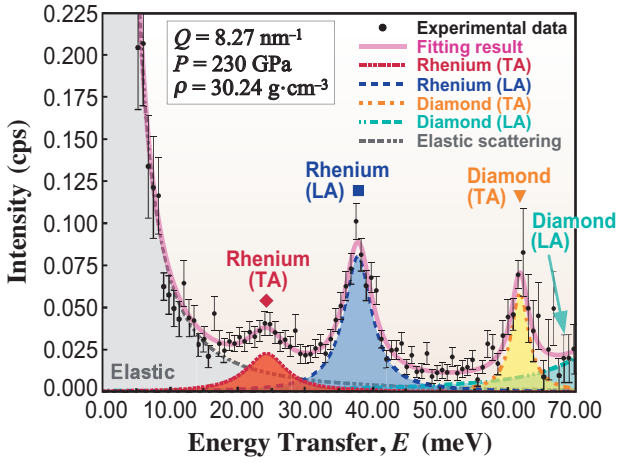

Fig. 1. An IXS spectrum of rhenium at 30.24 g·cm^{-3} corresponding to 230 GPa [3]. The experimental data (black dot with 1σ error bar) was fit (magenta solid line) with peaks for the IXS signal of TA (red dotted line) and LA (blue dashed line) modes from rhenium and TA (orange dashed-dotted line) and LA (green dashed-dotted line) modes from diamond.

the transverse acoustic (TA) modes of rhenium and diamond, allowing determination of a new primary pressure scale up to 230 GPa.

Figure 2 shows the density–pressure relations of rhenium metal, the new primary pressure scale, which can be applied to the extreme pressures of the Earth's core. Compared to curves of rhenium based on previous pressure scales, we found that the pressure value previously used was overestimated by 20% under the Earth's core pressures.

The composition of the Earth's core is a hot topic in the Earth science, as it is important for understanding the evolution of the Earth and planets in the solar system. While it is generally accepted that the Earth's core is mostly iron, the core also contains lighter materials. Therefore, investigating the compressional behavior of metallic iron at extreme pressures is important for determining the amount of light materials in the Earth's core. Figure 3 shows the density–pressure relations of hexagonal close-packed (hcp) iron, which is the main component of the Earth's core, evaluated by using our new rhenium pressure scale. Comparing the density of hcp-iron with that of the PREM at the Earth's inner core boundary (pressure and temperature are estimated to be 330 GPa and 6000 K), the density difference between metallic iron and PREM, which was previously estimated to be about 4%, is determined to be about 8%. The present density deficit can be interpreted as indicating that the light material hidden in the Earth's inner core is probably about double what was previously expected, and the total mass of light material in the entire core is probably about five times that of the Earth's crust assuming the core temperature is the same as previously estimated, or the core temperature should be by about 3000 K higher than the previous estimate if the previous amount of light material is assumed, or some combination thereof. Similar changes, perhaps even larger in magnitude, may be expected in considering the structure of other planets. This is an important finding that forces us to change the conventional discussion about the internal structure of the terrestrial and extraterrestrial planets, such as super-Earths.

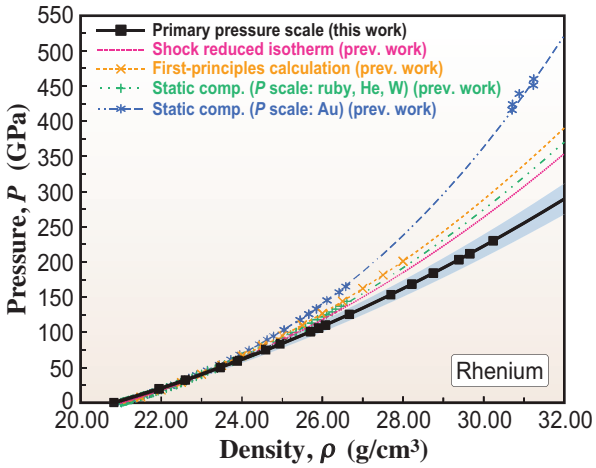

Fig. 2. Primary pressure scale for rhenium. The black curve is the compression curve of new rhenium pressure scale with the density determined experimentally and the pressure evaluated by our rhenium scale determined from density and sound velocities experimentally measured, and other colored curves and symbols are the compression curves of rhenium with experimental data based on pressure scales from previous studies [3].

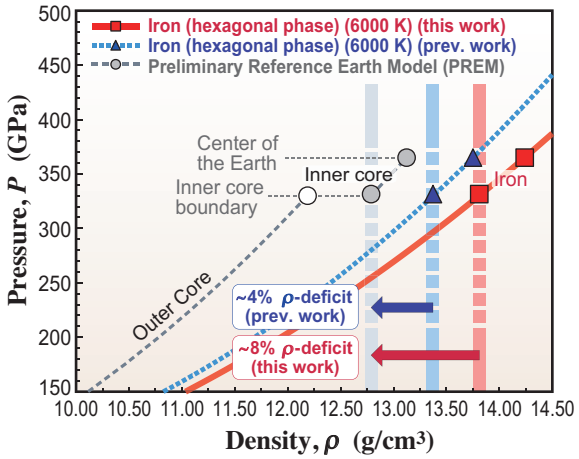

Fig. 3. Density–pressure relations of metallic iron (hexagonal phase) at the inner core conditions (330–365 GPa and 6000 K) compared with the PREM inner core. The relation at 6000 K re-evaluated by the new rhenium scale is shown as red symbols and solid line, and that by the previous scale is shown as blue symbols and dotted line [3]. The relation for the PREM inner core [1] is shown given as the gray symbols with dashed line.

Daijo Ikuta[a,*], Eiji Ohtani[b] and Alfred Q. R. Baron[c,d]

[a] Institute for Planetary Materials, Okayama University
[b] Department of Earth Science, Tohoku University
[c] RIKEN SPring-8 Center
[d] Japan Synchrotron Radiation Research Institute (JASRI)

*Email: dikuta@okayama-u.ac.jp

References

[1] A. M. Dziewonski and D. L. Anderson: Phys. Earth Planet. Inter. **25** (1981) 297.
[2] C. S. Zha *et al.*: Proc. Natl. Acad. Sci. USA **97** (2000) 13494.
[3] *D. Ikuta, E. Ohtani, H. Fukui, T. Sakamaki, R. Heid, D. Ishikawa and A. Q. R. Baron: Sci. Adv. **9** (2023) eadh8706.*
[4] A. Q. R. Baron: SPring-8 Inf. **15** (2010) 14.
[5] A. Q. R. Baron *et al.*: AIP Conf. Proc. **2054** (2019) 020002.

Multiscale water visualization inside polymer electrolyte fuel cells

The effective use of hydrogen, which is produced from renewable energy sources, is key to achieving sustainable development goals. Polymer electrolyte fuel cells (PEFCs) are used as a power source for automobiles because they generate electricity from hydrogen and air and discharge only the produced water as a byproduct. To realize a carbon-neutral society by 2050, PEFCs are expected to be used in a wide range of applications, including trucks, ships, railways, and smart cities. To satisfy the demand for heavy-duty applications, PEFCs must be improved not only to in terms of their catalytic activities but also their water management. If the produced water remains inside a PEFC, then the supply of reactant gases to the electrodes is inhibited. However, excessively dry conditions significantly reduce proton conductivity. Therefore, water management is critical in the development of PEFC materials and operating protocols. We established a multiprobe technique for multiscale water visualization inside PEFCs using *operando* neutron and synchrotron X-ray radiography at J-PARC BL22 and SPring-8 **BL33XU**, respectively [1,2]. Figure 1 illustrates the concept of the multiscale water-visualization technique for PEFCs. Wide-field observations of water distribution in the planar direction of the PEFCs are evaluated using neutron radiography. Furthermore, high-resolution observations of the water dynamics in the stacking direction of the PEFCs are achieved using synchrotron X-ray radiography. The complementary use of multiprobe radiography can reveal the three-dimensional water distribution inside PEFCs.

Figure 2 shows the PEFC setup used for the water-visualization experiments. For *operando* neutron radiography, we used a single cell comprising a membrane electrode assembly (MEA) assembled using separators with gas channels (Fig. 2(a)). The single cell was sandwiched between cooling pads under Fluorinert flow to control the cell temperature (Fig. 2(b)). The RADEN instrument at the J-PARC can acquire one image per second with a spatial resolution of 0.3 mm, where the image encompasses the entire MEA area with a width of approximately 25 cm [1]. For *operando* synchrotron X-ray radiography, we can use the same MEA as that used for neutron radiography and in-house carbon separators with three gas channels (Fig. 2(c)) [2]. The Toyota beamline instrument can output one image of the in-house cell per second over an area of 1.59×2.65 mm^2 with a spatial resolution of 1.3 μm (Fig. 2(d)).

Figure 3 shows an example of water-visualization images for the planar and cross-sectional directions of a PEFC operating at a constant current density of 1.47 A·cm^{-2} and a cell temperature of 60°C. Figure 3(a) shows the inhomogeneous water distribution in the planar direction of the PEFC. If water generated at the cathode flows toward the air outlet, then the accumulated water should be observed on the right side of Fig. 3(a), which corresponds to the air outlet. However, *operando* measurements showed nonuniform accumulation of water in the PEFC center. This suggests that some of the produced water was transported toward the anode outlet owing to water back-diffusion. Figure 3(b) shows the water distribution in the cross-sectional direction of the PEFC. Water accumulation was observed at the cathodes. Similarly, water accumulation was observed at the anode, thus indicating that water back-diffusion occurred from the cathode to the anode. Water movement due to back-diffusion was clearly observed in the video (data not shown). These results suggest that back-diffusion discharges excess

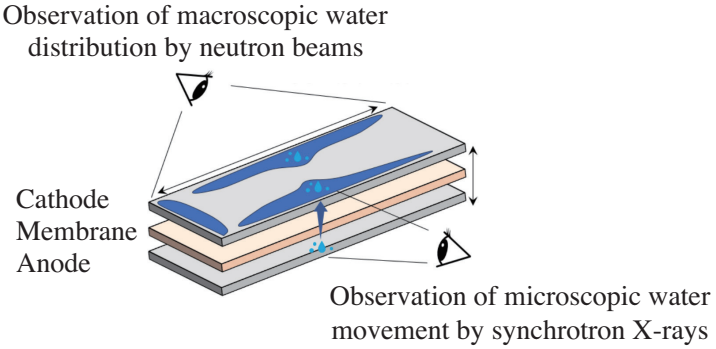

Fig. 1. Concept of multiscale water visualization inside PEFCs.

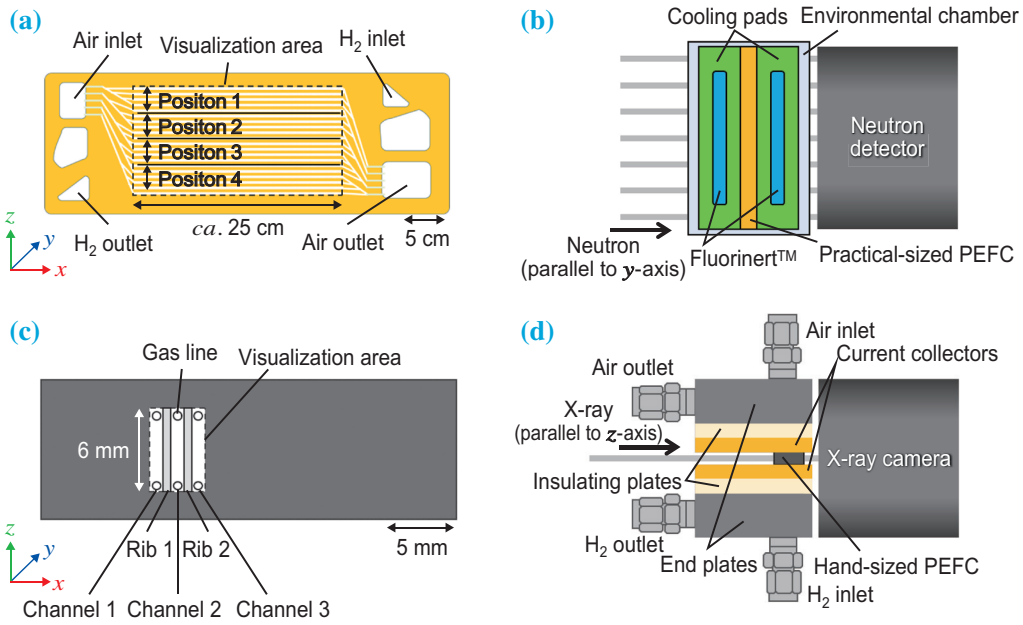

Fig. 2. Experimental setups for *operando* **(a,b)** neutron and **(c,d)** synchrotron X-ray radiography. [1]

water from PEFCs. Furthermore, they indicate that thin MEAs (<10 μm) for automotive applications not only reduce proton transport resistance but also facilitate water back-diffusion.

In conclusion, we established a multiscale water-visualization technique to achieve rational water management for PEFCs. The present results suggest for the first time that not only water discharge at the cathode, which has been improved by engineers, but also water discharge by back-diffusion to the anode is an effective method for the water management of PEFCs. This established technique for material and protocol development shall be utilized in the near future.

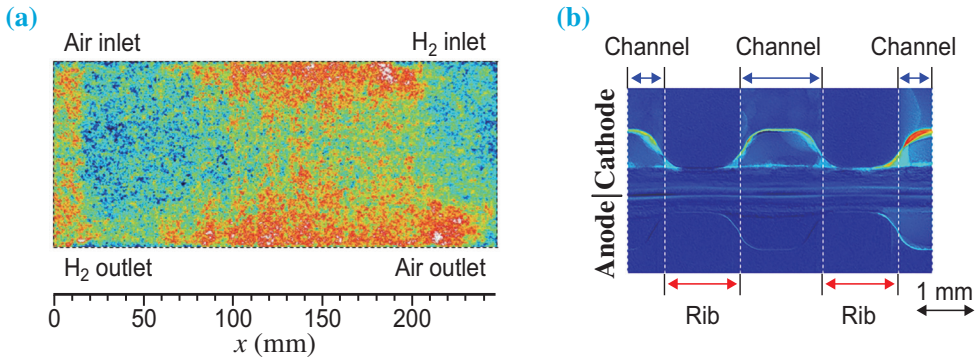

Fig. 3. Water distribution in **(a)** planar and **(b)** cross-sectional direction of PEFC. Blue and red indicate low and high water contents, respectively. [1]

Wataru Yoshimune

Toyota Central R&D Labs., Inc.

Email: yoshimune@mosk.tytlabs.co.jp

References

[1] *W. Yoshimune, Y. Higuchi, A. Kato, S. Hibi, S. Yamaguchi, Y. Matsumoto, H. Hayashida, H. Nozaki, T. Shinohara, S. Kato: ACS Energy Lett.* ***8*** *(2023) 3485.*
[2] A. Kato *et al.*: J. Power Sources **521** (2022) 230951.

Confirmation of permeation of iodide and iodine into hole-transport layer in lead halide perovskite solar cell using hard X-ray photoelectron spectroscopy

Recently, the initial power conversion efficiency (PCE) of organic-inorganic lead halide perovskite solar cells has reached 26.4% [1], a notable increase since the first PCE of 3.8% was demonstrated by Kojima *et al.* back in 2009 [2]. However, the long-term reliability of light and thermal stresses poses a challenge for practical use. In the light-induced degradation (LID) pathway, formation of PbI_2, metallic lead (Pb^0), CH_3NH_2, CH_3I, NH_3, I_2, and others has been reported. Based on these previous results and on our data, we acquired using hard X-ray photoelectron spectroscopy (HAXPES), impedance spectroscopy, and microwave photoconductivity decay, we suggested the following pair reaction model for the LID of perovskite solar cells [3]:

$$\text{Cathode reaction: } Pb^{2+} + 2e^- \rightarrow Pb^0 \quad (1)$$
$$\text{Anode reaction: } 2I^- + 2h^+ \rightarrow I_2\uparrow, \quad (2)$$

where the cathode and anode reactions mainly occur near the electron transport layer (ETL)/perovskite and perovskite/hole transport layer (HTL) interfaces, respectively. Moreover, the light stability of cells is strongly affected by experimental conditions, such as the ambient atmosphere and temperature. We investigated the influence of oxygen on the LID of perovskite using HAXPES and suggested that the presence of O_2 around a cell enhances anode reaction (2) according to the following reaction [4]:

$$\text{Additional cathode reaction: } O_2 + e^- \rightarrow O_2^-, \quad (3)$$

where the oxygen captures photoinduced electrons at the adsorbed sites and superoxide (O_2^-) is produced; O_2^- contributes to the production of H_2O and CH_3NH_2 gas via oxidation process, resulting in PbI_2 formation and photodecomposition.

Effective interfacial layers between the ETL and perovskite layer, self-assembled monolayers (SAMs) such as 4-(1',5'-Dihydro-1'-methyl-2'*H*-[5,6]fullereno-C_{60}-I_h-[1,9-*c*]pyrrol-2'-yl)-benzoic acid (C_{60}SAM), and other approaches have been proposed to improve the light stability of perovskite cells [5]. Surface passivation of the ETL using SAMs, such as C_{60}SAM, suppresses cathode reaction (1). We investigated the change in the HTL induced by illumination of a sample with a C_{60}SAM layer using HAXPES measurements [6]. We prepared a sample with a glass/indium tin oxide (ITO)/antimony-doped tin oxide (ATO)/compact titanium oxide (TiO_2)/mesoporous TiO_2/C_{60}SAM/perovskite 550 nm/n-butylammonium bromide/thick poly(triaryl amine) (PTAA) 100 nm structure (Fig. 1), where the Lewis acid tris(pentafluorophenyl)borane (TPFPB) was added to the PTAA as a dopant. The samples were encapsulated with a glass cover and absorber, and sealed under a nitrogen atmosphere (oxygen concentration <10 ppm). The substrate and glass cover were glued using a UV-cured epoxy resin. One-half of the samples were shaded using a mask; then, 1 sun light was irradiated on the glass substrate side of the sample for 3 h in dry air at ~28.8°C using a light source. The HAXPES samples before and after the light illumination test (LIT) were prepared by cutting the shaded and illuminated areas. The HAXPES samples had dimensions of 5 mm × 5 mm. A HAXPES apparatus at SPring-8 **BL16XU** was used. The incident angle of the X-ray beam was 85° and

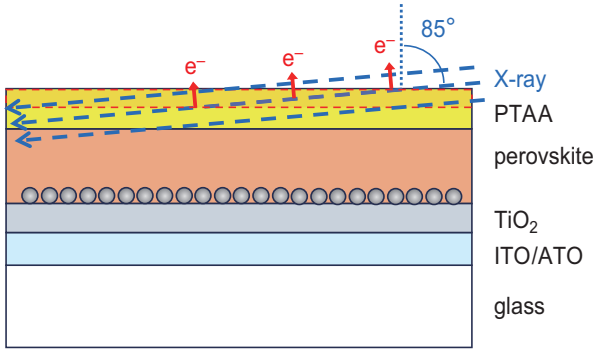

Fig. 1. Schematic of the HAXPES sample. The incident angle of the X-ray beam was 85° and the hard X-rays were incident on the side of the PTAA.

the excitation energy was 6 keV. Hard X-rays were incident on the side of the PTAA. The experimental sampling depth of the HAXPES was estimated to be approximately 50 nm. HAXPES measurements began more than 18 h after completing the LIT; thus, irreversible changes in the samples caused by long-term light illumination were mainly detected. Given that the PTAA was sufficiently thicker than the photoelectron escape depth of ~50 nm, Pb 4*f* signals originating from the perovskite layer were not observed. However, I 3*d* signals of I^- (~619.5 eV) and I^0 (~620.7 eV) were detected in both cases before and after the LIT. This indicates that iodide and iodine diffused to some extent from the perovskite to the PTAA during the first deposition of the PTAA. After LIT, the fractions of I^- and I^0 increased with respect to the amount of F 2*s* and B 1*s* spectra derived from TPFPB, as shown in Fig. 2. This indicates that during illumination, the iodine species permeated the PTAA. The permeation of iodine species into the PTAA proceeded gradually, even though C_{60}SAM was used to suppress the degradation of the HTL side under illumination. However, despite the permeation of iodine species into the PTAA, the solar cell with the C_{60}SAM interlayer showed almost no LID after the light stability test. Based on the pair reaction model, the suppression of the cathode reaction near the ETL/perovskite interface by introducing C_{60}SAM should lead to the suppression of anode reaction (2) near the perovskite/HTL interface under illumination, corresponding with the decrease in the peak area ratio of I^0/I^- after the LIT, as shown in Fig. 2.

Finally, we developed a new structure for improving both the PCE and light stability in which the surface of the ETL was modified by combining C_{60}SAM with a suitable gap-filling self-assembled monolayer (GFSAM) [6]. This GFSAM was formed using an isonicotinic acid solution. We confirmed a decrease in the band offset and an improvement in electron extraction at the TiO_2/perovskite interface using HAXPES and time-resolved microwave conductivity data for the sample based on a combination of C_{60}SAM and isonicotinic acid, respectively. After six months of outdoor exposure, the PCE of solar cells with C_{60}SAM and isonicotinic acid remained almost unchanged, with a retention rate of ~100%.

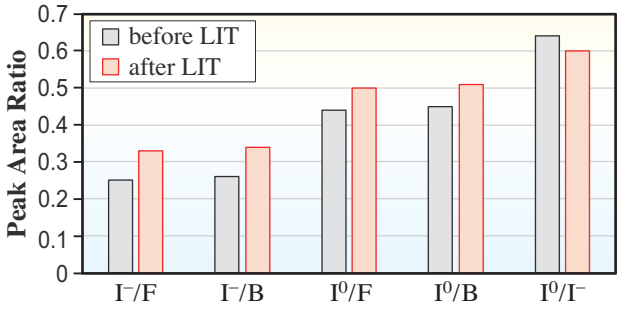

Fig. 2. Peak area ratios (peak areas of I 3*d* spectra divided by those of B 1*s* or F 2*s* spectra) for the samples with glass/ITO/ATO/c-TiO_2/mp-TiO_2/C_{60}SAM/perovskite 550 nm/BABr/PTAA 100 nm before and after LIT.

Takeyuki Sekimoto

Technology Division, Panasonic Holdings Corporation

Email: sekimoto.takeyuki@jp.panasonic.com

References

[1] C. Liu *et al.*: Science **382** (2023) 810.
[2] A. Kojima *et al.*: J. Am. Chem. Soc. **131** (2009) 6050.
[3] T. Sekimoto *et al.*: ACS Appl. Energy Mater. **2** (2019) 5039.
[4] T. Sekimoto *et al.*: ACS Appl. Energy Mater. **5** (2022) 4125.
[5] M. Hiraoka *et al.*: ACS Appl. Energy Mater. **5** (2022) 4232.
[6] *T. Sekimoto, T. Yamamoto, F. Takeno, R. Nishikubo, M. Hiraoka, R. Uchida, T. Nakamura, K. Kawano, A. Saeki, Y. Kaneko and T. Matsui: ACS Appl. Mater. Interfaces* ***15*** *(2023) 33581.*

Imaging of dislocations in β-Ga_2O_3 via X-ray topography based on anomalous transmission

β-Ga_2O_3 is a promising ultrawide bandgap semiconductor suitable for use in high-voltage and high-current power electronics applications [1]. Single-crystal substrates with highly crystalline structures are a prerequisite for guaranteeing high-performance and reliable β-Ga_2O_3 devices. Although high-quality and large-diameter (~10 cm) bulk crystals are now commercially available [2], a further reduction in crystallographic defects is required. A major type of crystallographic defect in β-Ga_2O_3 that limits device performance is dislocations present at the densities of 10^3–10^5 cm^{-2}. The knowledge of their character and distribution over an entire crystal volume is of considerable scientific and industrial importance. However, this knowledge has not been available for β-Ga_2O_3 owing to the lack of available techniques to probe dislocations located in the deep interiors of thick crystals.

In this study, we performed a transmission XRT observation at SPring-8 **BL24XU** to reveal the dislocation distribution over the entire volume of a large β-Ga_2O_3 substrate [3,4]. This technique takes advantage of the anomalous transmission (AT) of X-rays, which is a dynamical diffraction phenomenon known as the Borrmann effect [4]. The sample was a Sn-doped (001)-oriented β-Ga_2O_3 single-crystal substrate fabricated via edge-defined film-fed growth (EFG). The rectangular substrate had the dimensions of 10 mm × 15 mm and a thickness of 680 μm. Monochromatic X-rays of wavelength λ = 1.24 Å were used to irradiate the sample, which had a μt value of approximately 9.7 at this wavelength, where μ is the linear absorption coefficient and t is the sample thickness. A forward-diffracted beam (o-wave) was used for imaging.

Figure 1(a) shows a schematic of the substrate geometry and optical system using the diffraction vector $\boldsymbol{g}$ = 020. X-rays entered the sample from one of the (001) surfaces, and the exiting X-rays were first irradiated onto a vertically movable fluorescent screen (FS). The occurrence of AT was determined by observing the spot intensity on the FS, which corresponded to the o-wave and h-wave (diffracted beam). According to the theoretical description of AT using dynamical XRD theory, the two plane waves are coherently coupled in the crystal, and their interference produces a set of standing waves. When the zero-amplitude points (nodes) of standing waves coincide with the atomic planes used for Bragg reflection, the intensity of the photoelectric absorption is significantly reduced, leading to a marked increase in the intensity of the transmitted X-rays [5]. Figures 1(b,c) show the photographs of the o- and h-wave spots on the FS under normal absorption and AT conditions at $\boldsymbol{g}$ = 020, respectively. There was a 180 arcsec difference in the ω angle of the two conditions. Under normal absorption, a significant attenuation caused by the large value of μt (~9.7) led to a faint o-wave spot, and the h-wave spot was not recognizable (Fig. 1(b)). In comparison, when the ω angle was carefully adjusted to satisfy the exact Bragg condition of $\boldsymbol{g}$ = 020, which allowed AT to occur, two equally strong spots corresponding to the o- and h-waves were observed (Fig. 1(c)). Figures 1(d,e) show the photographs of $\boldsymbol{g}$ = 022 under similar conditions. After two equally strong spots were confirmed, the FS was moved upward to allow the o-wave to advance toward the camera for image recording.

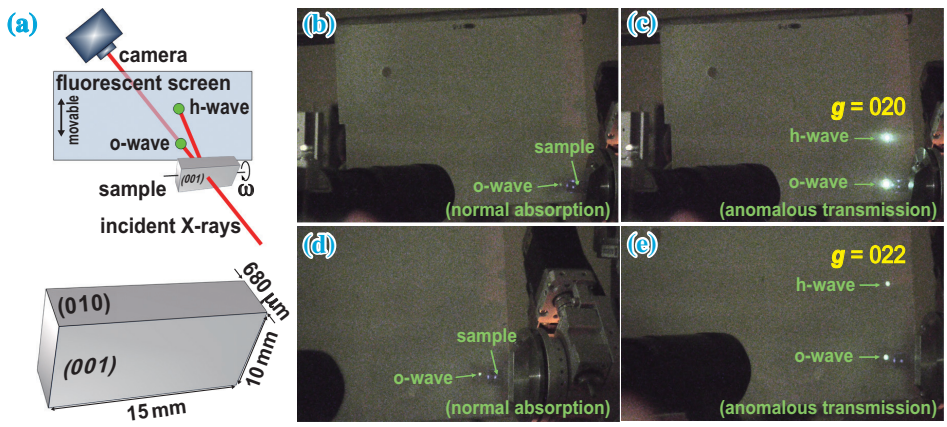

Fig. 1. **(a)** Schematic of the substrate geometry and the optical system; **(b)–(e)** photographs of the o- and h-wave spots on the FS under normal absorption or anomalous transmission conditions.

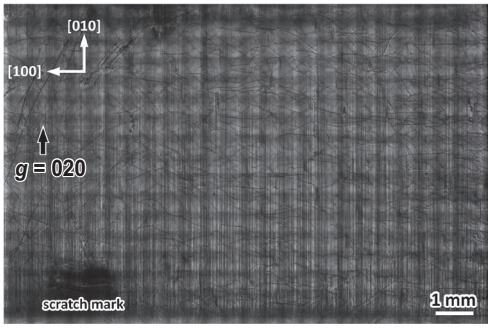

Fig. 2. BF-XRT of the entire sample obtained with $\boldsymbol{g} = 020$.

Figure 2 shows the BF-XRT results for the entire sample obtained at $\boldsymbol{g} = 020$. Dislocations having a Burgers vector $\boldsymbol{b} = [uvw]$, with $v \neq 0$, were revealed. The dominant feature of the topograph is highly dense vertical lines. The vast majority of them corresponded to dislocations parallel to the [010] direction, indicating that threading dislocations in the [010] direction were the most stable and frequently generated dislocations during EFG. In comparison, the curved lines had a lower density, and most were associated with dislocations lying on the (001) plane. Dynamical XRD theory predicts that dislocations close to the exit surface generate a sharper contrast than those close to the entrance surface. Therefore, the degree of sharpness of the curved lines indicated the depth of the dislocations from the (001) surfaces.

To identify the character of the dislocations, that is, their Burgers vectors, transmission XRTs of the same area were acquired at $\boldsymbol{g} = 022$ and $\boldsymbol{g} = 400$. A comparison between $\boldsymbol{g} = 020$ and $\boldsymbol{g} = 022$ (Fig. 3) reveals a significant number of additional vertical lines that are not observed in Fig. 2. Judging by the $\boldsymbol{g}\cdot\boldsymbol{b}$ invisibility criterion, these dislocations must have a Burgers vector of $\boldsymbol{b} \| [001]$, presumably $\boldsymbol{b} = [001]$ (or $\boldsymbol{b} = [00\bar{1}]$). A remarkable feature of the 400 topograph is the complete extinction of all curved dislocations, indicating that these dislocations have a Burgers vector of the form $\boldsymbol{b} = [0vw]$, that is, they possess no *a*-axis components. Moreover, the curving feature strongly suggests that they were not generated via dislocation propagation in the [010] direction during EFG pulling-up, but were highly likely to have been generated via dislocation glide on the (001) plane under thermal stress. To glide on the (001) plane, *w* in $\boldsymbol{b} = [0vw]$ must be zero. Therefore, we conclude that all the curved dislocations share the same Burgers vector $\boldsymbol{b} = [010]$ (or $\boldsymbol{b} = [0\bar{1}0]$) and that the glide belongs to the [010](001) slip system.

The dislocation visibilities and corresponding dislocation types are listed in Table I. Thus, we successfully revealed the dislocation distribution and dislocation characters for a large-area β-Ga_2O_3 substrate. The transmission XRT technique based on AT is a powerful tool for imaging dislocations in highly absorbing β-Ga_2O_3, which can provide important feedback for the improvement of crystal growth.

Table I. Dislocation visibility at various $\boldsymbol{g}$-vectors and the corresponding dislocation type

Label	$\boldsymbol{g}$			$\boldsymbol{b}$	ξ	Type
	020	022	400			
1	Yes	Yes	Yes	N/A	N/A	Macro defects
2	Yes	Yes	No	[010]	[010]	*b*-axis screw
3	No	Yes	No	[001]	[010]	*b*-axis edge
4	Yes	Yes	No	[010]	curved, $\in(001)$	Mixed type
5	No	Yes	Yes	$[u0w]$, likely $[10\bar{1}]$	roughly [010]	Edge

(Yes = visible; No = invisible; N/A = not applicable).

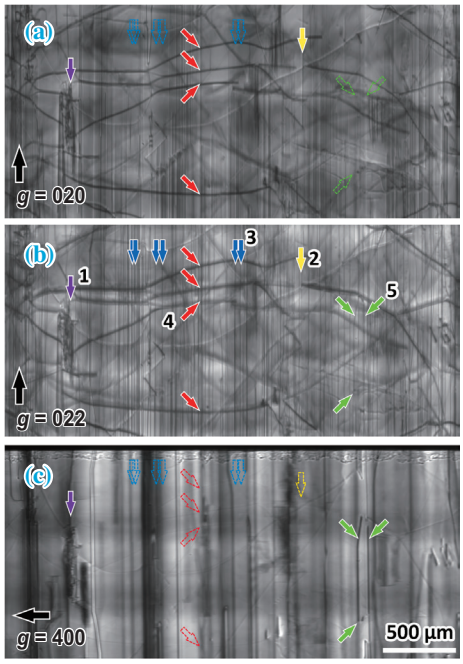

Fig. 3. Comparison of dislocation visibility among: **(a)** $\boldsymbol{g} = 020$; **(b)** $\boldsymbol{g} = 022$; and **(c)** $\boldsymbol{g} = 400$. The scale bar applies to all images.

Yongzhao Yao†

Functional Materials Group, Japan Fine Ceramics Center

Email: y_yao@jfcc.or.jp

†Present address: Mie University

References

[1] S. Pearton *et al.*: Appl. Phys. Rev. **5** (2018) 011301.
[2] A. Kuramata *et al.*: Jpn. J. Appl. Phys. **55** (2016) 1202A2.
[3] Y. Yao *et al.*: APL Mater. **10** (2022) 051101.
[4] *Y. Yao, Y. Tsusaka, K. Sasaki, A. Kuramata, Y. Sugawara and Y. Ishikawa: Appl. Phys. Lett.* ***121*** *(2022) 012105.*
[5] G. Borrmann: Z. Phys. **127** (1950) 297.

Accelerators & Beamlines Frontiers

SPring-8 Beam Performance

Insertion Device

A new insertion device (ID) capable of switching the polarization states between left-handed circular, right-handed circular, horizontal, and vertical polarizations (LCP, RCP, HP, and VP, respectively) was constructed to replace the existing ID operating in BL17SU, comprising both electromagnet and permanent-magnet arrays. Since 2020, its capability for wavelength tunability and available polarization has been largely limited because of a malfunction in one of the electromagnet coils (water leakage). The new ID, which has a magnetic period of 120 mm and is referred to as "H8U120," is based on a Helical-8 undulator concept proposed in 2011 [1]. It is advantageous in that the HP and VP are available with significant less heat load than that in conventional elliptic polarized undulators.

The construction of H8U120 started in 2021, and the assembly of the mechanical components and evaluation of the magnetic array were completed in July 2022 [2]. Figures 1(a–e) summarize the magnetic performance of the H8U120 at a minimum gap of 20 mm. Figure 1(a) shows the distributions of the horizontal magnetic fields in three different modes of operation as measured by scanning a Hall probe; the blue, green, and red lines correspond to the clockwise (CW), counter-clockwise (CCW), and figure-8 modes, respectively, in which LCP, RCP, and HP/VP are generated. Figure 1(b) is the same as Fig. 1(a); however, for the vertical magnetic field, common to the three operation modes, only one result is shown as a black line. Figures 1(c), 1(d), and 1(e) show the electron trajectories projected onto the transverse plane in the CW, CCW, and figure-8 modes calculated using the magnetic distributions shown in Figs. 1(a) and 1(b). The electrons move along the CW helix, CCW helix, or figure-8-like orbit in each mode.

The constructed H8U120 was installed in the storage ring during the summer shutdown period (August 2022) and operated without problems.

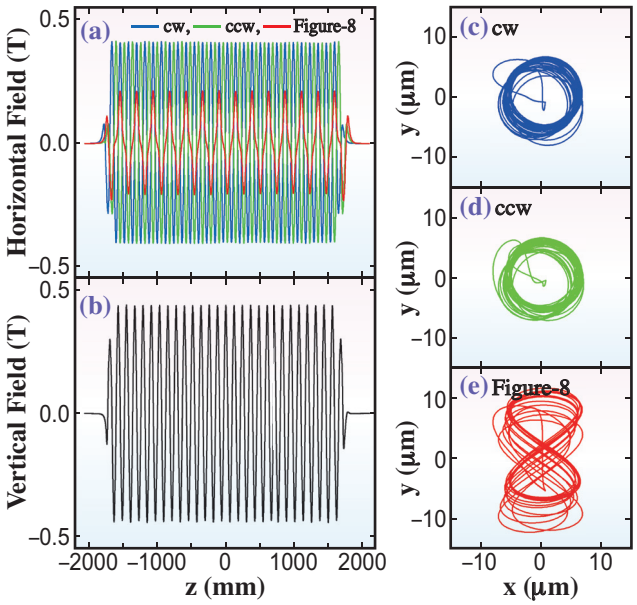

Fig. 1. Magnetic performances of the constructed H8U120 in three modes of operation: **(a,b)** horizontal and vertical field distributions, and **(c–e)** trajectories projected on the transverse plane.

Takashi Tanaka

RIKEN SPring-8 Center

Email: ztanaka@spring8.or.jp

References

[1] T. Tanaka and H. Kitamura: Nucl. Instrum. Meth. A **659** (2011) 537.
[2] T. Tanaka *et al.*: J. Synchrotron Rad. **30** (2023) 301.

SACLA Beam Performance

Recent update on accelerator

The time-resolved operation of the SACLA linear accelerator as a ring injector, introduced in April 2021, has been on track and is running smoothly. The pulsed quadrupole magnet system introduced for SACLA's multi-beamline operations has also been used routinely, contributing significantly to ensuring XFEL performance and reducing the accelerator tuning time. Prior to the resumption of SPring-8-II operation in March 2029, another pulsed quadrupole magnet system was installed in the upstream bunch compressor section to enable pulse-by-pulse switching of bunch compression conditions during XFEL generation and beam injection into the ring. Parameter tuning will be performed using these systems in the next year and beyond.

In SACLA, the XFEL requirements for each experiment have become increasingly detailed and complex in recent years. Weekly accelerator tuning has become increasingly difficult to provide proper FEL characteristics for each of the three FEL beamlines. Although SACLA is already state-of-the-art in the implementation of ML-based accelerator tuning programs, further improvement of the accelerator tuning program that can more precisely meet users' requests for XFEL, while increasing the number of performance indicators that can be handled, including not only intensity but also spectra and laser profiles, is currently underway. We hope to report the results clearly in the next issue.

The basis for efficient tuning and stable XFEL generation is to stabilize the XFEL amplification over a long period. In the case of SACLA, it has long been known that the compensation of accelerator parameter drifts, which fix the multi-stage bunch compression system under constant conditions from upstream, is critically important. Recent efforts have resulted in a drift feedback system of the accelerator parameters shown in Fig. 1, which isolates the parameter variations of the multi-stage bunch compression system and applies

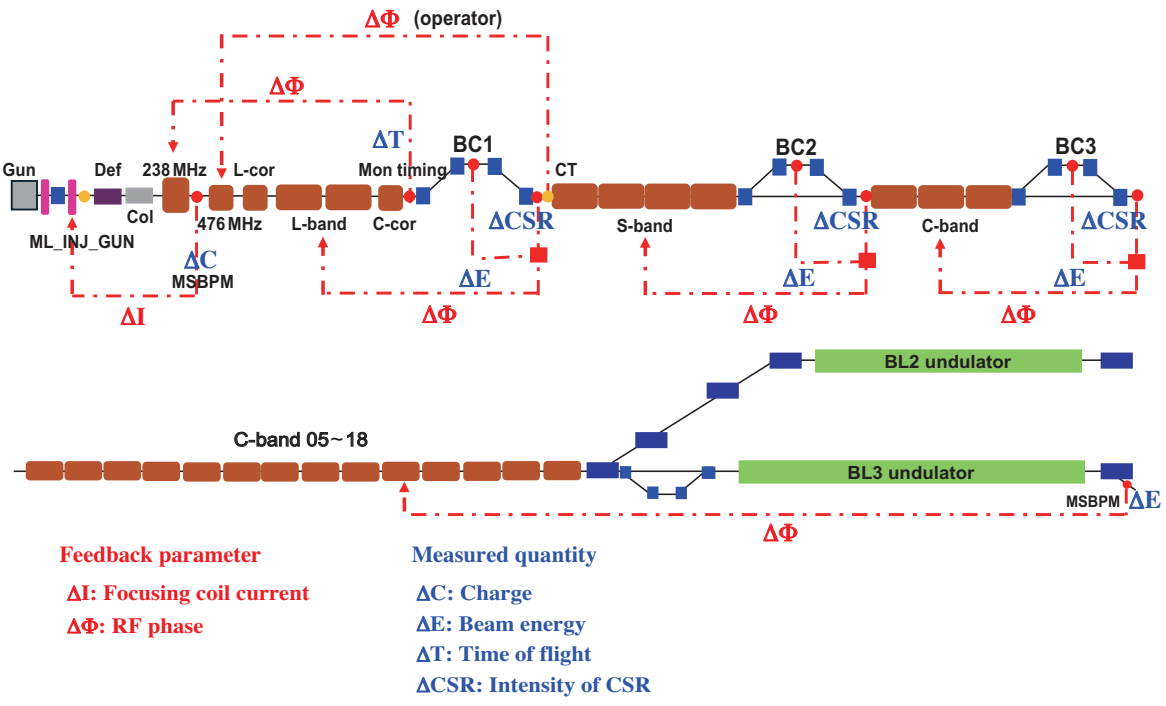

Fig. 1. Drift feedback system of accelerator parameters at the multi-stage bunch compression system at SACLA.

accurate feedback to the drift of each component, providing a stable XFEL for a long period of time. This feedback system contributed significantly to the stable operation of high-performance XFELs at SACLA.

To improve the reliability of the SACLA operation, the RF window system shown in Fig. 2 was installed step-by-step in the L-band, S-band, and C-band RF accelerator systems located upstream from the final bunch compressor, which had no spare RF system, to enable quick replacement in the case of klystron failure. The RF window system separates the vacuum between the directly connected klystron and accelerator tube, allowing the replacement of the klystron without releasing the vacuum of the accelerator tube. Three RF window systems were installed at by the end of 2023. The installation of the systems will continue with the aim of completing the modifications at the earliest.

The automatic recovery time from the RF system shutdown due to RF discharge or thyratron failure has been 30–50 s per event. To maximize the experimental efficiency, the shutdown time was reduced uniformly to 15 s. System modifications to enable a shorter recovery time from laser operation shutdown due to RF system down started in spring 2020, and all modifications of the RF acceleration systems were completed in the summer of 2023.

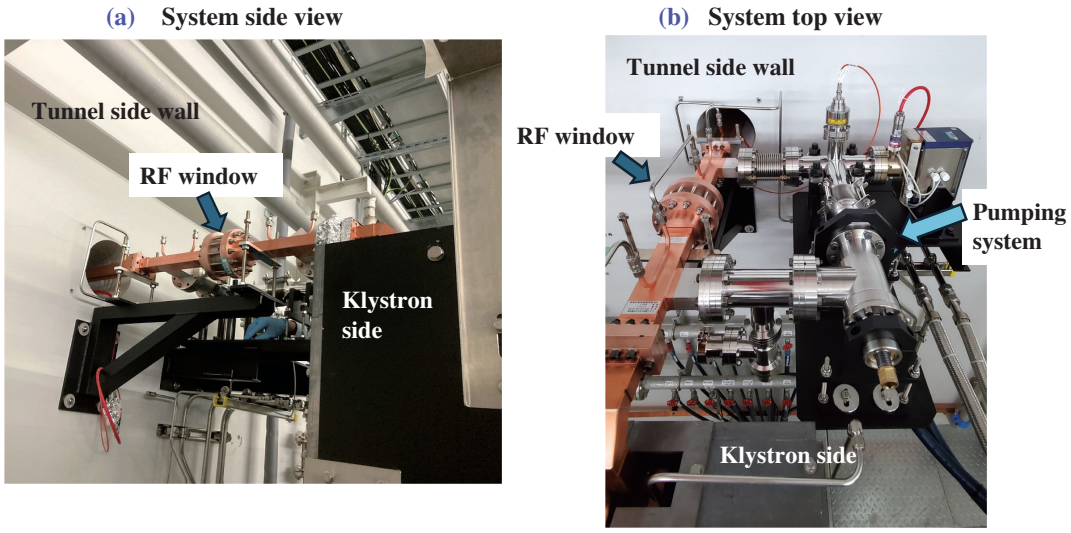

Fig. 2. RF window system installed at SACLA, **(a)** side view and **(b)** top view.

Hitoshi Tanaka

RIKEN SPring-8 Center

Email: tanaka@spring8.or.jp

FACILITY STATUS

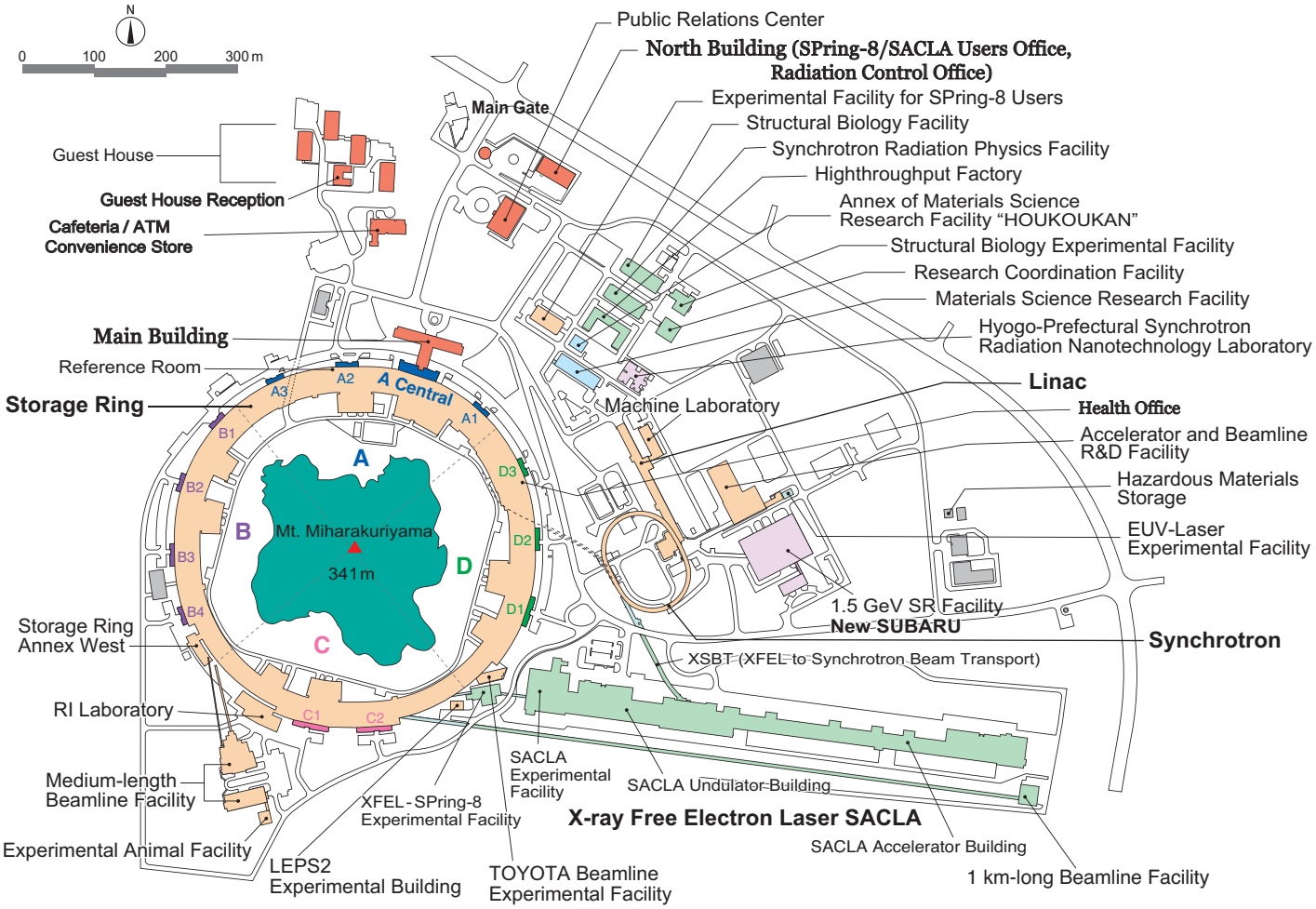

SPring-8

I. Introduction

SPring-8 was stably operated throughout FY2023 achieving a total accelerator complex operation time and user beam time of 5187.9 h and 4435.7 h, respectively, and a downtime of 24.2 h. SPring-8 completed all its operations by the end of February 2024.

For the contract beamlines, interim review was conducted for Advanced Batteries (BL28XU, Kyoto University). Subsequently, the project was authorized to continue. Post-evaluations of SUNBEAM BM (BL16B2, SUNBEAM Consortium) and SUNBEAM ID (BL16XU, SUNBEAM Consortium) were conducted.

At present, the number of SPring-8 users is as high as 15,000, all of whom are members of the SPring-8 Users Community (SPRUC).

To facilitate dialogue between users and facility staff, it is important for SPring-8 to organize scientific events in collaboration with SPRUC, such as the SPring-8 Symposium. In 2023, the SPring-8 Symposium was held online on September 26 – 27, with 489 participants. SPring-8 also facilitates communication between users and industry. The Joint Conference on Industrial Applications of SPring-8 was held in Hyogo Prefecture on September 7 – 8, 2023, with 221 participants. Moreover, as part of its continuous effort towards fostering human resources in synchrotron sciences, SPring-8 organized the 23rd SPring-8 Summer School with 87 students of graduate schools nationwide, in cooperation with the University of Hyogo, Kwansei Gakuin University, Okayama University, Osaka University, Ibaraki University, Japan Atomic Energy Agency, National Institutes for Quantum Science and Technology, and RIKEN. Furthermore, SPring-8 and SPRUC organized the 7th SPring-8 Autumn School with 76 participants, which included university students and corporate researchers.

II. Machine Operation

The operation statistics for the last five fiscal years are shown in Fig. 1. In FY2023, the operation time of the storage ring was 5187.9 h, 85.5% of which (4435.7 h) was devoted to the SR experiments. This excellent figure for the user time represents a storage ring availability of 99.4%. The total downtime caused by failures amounted to 24.2 h accounting for 0.55% of the total user time. For 99.8% of the user time in FY2023, the stored beam current was maintained at 100 mA via the top-up operation wherein the stored beam was filled up on demand at any time. An extreme stability of the light source intensity better than 0.1% was provided by the top-up operation.

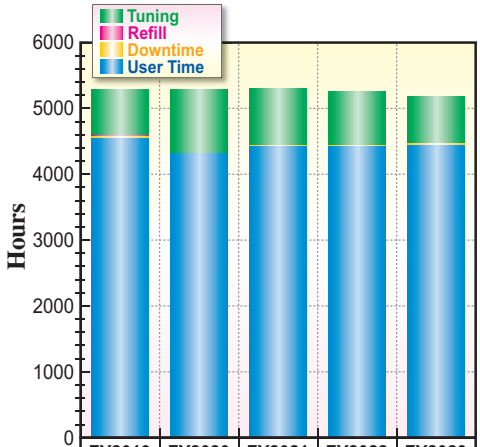

	FY2019	FY2020	FY2021	FY2022	FY2023
Accelerator Operation Time	5285.7	5284.6	5300.2	5259.3	5187.9
Storage Ring Operation Time	5271.2	5274.8	5300.2	5259.3	5187.9
Tuning & Study (Acc. & BL)	701.7	964.6	860.2	819.3	723.9
Refill	5.6	3.6	3.1	4.3	4.1
Downtime	40.5	7.4	10.0	19.7	24.2
Mean Time Between Failures	206.3	718.2	553.4	232.4	403.2
Achieved User Time	4537.9	4309.0	4426.9	4416.0	4435.7
Planned User Time	4584.0	4464.0	4440.0	4440.0	4464.0
Availability (%)	99.0	99.7	99.7	99.5	99.4

Fig. 1. Operation statistics for five most recent fiscal years.

Table 1. Operation modes in FY2023

	Single bunch current (mA)	Share of operation time (%)
203 bunches		42.0
4 bunch-train × 84		5.9
11 bunch-train × 29		18.8
1/7-filling + 5 single bunches	3	7.5
2/29-filling + 26 single bunches	1.4	0
1/14-filling + 12 single bunches	1.6	7.0
4/58-filling + 53 single bunches	1.0	0
406 × 11/29-filling + 1 single bunch	5	18.8

The variety of operation modes for the SR experiments is one of the characteristics of SPring-8. The operation modes are classified into two types: several-bunch and hybrid-filling modes. The several-bunch mode comprises equally spaced bunches or trains of bunches such as 203 bunches or 29 trains of 11 bunches. The hybrid-filling mode comprises a long train of bunches and isolated single bunches. Sufficient isolated bunch purity is maintained by the SACLA linac's spurious bunch sweeper and the storage ring's bunch cleaning system. The operation modes of SPring-8 are listed in Table 1, along with a share of each operation mode for FY2023. Table 2 summarizes the beam parameters of the storage ring.

Table 2. Beam parameters of SPring-8 storage ring

Energy [GeV]	8
Number of buckets	2436
Tunes (ν_x / ν_y)	41.14 / 19.325
Current [mA]:	
single bunch	12
multi bunch	100
Bunch length (σ) [psec]	13
Horizontal emittance [nm·rad]	2.4 *
Vertical emittance [pm·rad]	4.8 *
Coupling [%]	0.2
RF Voltage [MV]	14.4 ** ~ 16
Momentum acceptance [%]	3.2 (~256 MeV)
Beam size (σ_x / σ_y)* [μm]	
Long ID section	333 / 7
ID section	316 / 5
BM1 section	94 / 12
BM2 section	100 / 12
Beam divergence (σ_x' / σ_y')* [μrad]	
Long ID section	8 / 0.7
ID section	9 / 1.0
BM1 section	58 / 0.5
BM2 section	68 / 0.5
Operational chromaticities (ξ_x / ξ_y)	+2 / +2 ***
Lifetime [hr]:	
100 mA (multi bunch)	~250
1 mA (single bunch)	~30
Horizontal dispersion [m]:	
Long ID section	0.153
ID section	0.146
BM1 section	0.039
BM2 section	0.059
Fast orbit stability (0.1 – 200 Hz) [μm]:	
horizontal (rms)	~4
vertical (rms)	~1

* Assuming 0.2% coupling
** Power saving mode
*** With bunch-by-bunch feedback

III. Beamlines

The SPring-8 storage ring can accommodate up to 62 beamlines: 34 insertion devices, 4 long undulators, and 24 bending magnets. At present, 55 beamlines are in operation, covering a wide variety of research fields involving synchrotron radiation science and technology. The beamlines are classified into the following three types.

(1) Public Beamlines (26 beamlines operating),
(2) Contract Beamlines (13 beamlines operating), and
(3) RIKEN Beamlines (16 beamlines operating).

Currently, 26 public beamlines are fully operational. Beamlines that have been proposed and constructed by external organizations, such as universities, research institutes, private companies and consortiums, are referred to as contract beamlines and these are used exclusively by contractors for their own research purposes. At present, 13 contract beamlines are in operation. Beamlines constructed by RIKEN or transferred to RIKEN, except for public beamlines, are referred to as RIKEN beamlines and are primarily used for RIKEN's own research activities, with partial availability for public use. RIKEN is now operating 16 beamlines.

To illustrate the beamline portfolio of SPring-8, a beamline map is shown in Fig. 2 together with the beamline classification. The research fields of each beamline are presented in Table 3.

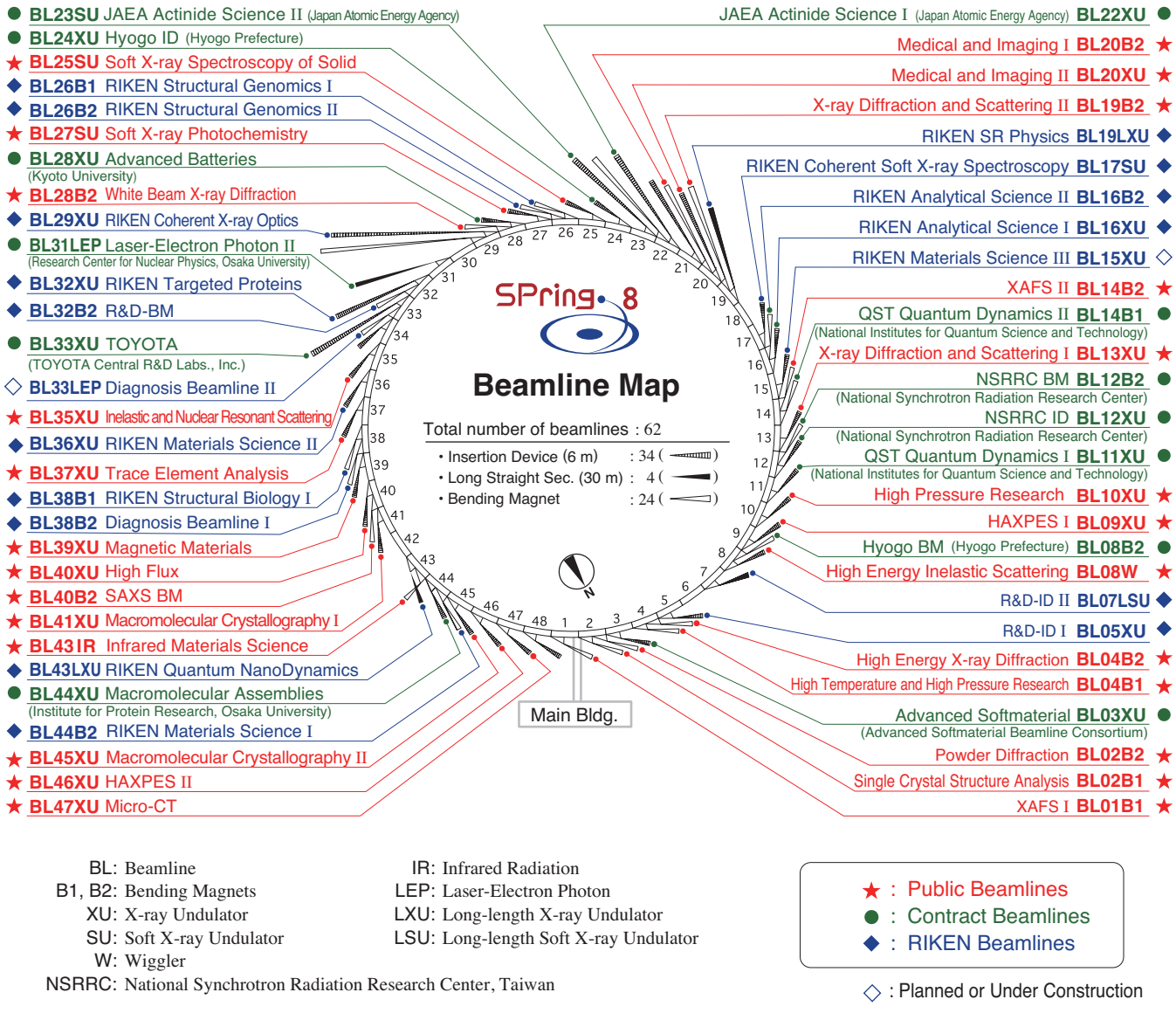

Fig. 2. Beamline map as of April 2024.

Table 3. List of beamlines

BL #	Beamline Name	(Public Use) or (First Beam)	Areas of Research and Available Techniques
★ Public Beamlines			as of April 2024
BL01B1	XAFS I	(Oct. 1997)	Wide energy range (3.8–113 keV), XAFS of dilute systems and thin films, time-resolved XAFS by quick scan (time-resolved QXAFS), depth-resolved XAFS, XAFS at low and high temperatures, simultaneous XAFS and XRD measurements, simultaneous XAFS and IR measurements.
BL02B1	Single Crystal Structural Analysis	(Oct. 1997)	Charge density study using high energy X-ray, *in situ* single crystal experiments, microcrystal structure analysis.
BL02B2	Powder Diffraction	(Sep. 1999)	Charge density study from powder diffraction, structural phase transition, *ab initio* structure determination from powder diffraction, crystal structure refinement by Rietveld method, *in situ* powder diffraction experiment under gas and vapor adsorption/desorption.
BL04B1	High Temperature and High Pressure Research	(Oct. 1997)	X-ray diffraction measurements and radiography under extreme conditions using large-volume press.
BL04B2	High Energy X-ray Diffraction	(Sep. 1999)	Structural analysis of glass, liquid, and amorphous materials.
BL08W	High Energy Inelastic Scattering	(Oct. 1997)	Magnetic Compton scattering, high-resolution Compton scattering, Compton scattering imaging, high-energy X-ray scattering, high-energy X-ray fluorescence analysis (XRF), time-resolved pair distribution function analysis (PDF).
BL09XU	HAXPES I	(Oct. 1997)	Resonant hard X-ray photoelectron spectroscopy (HAXPES), polarization-dependent HAXPES using diamond phase retarder, depth analysis of electron state, materials science, and applied materials science.
BL10XU	High Pressure Research	(Oct. 1997)	Crystal structure analysis under high pressure using diamond-anvil cells, *in situ*/*operando* observation of phase transition and compression behavior under extreme conditions, material sciences under extreme conditions, high pressure Earth and planetary science.
BL13XU	X-ray Diffraction and Scattering I	(Sep. 2001)	X-ray diffraction and reflectivity measurements, atomic-scale structural analysis of crystal surfaces and interfaces, ultrathin films, and nanostructures, residual stress measurement, time-resolved X-ray diffraction, *in situ* process observation using X-ray diffraction, *operando* X-ray diffraction, high-resolution powder X-ray diffraction and X-ray total scattering, structural refinement using Rietveld analysis, *in situ*/*operando* powder X-ray diffraction, time-resolved powder X-ray diffraction, analysis of local structures using nanodiffraction.
BL14B2	XAFS II	(Sep. 2007)	X-ray imaging, XAFS in a wide energy range (3.8–72 keV), XAFS of dilute systems and thin films, time-resolved XAFS by quick scan (time-resolved QXAFS), XAFS at low and high temperatures.
BL19B2	X-ray Diffraction and Scattering II	(Nov. 2001)	Residual stress measurement, structural analysis of thin film, surface and interface, powder X-ray diffraction, X-ray topography, ultrasmall-angle X-ray scattering.
BL20B2	Medical and Imaging I	(Sep.1999)	Micro-radiography, micro-angiography, micro-tomography, and refraction-contrast imaging are the mainly used techniques. BL20B2 is also applicable to small-animal experiments for medical research. Research and development of basic techniques for evaluation of optical devices and X-ray imaging.
BL20XU	Medical and Imaging II	(Sep. 2001)	X-ray micro-/nano-imaging: micro-tomography (micro-CT), nano-CT (15–37.7 keV), refraction/phase contrast imaging, X-ray diffraction tomography (XRD-CT), microbeam/scanning X-ray microscope, research and development of X-ray optics and optical elements, coherent X-ray optics, ultrasmall-angle X-ray scattering (USAXS, 23 keV).
BL25SU	Soft X-ray Spectroscopy of Solid	(Apr. 1998)	Research on electronic states by photoemission spectroscopy (PES), Research on electronic band structures by angle-resolved photoemission spectroscopy (ARPES), study of magnetic states by magnetic circular dichroism (MCD) of soft X-ray absorption, analysis of surface atomic arrangement by photoelectron diffraction (PED), nano-spectroscopic analysis using low-energy/photoemission electron microscope (SPELEEM).
BL27SU	Soft X-ray Photochemistry	(May 1998)	Soft X-ray absorption spectroscopy of dilute samples in partial fluorescence yield mode, surface and interface analysis using depth-resolved soft X-ray absorption spectroscopy, soft X-ray absorption spectroscopy under ambient atmospheric pressure, spectroscopy using soft X-ray microbeam, observation of electron state in solids by soft X-ray emission spectroscopy.
BL28B2	White Beam X-ray Diffraction	(Sep. 1999)	White X-ray diffraction: X-ray topography, energy-dispersive strain measurement, high energy (~200 keV) X-ray microtomography, high-speed X-ray imaging.
BL35XU	Inelastic and Nuclear Resonant Scattering	(Sep. 2001)	Phonons in solids and atomic dynamics in disordered materials by inelastic X-ray scattering, atomic and molecular dynamics by nuclear resonant inelastic scattering and quasi-elastic scattering, synchrotron-radiation-based Mössbauer spectroscopy, nuclear excitation.
BL37XU	Trace Element Analysis	(Nov. 2002)	X-ray microbeam/nano-beam spectrochemical analysis, X-ray spectroscopic imaging, ultratrace-element analysis, high-energy X-ray fluorescence analysis. Projection/scanning/imaging XAFS microscopy, high brightness XAFS, coherent diffraction imaging XAFS microscopy.
BL39XU	Magnetic Materials	(Oct. 1997)	X-ray magnetic circular dichroism (XMCD) spectroscopy and element-specific magnetometry (ESM), XAFS and XMCD spectroscopy under extreme conditions (high pressure, high magnetic field, and low/high temperature), XAFS and XMCD spectroscopy using micro/nanobeam and variable X-ray polarization (horizontally/perpendicularly linear or circular), scanning XAFS and XMCD microscopy using micro/nanobeam, X-ray emission spectroscopy (XES) and high-energy resolution fluorescence detected (HERFD) XAFS spectroscopy.
BL40XU	High Flux	(Apr. 2000)	Fast time-resolved X-ray diffraction and scattering experiments, X-ray photon correlation spectroscopy, X-ray fluorescence analysis, microbeam X-ray diffraction and scattering experiments, micro-crystallography.
BL40B2	SAXS BM	(Sep. 1999)	Small-angle X-ray scattering (SAXS).
BL41XU	Macromolecular Crystallography I	(Oct. 1997)	Macromolecular crystallography, micro-crystallography, ultrahigh resolution structural analysis.
BL43IR	Infrared Materials Science	(Apr. 2000)	Infrared microspectroscopy.
BL45XU	Macromolecular Crystallography II	(Apr. 2019)	Macromolecular crystallography, micro-crystallography, automation and high throughput data collection for protein crystallography.
BL46XU	HAXPES II	(Nov. 2000)	Hard X-ray photoemission spectroscopy, ambient pressure hard X-ray photoemission spectroscopy.
BL47XU	Micro-CT	(Oct. 1997)	X-ray micro-/nano-imaging including CT (7–15 keV), refraction/phase contrast imaging, high speed X-ray imaging, microbeam/scanning X-ray microscope.

BL #	Beamline Name	(Public Use) or (First Beam)	Areas of Research and Available Techniques
	● Contract Beamlines	as of April 2024	
BL03XU	**Advanced Softmaterial** (Advanced Softmaterial Beamline Consortium)	(Nov. 2009)	Structural characterization of softmaterials using small- and wide-angle X-ray scattering, grazing-incidence small- and wide-angle X-ray scattering for thin films.
BL08B2	**Hyogo BM** (Hyogo Prefecture)	(Jun. 2005)	Small angle X-ray scattering, X-ray imaging, X-ray computed tomography, X-ray topography.
BL11XU	**QST Quantum Dynamics I** (National Institutes for Quantum Science and Technology)	(Oct. 1998)	Mössbauer spectroscopy, resonant inelastic X-ray scattering, X-ray emission spectroscopy, surface X-ray diffraction (*in situ* studies on crystal growth of III-V group semiconductor).
BL12B2	**NSRRC BM** (National Synchrotron Rad. Res. Center)	(Oct. 2000)	X-ray absorption spectroscopy, powder X-ray diffraction, high resolution X-ray scattering, protein crystallography.
BL12XU	**NSRRC ID** (National Synchrotron Rad. Res. Center)	(Dec. 2001)	Non-resonant or resonant inelastic X-ray scattering, hard X-ray photoemission spectroscopy.
BL14B1	**QST Quantum Dynamics II** (National Institutes for Quantum Science and Technology)	(Dec. 1997)	High-temperature and high-pressure X-ray diffraction measurements mainly on hydrogen materials, XAFS for dilute samples, time-resolved energy-dispersive XAFS, irradiation research on biomaterials.
BL22XU	**JAEA Actinide Science I** (Japan Atomic Energy Agency)	(May 2002)	HAXPES, microbeam XAFS, residual stress/strain distribution analysis, X-ray imaging, time-resolved X-ray diffraction, surface X-ray diffraction, high-energy X-ray diffraction, high-pressure science, coherent X-ray diffraction.
BL23SU	**JAEA Actinide Science II** (Japan Atomic Energy Agency)	(Feb. 1998)	Surface chemistry with supersonic molecular beam, photoelectron spectroscopy, magnetic circular dichroism, STXM.
BL24XU	**Hyogo ID** (Hyogo Prefecture)	(May. 1998)	Microbeam small- and wide-angle X-ray scattering for local structure analysis, scanning and imaging microscope, micro-tomography, coherent diffraction, microbeam X-ray diffraction and bright field X-ray topography for electronic device materials, near-ambient pressure hard X-ray photoelectron spectroscopy.
BL28XU	**Advanced Batteries** (Kyoto University)	(Apr. 2012)	Characterization of rechargeable battery reactions and battery related materials by resonance X-ray diffraction, X-ray absorption spectroscopy (XAS), X-ray diffraction spectroscopy (XDS), and hard X-ray photoemission spectroscopy (HAXPES).
BL31LEP	**Laser-Electron Photon II** (RCNP, Osaka University)	(Oct. 2013)	Quark nuclear physics (hadron physics) studied in photon-nucleon and photon-nucleus reactions using high-intensity linearly polarized GeV photon beams from laser-induced Compton scattering; testing detectors using electrons or positrons converted from GeV photons.
BL33XU	**TOYOTA** (Toyota Central R&D Labs., Inc.)	(Apr. 2009)	Time-resolved XAFS. 3DXRD, characterization of industrial materials and devices (e.g., catalysts, lightweight bodies, secondary batteries, fuel cells, and power modules).
BL44XU	**Macromolecular Assemblies** (IPR, Osaka University)	(May 1999)	Crystal structure analysis of biological macromolecular assemblies (e.g., membrane protein complexes, protein complexes, protein-nucleic acid complexes, and viruses).
	◆ RIKEN Beamlines		
BL05XU	**R&D-ID I**	(Mar. 2004)	R&D of high-energy X-ray optics, instruments, and applications; structural and dynamical research using small and wide angle scattering.
BL07LSU	**R&D-ID II**	(Oct. 2009)	R&D of soft X-ray optics, instruments, and applications.
BL15XU	**RIKEN Materials Science III**	(Oct. 2021)	Advanced diffraction and scattering with high-energy X-rays.
BL16XU	**Analytical Science I**	(Oct. 1998)	Characterization of materials and products using multiple analytical techniques. (e.g., multi-axis diffractometer)
BL16B2	**Analytical Science II**	(Oct. 1998)	Characterization of materials and products using multiple analytical techniques. (e.g., X-ray digital topography)
BL17SU	**RIKEN Coherent Soft X-ray Spectroscopy**	(Sep. 2003)	High resolution photoemission spectroscopy; soft X-ray emission spectroscopy; soft X-ray diffraction spectroscopy; soft X-ray microspectroscopy.
BL19LXU	**RIKEN SR Physics**	(Oct. 2000)	SR science with highly brilliant X-ray beam.
BL26B1	**RIKEN Structural Genomics I**	(Apr. 2002)	Structural biology research based on single crystal X-ray diffraction.
BL26B2	**RIKEN Structural Genomics II**	(Apr. 2002)	Structural biology research based on single crystal X-ray diffraction.
BL29XU	**RIKEN Coherent X-ray Optics**	(Dec. 1998)	X-ray optics, especially coherent X-ray optics.
BL32XU	**RIKEN Targeted Proteins**	(Oct. 2009)	Protein microcrystallography.
BL32B2	**R&D-BM**	(May 2002)	X-ray computed tomography; X-ray diffraction; X-ray absorption fine structure; R&D of SR instruments.
BL36XU	**RIKEN Materials Science II**	(Mar. 2020)	Time resolved XAFS and X-ray diffraction; 2D/3D scanning XAFS imaging; 3D computed tomography/laminography XAFS imaging; X-ray emission spectroscopy; pink beam experiments.
BL38B1	**RIKEN Structural Biology I**	(Oct. 2000)	Structure study of non-crystalline biological materials using small-angle scattering and diffraction techniques.
BL38B2	**Diagnosis Beamline**	(Sep.1999)	Accelerator beam diagnostics.
BL43LXU	**RIKEN Quantum NanoDynamics**	(Oct. 2011)	High resolution inelastic X-ray scattering for investigating atomic and electronic dynamics.
BL44B2	**RIKEN Materials Science I**	(Feb. 1998)	Structural materials science research using powder X-ray diffraction.

IV. User Program and Statistics

In principle, SPring-8 calls for public use proposals twice a year. Since the 2022B term, nine public beamlines have started inviting proposals six times annually, including the beamlines previously intended for industrial applications. Submitted proposals are reviewed by the SPring-8 Proposal Review Committee (SPring-8 PRC). Since 1997, SPring-8 has accepted a variety of proposals. For the promotion of research on industrial applications at SPring-8, currently, Industrial Application Proposals account for approximately 16%–19% of the total number of proposals conducted at various public beamlines. Certain companies and research institutes find retaining specialized staff and accommodating the need for quick access to SPring-8 difficult. The SPring-8 Measurement Service has been provided to appropriately respond to these circumstances.

In this framework of service, JASRI staff members perform measurements on behalf of users. Users may visit SPring-8 and be present during the measurements or simply send their samples to SPring-8. BL28B2 was added to the Measurement Service BL in 2022B. JASRI expanded the purview of the SPring-8 Measurement Service to include five measurement methods (XAFS, Powder X-ray Diffraction, Small Angle X-ray Scattering, High energy X-ray CT, Hard X-ray Photoemission Spectroscopy). In addition, JASRI provides Protein Crystallography Automatic Data Collection at the Macromolecular Crystallography beamlines. Therefore, users can choose to be present at SPring-8 during the measurements or simply send their samples to SPring-8. Since 2022A, JASRI has begun suggesting Hour-based usage at most public beamlines as part of its proprietary time-designated proposals. According to this change, the feasibility study proposals for industrial applications have been integrated into this proposal program. Further, SPring-8 is developing a remote operation system that allows users to control the experimental instruments from outside to promote remote access. The numbers of experiments conducted and user visits to public and contract beamlines are presented in Fig. 3. Part of the proposals are for proprietary use, and do not require refereed reports. Figures 4 to 13 show information related to the user programs.

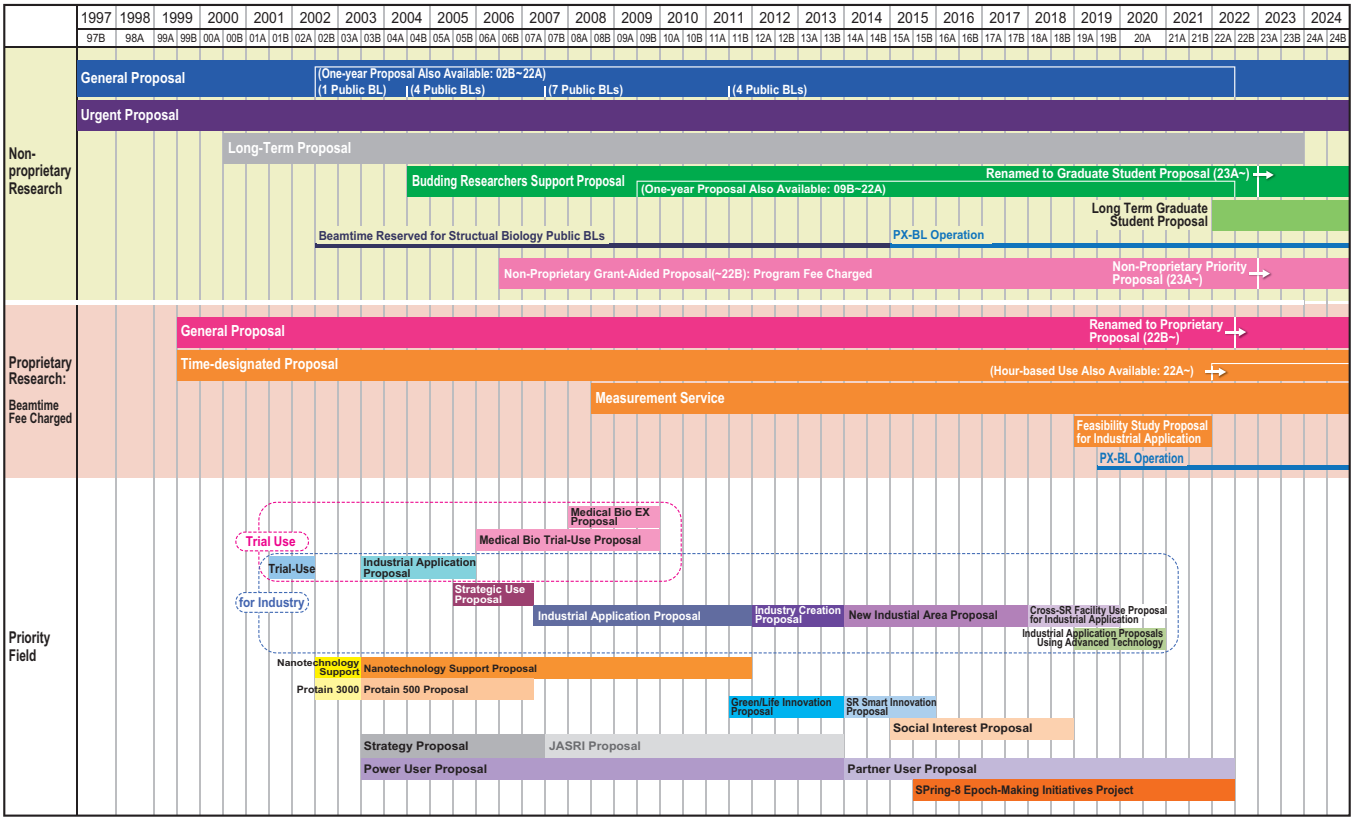

Fig. 3. Categories of proposals for the public beamlines.

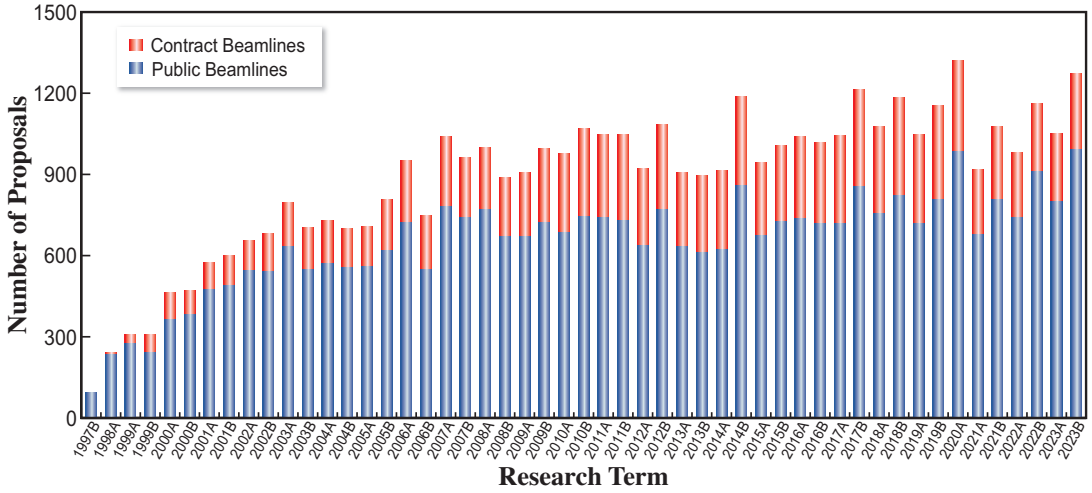

Fig. 4. Numbers of conducted experiments.

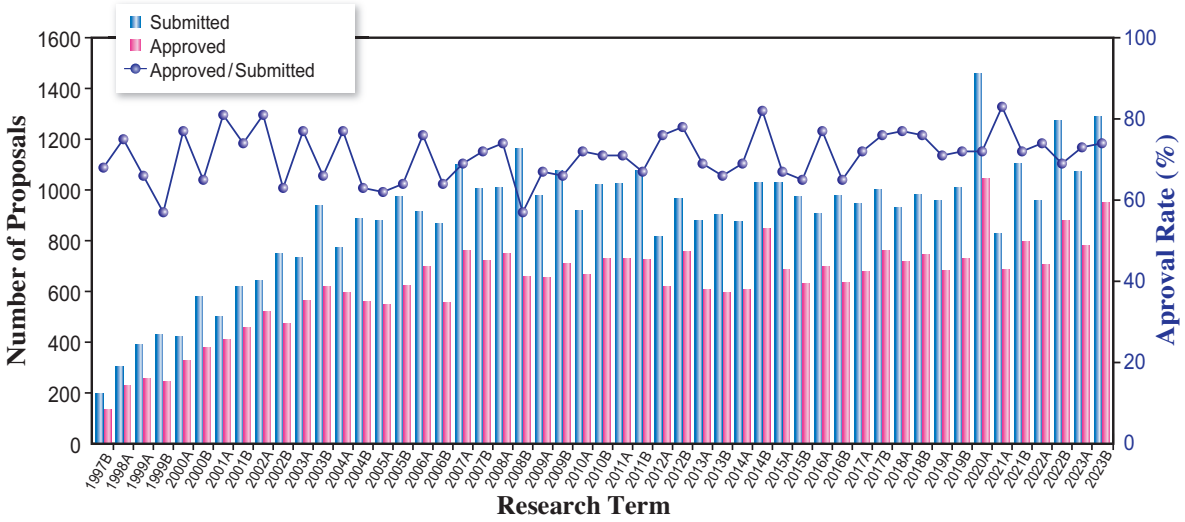

Fig. 5. Numbers of submitted proposals and approved proposals by research term (public beamlines).

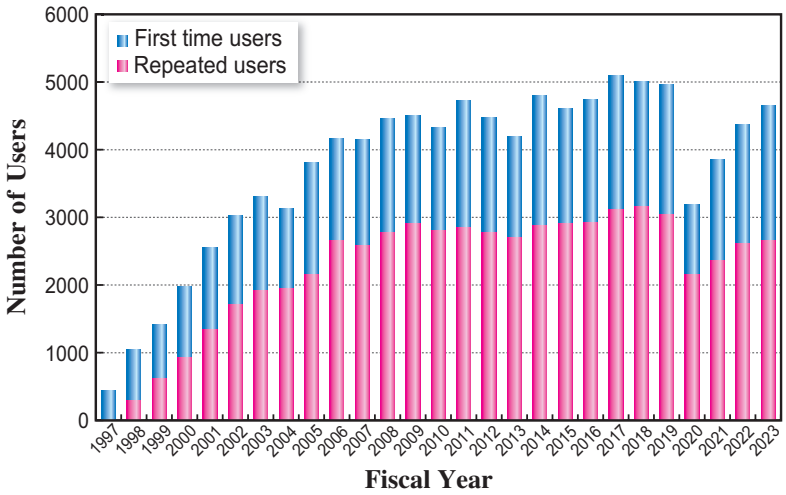

Fig. 6. Numbers of users by fiscal year.

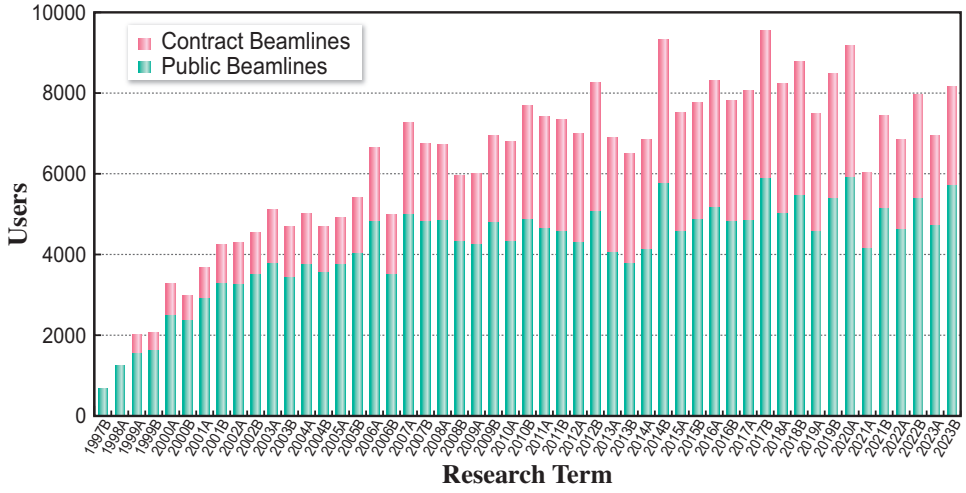

Fig. 7. Numbers of users visits by research term.

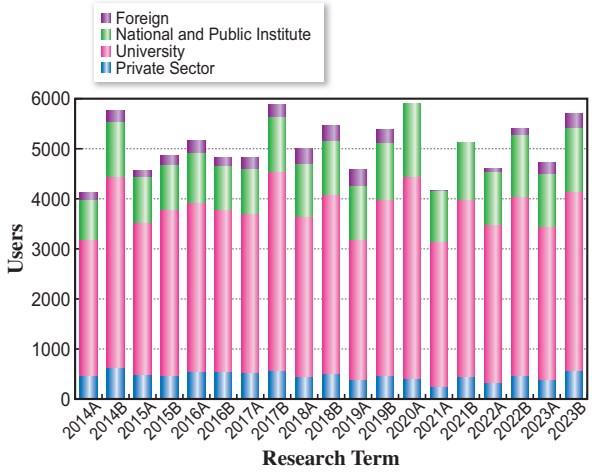

Fig. 8. Numbers of users by affiliation categories (public beamlines).

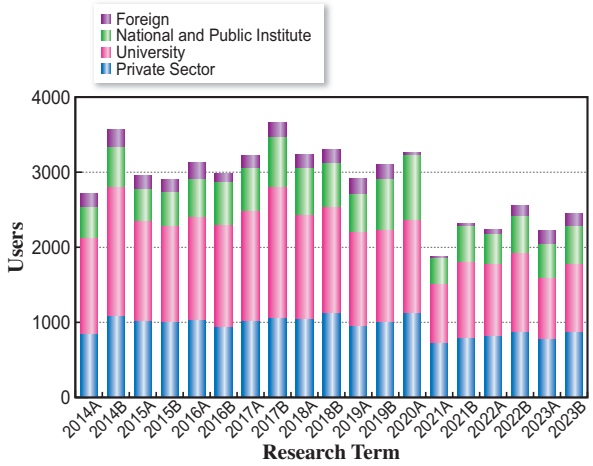

Fig. 9. Numbers of users by affiliation categories (contract beamlines).

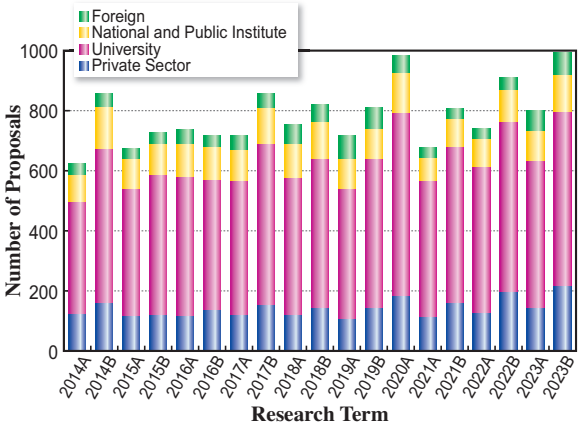

Fig. 10. Numbers of conducted proposals by affiliation (public beamlines).

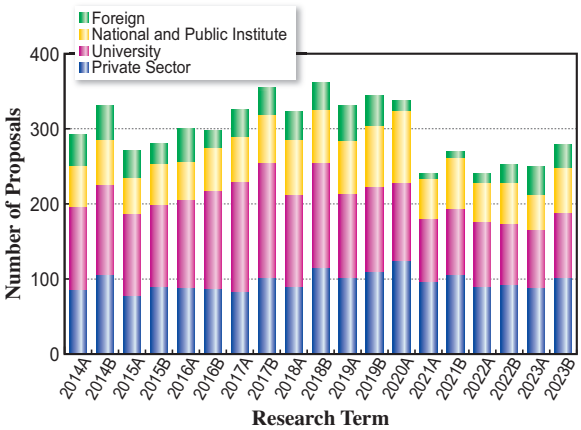

Fig. 11. Numbers of conducted proposals by affiliation categories (contract beamlines).

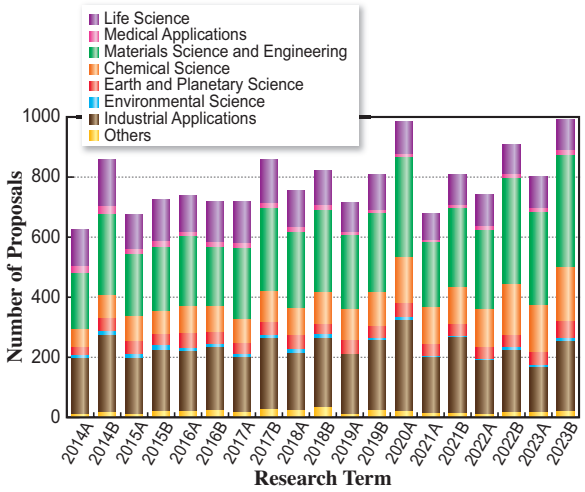

Fig. 12. Numbers of conducted proposals by research area (public beamlines).

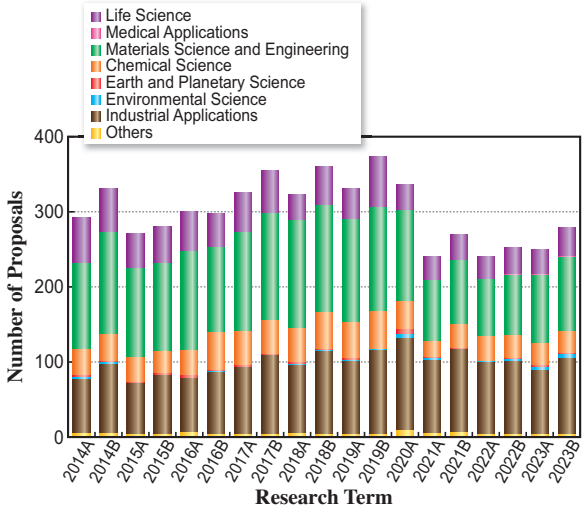

Fig. 13. Numbers of conducted proposals by research area (contract beamlines).

V. Research Outcome

As of March 2024, the total number of registered refereed papers from SPring-8 is 22,211. Figure 14 shows the annual statistics of refereed papers.

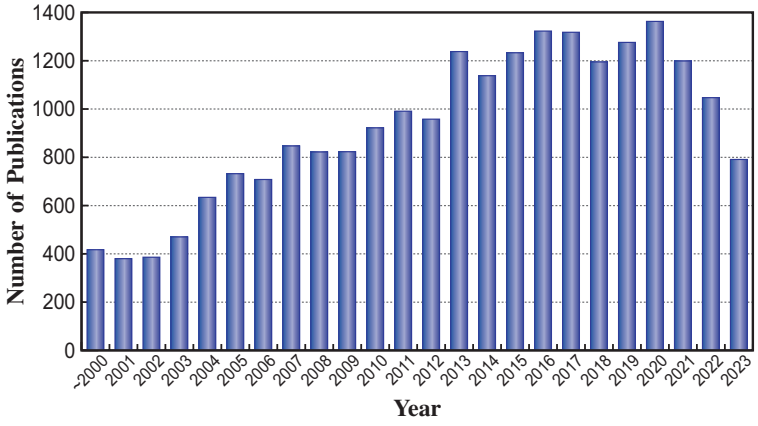

Fig. 14. Number of refereed publications.

VI. Research Complex

The facilities of SPring-8, SACLA, and NewSUBARU form the Center of Excellence (COE) on the SPring-8 campus where JASRI, public beamline users, contractors of contract beamlines, RIKEN, and the University of Hyogo work in close cooperation. Thus, a research complex has been formed, where each member has their own role in achieving high-quality results in the field of synchrotron radiation science and technology. The organizational charts of RIKEN and JASRI, which are at the center of this research complex, are shown in Fig. 15 and Fig. 16, respectively.

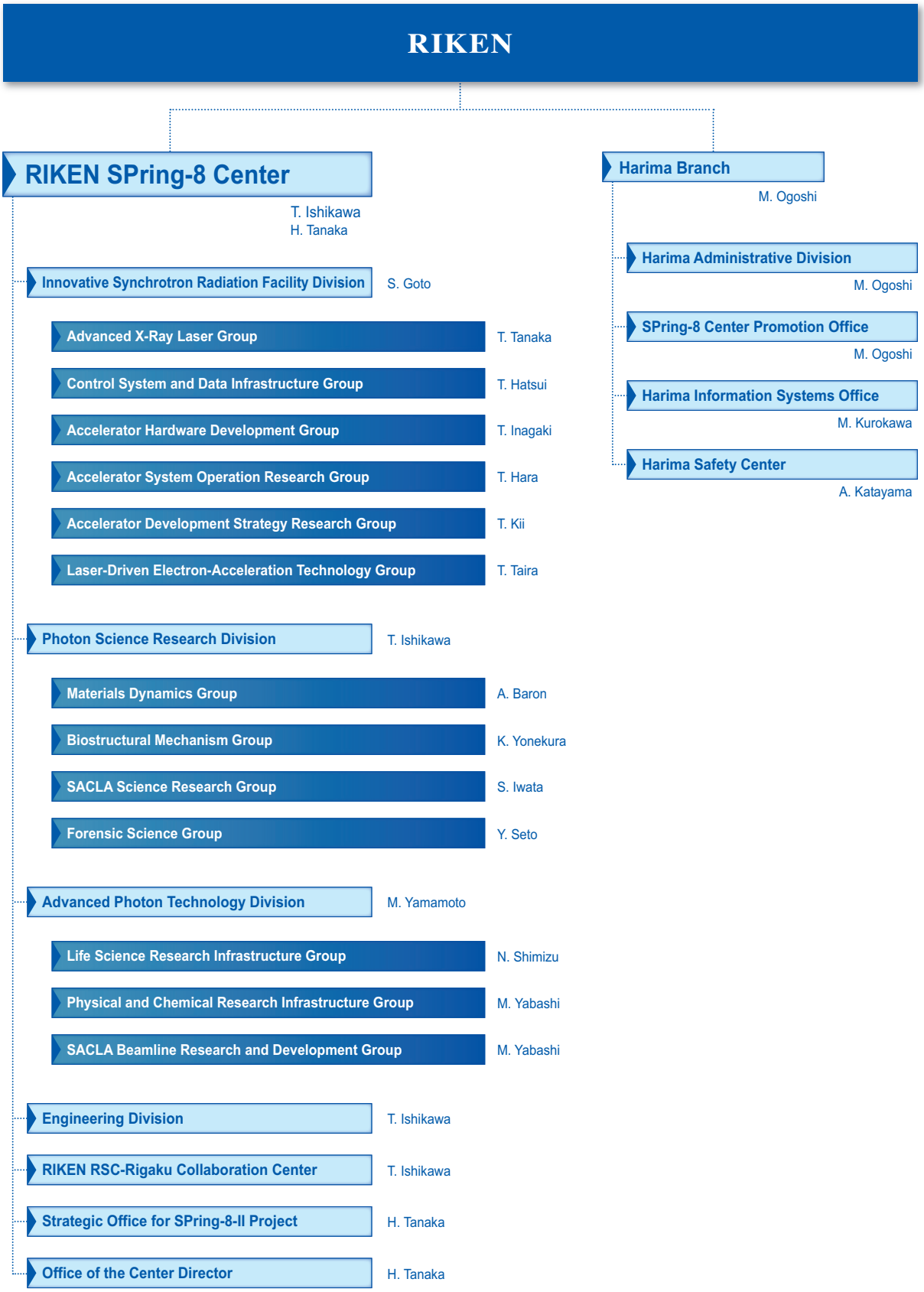

Fig. 15. RIKEN Harima Campus chart as of April 2024.

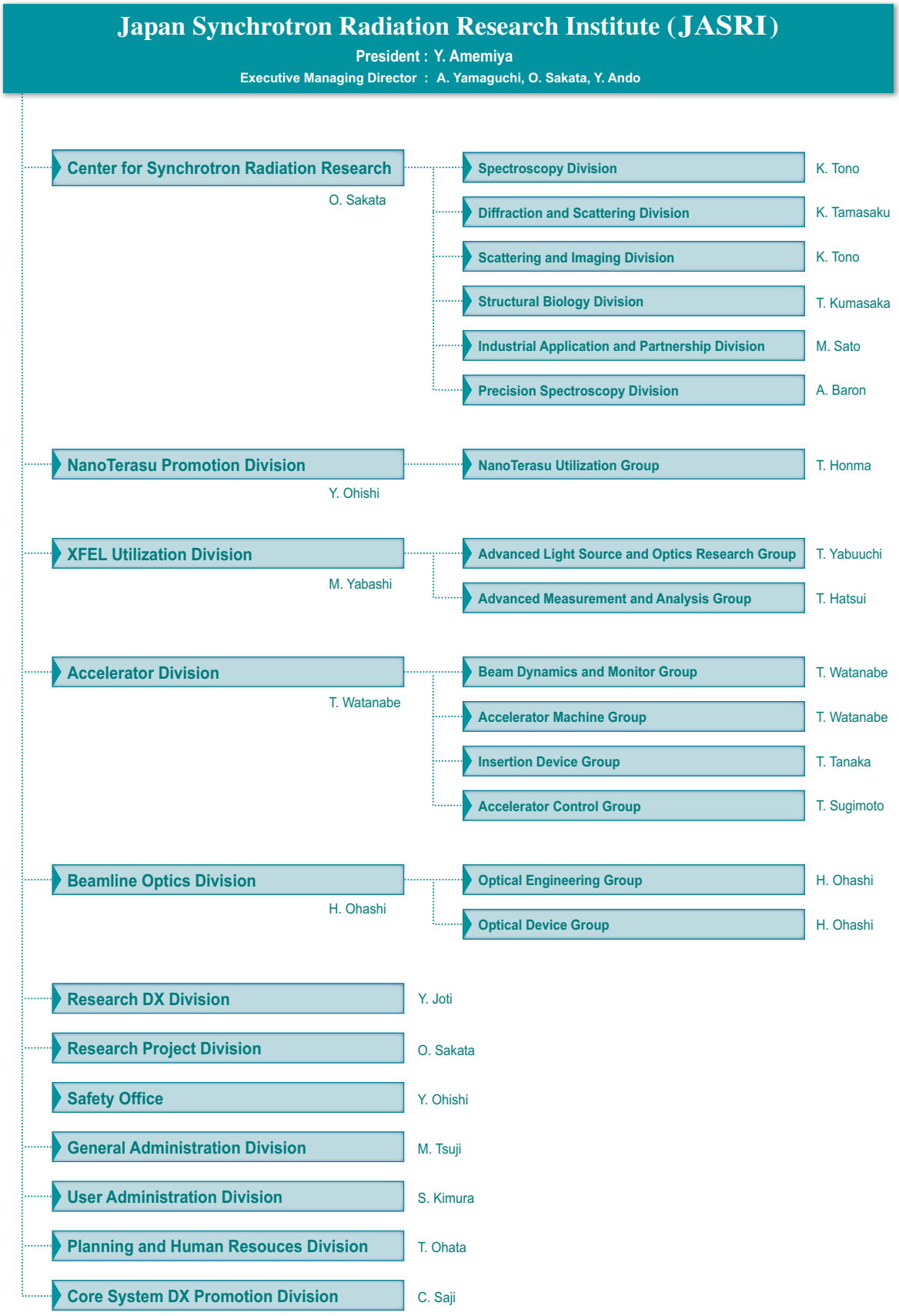

Fig. 16. JASRI chart as of April 2024.

VII. SPring-8 Users Community (SPRUC)

Professor E. Nishibori
University of Tsukuba
SPRUC Chairman FY2023

The SPring-8 Users Community (SPRUC) is a user society comprising of all users of SPring-8/SACLA. In addition to individuals, representative organizations comprising 26 institutes (principal universities, national/international research institutes, industries, and beamline consortiums) participate in SPRUC to discuss strategies and perspectives to promote the utilization of SPring-8 and SACLA.

The SPring-8 Symposium is an important annual event of SPRUC. SPring-8 Symposium 2023 was jointly organized by Osaka University, RIKEN, and JASRI, and held on September 26–27 at Osaka University Hall and streamed online. A total of 489 people attended the symposium, 268 of whom participated online. The symposium theme was "Possibilities Generated by Integrations of SPring-8/SACLA and Data Science." This theme was designated to create a vision for the future of next-generation synchrotron radiation science We discuss how to handle the big data produced by SPring-8, which is increasing explosively, as well as the progress of SPring-8, and what kinds of new science will be created. In addition, the 12th SPRUC Young Scientist Award ceremony was held. This year, the selection committee conferred awards on Professor Shunsuke Kitou from the University of Tokyo, and Professor Ken-ichi Otake from Kyoto University. The upcoming SPring-8 Symposium in 2024 will be held at Kyusyu University.

SPRUC supported the “SPring-8 Summer School” held on July 9–12 for enhancing users’ research competency, and hosted the “SPring-8 Autumn School” on September 10–13 with JASRI for acquiring new users and developing human resources. SPring-8 Summer School is an event using SPring-8 and consists of lectures and practical training, mainly targeted at graduate students in master's courses. In contrast, the SPring-8 Autumn School targets third- and fourth-year students, graduate students, and researchers from companies, which is open to those who are not registered as radiation workers. The SPRUC research groups contributed to the planning of lectures at the Autumn School. This year, 76 participants attended lectures and underwent simulated hands-on training at SPring-8.

SPRUC2023 Young Scientist Award
Prof. M. Oshima, Prof. K. Otake, Prof. E. Nishibori, and Prof. S. Kitou

SPRUC hosted the sixth beamline upgrade workshop on February 29 with RIKEN and JASRI, as in previous years. In the workshop, the beamlines (BL08W, BL13XU, and BL46XU) that completed upgrades and related research groups presented their recent status and feedback. This was followed by the reporting of the progress of beamline reorganizations (BL04B2, BL15XU, BL39XU, and BL40XU). We shared the progress of ongoing beamline upgrades, the development of new equipment and methods, the latest information on SPring-8-II and the SPring-8 Data Center, and requests from research groups as well as proposals for future beamline upgrades toward SPring-8-II to exchange opinions among facilities and users.

The sixth-term SPRUC research groups were voluntarily organized in each research field, and comprised 35 research groups. The research groups actively held meetings to collect ideas and determined the need for beamline upgrades in each research field. This year, most research meetings were held face-to-face, rather than online. SPRUC calls for the application of seventh-term SPRUC research groups, as of March 4. The next term of research groups begins with a review process in April.

SPring-8 Symposium 2023

VIII. Outreach Activities

To reach new users in unexplored application fields, SPring-8 holds various serialized seminars named "Workshop on Advanced Techniques and Applications at SPring-8." Representative examples are as follows:

- 89th: Synchrotron Radiation and Neutron Beam Joint Usage Workshop
  April 26, 2023 • Video conference
- 94th: Current Status and Future of Protein Structural Biology Research at SPring-8
  September 25 and 26, 2023 • Osaka University
- 92nd: Cutting-Edge of SiC Power Device Development in Synchrotron Radiation
  November 29, 2023 • Shin-Osaka Brick Building

SACLA

I. Machine Operation & Beamlines

Our twelfth year of operations proceeded without any significant issues. Operation statistics are summarized in Table 1. The ratio of downtime to user time was kept below 3%, a reasonably low rate for linac-based light sources.

Table 1. Operation Statistics for FY2023

		Time (h)
Total operation time		5690.55
User time		
	BL1	1308
	BL2	1992
	BL3	2928
Facility tuning time		696
Downtime		134.1

In 2012, two beamlines, BL3 for XFEL and BL1 for broadband spontaneous light, were opened for users, while all experiments were conducted at BL3. As the newest beamline, construction of BL2 was completed during the summer shutdown of 2014, and first laser amplification was achieved on October 21. An upgraded beamline for soft X-ray FEL, BL1, which combines the prototype accelerator of SACLA (SCSS), started operation in 2016. Parallel user operation of BL2 and BL3 started in 2018.

II. User Program and Statistics

SACLA normally calls for public user proposals twice per year. Moreover, SACLA Feasibility Study Program has started since 2021A to provide an opportunity to experience the use on a trial basis for the purpose of dissemination and enlightenment.

In FY2016, JASRI introduced the proprietary research of General Proposals and the Proprietary Time-Designated Proposals. The project leaders of these proprietary proposals are not required to publish their research results, but required to pay each beamtime fee. In addition, to apply for the proprietary research the project leaders should be affiliated with corporate enterprises or academic research institutions, which are located and registered in Japan.

Figures 1 and 2, and Table 2 provide statistics on proposals, users, and beamtime.

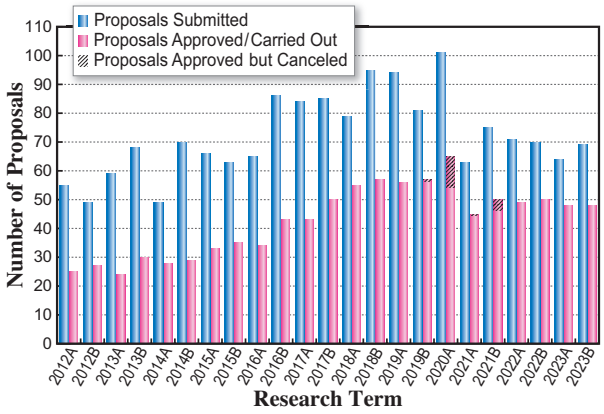

Fig. 1

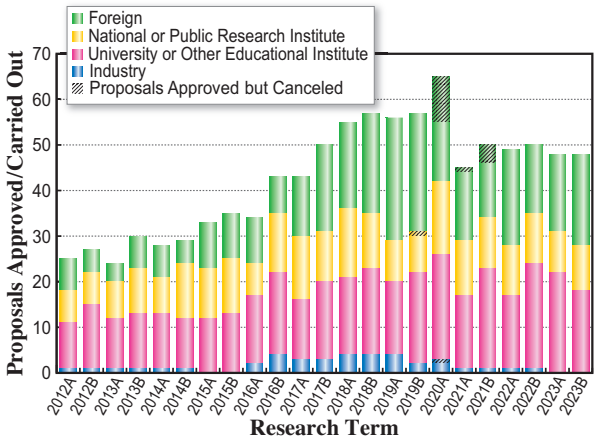

Fig. 2

Table 2. Number of proposals submitted, proposals approved/carried out, cumulative users, and beamtime available by research term

Half-year Research Term	Proposals Submitted	Proposals Approved / Carried Out					Cumulative Users	Beamtime Carried Out (Shifts)
			Priority Strategy Proposals	Non-proprietary	Proprietary			
				General Proposals	General Proposals	Time-Designated Proposals		
2012A	55	25	(12)	(13)	–	–	297	126
2012B	49	27	(19)	(8)	–	–	461	154
2013A	59	24	(15)	(9)	–	–	268	117
2013B	68	30	(19)	(11)	–	–	410	139
2014A	49	28	(20)	(8)	–	–	400	147
2014B	70	29	(17)	(12)	–	–	430	140
2015A	66	33	(23)	(10)	–	–	527	144
2015B	63	35	(23)	(12)	–	–	552	152
2016A	65	34	(21)	(12)	(1)	–	538	158
2016B	86	43	(21)	(20)	(1)	(1)	650	197
2017A	84	43	–	(43)	(0)	(0)	577	210
2017B	85	50	–	(50)	(0)	(0)	642	244
2018A	79	55	–	(55)	(0)	(0)	643	257
2018B	95	57	–	(56)	(0)	(1)	653	264
2019A	94	56	–	(55)	(0)	(1)	564	259
2019B	81	57	–	(56)	(0)	(0)	650	266
2020A	101	65	–	(54)	(0)	(0)	461	276
2021A	63	45	–	(44)	(0)	(0)	465	248
2021B	75	50	–	(46)	(0)	(0)	468	254
2022A	71	49	–	(49)	(0)	(0)	570	249
2022B	70	50	–	(50)	(0)	(0)	588	259
2023A	64	48	–	(48)	(0)	(0)	519	248
2023B	69	48	–	(48)	(0)	(0)	560	269

One shift = 12 hours at SACLA beamlines

SPring-8/SACLA

Budget and Personnel

When SPring-8 started operations in 1997, it was jointly managed by RIKEN, JAERI (now JAEA), and JASRI. However, JAEA withdrew from the management of SPring-8 on September 30, 2005. Currently, SPring-8 is collaboratively administered by RIKEN and JASRI.

RIKEN established specific synchrotron radiation facilities (i.e., SPring-8 and SACLA) and is responsible for their operation and maintenance. JASRI selects and supports users of these facilities under the "Act on the Promotion of Public Utilization of the Specific Advanced Large Research Facilities."

Figure 1 shows government subsidy for SPring-8 and SACLA. Figure 2 shows the manpower of JASRI and RIKEN.

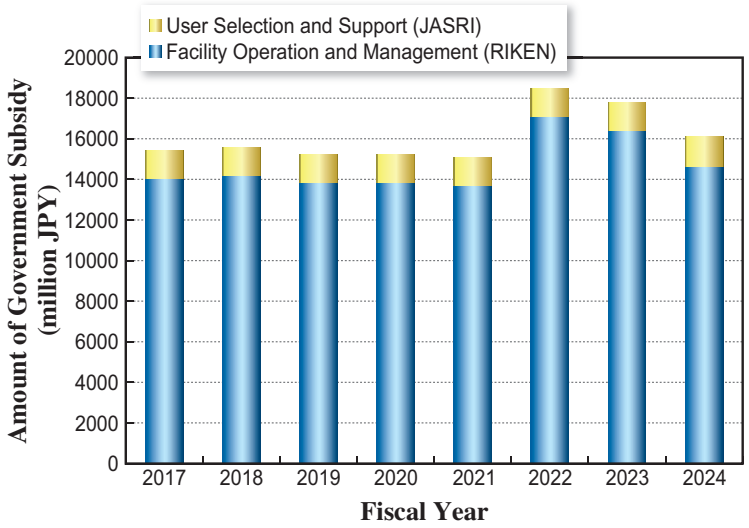

Fig. 1. Government subsidy (SPring-8 and SACLA).

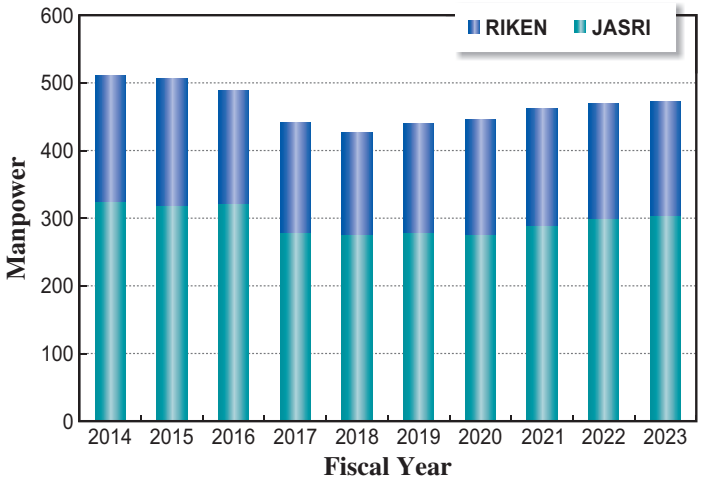

Fig. 2. Manpower at SPring-8: JASRI and RIKEN.

SPring-8 SACLA
Research Frontiers 2023

Editor

Toyohiko Kinoshita
Japan Synchrotron Radiation Research Institute (JASRI)

Editing, Design & Layout

Marcia M. Obuti-Daté
Japan Synchrotron Radiation Research Institute (JASRI)

Printing
Hokuoh Printing Co.

JASRI
Information & Outreach Section
Users Administration Division

1-1-1 Kouto, Sayo-cho, Sayo-gun
Hyogo 679-5198 • JAPAN
Tel: +81-(0)791-58-2785 Fax: +81-(0)791-58-2786

Email: frontiers@spring8.or.jp
http://www.spring8.or.jp/

August 2024

SPring-8 SACLA

http://www.spring8.or.jp

Japan Synchrotron Radiation Research Institute (JASRI)
1-1-1 Kouto, Sayo-cho, Sayo-gun, Hyogo 679-5198, Japan